Engineering Electronic Pathways Within Cathode Microstructures Through Carbon-Coated NMC via Mechanofusion

A thesis submitted in partial fulfilment of the requirements for the degree of

DOCTOR OF PHILOSOPHY

By

Guo Jung Lian

Under the supervision of Prof Rachel Smith and Dr Denis Cumming

The University of Sheffield

Faculty of Engineering

Department of Chemical and Biological Engineering

August 2024

Declaration

I, the author, confirm that the Thesis is my own work, except as acknowledged in the text. I am aware of the University's Guidance on the Use of Unfair Means. This work has not previously been presented for an award at this, or any other, university.

Guo J. Lian

Acknowledgements

I would first like to express my sincere thanks to my supervisors, Prof Rachel Smith and Dr Denis Cumming, for the opportunity to carry out this PhD. Your expertise, ideas and guidance have been invaluable and our conversations have profoundly shaped my academic and personal growth. This has been a life-changing experience, challenging and rewarding in equal terms, one that I will forever be grateful for.

I would like to thank all members of the Nextrode group and Particle Technology Group, past and present. In particular, I want to thank Prof Jim Litster for his recommendation for this PhD position. I am very grateful to Dr Jake Entwistle, Dr Xuesong Lu, Dr Milan Sadan and Dr Andrew Dennison for their advice and guidance. Special thanks to Charlie Stothard for his technical expertise and Carla Teale for her administrative support. I am immensely grateful to the best post-doc anyone could ask for, Dr Kate Pitt, for her relentless support, both academically and personally, starting back in my undergraduate Masters research project days in 2019. Without her encouragement, I wouldn't even have considered pursuing a PhD. Thank you for making me feel so welcome in the group, for your invaluable advice, and for the enjoyable fun times and drinks.

I would like to thank the staff at the Sorby Centre for Electron Microscopy and Dr Oday Hussein at the Royce Discovery Centre for their expertise. I would like to acknowledge the workshop and lab technician team for their services and assistance. In terms of collaborative work, I extend my appreciation to Prof Emma Kendrick, Dr Carl Reynolds and Sam Gray for their support at the University of Birmingham. Additionally, I would also like to thank Tian-Jay Mason, Ellie Bibby, Prateek Verma and Oliver Kerton for their contributions to the project through their research projects.

Thank you to Jed, Kavi, James, Hamza, Suruthi, Georgia, Victoria, Calum and Peyman for being great PhD buddies. Starting a PhD during the pandemic was never the best idea but I am lucky to have the accompaniment of the gang at work and 165 West Street. Thank you to Joanne, Jen, Jordan, Emily, Nic, Teck Sing, Nat, Nellie, Eugene, Thien Hee, Eddie and Zac, I will forever cherish the great memories outside the PhD bubble over the years. To Connor; Jasmie, Reece and Ernest on the other side of the world and everyone elsewhere. This list of people to thank is obviously endless but I appreciate each and every one of you.

Finally, my deepest gratitude goes to my family. They have provided me with the fullest support over the years and this accomplishment would not have been possible without their unwavering belief in me. I owe it all to them.

List of Outputs

Publications

- X. Lu, **G. J. Lian**, R. Ge, J. Parker, M. K. Sadan, R. M. Smith, D. Cumming, 'Effect of carbon blacks on electrical conduction and conductive binder domain of next-generation lithium-ion batteries', Journal of Power Sources, vol. 592, p. 233916, Feb. 2024, doi: 10.1016/j.jpowsour.2023.233916.

- M. K. Sadan, **G. J. Lian**, R. M. Smith, and D. Cumming, 'Co, Ni-Free Ultrathick Free-Standing Dry Electrodes for Sustainable Lithium-Ion Batteries', ACS Appl. Energy Mater., vol. 6, no. 24, pp. 12166–12171, Dec. 2023, doi: 10.1021/acsaem.3c02448.

- X. Lu, **G. J. Lian**, R. Ge, J. Parker, M. K. Sadan, R. M. Smith, D. Cumming, 'Microstructure of Conductive Binder Domain for Electrical Conduction in Next-Generation Lithium-Ion Batteries', Energy Tech, p. 2300446, Aug. 2023, doi: 10.1002/ente.202300446.

- **G. J. Lian**, P. Verma, D. Cumming, R. M. Smith, 'Probing carbon black deagglomeration in lithium-ion battery cathode manufacturing using powder resistivity metrics' *Under review*

Oral Presentations

- **Nextrode Consortium Meeting** – University of Sheffield, May 2024
- **The Faraday Institution Expert Panel Review Meeting –** Birmingham, March 2024
- **International Battery Production Conference –** Braunschweig, Germany, November 2023

Poster Presentations

- **ChemEngDay 2024 –** Imperial College London, April 2024
- **Nextrode Consortium Meeting –** University of Sheffield, May 2024
  – University of Oxford, December 2023
  – UK Battery Industrialisation Centre, March 2023
  – University of Warwick, September 2022
  – Edgbaston, Birmingham, March 2022
- **Battery Symposium –** University of Sheffield, December 2023
  – University of Sheffield, December 2022
- **The Faraday Institution Conference –** University of Birmingham, September 2023
- **The Faraday Institution ECR Conference –** University of Warwick, November 2022
- **CBE Summer 2022 PGR Conference –** University of Sheffield, August 2022

Collaborations

- **Slurry Rheology of Coated Particles**
  Prof Emma Kendrick, Dr Carl Reynolds and Sam Gray, University of Birmingham, 2024

- **Electrochemical Impedance Spectroscopy of Cathode Slurries**
  Oliver Kerton, MEng Research Project 2023/24

- **Mechanofusion for Next-Generation Lithium-Ion Battery Cathode Manufacturing**
  Prateek Verma, Faraday Undergraduate Summer Experience 2023

- **Novel Coating Method of Sustainable Dual-Cathode Materials for Li-Ion Batteries**
  Ellie Bibby, MEng Research Project 2022/23

- **Improving the Conductivity of NMC622 Cathodes by Coating Carbon Nanotubes with a Facile Mechanofusion Method**
  Tian-Jay Mason, MEng Research Project 2022/23

Abstract

Achieving high energy and power density in lithium-ion batteries requires precise control of conductive additive distribution within the electrode microstructure. Despite its critical role, the understanding of electronic pathways within electrodes remains limited. Moreover, existing manufacturing practices rely heavily on empirical knowledge and lack a mechanistic understanding. This thesis introduces a novel approach to optimise conductive additive utilisation through particle and electrode engineering. For the first time, a high-shear dry mixing technique, mechanofusion, was employed to create carbon-coated NMC particles and engineer electronic pathways within electrodes. The impact of processing parameters on coating characteristics, carbon black deagglomeration, and particle-level properties was investigated. The correlation between coating properties, slurry mixing and drying behaviour, and the slurry and electrode microstructure and electronic conductivity was explored. Conductive pathway design within electrodes was explored by systematically varying carbon content and mixing methods. The mechanofusion process effectively facilitated carbon black deagglomeration and coating formation on NMC particles. Coating characteristics were controlled through process parameters, with free carbon content decreasing with prolonged dry mixing. A novel powder resistivity measurement technique revealed that a short dry mixing time is sufficient to achieve minimal deagglomeration for low powder resistivity. Carbon black properties (i.e. structure level, particle size and graphitic character) impacted deagglomeration and the final resistivity. Coated NMC surfaces influenced PVDF adsorption and drying behaviour, which in turn affected slurry and electrode properties and their microstructure. High free carbon content during wet mixing was crucial for forming CB-PVDF clusters, facilitating bridge structure formation for long-range conduction in electrodes. While designed conductive pathways were achieved, the initial electronic conductivity did not surpass conventional methods. This research demonstrates the potential of mechanofusion for tailoring electrode microstructures. While further optimisation is necessary, the findings provide valuable insights into the complex relationship between particle-level properties, mixing and drying behaviour and slurry and electrode properties. This work lays the groundwork for developing engineered electrode architectures in next-generation lithium-ion batteries.

Table of Contents

List of Figures

List of Tables

List of Abbreviations

AC	Alternating current
AM	Active material
BET	Brunauer–Emmett–Teller
BSE	Backscattered electron
CB	Carbon black
CBD	Carbon binder domain
CEI	Cathode electrolyte interface
DC	Direct current
DEM	Discrete element method
EDX	Energy-dispersive X-ray spectroscopy
EIS	Electrochemical impedance spectroscopy
ERS	Energy recovery system
EV	Electric vehicle
FEM	Finite element method
FIB	Focused ion beam
FRO	Full-range output
FTIR	Fourier-Transform infrared spectroscopy
HFR	High frequency range
LCO	Lithium cobalt oxide
LFP	Lithium iron phosphate
LIB	Lithium-ion battery
LMO	Lithium manganese oxide
MIP	Mercury intrusion porosimetry
(MW)CNT	(Multi-walled) carbon nanotubes
NCA	Lithium nickel cobalt aluminium oxides
NMC	Lithium manganese nickel cobalt oxide
NMP	N-Methyl-2-pyrrolidone
OAN	Oil absorption number
PET	Polyethylene terephthalate
PMMA	Polymethyl methacrylate
PVDF	Polyvinylidene fluoride
SE	Secondary electron
SEI	Solid electrolyte interface

SEM	Scanning electron microscopy
TEM	Transmission electron microscopy
TGA	Thermogravimetric analysis
V-I	Voltage-current
XPS	X-ray photoelectron spectroscopy

Chapter 1 Introduction

1.1 Background

Lithium-ion batteries (LIB) have become a fundamental part of modern society, underpinning the functionality of portable electronic, electric vehicles and more recently, large-scale energy storage. The remarkable impact can be attributed to a significant history of scientific advancements, dating back to the 1970s where M. Stanley Whittingham first discovered intercalation electrodes. John B. Goodenough's breakthrough in 1980 with the discovery of $LiCoO_2$, followed by Akira Yoshino's discovery of carbonaceous anodes in 1987 paved the way for the development of safe and commercially viable LIB. In 1991, the successful commercialisation of LIB by Sony marked a new era for portable electrochemical energy storage.

The remarkable properties of LIB, particularly their high energy and power densities, make them one of the best options for portable electrochemical energy storage. LIB were first used to power almost all portable electronic devices we use in our daily lives, ranging from mobile phones to laptops. More recently, the global push towards net-zero carbon emissions by 2050, coupled with the electrification of transportation, has propelled electric vehicles (EVs) and even Battery Energy Storage Systems (BESS) to the forefront of energy solutions [1]. However, EV applications pose unique challenges. Battery packs require high energy density for extended-range autonomy, but must also be capable of delivering high power for rapid acceleration [2]. For regular users, a common concern is the capabilities for fast charging, where efficient electronic and ionic conduction within electrodes must be maintained at high current rates [3]. These contrasting demands highlight the limitations of current LIB technology and underpin the need for extensive research in this area.

Optimising LIB performance for these diverse applications requires innovation across the entire battery manufacturing chain. Traditional LIB manufacturing relies heavily on industrial know-how and empirical knowledge. However, to unlock the next level of performance and to address the limitations of current technology, a shift towards a more mechanistic understanding of the electrode manufacturing processes is crucial. This involves developing a deeper scientific understanding of the relationships between material properties, manufacturing processes and product performance. Identifying limitations and inefficiencies within the manufacturing process can enable targeted optimisations, and allow greater predictability control to obtain consistent quality and performance [4]. Additionally, the ability to retrofit existing battery manufacturing techniques with these innovations will be vital for cost-effective and rapid, short-term improvements in LIB technology.

1.2 Motivation

LIB, with their favourable energy storage characteristics, have navigated advancements in modern portable electronics. Recent research has focused on optimising the performance of batteries, particularly on energy and power density, for a range of demanding EV applications. While novel material discovery has been a major focus, less emphasis has been placed on understanding the intrinsic processes and mechanisms that govern within.

The main challenge in achieving further performance gains lies within the electrode, often with the cathode being the limitation. Cathode materials have a lower capacity compared to anode materials. Conductive additives are essential to enhance electronic conduction but their inactive nature reduces overall energy density. Optimising their use enables less quantity needed but requires a fundamental understanding of how electrode manufacturing influences battery performance. Furthermore, there is ongoing debate regarding the relative importance of electronic and ionic conduction within electrodes. While increasing conductive additives may enhance electronic conductivity, it may also increase the tortuosity during carbon binder domain (CBD) formation and impede ionic diffusion [5]. A deeper understanding of how these CBD structures and conductive pathways are formed and their relationship to electrode performance is crucial for the development of next-generation electrodes.

This knowledge gap presents a barrier to the rational design of novel processing techniques and the utilisation of novel materials with unique structures or chemistries. Developing a more comprehensive understanding will also enable the development of more robust, scalable and environmentally friendly manufacturing methods. Ultimately, these advancements are essential for the next generation of batteries with greater power and energy density. Such advancements are also crucial for achieving extended battery lifespans with a sustainable, design-led and process-oriented approach to manufacturing.

Current manufacturing practices heavily rely on wet slurry mixing with a toxic solvent that is harmful to the environment. Growing sustainability concerns about the use of toxic solvents pave the way for low-solvent or solvent-free processing methods that hold promise for both commercially mature or new emerging high-performance battery systems. Additionally, wet mixing offers less control over the formation of CBD within electrodes, highlighting opportunities for dry mixing alternatives such as intensive high-shear mixing. The motivation behind this research lies in overcoming the limitations of current manufacturing practices that rely on harmful solvents and lack precise control over electrode structure. Consequently, mechanofusion has emerged as a promising dry mixing technique due to its ability to utilise high shear and compression forces to simultaneously deagglomerate and coat carbon black on active materials simultaneously.

1.3 Aim and Objectives

The carbon binder domain (CBD) plays a pivotal role in determining the electrochemical performance of batteries. Precise control of the formation of CBD structures through particle and electrode engineering enables the strategic design of conductive pathways within electrodes. This thesis aims to establish a novel dry processing approach, mechanofusion, to control the spatial distribution of conductive additives and the formation of CBD structures for the design of electronic pathways within electrodes. Developing a mechanistic understanding can offer precise manipulation of CBD structures, thereby improving their microstructure to enhance the electrochemical properties of electrodes.

The objectives set out to achieve the aim are:

(1) Controlling carbon coating formation on NMC through mechanofusion approaches as CBD film structures, with a mechanistic understanding of the process-product relationship;
(2) Developing a comprehensive understanding of conductive additive dispersion behaviour in mechanofusion through novel, powder relevant metrics;
(3) Evaluate the slurry and electrode microstructures with designed conductive pathways and electronic conductivities.

1.4 Thesis Structure

Chapter 1 introduces the background and establishes the motivation for the study. **Chapter 2** provides a comprehensive literature review on particle engineering and electrode engineering approaches for enhancing electronic conduction in cathodes. **Chapter 3** outlines the materials and research methodology used in this thesis. **Chapter 4** demonstrates the scope for the use of mechanofusion as a method to control coating formation as film structures on NMC to establish short-range electronic pathways. **Chapter 5** details the adapted use of a conventional resistivity measurement technique to probe carbon black deagglomeration during mechanofusion mixing. **Chapter 6** starts to unravel the microstructures and the resulting electronic conductivity of slurries and electrodes with designed conductive pathways. **Chapter 7** offers a summary and key conclusions of this thesis and highlights areas for future research.

Chapter 2 Literature Review

2.1 Lithium-Ion Batteries

The core principle governing the operation of LIB is intercalation, which refers to the reversible insertion and removal of lithium ions (Li^+) between the anode and the cathode (Figure 2.1). For LIB, the cathode is typically a metal oxide compound and is the source of Li^+ ions. During charging, the power source creates a potential difference that drives the movement of ions and electrons. Li atoms stored in the cathode forfeit their electrons and become Li^+ ions. Within the electrolyte exists a separator that is insulating but exclusively permeable to Li^+ ions. This causes electrons to move through the external circuit to the anode. The positively charged Li^+ ions deintercalate from the cathode structure and move through the electrolyte past the separator towards the anode. At the anode, the Li^+ ions recombine with electrons to form Li atoms and are stored as chemical energy. The reactions occurring at the cathode and anode during charging are shown below:

$$\textbf{Cathode:} \quad LiMO_2 \rightarrow Li_{(1-x)}MO_2 + x \cdot e^- + x \cdot Li^+$$

$$\textbf{Anode:} \quad C_6 + x \cdot e^- + x \cdot Li^+ \rightarrow Li_xC_6$$

$$\textbf{Overall cell reaction:} \quad C_6 + LiMO_2 \rightarrow Li_xC_6 + Li_{(1-x)}MO_2$$

During discharge, a reverse process of charging occurs where Li^+ ions move to the metal oxide to return to its stable state. At the anode, Li atoms are oxidised from Li to Li^+. The Li^+ ions again deintercalate from the cathode structure and move back to the anode through the electrolyte. Electrons are forced through the external circuit, which powers the connected device. Similarly, the Li^+ ions recombine with electrons at the cathode to form Li atoms. The reactions occurring at the cathode and anode during discharging are shown below:

$$\textbf{Cathode:} \quad Li_{(1-x)}MO_2 + x \cdot e^- + x \cdot Li^+ \rightarrow LiMO_2$$

$$\textbf{Anode:} \quad Li_xC_6 \rightarrow C_6 + x \cdot e^- + x \cdot Li^+$$

During the initial charging stages, electrons flow from the cathode to the anode via an external conductor. This movement of electrons requires a counterbalancing flow of positive charge to ensure charge neutrality. Li^+ ions are solvated by solvent molecules as they move from the cathode to the anode through the electrolyte. As Li^+ ions reach the anode, typically comprised of graphitic carbon, the solvated Li^+ ions react with the graphite lattice to form a solid electrolyte interface (SEI). Similarly, on the cathode side, a cathode electrolyte interface (CEI) is also formed. These interfaces are essential for the long-term, reversible performance of LIB. They are selectively permeable to Li^+ ions while effectively blocking the direct contact between the electrode and electrolyte. This minimises the detrimental side reactions that would consume vital electrode materials. The SEI and CEI layers should be porous and ionic conductive for Li^+ ion movement and critically affect the overall performance of LIB [6].

The movement of Li^+ ions during the charging and discharging process can be described by the rocking chair principle [7]. This analogy describes the movement of electrons between the anode and cathode, akin to a person rocking back and forth in a chair. However, the initial first cycle where an irreversible loss of Li^+ ions during the formation of the SEI and CEI can translate to an irreversible loss of Li^+ ions [8]. This initial loss results in a reduced number of Li^+ ions available for subsequent charge cycles, which will ultimately lead to a gradual decrease in battery capacity, known as capacity fade.

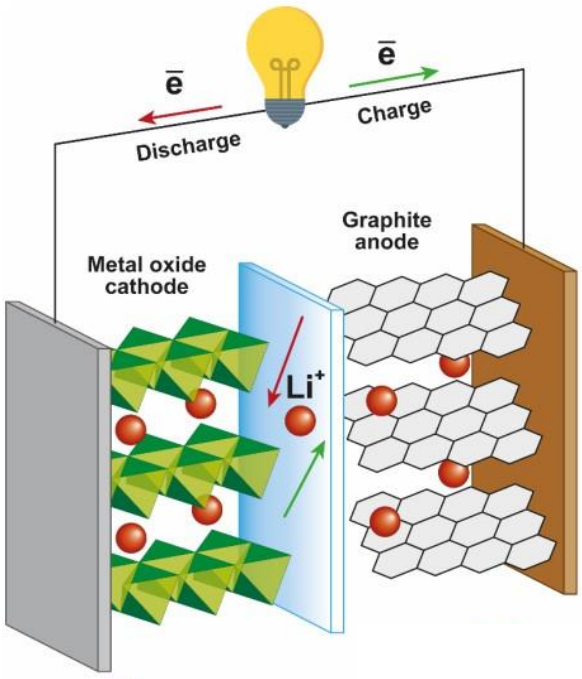

Figure 2.1: Schematic representation of a lithium-ion battery depicting the intercalation and deintercalation of Li^+ ions at both the cathode and anode during charge and discharge [9].

Two critical metrics to describe the performance of batteries are their energy and power density, which can influence their applications across various industries. A Ragone plot with an overview of the performance metrics of EVs, detailing the requirements of power and energy density together with considerations for weight and cost, is shown in Figure 2.2. Energy density, measured in terms of gravimetric (Wh kg^{-1}) or volumetric (Wh L^{-1}), is defined as the amount of energy a battery can store per unit mass or volume respectively. High energy density is particularly desirable for applications requiring extended durations of energy supplied [10]. For example, in the context of EVs, a high energy density translates to a vehicle capable of travelling longer distances on a single charge, which is the basic expectation of consumers for the transition to electrified transportation. Similarly, for grid storage, high energy density means backup power can be provided for extended periods during outages or to address power demand fluctuations. This relies on the development of novel electrode materials with superior properties that are capable of increasing a battery's overall charge storage capability. The design of electrode structures is also crucial in enhancing efficiency and capacity. For example, porous electrodes may offer a high surface area between electrolyte and electrode materials to maximise ionic conductivity [11]. The product of specific capacity (C) and the mean discharge voltage (U) provides the specific energy (E) as shown in Equation 2.1. As such, great attention is focused on novel cathode materials with higher operation voltages or higher specific capacities, which can both increase the total energy of batteries.

$$E = C \cdot U \tag{2.1}$$

Power density, similarly, measured in gravimetric and volumetric terms, is used to describe the ability to deliver power rapidly, reflected by the rate at which a battery can discharge energy. High power density is significant for applications that require a short burst of power output, such as during the acceleration of EVs or the application in high performance in EVs. To achieve this, the rapid movement of Li^+ ions and electrons within the electrochemical system is the key factor. Therefore, materials with both high ionic and electronic conductivity are key to achieving high power density [3]. A prime example is the energy recovery system (ERS) in Formula 1 cars where the battery is discharged and charged multiple times per lap, typically within a short time period [12].

Although both high energy and high power density are highly desirable, designing batteries that simultaneously capture these two properties is extremely challenging. Materials which are ideal for high energy density usually exhibit poor ionic conductivity, which undermines power density. This is due to a relatively dense and tightly packed crystal structure for Li^+ ions. Conversely, materials with high ionic conductivity often have more porous structures for ion movement and therefore reduced space for Li^+ ions, which limits energy density. This presents the inherent conflict to achieve high energy and power density electrodes.

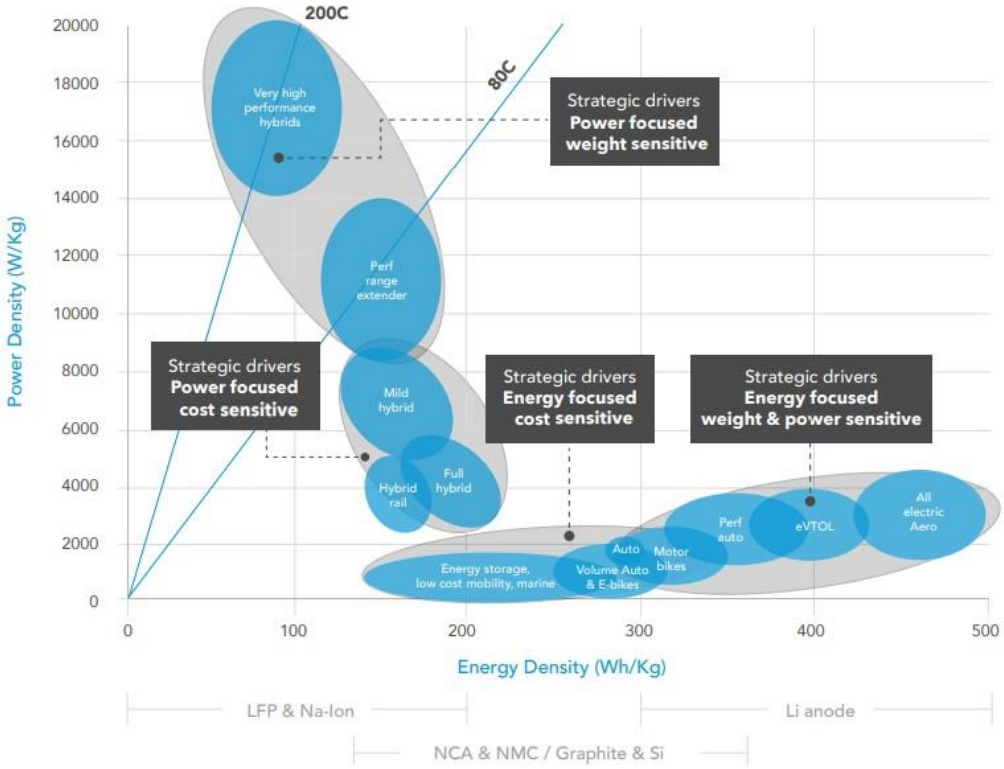

Figure 2.2: Ragone plot illustrating the power and energy density requirements for EV applications, with weight and cost considerations [13].

Lithium-ion battery cathodes are composite electrodes consisting of agglomerated primary particles of active intercalation compounds (i.e. active materials) and inactive materials such as the polymeric binder and conductive additives. The active material serves as the lithium reservoir in the electrode while the polymeric binder is responsible for structurally binding the active materials and conductive additives to each other and adherent to the current collector. The current collector is a thin metal foil that acts as a bridging component to collect the electrical current generated and to form external circuit connections [14].

Both the active and inactive materials in LIB and their chemistries influence their performance and cost varies across different usage. For anode materials, graphite is traditionally used due to its electrically conducting nature and ability to intercalate Li^+ ions with small-volume expansion (~10 %) compared to alternatives such as silicon anodes (~300 %) [15]. It is also a low-cost material with low voltage and possesses good energy density. According to Andre et al. [16], graphite is favourable commercially as most alternative materials have a lower energy. However, the major limitation is its capacity of 372 mAh g^{-1} at its fully lithiated state [17]. Significant efforts have been made to overcome these limitations by discovering alternatives such as nano-silicon, lithium titanate ($Li_4Ti_5O_{12}$) and conversion or alloyed-type materials. These materials show very promising progress, in particular, conversion materials with enhanced capacities of up to 1500 mAh g^{-1} [18]. These advantages however come with consequences of lower delithiation potential and poor first-cycle Coulombic efficiency, thus leading to poor anode/cathode capacity balancing ratio [19].

Current cathode materials are transition metal oxides, which may take the form of layered, spinel or olivine structures (Figure 2.3). Layered oxides, such as $LiCoO_2$, $LiNiCoAlO_2$ and $LiNi_xCo_yMn_zO_2$, are sheets of transition metal oxides alternated with layers of Li^+ ions arranged in a cubic arrangement with an *ABCABC…* stacking sequence [20]. This layered structure allows for a large number of Li^+ ions to be accommodated which contributes to their high theoretical capacity, but also leads to thermal instability. Spinel oxides, such as $LiMn_2O_4$, have a 3D framework where Li^+ ions occupy the tetrahedral sites. This structure makes Li^+ ions more accessible and allows faster movement, which can lead to better rate capabilities but may suffer from irreversible loss of capacity at elevated temperatures. Olivine oxides, i.e. $LiFePO_4$, have a unique backbone formed by phosphate groups and Li^+ ions occupy specific spaces within this structure. Its robust structure exhibits better thermal stability and long cycle life but suffers from lower energy density. A brief overview of the key characteristics of these cathode chemistries is shown in Table 2.1.

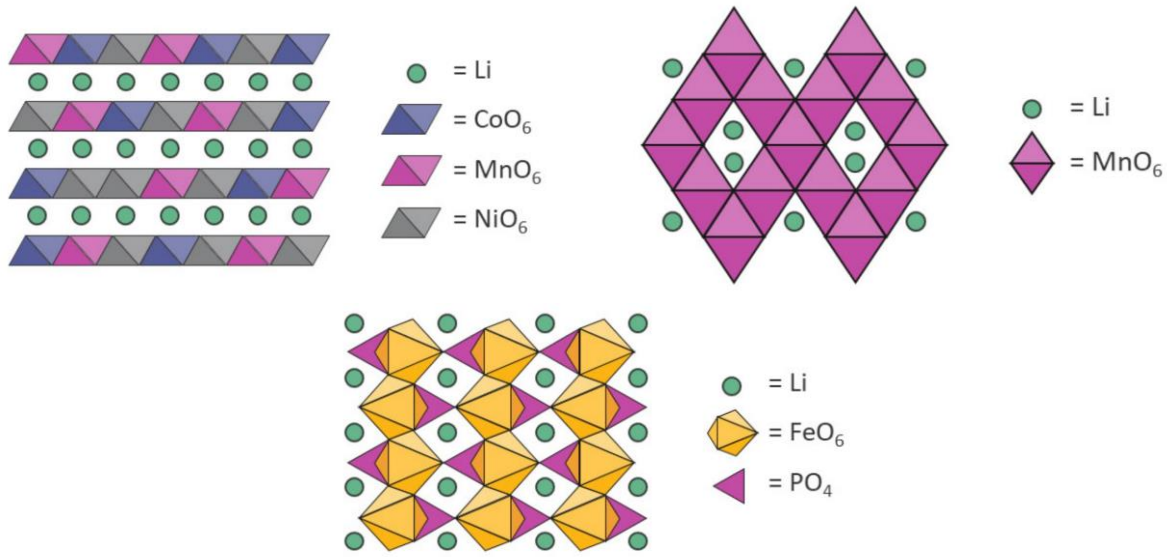

Figure 2.3: Schematic depicting the crystal structures of common cathode chemistries: (a) layered, (b) spinel, (c) olivine. Adapted from [21].

Table 2.1: Key characteristics of common cathode chemistries. Adapted from [21].

Structure	Formula	Abbreviation	Cost	Energy Density	Thermal Stability	Cycle Life
Layered	$LiCoO_2$	LCO	High	Moderate	Poor	Good
	$LiNiCoAlO_2$	NCA	High	High	Poor	Moderate
	$LiNi_{0.6}Co_{0.2}Mn_{0.2}O_2$	NMC622	High	High	Moderate	Good
	$LiNi_{0.8}Co_{0.1}Mn_{0.1}O_2$	NMC811	High	High	Poor	Moderate
Spinel	$LiMn_2O_4$	LMO	Low	Moderate	Good	Poor
Olivine	$LiFePO_4$	LFP	Low	Low	Good	Good

$LiNi_xMn_yCo_zO_2$ (NMC), where x/y/z represents the mole fractions of Ni, Mn and Co respectively, has been a commercially attractive active material due to its unique composition versatility and associated material properties. Its compositional elements play different roles; Ni improves specific density, Mn provides structural stability and Co enhances rate capability. It is also relatively low cost resulting from its lower Co content compared to other layered oxides such as LCO and NCA. Common variations of NMC include NMC111, NMC532, NMC622 and NMC811. Recent progress in research aims to optimise the compositions by maximising the energy density through higher Ni content while reducing the dependence on Co, due to ethical concerns regarding its sourcing.

2.2 Particle and Electrode Engineering

While the development of novel materials and chemistries is an important and popular research focus, applying particle science approaches to tailor existing active materials can also offer significant potential for enhanced performance (Figure 2.4). From a particle design perspective, tailoring active material at the structural level can be beneficial to both electrode design and downstream processing.

Nanostructured materials, synthesised through various methods (e.g. templating, solvothermal or hydrothermal routes, solid-state reactions), enable precise control of particle structure, size and shape. These materials have shown improved capacity due to reduced Li^+ diffusion path lengths [22]. Single crystal structures can improve particle stability, reduce side reactions and minimise particle cracking that is commonly observed in conventional polycrystalline structures [23]. Primary particle alignment can result in a more direct Li^+ diffusion pathway and reduces intergrain stress that causes cycling stability [24]. Core-shell structures enable the combination of a high-capacity core shielded by a stable shell (i.e. Ni-rich core with Mn-rich shell) [25]. Hybrid composite particles, formed through coating or doping, can modify the crystal structure to improve conductivity or stability [26]. Finally, surface coatings can achieve various benefits such as electronic [27] and ionic [28] conduction enhancements and the suppression of unwanted side reactions [29].

Beyond material development, electrode engineering also offers significant promise to enhance battery performance in modern electrode manufacturing. One straightforward approach is to manufacture thicker electrodes, which directly increase energy density due to increased active material content and have been shown to enhance performance at low to medium C rates [30]. However, extra considerations must be taken to maintain power density due to increased diffusion limitations within a thick electrode structure [31]. Additionally, efforts to minimise the use of conductive additives in electrodes for higher active material loading require optimal use of these additives during dispersion to maintain efficient electronic networks [32]. At the same, the ratio between conductive additive and binder must also be considered as it affects carbon binder domain (CBD) formation and electrode integrity [33]. CBD engineering can also be particularly useful in

enhancing electronic and ionic conduction within electrodes. Optimising the CBD structure ensures the formation of a well-connected percolated conductive network, from the active material surface to the current collector, for efficient electronic transport. The formation of carbon coatings on active material particles can enhance the contact areas with conductive additives for improved electronic conduction. Intensive dry mixing can also be utilised for a more homogenous coverage as compared to wet mixing. Recent research has also shown the synergistic effects of different dimensional carbon allotropes as conductive additives within electrodes to optimise performance [34]. Crucially, developing an understanding of the interplay between active material, conductive additives and the binder is vital for maximising electrode performance and maintaining its structural integrity [33], [35].

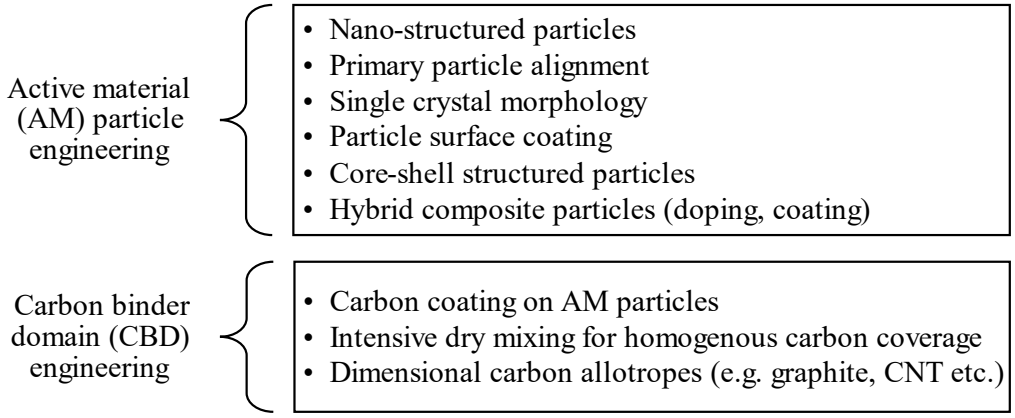

Figure 2.4: Particle and electrode engineering approaches to enhance electrode performance.

2.3 Electrode Engineering for Enhanced Conduction

2.3.1 Electronic Conduction Within Electrodes

Cell characteristics are critical indicators of the overall performance of EVs which, in turn, are governed by the electronic and ionic conductivity within the electrode [11]. These properties are ultimately dictated by the nano-, meso- and macrostructure of the electrodes [36]. Understanding these structural features is especially critical for NMC electrodes, where micron-sized active material and nano-sized carbon conductive additive play independent roles. As such, a fundamental understanding of the electrode structures and how they are influenced by the manufacturing process is essential for guiding optimal electrode and cell design.

Electrode performance is dependent on the complex interplay between structural features spanning multiple length scales, all directly controlled by the manufacturing processes. On a nanoscale (< 1 μm), slurry mixing influences the dispersion of active materials and conductive additives [37]. A homogenous dispersion is required to achieve a well-connected conductive network throughout the electrode. On a mesoscale (~1 – 10 μm), the coating and drying stages, particularly during solvent

evaporation, can influence the particle arrangement within the electrode [38], [39]. Here, the electrode porosity and conductive network are affected and are crucial for electrolyte accessibility. Lastly, on a macroscale (> 50 µm), coating, drying and calendering can also affect film thickness and uniformity, which can affect the overall capacity of the electrode [38], [40]. In general, a percolated conductive network at the nanoscale is required for efficient electron transport throughout the electrode. The interconnected porosity at the mesoscale is required for efficient ionic transport. At the macroscale, electrode thickness may dictate the energy and power density [2].

These descriptions fit well for NMC cathodes. NMC particles, with a typical size of ~10 µm, form voids between them. These voids need to be filled with nano-sized conductive additives to establish a conductive network for effective electron transport. Figure 2.5 shows an NMC cathode with micropores between NMC particles together with the CBD phase consisting of the nano-sized carbon black and its associating nanopores. Moreover, since NMC is semi-conducting and the binder is an insulator, the addition of conductive carbon can provide more electronic pathways and therefore significantly increase the overall electronic conductivity within the electrode. During slurry mixing, there is competition between the NMC particles and conductive additives for the limited binder available [41]. Conductive carbon particles have a larger specific surface area compared to NMC particles and therefore cause the available binder to largely bind to them [42]. This leads to the formation of a homogenised cluster phase consisting of the binder and the conductive carbon particles i.e. carbon binder domain. The CBD is an important aspect of lithium-ion battery cathodes acting as a conductive network that facilitates both electronic and ionic conductivity and ensures structural mechanical stability.

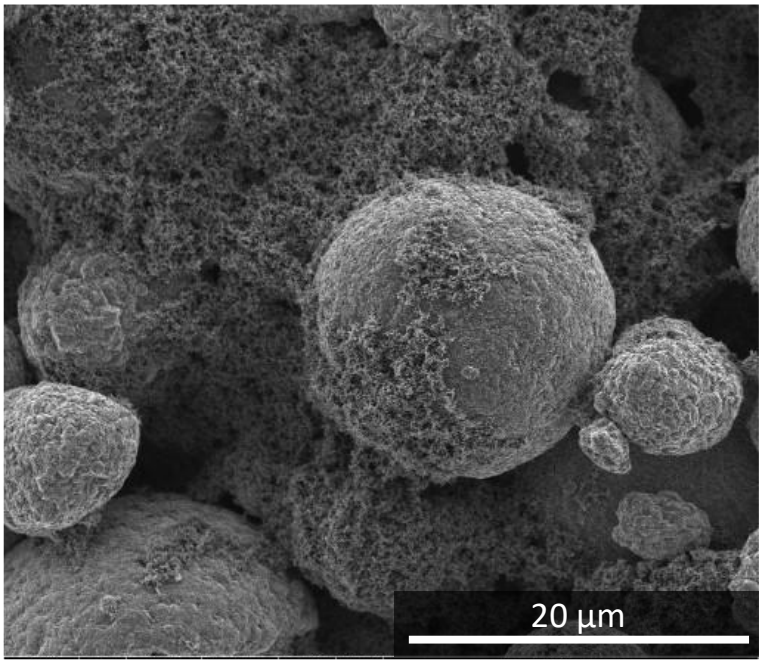

Figure 2.5: SEM micrograph of an NMC electrode showing micropores between NMC particles surrounded by the CBD with nanopores within the CBD phase.

To design a functioning electrode with efficient conduction networks, it is essential to develop an understanding of the role of electronic conductivity and its influence on cell performance. Efficient electron transport is critical during the intercalation and deintercalation of Li^+ ions within the cathode. This requirement is more apparent at high current rates where large amounts of charge are present and the efficient movement of Li^+ ions and electrons must be facilitated to maintain optimal performance.

Electrical properties of materials can be categorised into insulator (non-conducting), conductor or semiconductor that originates from their band structures described by quantum mechanics [43]. Insulators, with the addition of conductive material, can be converted into an electrically conductive material. For a system of conducting and insulating phases such as electrodes, electrical conduction can occur through percolation in a continuous conducting network and quantum mechanical tunnelling [44], [45]. The percolation theory describes the change in the electronic conductivity of a binary mixture of a certain material and conductive additives. The percolation curve is depicted using a typical S-curve where the resistivity (or conductivity) of a material is described as a function of the conductive additive content within the binary mixture, as shown in Figure 2.6. The percolation network can be described as a continuous path for the flow of electrons [46]. In a single carbon black aggregate consisting of multiple primary particles, electrons move along the connected aggregate pathways until they approach a separate aggregate where contact must be made between the two to allow the continuation of the electron movement [47], [48]. Similarly, for carbon black primary particles, the movement of electrons relies on particle contact to form a continuous pathway.

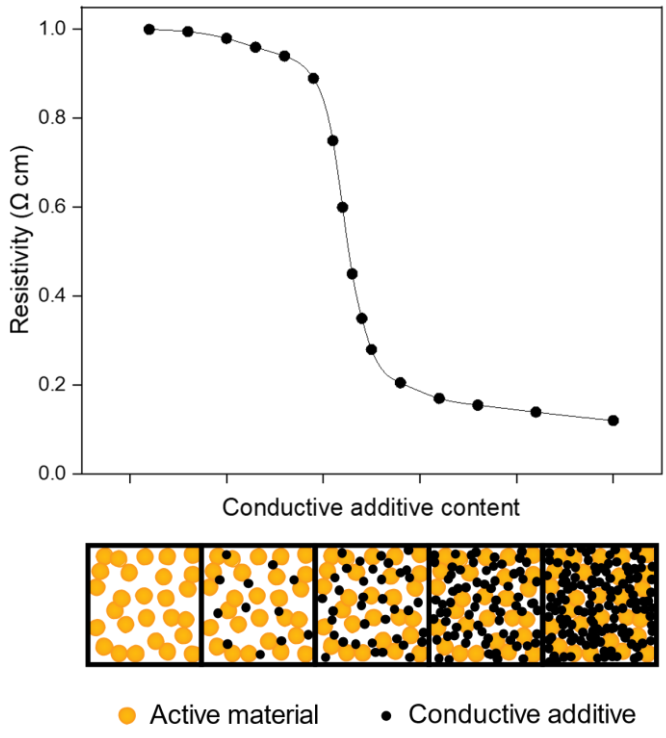

Figure 2.6: Percolation curve showing the resistivity as a function of conductive material content. A sharp drop in resistivity is obtained when conductive additive content reaches the percolation threshold. Adapted from [49].

Several different models have been proposed to describe the percolation curve and the sharp change in conductivity at a critical conductive additive concentration. Firstly, based on Flory's concept of polymer gelation [50], Bueche [51] proposed that the S-shaped curve for a binary powder mixture can be described using Equation 2.2:

$$\frac{\rho}{\rho_m} = \frac{\rho_f}{(1-V)\rho_f + V\omega\rho_m} \tag{2.2}$$

where ρ is the resistivity of the mixture, ρ_m is the resistivity of the insulating material, ρ_f is the resistivity of conductive material, V is the volume fraction of the conductive phase, ω is the fraction of conductive additive in the conductive network, determined by f and α. f is the maximum number of contacts of a particle with its surroundings and α is the probability of a particle establishing contact with surrounding particles.

This model considers the drastic changes in conductivity if f is a variable parameter. It also describes the change in conductivity beyond the percolation threshold. The percolation theory also suggests that the electrical conductivity of a mixture follows the power law equation when it approaches the percolation threshold [52]. Kirkpatrick [53] proposed an equation based on the percolation theory to predict the conductivity above the percolation threshold as shown in Equation 2.3:

$$\sigma = \sigma_0(V - V_c)^t \tag{2.3}$$

where σ is the conductivity of the mixture, σ_0 is the intrinsic conductivity of the conductive material, V is the volume fraction of the conductive material, V_c is the percolation threshold and t is a power law exponent.

This can be applied to different systems of active material and conductive additives. In a study by Mandal et al. [54], they proposed values for the percolation threshold (V_c) and power law exponent (t) as 0.03 and 1.7 respectively for $LiMn_2O_4$ with carbon black as the conductive additive.

If sufficient energy is present, electron tunnelling can also occur and contribute to overall electronic conduction. Quantum mechanical tunnelling is a conduction mechanism where electrons are excited and possess higher kinetic and potential energies and can subsequently tunnel through or jump over the potential barrier gap to continue the movement of electrons [47], [55]. Toker et al. [44] reported that a system can be accurately described by the percolation theory when the conduction mechanism relies only on percolation and nearest-neighbouring tunnelling exclusively (Figure 2.7). While non-neighbouring tunnelling is possible, it was shown to not contribute significantly to the overall conductivity, thus confirming carbon black-polymer composites conform to the typical behaviour of a percolation system [44]. This demonstrates the need to establish neighbouring electrical contacts

between particles in electrodes, thus emphasising the need for efficient techniques to control the distribution of conductive additives. Although these mechanisms are universally agreed upon and their considerations have been applied to different applications [45], [56], [57], [58], differentiating, and quantifying these different mechanisms of electronic conduction remains extremely challenging, especially within the complex matrix of the CBD.

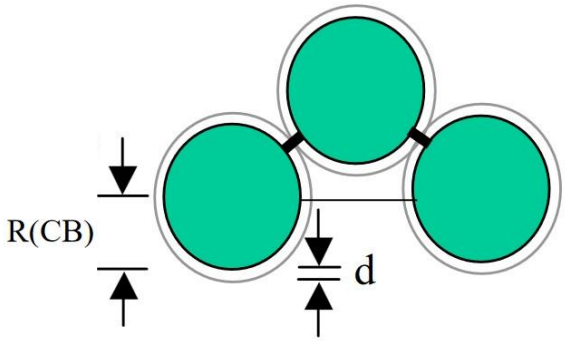

Figure 2.7: Schematic (representative of carbon black-polymer composites) indicating large green circles as conducting particles and grey shell representing the effective tunnelling range (d). Thick lines between particles represent tunnelling connections between nearest neighbours whereas thin lines represent tunnelling between further neighbours. Adapted from [44].

To achieve an efficient percolated network within the complex structure of an electrode, it is crucial to understand the role of different electronic pathway lengths: the short-range and long-range electronic pathways. This is particularly important for the micron-sized NMC and nano-conductive carbon systems. A comprehensive review of electrode structures and electronic conductivity was published by Entwistle et al. [49]. Current thinking defines these two pathway lengths vaguely based on their length scales [38], [49], [59], [60]. Long-range electronic pathways can be categorised as the conventional understanding of electronic conduction where the interconnected network spans between the active material particles within the 0.1 – 10 µm range. This pathway length corresponds to the long-range scale, made up of multiple long-range electronic pathways that span the entire electrode structure, from active material particles to the current collector. In contrast, short-range electronic contacts involve the nearest neighbouring interactions between active material particles and their surrounding CBD or other active material particles, typically within the 1 – 100 nm length scale. Figure 2.8 schematically illustrates these electronic pathway lengths and the associated electrical conduction mechanism involving percolation and tunnelling. A detailed review of the theoretical design of the CBD within electrodes by Baumgärtner et al. [60] discusses the concept of a medium-range electronic pathway through the active material, differentiating from short-range pathways that solely represents the interfacial resistance between the active material and conductive network. They have also proposed an ordered conductive network with the aid of carbon coatings on the active material surface. This concept of ordered network assumes active materials are uniformly distributed and closely packed, and therefore the maximum distance of electron movement is equal to the particle radius of the active material.

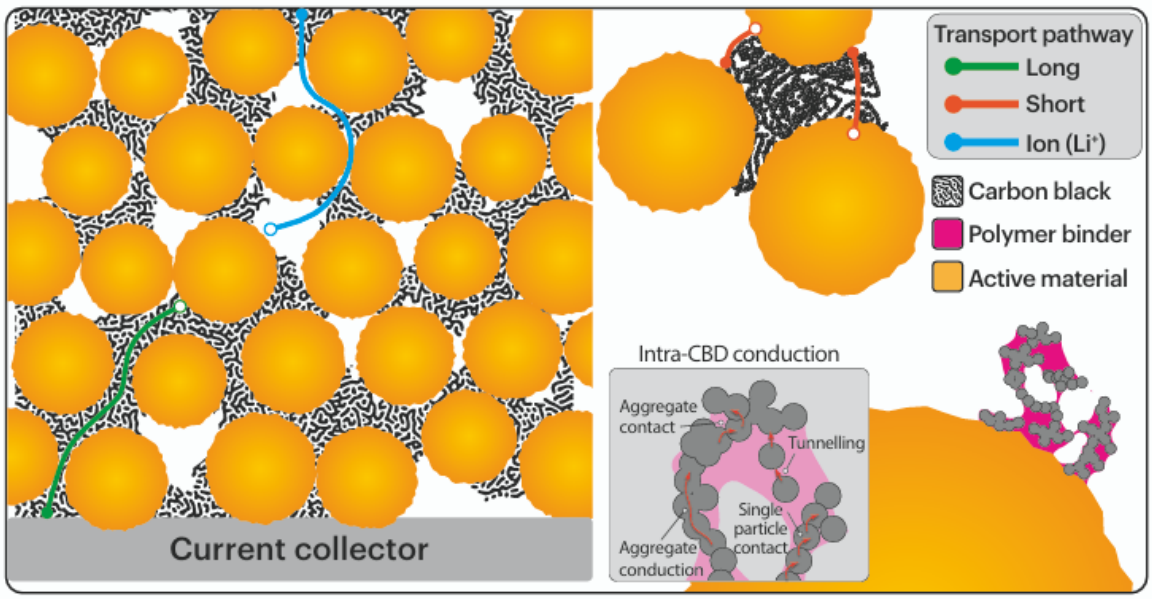

Figure 2.8: Schematic depicting the two electronic pathway lengths within electrodes [49]. Long-range pathways span throughout the entire electrode structure, from active material to the current collector while short-range pathways act as electrical contact points to the neighbouring CBD structures or active material particles. Ionic conduction pathways and the conduction mechanisms within CBD structures are also shown.

The importance of these two pathway lengths and their synergistic effects leading to better electrode performance have been widely reported [38], [61], [62]. There are, however, some publications that suggest the dominance of one pathway length over the other. Trembacki et al. [63] showed that long-range contacts are more dominant than short-range contacts as conductivity increases by 950 % and 220 %, respectively, for a nanoporous CBD structure through FEM simulations. Similarly, other reports highlight the need to re-establish long-range pathways when active materials are coated with carbon to form short-range contacts [42], [64], [65], [66].

On the other hand, Morelly et al. [59] reported a substantial increase in rate capability when total carbon content is increased from 2.5 wt% to 3.0 wt% carbon black. Within these findings, the total free carbon actually decreased after dry mixing as reflected by the slurry modulus. This led them to conclude that short-range contacts play a more dominant role than long-range contacts and even ionic conduction in determining rate capability. Dominko et al. [67] showed that short-range contacts are important, where localisation of both Li^+ ions and electrons on active material surfaces is crucial for the insertion of Li^+ ions without excessive polarisation. Additionally, Hamed et al. [68] emphasised that the significance of polarisation arising from both short and long-range contacts is dependent on the particle sizes within the system and their intrinsic conductivity.

These conflicting perspectives highlight the complexity of the electrode microstructure and suggest that both pathway lengths could potentially contribute synergistically to overall electrode performance. However, a significant knowledge gap on the precise relationship between these pathways and their effect on the electrochemical performance remains. Therefore, developing a comprehensive understanding of both short and long-range pathways is crucial.

2.3.2 Conductive Additive Distribution

In a standard dispersing process, the active material, conductive additive and polymeric binder are mixed in the one-step process resulting in an uncontrolled, non-uniform distribution within the electrode. While electrode homogeneity is often assumed to be optimal for conduction, studies have shown that some degree of heterogeneity may contribute to better performance [69]. In terms of the electronic pathway lengths, an ideal distribution would consist of strategically depositing conductive additives onto active material for increased short-range electrical contacts, and throughout the electrode microstructure for long-range conduction. The formation of long-range pathways could be promoted by distributing carbon black particles in a less dispersed state (i.e. in aggregate or agglomerate form) to better facilitate its formation and reduce the amount required [70].

Lu et al. proposed two CBD structures influencing electronic conductivity in LIB cathodes (Figures 2.9a and 2.9b): a bridge structure occupying the spaces between NMC particles and forming the contact points between two particles, and a film structure covering the surface of NMC particles [71], [72]. The bridge structure correlates to the long-range electronic pathways that promote the formation of a percolated electrical network within electrodes. Within the bridge structure, it was proposed that two "nested" percolation systems exist that contribute to overall conductivity (Figure 2.9c). The first is the carbon black-polymer structure that is dispersed within the space among active materials, corresponding to the conventional understanding of CBD structures. The second system is the carbon black that is dispersed within each cluster structure. An increase in both percolation systems increases the overall electronic conductivity.

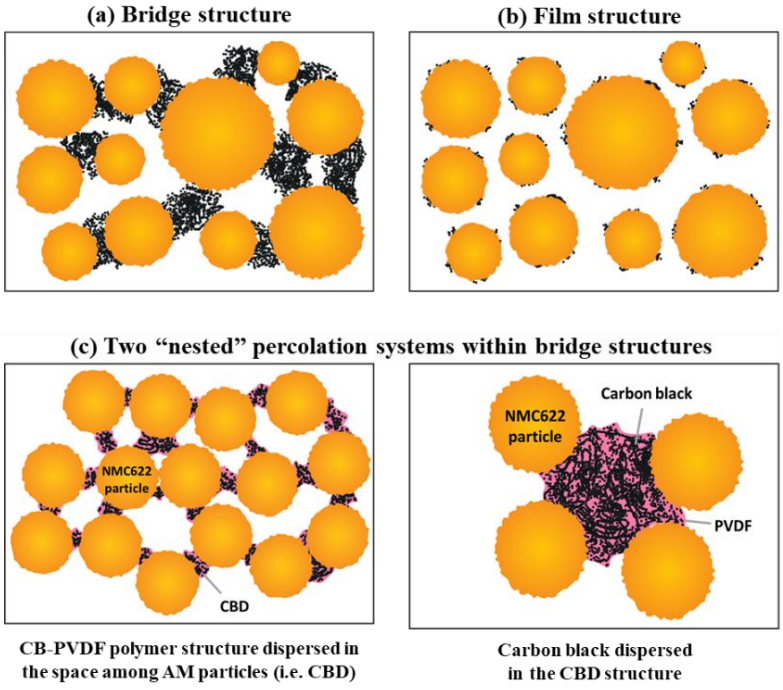

Figure 2.9: Schematic showing two CBD structures: (a) a bridge structure that connects two or more active material particles and (b) a film structure that deposits and covers the active material surface. (c) Two "nested" percolation systems within bridge structures. Adapted from [71].

The film structure correlates to the short-range contacts, providing interparticle electrical contact points to facilitate electronic conduction between active material particles and the neighbouring CBD. Subsequent calendering could further increase the contact between the particles and CBD structures to enhance electrode performance [73], [74]. The film structure is analogous to carbon coatings established through wet or dry routes as demonstrated in various publications [75], [76], [77], [78].

Bauer et al. [42] highlighted the importance of the control of film formation on active material. As depicted in Figure 2.10, they showed that dry mixing causes immobilisation of carbon black particles which can inhibit its interactions with the binder within the slurry to form a porous CBD structure. Furthermore, binder deposition on the carbon coating can create an insulating polymer shell that can impede both electronic and ionic conduction. This process can also disrupt the typical gel-type behaviour of cathode slurries due to the lack of free carbon particles within the slurry [79]. To re-establish long-range conduction, additional carbon black must be introduced into the binder to complement the short-range contacts on active material particles.

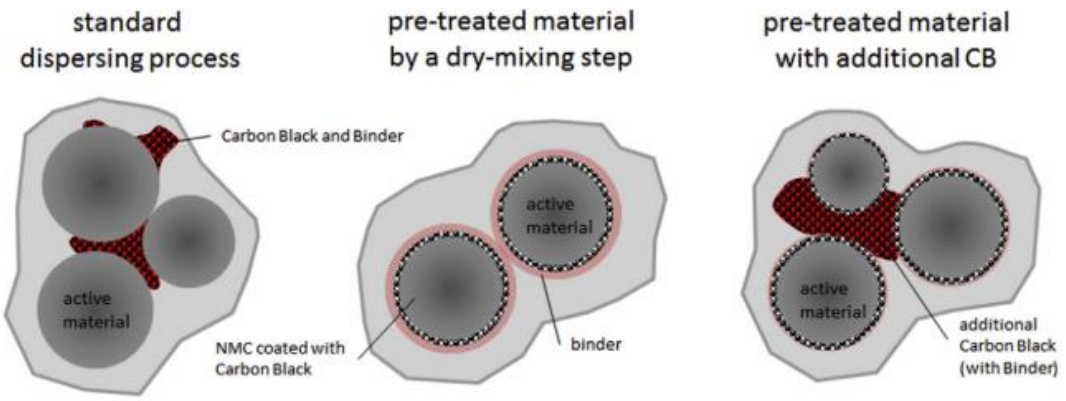

Figure 2.10: Schematic illustrating the distribution of active material, carbon black particles and binder for different mixing procedures. The binder forms an insulating polymer shell on the carbon coating of pre-treated active materials and requires the addition of additional carbon black during slurry mixing to re-establish the formation of the CBD [42].

Due to the small primary particle size, carbon black particles experience interparticle interactions through van der Waals forces, giving rise to the formation of larger aggregates or agglomerates. These aggregates are in the size ranges of ~100 nm and for agglomerates, up to a few microns. When two carbon black particles come together, both attractive and repulsive forces increase with different respective magnitudes. The resultant force response curve indicates that a maximum attraction is reached at the minimum of the potential well (Figure 2.11). Carbon black particles that are trapped in this potential well form agglomerates. To separate them, by moving out of this potential well, energy input is required [80]. Therefore, for optimal electronic contact within electrodes, it is critical to consider the breakdown of these agglomerates into smaller constituents to promote dispersion within the voids of NMC particles. Dispersion of carbon black is well-studied in industrial rubber applications and dispersibility remains the same point of focus for battery manufacturing [81].

Carbon black properties such as particle size and structure can significantly impact both dispersibility and electronic conductivity. High surface area and high structure carbon blacks are known to possess higher conductivity [45]. However, the influence of carbon black structures is debated, with studies suggesting an increased dispersibility [82] and others suggesting a decreased dispersibility [45]. Although there is a lack of literature to clarify this, the apparent contradiction could be explained by the fact that high structure carbon black might initially disperse more easily due to its branched structure which offers higher accessibility. However, achieving a uniformly well-dispersed state might be more difficult compared to low structure carbon black. Additionally, Spahr et al. [34] reported the need to identify and select appropriate mixing techniques that are compatible with the specific properties of carbon blacks of interest.

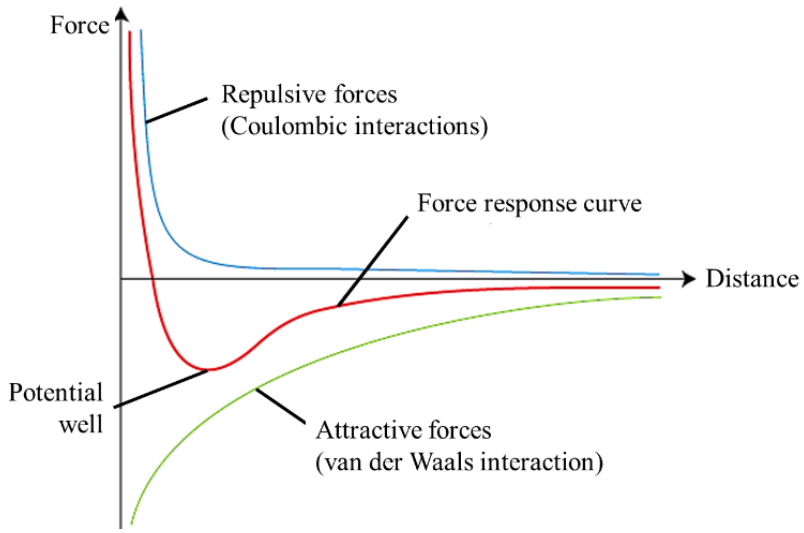

Figure 2.11: Resultant force response curve due to repulsive and attractive forces, where a minimum well is present indicating maximum attraction between particles. Adapted from [83].

Carbon black deagglomeration can be separated into two steps: rupture and erosion [84], [85], as shown in Figure 2.12. Rupture is the abrupt breakage of agglomerates into aggregates that occurs at a critical shear stress. This is related to the energy required to overcome the van der Waals forces between primary particles that hold them together to form the agglomerates. Sufficient energy input must be achieved to move out of the potential well to separate these particles. Erosion refers to the further deagglomeration of aggregates resulting in a decreased aggregate size or reduction into primary particles. This process occurs at a lower shear stress over a longer period of time so larger aggregates are gradually reduced to smaller aggregates or primary particles.

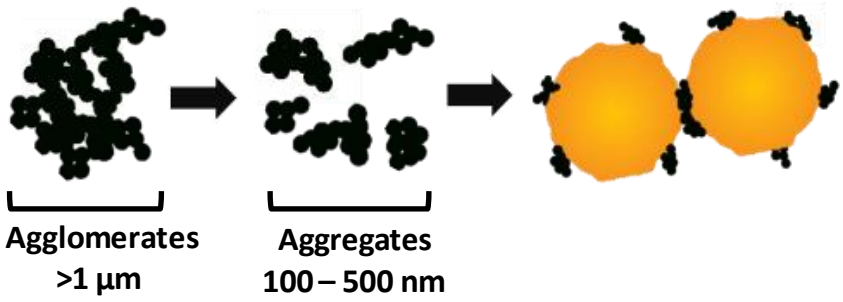

Figure 2.12: Two-step deagglomeration process of carbon black followed by coating onto active material particles. Agglomerates undergo rupture to form aggregates once a critical shear stress is achieved.

2.3.3 Quantifying Carbon Black Dispersion

Dispersion of carbon black involves the use of energy to overcome the van der Waals forces between particles to achieve deagglomeration. To understand the optimal conditions and behaviour of carbon back deagglomeration, it is necessary to identify and quantify the extent of deagglomeration during dispersion. Complexities are present as carbon black exhibits an intricate, branched structure and dispersion progress is dynamic. Therefore, various studies have demonstrated the development and correlations between different techniques that can capture the variation in structures across different length scales to provide insight into the carbon black dispersion process.

Rwei et al. [85] first investigated carbon black deagglomeration via simple shear flows and proposed the rupture and erosion deagglomeration mechanism. Using bulk powder density and powder conductivity measurements, Lischka et al. [86] reported that prolonged mixing causes carbon black to completely coat NMC622 particles, thus hindering interconnected electrical contacts within the powder sample. They also proposed a dimensionless mixing index, incorporating bulk powder density, and a dimensionless mixing tool rotations number for analysing the progression of deagglomeration. Mayer et al. [87] showed that carbon black deagglomeration can be analysed through bimodal particle size distributions where a shift towards smaller diameters was observed with increased dispersion time as shown in Figure 2.13a. The corresponding decrease in peaks between 1 – 10 µm and 0.1 – 1 µm is attributed to deagglomeration of large agglomerates followed by continued breakage of aggregates as mixing progresses. They observed that higher mixing tip speeds yielded smaller particle sizes due to higher specific energy. It was proposed that particle size following prolonged dispersion follows a power law function that is dependent on shear stress produced during dispersion. Grieβl et al. [37] studied how carbon black loading influences slurry rheology and developed a model to predict the progression of particle sizes with varying process conditions. Their findings validated the occurrence of carbon black deagglomeration where increased mixing speed and mixing time led to a lower slurry viscosity across a range of carbon black loading. Furthermore, smaller d_{50} values for carbon black and a similar shift towards smaller sizes within the bimodal

particle size distributions, similar to that reported by obtained by Mayer et al. [87], were observed. Finally, they developed a model function based on the power law function to describe deagglomeration as influenced by mixing time, circumferential tip speed and carbon black loading.

Bauer et al. [42] measured the resistivity of powder mixtures and electrodes with varying mixing speeds to study the distribution of conductive additives within electrodes. Although the study did not explicitly investigate deagglomeration, a lower resistivity resulting from an increase in mixing time for both dry preprocessing and slurry mixing suggests an increased dispersion of carbon black within the powder mixtures and subsequently electrodes. Amplitude sweeps of slurries show that dry mixed samples loss modulus dominates even at low strain, indicating the absence of free carbon black particles. SEM micrographs of dry mixed particles further confirm the deagglomeration of carbon black and coating formation on NMC particles. Similarly, Westphal. et al. [78] evaluated electrode resistivity over a range of mixing intensities and correlated to observations from SEM to identify deagglomeration and distribution of carbon black on graphite particles. They concluded that higher mixing intensity leads to high deagglomeration and identified an optimal range for low resistivity.

Bockholt et al. [64] evaluated electrode porosity using mercury intrusion porosimetry (MIP) and found that the pore diameters (~0.05 – 0.5 µm) correlated to voids in carbon black particles decreased with dry mixing time. The void volume inside carbon black decreases as its structure becomes smaller and shifts the peaks to the left (Figure 2.13b). The peaks correlated to voids between NMC (~1 – 10 µm) initially decrease in height and increase in pore diameter as smaller carbon black agglomerates result in better packing of NMC particles and less pore volume. With longer mixing times, carbon black attaches to the NMC surface, and the CBD produced is localised next to NMC, resulting in an increase in voids between NMC.

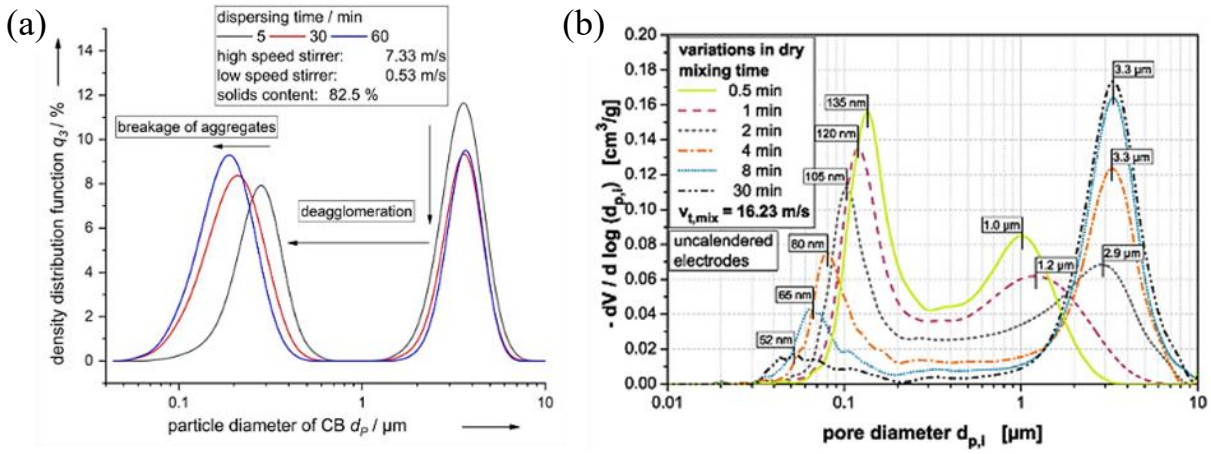

Figure 2.13: (a) Evolution of particle size distribution of carbon black particles with increased mixing time [87] and (b) evolution of pore size distributions within electrodes with active materials subjected to different mixing times [64].

Through particle size analysis and electrode pore size analysis, various parameters have been proposed to quantify carbon black structures and track dispersion. Mayer et al. [88] used MIP and developed a characteristic parameter through carbon black porosity (ε_{CB}) to describe electrode microstructure, which is influenced by carbon deagglomeration as shown in Equation 2.4:

$$\varepsilon_{CB} = \frac{\varepsilon_C - \varepsilon_{C,NMC}}{1 - c_{v,NMC} - \varepsilon_{C,NMC}} \tag{2.4}$$

where ε_C is the porosity of the carbon coating, $\varepsilon_{C,NMC}$ is the porosity between NMC particles and $c_{v,NMC}$ is the volume ratio of the NMC particle to the carbon coating and is represented by $\left(\frac{V_{NMC}}{V_C}\right)$, as shown in Figure 2.14.

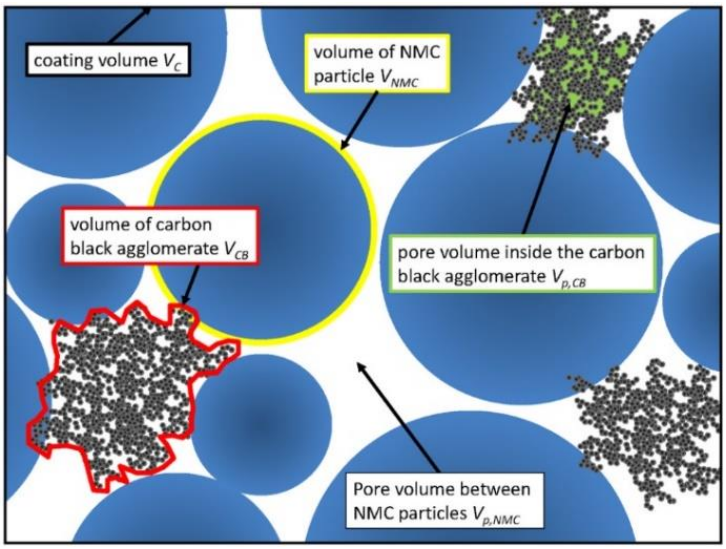

Figure 2.14: Schematic of an electrode microstructure depicting particle and pore volumes of NMC and carbon black [88].

This parameter ranges from 0 to 1 and can be used to indicate dispersion progress between a fully dispersed structure (0) down to a non-dispersed structure (1). They have also demonstrated its sensitivity to process conditions in NMC111 and NMC622 electrodes which indicates its effectiveness in predicting carbon black sizes within electrode microstructures.

Weber et al. [84] studied the dispersion for carbon black-containing slurries using a laser diffraction-based particle size distribution and proposed a carbon black dispersion index (DI_{CB}), as shown in Equation 2.5, by isolating the bimodal volume distribution of carbon black:

$$DI_{CB} = \frac{Q_3(x_D)}{x_{50,C1}} \tag{2.5}$$

where $Q_3(x_D)$ represents the particle size cumulative distribution of section C1 and $x_{50,C1}$ is the median particle size of section C1.

By setting a threshold of x_D = 0.8 µm, the particle size distribution was separated into sections representing well-dispersed carbon black aggregates (C1) and undispersed agglomerates with other materials present (C2) as shown in Figure 2.15. The dispersion progress was exclusively quantified through section C1 where a monomodal distribution is observed. This dispersion index was shown to correlate well with specific energy and tip speed and showed good consistency when applied to assess a silica nanoparticles system and their historical data where short mixing time showed a lower DI_{CB} value compared to long mixing times. They have noted that the threshold (x_D) should be adjusted accordingly for different materials.

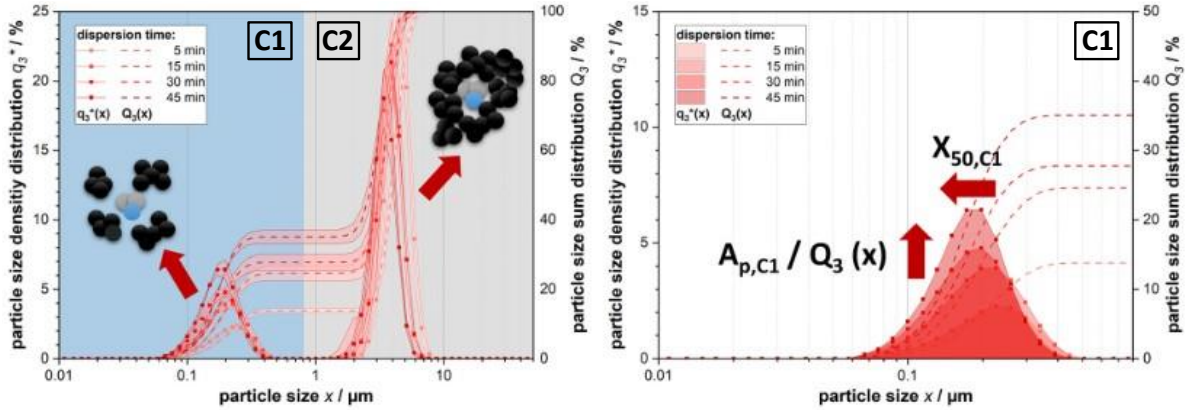

Figure 2.15: Particle size distribution of carbon black particles with two distinct sections representing well-dispersed carbon black (C1) and undispersed carbon black agglomerates (C2). Evolution in peak distribution and peak height can be used to determine the dispersion index DI_{CB}. Adapted from [84].

To summarise, many of the techniques used to quantify carbon black deagglomeration are directly correlated to slurry and electrode properties. While these methods may offer valuable insights, their implementation requires substantial experimental effort for sample preparation. It is also worth pointing out that these are conventional characterisation techniques developed to be compatible with wet slurry manufacturing. The use of slurry and certain electrode properties may not apply to or be suited for dry electrode processing. For dry electrodes, the dispersion of conductive additives remains an important aspect, along with the distribution of binder. Characterisation methods must be designed or adapted to directly evaluate these properties within dry powders or solid electrode systems.

Several powder characterisation methods can be utilised to investigate carbon black deagglomeration in dry powder systems: (1) volume resistivity measurements where the dispersion can be correlated to bulk resistivity within a binary powder mixture [34]; (2) bulk [86] and tapped density [89] of powders where deagglomeration generally results in better particle packing ; (3) particle size distribution where deagglomeration can be correlated to the shift in distribution peaks similar to that observed in slurries [84], [87]. Among these techniques, volume resistivity stands out as a popular technique due to its relative simplicity and direct relevance to the electrochemical properties of the materials studied, i.e. its resistivity or conductivity. The use of volume resistivity has long been used to evaluate the conductivity of powder compacts and electrodes.

As discussed previously, Westphal et al. [78] applied this technique on electrodes to study carbon black deagglomeration. More specifically for powder characterisation, a resistivity by compression is usually employed to study the change in resistivity with increased contact during compression. These methodologies were also demonstrated by Bauer et al. [42]. Marinho et al. [90] measured the conductivities of powder compacts of multi-wall carbon nanotubes, graphene sheets, carbon black and synthetic graphite and concluded that the bulk conductivity is dependent on the packing density of these conductive additives. Spahr et al. [34] studied the resistivities of LCO and various grades of carbon black and graphite to understand the evolution of electrical properties during dry mixing. They also studied the differences in resistivity when samples are prepared through wet and dry mixing showing that C-NERGY Super C45 and C65 carbon blacks are preferable for cathode manufacturing. With a focus on carbon black properties, they also showed that BET specific surface area affects dispersion, with high specific surface area carbon black exhibiting a higher viscosity at low shear rates.

Resistivities are usually measured through the two-point method with the assumption that all component and contact resistances are negligible. A shortcoming of the two-point measurement is that it may over- or underestimate resistivity in certain circumstances, such as current leakage, contact resistances, and variation in experimental setups. Kuo et al. [91] reported that the contact resistances from two-point measurements on NMC-carbon surfaces may contribute to resistances of up to 6 mm of the bulk NMC material. In other words, if the sample length is less than 6 mm, the measured resistance is dominated by the contact resistance. Contact resistances originate from constriction effects rather than interfacial electronic contact on electrodes. There are also studies that propose optimisations to the current two-point method to minimise or eliminate these extra resistances. Kane et al. [92] introduced a guard-electrode method coupled with the two-piston setup to characterise carbon black, graphite and copper for more accurate and repeatable measurements. Mainusch et al. [93] proposed a novel powder probe consisting of stainless steel particles covered with conductive silver paint that act as the contact media with samples. This advanced powder probe technique was used to evaluate LMO and LFP electrodes and demonstrated a reduction of contact resistances. One interesting study by Rey-Raap et al. [94] discusses the correlation between the two-point compression method and conventional four-point probe methods. They proposed a relationship between the conductivity obtained through these two characterisation techniques but noted that high anisotropy carbonaceous materials with very high conductivity (e.g. graphite) may not be applicable.

2.4 Particle Engineering Through Coating Formation

2.4.1 Carbon Coatings

The conventional slurry casting process remains the dominant technique for commercial LIB electrode manufacturing due to its scalability and cost-effectiveness [4]. This multi-step process begins with slurry mixing, where electrode active materials, conductive additives and binders are mixed in a compatible solvent using intensive mixers such as Eirich and Bühler mixers, or large-scale planetary mixers. Specifically for cathode manufacturing, a high active material loading (often > 90 wt%) along with conductive carbon additives and a binder dissolved in a suitable solvent (i.e. N-methyl-2-pyrrolidone, NMP). Key slurry properties include high slurry density for compression during calendering and optimised viscosity for uniform coating during casting. The amount of solvent used is critical as it directly affects viscosity and, consequently, coating quality and drying behaviour. Binder dispersion is equally important as it needs to be well dispersed to maintain their network structure as active material expands and contracts due to thermal effects during cycling.

Lu et al. [71] showed that bridge structures that facilitate long-range conduction can be controlled by varying the carbon black loading during slurry mixing. However, for film structures, applying control to its formation is relatively challenging in wet slurry mixing. Uncontrolled film formation arises from uncontrolled dispersion of carbon black in wet slurry mixing. This can lead to a decrease in the effective interface between active material particles and electrolyte. Therefore, it is important to control carbon black dispersion through a mechanistic approach to tailor the desired film structure. For optimised slurry properties and homogeneity, certain manufacturers also differentiate between a preliminary dry mixing stage for initial blending and a subsequent wet dispersion step for thorough homogenisation. Therefore, the use of a pre-processing technique, separate from wet slurry mixing, to deposit carbon black on the active material surface may introduce more control on film formation.

Carbon coating formation is a common particle engineering technique, primarily used to increase the electronic conductivity of active materials with low inherent electronic conductivity, such as LFP ($< 10^{-9}$ S cm^{-1}) [95]. As such, commercially available LFP is often provided in a carbon-coated form. This carbon coating is typically formed by mixing an iron phosphate precursor with lithium carbonate, along with a carbon source, followed by sintering at 600 – 800 ^{o}C. During sintering, the amorphous mixture transforms into the characteristic olivine structure of LFP [96]. In industrial LFP production, carbon loading is generally limited to below 1.5 wt% to avoid interfering with Li-ion transport or introducing impurities [97]. While the thickness of the carbon coatings is rarely reported, studies suggest it should be maintained between 1 – 10 nm, with coatings as thin as 2 nm being demonstrated in lab-scale research [98]. For NMC, carbon coatings are uncommon at an industrial scale due to their higher inherent electronic conductivity. Instead, cycling stability is the primary concern for these materials and is typically addressed through doping or oxide coatings [99], [100], [101]. Nevertheless,

from an electrode design viewpoint, carbon coatings can be beneficial in tailoring the electronic pathways, potentially improving the overall performance of NMC electrodes.

Coating morphologies can be broadly divided into 3 categories (Figure 2.16). A rough coating is an uneven layer with variations in distribution and coverage of the coating material, usually obtained through mechanical mixing and heat treatments of materials. A core-shell structure consists of an outer shell that acts as a protective layer for the inner core material. Lastly, ultra-thin film coatings are uniform, dense, homogenous coatings that are held by strong chemical bonds to maintain their physical integrity. For electronic enhancements, there are suggestions that complete coverage of the active material surface is favourable and thickness control is critical to maintaining ionic conductivity [102]. However, it is also sensible that a rough coating to facilitate surface electrical contacts is sufficient, ensuring minimal compromise on ionic conduction.

Figure 2.16: Schematic depicting three different coating characteristics: rough, core-shell and ultra-thin film coating. Adapted from [102]

The selection of appropriate coating methods is important as the coating morphology and functionality can vary significantly. Wet and dry processing techniques differ fundamentally and can lead to distinct coating properties and subsequent effects on CBD formation. In the context of conductive additives, the breakdown of conductive additives during processing can hinder their ability to facilitate long-range electrical contacts. Additionally, the processing intensity and the degree of intimacy between conductive additives and the active material can significantly influence short-range contacts [49]. Furthermore, different coating methods can result in variations in coating microstructures, ultimately changing the transport ability of electrons and Li^+ ion diffusion. It is also important to note that some coating techniques may introduce modifications to the active material surface structure, potentially leading to secondary implications.

Both wet and dry techniques have been demonstrated to achieve versatile carbon coatings on various active materials. Wet methods, such as hydrothermal or solvothermal methods [103] and sol-gel synthesis [104], are considered conventional approaches employed in industrial manufacturing. These techniques have a proven record of enhancing electrochemical performances.

Dry methods present an increasingly attractive alternative to eliminate the use of fugitive solvents used in typical wet methods. Common dry techniques include mechanical dry coating, dry powder spraying and deposition technologies such as chemical vapour deposition and atomic layer deposition.

Mechanical dry coating relies on high-energy collisions between larger host particles and smaller coating particles to induce coating formation. The mixing mechanisms are relatively simple and versatile for scale-up purposes. Dry powder spraying requires the use of an electrostatic or fluidised bed to distribute the cathode materials where the coating material is sprayed onto the surface. This process is ideal for continuous processes, but precise control of powder flow must be considered for good coating properties. Dry deposition technologies have fine control over coating properties such as thickness and uniformity but are relatively slow and high cost due to complex specialised equipment.

Mechanical dry coating has gathered wide attention due to its simplicity and relevance in the development of dry electrode processing. Several common techniques developed for carbon coating formation include ball milling, planetary mixing, and high shear mixing. In particular, planetary mixers and high-shear mixers such as Eirich and Nobilta mixers have been widely referred to as "intensive" or "high-shear" mixers and are used for mixing cathode active materials and conductive additives. Bockholt et al. [105] studied four different dry mixers: a conventional drum mixer, a planetary mixer and high-shear mixers (Eirich and Nobilta mixers). The findings showed that all these mixers can facilitate carbon black deagglomeration to varying degrees (Figure 2.17). High powder conductivities yielded from the Eirich mixer and planetary mixer indicate a well-distributed carbon black network that facilitates good electronic conduction. The low conductivity obtained from the rotary drum mixer is likely due to its inability to effectively break down large agglomerates, leading to a poor conduction network. The intermediate conductivity but high packing density indicates that the Nobilta mixer has a higher mixing intensity and therefore results in smaller aggregates compared to the Eirich mixer and planetary mixer. This highlights the ability of the Nobilta, Eirich and planetary mixers to facilitate deagglomeration. This study, however, lacks a comprehensive comparison as the mixing intensities are different due to varying mixing conditions for each mixer.

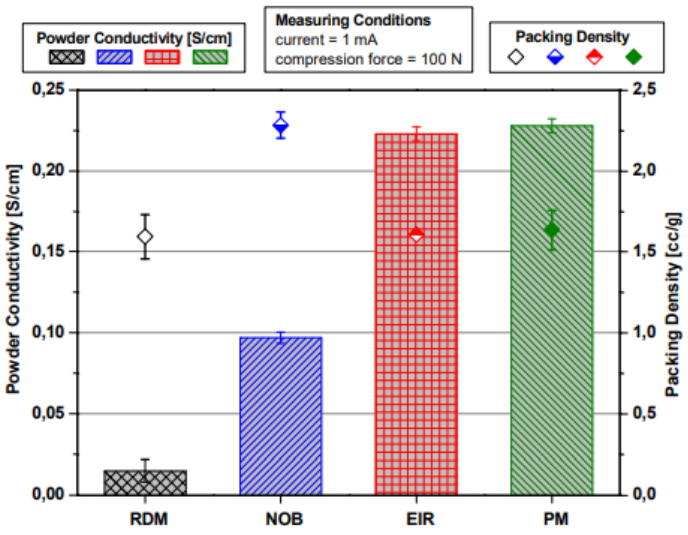

Figure 2.17: Two-point powder conductivity and packing density of AM and CA mixed in a rotary drum mixer, Nobilta mixer, Eirich mixer and a planetary mixer [105].

2.4.2 Intensive Dry Mixing for Coating Formation

Each of the three high-shear dry mixers discussed in Section 2.4.1 utilises different mixing principles. Planetary mixers achieve mixing through a unique dual-motion system (Figure 2.18a). The mixing elements rotate independently on their respective axes while also revolving around a central axis. This combination of rotation and revolution generates shear forces for effective mixing and simultaneously promotes the redistribution of material for homogeneity. In contrast, the Eirich mixer relies on both a rotating, titled mixing pan and an eccentrically aligned mixing element that also rotates to induce shear forces (Figure 2.18b). A fixed scraper is usually present on the wall to ensure material redistribution. Lastly, the Nobilta mixer differs from conventional mixers with its horizontally oriented mixing chamber (Figure 2.18c). This configuration introduces unique flow patterns, contrasting with conventional vertical or tilted mixers. Its primary mixing mechanism involves forcing particles through the narrow gap between the rotating blade and chamber wall, creating strong shear forces for dispersion. Its horizontal orientation allows materials to be redistributed easily.

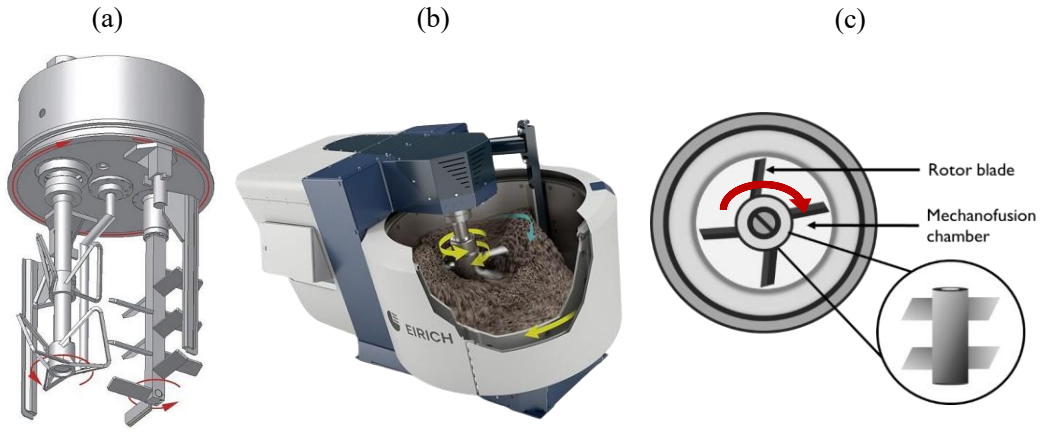

Figure 2.18: Schematic depicting the mixing principles of a (a) planetary mixer [106], (b) Eirich mixer [107] and (c) Nobilta mixer.

The mixing process for the Nobilta mixer is referred to as mechanofusion, where it uses a high shear field to spheronise or dry coat powders with fines without the use of any liquids [108]. The term “mechanofusion” refers to the use of strong mechanical energy to modify tribological and surface functional characteristics of particles or induce mechano-chemical reactions between different particles. There are various variations of the mechanofusion system depending on the application, but the Nobilta mixer manufactured by Hosokawa Micron is the most common configuration used in academic research. Mechanofusion is a useful technique that preserves the median particle size and has relatively fewer process parameters that directly influence the performance and subsequent particle properties. In mechanofusion, a powder mixture of two or more groups of particles is subjected to mechanical forces as it passes through a variable gap in a mixing chamber. The process breaks up agglomerates of small particles and distributes them effectively to form coatings on host particles.

A general description of the mechanofusion process and its mixing mechanism was reported by the Ghadiri Research Group [109]. The system features a cylindrical mixing chamber with a rotor blade that rotates clockwise, generating a centrifugal field. There is a clearance between the tip of the blades and the chamber wall. During mixing, the powder mixture is forced towards the chamber walls by centrifugal forces to form a powder layer. This powder layer is forced through the narrow gap between the tip of the rotor and the chamber wall, generating high shear forces due to the radial velocity gradient. Intense collisions between particles themselves and against the chamber wall promote the smearing action of small particles onto the surface of larger particles. Simultaneously, these forces can break up agglomerates of guest particles to enhance adhesion onto larger particles. The mixture is then redispersed into the chamber and continuously undergoes the process of compression, frictional shearing and deagglomeration (Figure 2.19).

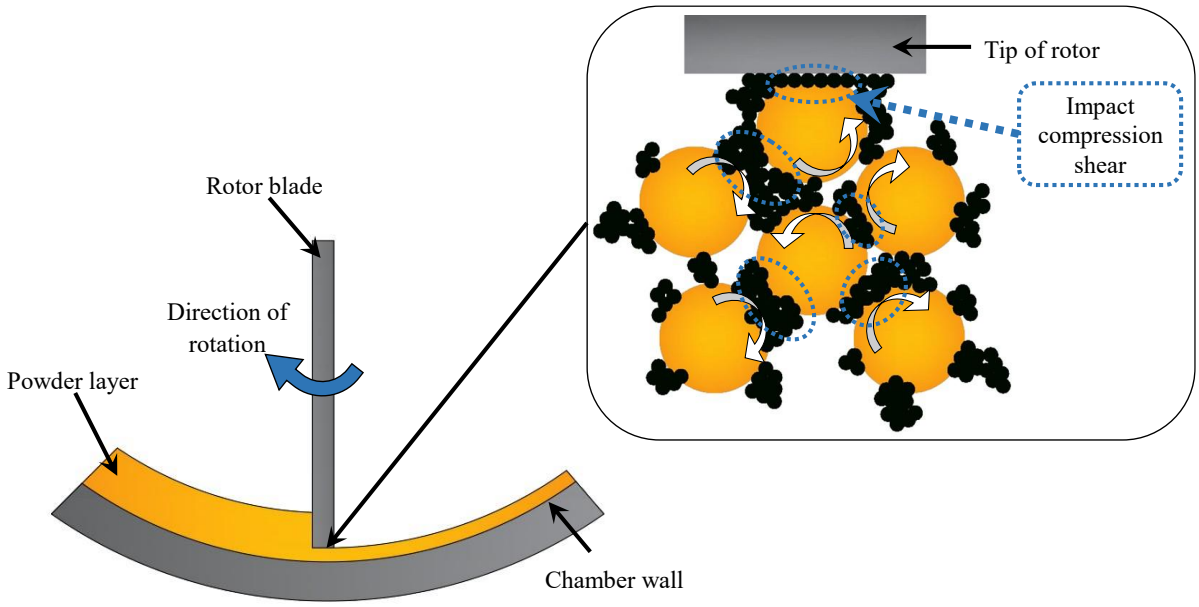

Figure 2.19: Principle of the mechanofusion process where a powder layer is forced through the narrow gap between the tip of the rotor and the chamber wall. Intense shear forces between particles themselves and the chamber wall lead to the breakdown of agglomerates or small particles. Continuous compression promotes coating onto large particles. Adapted from [110].

The blade gap is critical for controlling the thickness of the coating and can be adjusted based on the desired powder properties. At high rotational speeds, intense interactions can generate thermochemical energy that may promote the coating of guest particles onto the host particles [111]. Spheronisation and coating are usually achieved rapidly, often within minutes. For battery material processing, the blade geometry and gap space are generally not varied. Therefore, mechanofusion may provide a greater degree of control over energy input compared to traditional intensive mixing methods.

The mechanofusion process is relatively simple to operate, with mixing time and rotation speed serving as the critical operating parameters [112]. The rotation speed directly affects powder flow properties which can result in variations in mixing profiles. For mixing time, a minimum time is necessary to ensure the breakdown, dispersion and subsequent adhesion of guest particles onto the surface of host particles. Despite being a valuable dry processing technique, literature is rarely published as its parameters are not clearly defined and understood mechanistically [113]. Available literature usually demonstrates particles being spheronised or coated with another phase but only using specific sets of mixing conditions. In terms of scale-up possibilities, the reduced reliance on bulk flow for mixing and a small, defined zone for particle interaction may offer a more predictable scale-up. However, other aspects to consider should include the blade geometry at large scales, significant heat generation in larger mixers and the effect of loading on mixing efficiency.

2.4.3 Mechanofusion Coating Applications

The application of mechanofusion has been reported in several studies in fields ranging from pharmaceuticals to metallurgy. For example, Zhou et al. [112], [114] found that mechanofusion of magnesium stearate and silica on lactose monohydrate led to coating formation which reduces cohesion and improves particle morphology, leading to enhancements in tapped density, compressibility and flow properties. Similar benefits are also reported in a study where polymethylmethacrylate (PMMA) particles coated with TiO_2 flow freely with a near-zero angle of repose compared to a high angle of repose of pristine particles [115]. Additionally, Gauthier et al. [116] reported that an alumina coating on iron particles offers protection by slowing down surface oxidation reactions.

More recently, mechanofusion has been applied in battery manufacturing to enhance active material properties. One of the primary applications of mechanofusion is the production of tailored particle structures, through composite particles or coating formation. Zheng et al. [117] demonstrated the spheronisation of NMC622 using mechanofusion, resulting in particles with a smooth and reduced surface area, with a thin (~20 nm) coating layer of the same bulk material with a homogenous distribution of Ni, Mn and Co. This coating minimises parasitic reactions with the electrolyte and leads to improved capacity retention and cycle life. However, prolonged mixing resulted in decreased rate capacity and increased cell polarisation and degradation due to excessive surface smoothness.

Zheng et al. [118] also produced a homogenous, dense and robust Al_2O_3 coating on NMC622 via mechanofusion which remained intact after slurry mixing. However, complete coating coverage on the NMC surface led to a low capacity, likely due to low ionic conduction but exhibited minimal capacity fade compared to uncoated samples. Core-shell nanocarbon-NMC811 from mechanofusion showed increased stability and higher capacity due to a protective, conductive coating [119]. Further, Liu et al. [120] showed the feasibility of a lithium lanthanum titanate coating as an ionic conductor on

NMC particles. Cao et al. [108] utilised mechanofusion for the synthesis of Si-alloy/graphite composite particles, by incorporating a well-dispersed Si phase embedded between graphite layers that provides a buffer for expansion. These composite anode particles exhibited high cyclability and rate capability compared to conventional Si-alloy graphite coatings. Similar approaches have also been used to produce carbon-encapsulated Si particles that allow free Si expansion within the buffer shell [121]. These studies collectively demonstrate the versatility of mechanofusion in battery processing, which includes particle spheronisation for enhanced surface morphology, synthesis of composite particles and the formation of dense, robust coatings of various materials that offer physical, electronic and ionic enhancements.

Recent studies, primarily led by Arno Kwade, have exploited the high shear mixing mechanism of mechanofusion for simultaneous carbon black deagglomeration and direct coating formation on active material particles [42], [64], [78], [122]. Bockholt et al. [64] showed that mechanofusion allows carbon black to directly attach to the active material surface for short-range electrical contacts while subsequent calendering promotes the formation of long-range conduction, thus resulting in enhanced cycling stability. Moreover, they reported that the solid content of slurries can also be increased with less solvent used, which benefits the drying process. Wenzel et al. [122] presented a systematic investigation between the mechanofusion parameters (i.e. temperature, motor current) and material properties (i.e. bulk density, conductivity), revealing correlations with the expected structural change of carbon black. Westphal et al. [78] studied carbon black deagglomeration and coating through the evolution of electrode resistivities with a dimensionless Froude-tool number that describes mixing intensity. They showed that an optimal mixing intensity exists and beyond this optimum leads to increased resistivity. Bauer et al. [42] reported that only a thin carbon black coating on NMC111 is sufficient for electronic conduction enhancements. They also highlighted the importance of evaluating the spatial distribution of conductive additives that correlates well with the various length scales within electrode structures as discussed in Section 2.3.1; at the nanoscale (active material surface), mesoscale (localised proximity to active material) and macroscale (homogenous distribution throughout electrode). The addition of graphite during mechanofusion showed that graphite flakes can penetrate the wrapping polymer shell to decrease resistivity. Lastly, other conductive additives such as carbon nanotubes (CNT) have also been used as a coating through mechanofusion, leading to improvements in initial Coulombic efficiency and rate capability [123].

2.4.4 Coating Implications

While the traditional wet manufacturing process remains the industry standard, its full impact on the final electrode structure and performance is not fully understood. This lack of mechanistic understanding regarding the process-property relationships (Figure 2.20) hinders process optimisation and quality control. Slurry mixing is critical in achieving homogeneity, with inconsistent dispersion leading to localised resistance and polarisation or potential mechanical instability. Coating and drying impacts electrode porosity, thickness and even adhesion to the current collector. Any deviations may lead to uneven current density and accelerated degradation or electrode delamination. Calendering, while crucial for energy density, may also influence electrolyte accessibility and damage electrode integrity if not carefully controlled. Studies demonstrate that coated particles can significantly alter electrode structure, which affects electronic and ionic conduction [42], [64], [65], [66]. These differences can be traced back to the processes involved as the conductive network formation is ultimately linked to mixing, coating, and drying.

Mixing

Mixing Variables
- Mixer type
- Rotational speed
- Temperature
- Shear rate

Slurry Properties
- Surface tension
- Rheology
- Density
- Agglomerate size/structure

Coating

Coating Variables
- Coater type
- Coating speed
- Coating gap
- Shear rate
- Web tension
- Temperature

Wet Film Properties
- Thickness
- Coatweight
- Defects
- Adhesion
- Structure

Drying

Drying Variables
- Dryer type
- Time
- Temperature
- Zones
- Air flow

Dry Film Properties
- Thickness
- Coatweight
- Defects
- Adhesion
- Structure

Calendering

Calendering Variables
- Gap
- Pressure
- Speed
- Temperature

Electrode Properties
- Thickness
- Coatweight
- Defects
- Adhesion
- Structure
- Wetting
- Electrochemistry

Figure 2.20: Summary of process parameters and product properties involved in conventional electrode manufacturing. Adapted from [124].

2.5 Challenges and Opportunities

Particle and electrode engineering offer promising avenues to further unlock the potential of electrode performance. While conventional wet slurry mixing facilitates long-range electronic conduction through bridge structures, its lack of control over film formation limits the ability to optimise electrode structures for better performance. This motivates the research into pre-processing techniques for carbon black deagglomeration and coating formation as a means of tailoring film structures. Studies demonstrated the importance of conductive additive proximity to active materials for short-range contacts and methods for analysing dispersion. Various carbon coating techniques, particularly dry methods have been reviewed, with mechanofusion emerging as a novel approach that holds the potential for superior control over film formation.

Despite progress in understanding carbon black deagglomeration and coating via mechanofusion, several critical gaps remain. A comprehensive understanding of achievable particle and coating characteristics (e.g. carbon black structure; coating morphology, coverage, thickness) is lacking. Additionally, while particle properties like size and density are frequently used to infer carbon black deagglomeration, the impact of mixing on manufacturing factors such as storage and flowability is rarely considered. Further research is also needed to explore the amount of unbound, free carbon for insights into coating efficiency.

Existing literature emphasises the use of slurry and electrode properties to understand deagglomeration. While resistivity by compression is a valuable supporting metric, its potential as a direct tool for studying deagglomeration in dry powders needs further exploration. A systematic understanding of critical mixing parameters (mixing time and speed) is needed for informed process selection. Additionally, the effects of carbon black properties and other unconventional conductive additives require deeper investigation.

Current findings often focus on final electrochemical performance, overlooking the evolution of powder, slurry and electrode properties. Furthermore, there is limited investigation into how the distribution of short and long-range contacts can be manipulated within electrodes. Moreover, the influence of these deliberately manipulated pathways on resulting electrode structures and conductivity together with the corresponding mixing and drying behaviours should be studied.

Developing a precise process-structure-property relationship may unlock the potential for improvements in the manufacturing process through targeted process adjustments for specific performance goals. It may also aid in pinpointing the exact origins of defects, leading to improved quality control.

Chapter 3 Materials and Methods

3.1 Introduction

This chapter outlines the experimental procedures used to prepare carbon-coated NMC particles through mechanofusion as a method of controlling the formation of film structures on NMC. The first section outlines the mechanofusion mixing procedures followed by slurry and electrode preparation. The second section discusses the characterisation techniques used to study the dry mixing process, coated particles, and subsequently the designed electronic networks within slurries and electrodes, as well as their suitability for the work, throughout Chapters 4 to 6.

3.2 Materials

All materials were purchased or supplied from commercial suppliers. The cathode active material was lithium nickel manganese cobalt oxide, $LiNi_{0.6}Mn_{0.2}Co_{0.2}O_2$ (NMC622, BASF SE). The conductive additives were carbon black C-NERGY™ Super C45, C65 (Imerys), LITX® HP, 200, 300 (Cabot Corp.) and multi-walled carbon nanotubes CNT1015, CNT3080 (Gelon Lib Group Co.). The polymeric binder was poly(vinylidene) fluoride (Solvay Solef® 5130 PVDF) from Sigma Aldrich. The solvent for slurry preparation was N-methyl-2-pyrrolidone (NMP) from Sigma Aldrich. The main material properties are shown in Table 3.1. Additional material properties are given individually in subsequent chapters where relevant. All materials were used as received unless otherwise stated.

Table 3.1: Properties of key materials used in this study.

Material	Chemical Formula	Density (g cm^{-3})	d_{50} (µm)
NMC622	$LiNi_{0.6}Mn_{0.2}Co_{0.2}O_2$	4.74 [a]	11.1 [d]
Carbon black C65	C	1.9 [b]	32 (nm) [b]
PVDF	$-(C_2H_2F_2)_n-$	1.7 [c]	< 300 [c]
NMP	C_5H_9NO	1.028 (g mL^{-1}) [3]	-

[a] Obtained from data sheet provided by manufacturer, BASF SE

[b] Obtained from data sheet provided by manufacturer, Imerys

[c] Obtained from data sheet provided by supplier, Sigma Aldrich

[d] Volume-weighted average measured using Malvern Mastersizer 3000

NMC622 offers a good balance between high energy density and stability, therefore making it a suitable cathode material to be processed in ambient environments. Compared with NMC811, it exhibits lower sensitivity to environmental factors such as moisture and surface reactivity. Additionally, NMC622 is well-studied and widely used in academic research and commercial batteries, enabling the findings in this work to be benchmarked against existing electrochemical data Carbon black (C65) was selected for its high conductivity and low production cost. Similarly, its extensive use in NMC-C65 systems also provides a wide range of baseline data for comparison. NMP

was chosen as the solvent due to its ability to dissolve PVDF, and its compatibility with all other materials to form a rheologically stable slurry

The handling of battery materials requires stringent health and safety procedures to protect lab personnel and prevent material degradation. All experimental work was conducted using standard personal protection equipment, i.e. lab coat, nitrile gloves and safety glasses, and performed under extraction either in a fume hood or a portable downflow booth. Additional precautions were taken when handling conductive additives such as carbon black or carbon nanotubes as they can easily become airborne. When working with large quantities of these additives, FFP3 class respirators and protective sleeves were used to minimise respiratory and skin exposure. Lastly, NMP is a potent solvent known for its skin irritant properties and reproductive toxicity. Handling of NMP was carried out in a glovebox with an Ar atmosphere whenever possible. When NMP is used in a fume hood, latex or butyl rubber gloves were used as NMP can permeate nitrile gloves. If this was not feasible, double-gloving was carried out to provide additional protection.

3.3 Sample Preparation

Binary powder mixtures of NMC and C65 were dry mixed in a Nobilta^{TM} Mini (Hosokawa Micron Corp.) mixer with varying NMC:C65 wt% formulations as needed (Figure 3.1). All mixtures were weighed accordingly to make up a total of 20 (± 0.1) g for each sample. The mixer was then rotated to a horizontal orientation. The powder mixture was first subjected to pre-mixing at 500 rpm for 2 min to disperse and homogenise the binary powder mixture and then mixed for up to 60 minutes at 1000/ 2300/ 5000 rpm (tip speed = 4.61/ 10.6/ 23.04 m s^{-1} respectively). The clearance between the tip of the rotor blade and the inner wall of the mixing chamber was 1 mm. The temperature of the mixer (average range of 19 – 22 °C) was regulated using a cooling water source and air flow was maintained at approximately 2.8 m^3 L^{-1}. Powder samples were retrieved at various mixing times for characterisation and subsequent experimental procedures.

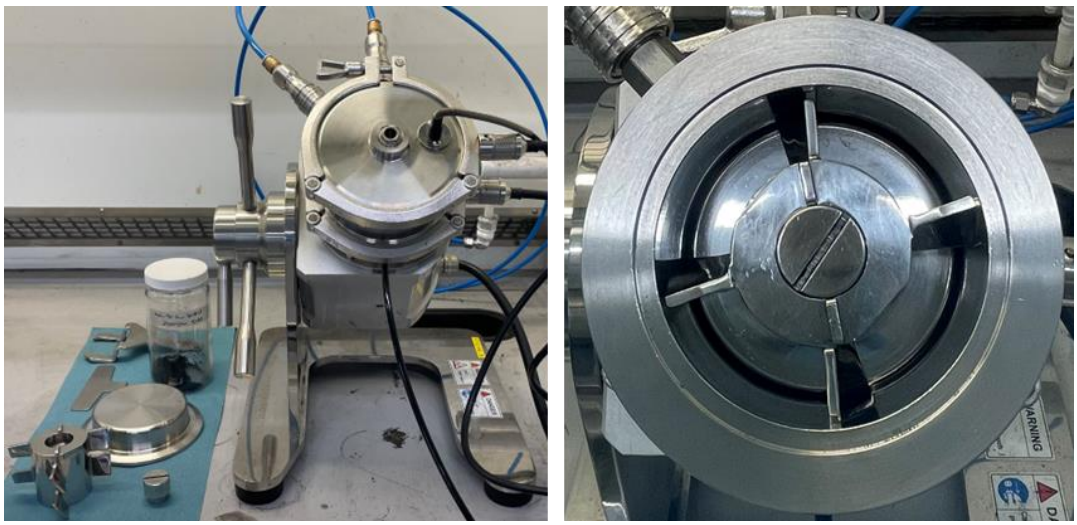

Figure 3.1: Nobilta^{TM} Mini mixer (left) and its internal mixing chamber (right).

All powder materials used for slurry preparation were stored overnight at 120 °C in a vacuum oven before use. The slurry was prepared according to two slurry formulations depending on the powder sample formulation. The standard formulation corresponds to 96:2:2 wt% of NMC:C65:PVDF. For this formulation, carbon black was added during the slurry step to allow the formation of long-range electronic pathways. Firstly, the binder mixture was prepared by making a solution of 8 wt% solid in NMP. The standard solid loading was 5 g, and the standard solid concentration was 60 %, giving a total amount of 3.33 g NMP required. 0.1 g of PVDF was weighed into a 9 mL Thinky pot in a fume hood or a portable downflow booth and then transferred into a glovebox with an Ar atmosphere (typical H_2O and O_2 <0.1 ppm) where 1.16 g of NMP was added. This mixture was mixed in a Thinky mixer (ARE-250) at 2000 rpm / 15 min. Next, 0.1 g of C65 and 1.09 g of NMP were added into the pot, mixed at 500 rpm / 1 min followed by 2000 rpm / 5 min. Finally, 4.8 g of NMC and the remaining 1.09 g of NMP were added into the pot, and mixed at 500 rpm / 1 min, then 2000 rpm / 10 min followed by a final degassing step at 2200 rpm / 3 min. All mixing sequences were programmed in such a way that there were no breaks in between using the memory function on the Thinky mixer. This ensures the consistency of the mixing process and reduces uneven mixing, sedimentation or variation in slurry homogeneity.

The second formulation corresponds to 98:2 wt% of NMC:PVDF. For this formulation, no carbon black was added during the slurry mixing step. Similarly, 0.1 g PVDF and 1.16 g NMP were first mixed at 2000 rpm for 15 min. 4.9 g NMC and the remaining 2.17 g of NMP were then added into this mixture and mixed at 500 rpm / 1 min, then 2000 rpm / 10 min followed by a final degassing stage at 2200 rpm / 3 min. For larger slurry samples and varied slurry solid concentrations, the amount of each material was adjusted accordingly.

Due to the change in the amount of free carbon and the carbon black structures arising from deagglomeration and coating during mechanofusion, the amount of NMP solvent used was estimated through trial and error, by observing the gel-behaviour of the slurry, to achieve the correct viscosity range. This involved visually assessing the gel-like behaviour of the slurry and comparing it to a conventionally prepared slurry of the same standard formulation without additional processing of the carbon black. A general guide was to increase the solid concentration (i.e. decrease the amount of NMP added) for samples with smaller carbon structures and less free carbon. Generally, with increasing mechanofusion mixing time and speed, a lower amount of NMP was used for slurry preparation. For example, for 2 wt% C65, 3.33 g of NMP (60 % solids) was used for samples mixed for 2 min and 2.7 g of NMP (65 % solids) was used for samples mixed for 60 min. A detailed explanation of the rationale for the measurements of NMP used will be discussed in Chapter 6.

The slurry was coated onto polyethylene terephthalate (PET) film (average thickness: 78 μm) using a doctor blade (MTI Corp.) with a blade gap of approximately 150 μm (calibrated using a metal shim). The slurry was poured in a bone-shaped line with slurries thicker at the edges, on one end of the PET film close to the doctor blade, to ensure uniform spreading. A draw-down table (MSK-AFA-L800-H-110, MTI Corp.) was used to coat the slurry onto the PET film at an arbitrary speed of 15. A calibration curve (Figure 3.2) was produced by measuring the time required for the full distance travelled by the pushing bar at various arbitrary speeds. Using this calibration curve, the coating speed was found to be approximately 5.21 mm s^{-1}. The coated film was then dried using a built-in overhead heater, starting at 25 °C and gradually increasing up to 80 °C for a total of 1 hour. The final dried film thickness was approximately 50 μm and the film was stored at 120 °C in a vacuum-sealed pouch until further use.

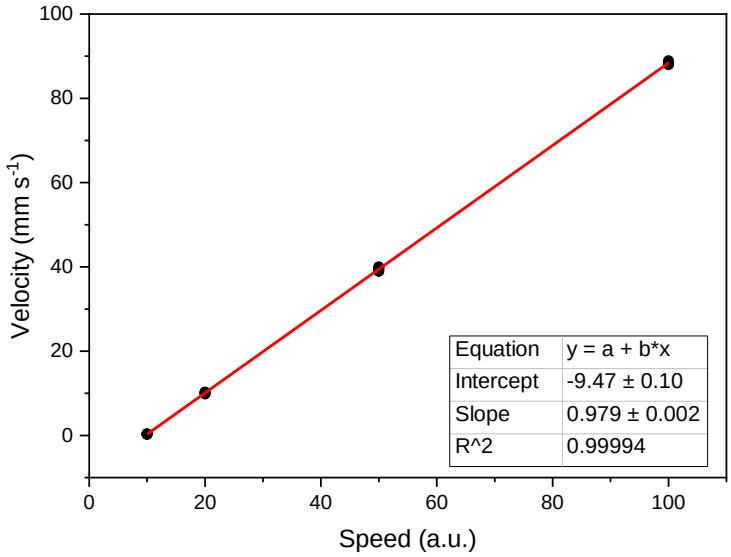

Figure 3.2: Coating speed calibration curve for the draw-down table.

3.4 Sample Characterisation

3.4.1 Scanning Electron Microscopy (SEM)

Scanning electron microscopy (SEM) is an imaging technique that uses a focused beam of electrons to create an image of a sample, with a typical set up as shown in Figure 3.3a. A beam of high-energy electrons that is accelerated by an electron gun is focused on the surface of a sample. The beam collides and interacts with the sample atoms, resulting in both elastic and inelastic scattering of electrons (Figure 3.3b). For elastic scattering, the scattered electron trajectory within the sample changes but retains most of the kinetic energy and velocity, resulting in the generation of backscattered electrons (BSE) [125]. BSE originates from deeper regions of the sample and shows high sensitivity to differences in atomic number. For inelastic scattering, the scattered electron trajectory is largely unaffected, but energy is lost and absorbed by the sample resulting in the generation of secondary electrons (SE) [125]. SE can only escape the sample if they originate from near-surface regions due to their low energy levels. Therefore, SE imaging can provide high spatial resolution and robust topographic contrast. BSE are collected by solid-state detectors and SE are collected by an Everhart-Thornley detector to be converted into images.

For coated NMC particles, samples were prepared by attaching loose powders to conductive carbon tape attached to an aluminium stub. Compressed air was blown from the edge of the carbon tape to remove excess powder and reduce particle overlap or accumulation for better imaging. Samples were coated with carbon/gold using a sputter coater prior to imaging. For electrode samples, a small section of the electrode film (typical size 3x3 mm) was prepared and attached to carbon tape on aluminium stubs. The edges of the electrode piece were painted with conductive silver paint and subsequently coated with carbon/gold to ensure the sample was grounded.

A field emission gun scanning electron microscope (FEG-SEM) was used to examine carbon-coated NMC622 particles and electrodes. Two models of SEM by FEI Company were used: Inspect F50 and Inspect F. The typical conditions used were dependent on the working distance, where a working distance of approximately 10 mm is associated with a spot size of 4, an aperture of 4 and an accelerating voltage of 10 – 15 kV. For a smaller working distance of 5 – 7 mm, the typical spot size used was 2.5 – 3, aperture of 3 and an accelerating voltage of < 5 kV. Additionally, a JSM-6010 SEM (JOEL Ltd.) was used for imaging of electrodes investigated in Section 4.3.

(a)

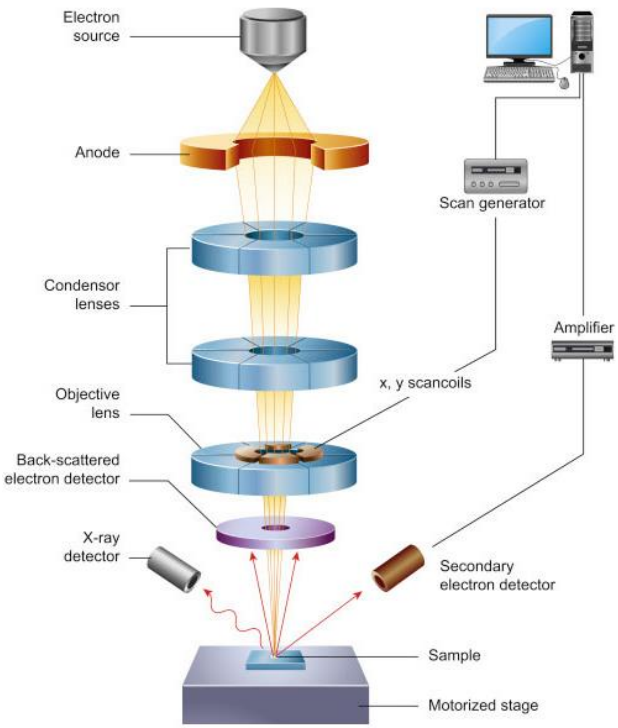

(b)

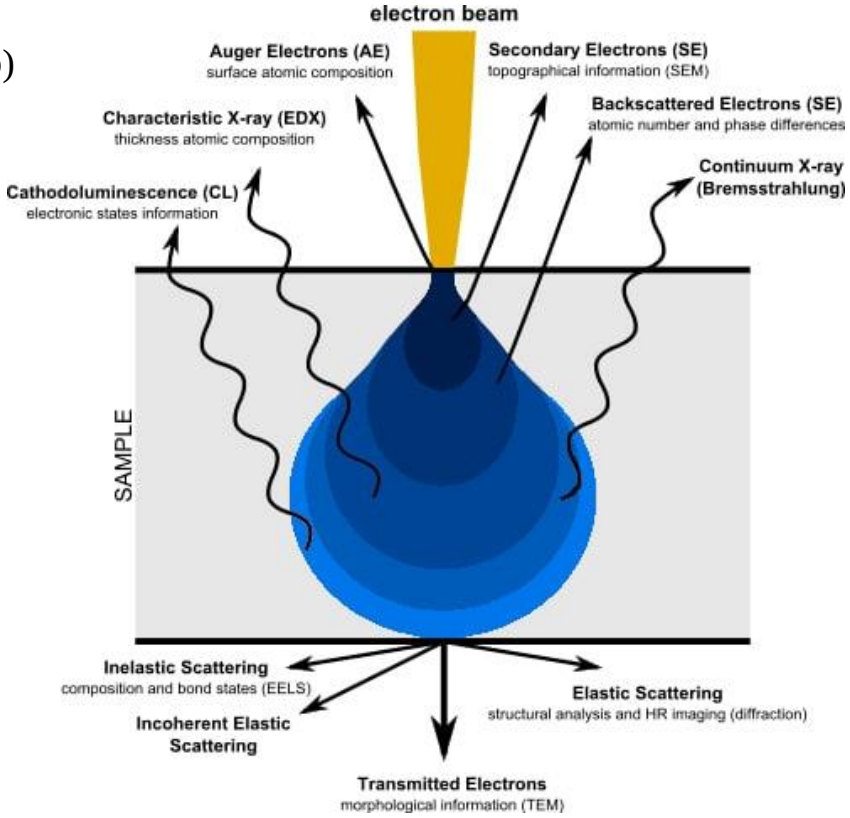

Figure 3.3: Schematic of a (a) scanning electron microscope [126] and (b) the effects produced by the electron-beam interaction with a sample specimen [127].

3.4.2 Energy Dispersive X-ray (EDX) Spectroscopy

Energy dispersive X-ray (EDX) spectroscopy utilises a similar interaction between a focused beam of electrons and a sample for compositional analysis. Characteristic X-rays that are produced from regions deeper than secondary or backscattered electrons are able to provide information on the relative quantity and distribution of atoms within the sample [128]. The X-rays that are produced are unique for each element, as heavier elements emit X-rays with higher energy compared to lighter elements. An EDX detector captures these characteristic X-rays and creates a spectrum that displays the peaks corresponding to the energies and intensity of the X-ray emitted. This information reveals the elements that are present within the sample based on a database of characteristic X-ray energies. However, limitations may arise when analysing samples containing very light elements (low atomic number) as their X-ray signals are very weak. EDX was carried out using a built-in EDX detector within a JSM-6010 SEM (JOEL Ltd.), and the data was recorded using JOEL's proprietary software.

3.4.3 Particle Size Distribution

Static light scattering techniques such as laser diffraction are commonly used for analysing particle size distributions. This method is able to provide a volume-weighted distribution where each particle relates to its volume. For a uniform density, the volume is equivalent to the mass and can be related proportionally to its size [129]. A laser beam is passed through the dispersed particle sample, where the angular variation in the scattered light intensity is measured. Large particles scatter light at smaller angles while small particles scatter light at larger angles, as shown in Figure 3.4. Similarly, a number-weighted distribution can also be obtained where the absolute number of particles within each size range is obtained.

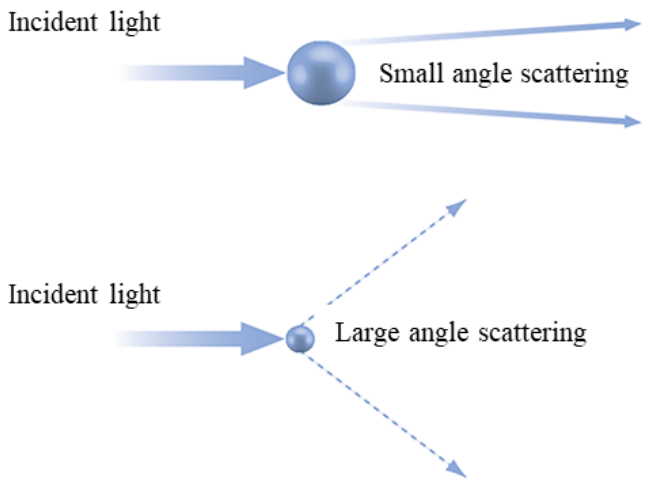

Figure 3.4: Differences in light scattering angle for small and large particles [129].

Samples are required to be dispersed for individual particles to be spatially separated. In wet dispersion, particles are suspended in a liquid dispersant with the aid of agitation or ultrasonic irradiation. Dry dispersion utilises a flowing gas stream and a vibratory feed to facilitate different dispersion mechanisms such as velocity gradients caused by shear stress, and particle-particle or particle-wall collisions [129]. Fine powders (< 1 μm) are less suited to this technique as the particle forces are very difficult to overcome.

Particle size distributions of the coated samples were measured using a Mastersizer 3000 particle size analyser (Malvern Panalytical). The wet cell configuration was used to feed samples through the instrument as samples contained free carbon particles which are difficult to separate using the dry cell method. Several grams of sample were gradually added to the agitated dispersant until the pre-set obscuration limit was achieved. An obscuration limit of 15 % and a stirrer speed of 2500 rpm was used. The weighted residual was kept as low as possible (recommended range < 1 %) for accurate results. Ultrasonic irradiation of 50% was used where required, usually at high free carbon content, where large, agglomerated carbon black particles are visible to the eye. The material optical properties used are shown in Table 3.2. 10 separate measurements were obtained and the averaged particle size distribution was evaluated for each sample of interest.

Table 3.2: Particle and dispersant properties for particle size measurements.

Particle and Dispersant Optical Properties	Value/Setting
Particle refractive index	3.00
Particle absorption index	0.02
Dispersant name	Water
Dispersant refractive index	1.33
Scattering model	Mie

3.4.4 Particle Density

The bulk density of powders is defined by the ratio of the mass of a freely settled powder sample and its corresponding volume which includes the interparticle void volume. This volume is determined by the spatial arrangement of particles within the powder bed. Bulk density is categorised as an extrinsic property as it is dependent on how the powders are handled, which makes it challenging to obtain reproducible results [130]. For battery manufacturing applications, the use of bulk density is less common, but it serves as a reference to determine powder flowability using the Hausner ratio, or for material handling and storage requirements.

The tapped density of powders is an important property in particle technology and is often used in conventional particulate industries such as pharmaceuticals and food processing. The tapped density represents the maximum packing density that can be achieved when particles pack more closely under repeated tapping or vibration. This is due to the rearrangement of particles during tapping, filling the voids for a more compact arrangement. For novel or pre-treated battery materials, tapped density can serve as a useful quality control parameter to assess a wide range of particle properties such as particle size distribution, flowability, packing dynamics and behaviour [131] etc.

Powder tapped density measurements were carried out using an automated tapped density analyser (Autotap, Anton Paar). First, a 5 cm^3 graduated cylinder was chosen and the empty weight (m_1) was recorded. Powder samples were filled into the cylinder to approximately 4 cm^3 (80 % maximum graduation as recommended by Anton Paar). The opening was covered with a piece of foil and securely held covered with a finger. The cylinder was then inverted back and forth for 6 – 7 inversions and set upright. This ensures the powder is loosely packed and eliminates any effects of initial compaction during sample filling. The initial volume (V_i) and the mass of the cylinder with the sample (m_2) was recorded. The mass of the powder sample (m_s) was calculated by the difference between the two recorded masses. The cylinder was then subjected to 500 taps and the final powder bed volume (V_f) was recorded. The tapping rate was preconfigured at 260 min^{-1} with a drop height was 3 mm.

The bulk density of the freely settled powder, ρ_b, was calculated using Equation 3.1:

$$\rho_b = \frac{m_s}{V_i} \tag{3.1}$$

The tapped density of the final tapped powder, ρ_t, was calculated using Equation 3.2:

$$\rho_t = \frac{m_s}{V_f} \tag{3.2}$$

The Hausner ratio can be calculated using Equation 3.3 and the flow character can be determined based on the calculated Hausner ratio as shown in Table 3.3.

$$Hausner\ ratio = \frac{\rho_t}{\rho_b} \tag{3.3}$$

Table 3.3: Classification of flow character according to the Hausner ratio [132].

Flow Character	Hausner Ratio
Excellent	1.00 – 1.11
Good	1.12 – 1.18
Fair	1.19 – 1.25
Passable	1.26 – 1.34
Poor	1.35 – 1.45
Very poor	1.46 – 1.59
Very, very poor (approx. non-flow)	> 1.60

3.4.5 Thermogravimetric Analysis (TGA)

Thermogravimetric analysis (TGA) is a technique where the change in mass of a sample is measured as a function of temperature (or time) under a controlled atmosphere. It provides useful information about specific physical (e.g. phase transitions) and chemical phenomena (e.g. oxidation/ reduction). A TGA measurement is carried out by gradually increasing the temperature of a sample while its weight is continuously measured on a balance that is situated outside the heating environment. The change in sample weight and/or derivative weight is plotted against temperature (or time). This can be particularly useful for moisture analysis or compositional analysis of materials.

Powder samples of coated particles were dried overnight at 120 °C in a vacuum oven before measurements were conducted. TGA measurements were carried out using a PYRIS™ 1 TGA (PerkinElmer). A clean, empty ceramic crucible was attached to the hanging microbalance and tared. Miniscule amounts (< 10 mg) of the powder samples were filled into the crucible and the sample mass was measured by the built-in microbalance through the software. The sample was then heated according to a pre-programmed heating profile. The sample was heated in an oxidative (air) atmosphere from 30 to 1000 °C at a heating rate of 10 °C min^{-1}. The gas flow was maintained at 20 mL min^{-1}. Once the temperature reached 1000 °C, the sample was then cooled down to room temperature. The analysis data was recorded by the proprietary software, Pyris Manager.

3.4.6 Slurry Rheology

Rheology is the measurement of the flow and deformation properties of a suspension. For a cathode slurry, its rheological properties depend on all the components, i.e. active material, conductive additive, polymeric binder and solvent. Conventionally, rheology is used as a guide to define the control space to achieve a uniform and defect-free coating. The rheological properties of a typical cathode slurry are dictated by the conductive additive [133]. When dispersed during slurry mixing, carbon black forms a carbon network that holds the active material particles and gives rise to the gel-like behaviour of the slurry. The mechanism and degree of dispersion can greatly affect the carbon network formed, which will be reflected in the slurry rheology.

A flow curve describes the change in viscosity (i.e. resistance to flow) with shear. This is crucial as slurries experience different shear rates during different stages of processing (e.g. mixing and coating). Understanding the slurry response to varying shear rates allows us to understand how the slurry behaves during these stages and to formulate slurries with optimal properties for uniform and defect-free coatings while optimising process design for efficient processing. The storage modulus (G') represents the elastic response during material deformation. A high G' indicates a more solid-like behaviour, which is critical to maintaining a rheologically stable slurry and preventing the aggregation and sedimentation of NMC particles. The loss modulus (G'') represents the inelastic component, corresponding to the heat dissipated during material deformation. A high G'' generally indicates a slurry that is too fluid-like and particles are not held in suspension. An amplitude sweep provides G' and G'' to give an indication of the rheological properties of a slurry, ensuring the slurry is stable, well dispersed and free from defects during processing [133].

Rheology work was carried out at University of Birmingham and supported by Prof Emma Kendrick, Dr Carl Reynolds and PhD candidate Sam Gray. Rheological measurements were carried out using a Netzsch Kinexus Pro+ rheometer with a 40 mm roughened parallel plate, a roughened lower plate and a measuring gap of 1 mm. Slurries were prepared according to the procedures outlined for the formulation of 98:2 wt% NMC:PVDF. Prepared slurries were loaded onto the lower plates and the gap was set to 1.05 mm to allow the sample to be trimmed. The gap was then set to 1 mm to ensure there was no underfilling. Measurements were performed at 25 °C using a Peltier plate and enclosure. Flow curves were measured with a shear rate range of 0.001 to 100 s^{-1}. Amplitude sweeps were carried out with a strain range of 0.1 to 100 % at 1 Hz.

3.4.7 Resistivity by Compression

Resistivity by compression is a two-point probe method used to measure the "through-plane" or bulk resistivity through a material. A current is passed through the sample where the voltage drop is measured and the resistance is determined. The resistivity can be determined if the sample thickness is known. This technique is useful to determine the conductivity of loose powders [34], [90] (e.g. battery active material, conductive additive etc.) but has also been used to evaluate the resistivity of electrodes [78], [93]. The main drawback of this technique is the effect of contact resistances between the surface of the probes and the sample. So far, one publication has reported that contact resistances dominate the measured resistance at length scales up to a few mm [91]. Additionally, it was also reported that the contact resistances arise from constriction effects, not interfacial resistance, and scale directly with bulk resistivity. Regardless of the accuracy of the actual material resistivity, this technique is still useful for assessing carbon black deagglomeration and providing a relative comparison between coated particles, which will be discussed in Chapter 5.

The electrical volume resistivity of the powder samples was measured using the two-point probe method through a pseudo-4-wire in-house designed compression jig, as shown in Figure 3.5. The set-up consists of an insulating top, bottom and middle support mould (material: Nylon 66) with a Ø12 mm die. The moulds are supported by two copper contact stamps from both ends, each attached to two insulated cables, connected to a digital multimeter (DMM7510, Keithley Instruments). The mould with contact stamps was fitted into a load frame (LF10CONF0001-P) equipped with a 10 kN load cell (TX00723) from GDS Instruments where precise compression load is applied. Contact stamps on both ends were each connected to the INPUT (current) terminals and SENSE (voltage) terminals on the multimeter. The 4W-Ω configuration was used with the "offset compensation" setting enabled to minimise the effect of lead resistances and thermoelectric EMFs in low-level resistance measurements respectively. Contact stamps were cleaned as required and polished to minimise the interfacial contact resistance between the copper stamps and the sample.

Compression of powders will lead to an increase in temperature which can greatly influence resistivity. The change in resistivity is dictated by the temperature coefficient of the material, where a positive coefficient corresponds to an increase in resistance with temperature and vice versa. To obtain reliable and comparable measurements, the measured resistance must exhibit an ohmic relationship over the compression range. V-I sweeps were carried out using a source meter (DMM2450, Keithley Instruments) with a passing current of 0 – 0.1 A through the sample where the voltage drop was recorded. V-I sweeps were conducted for selected compression forces over the entire range of 0.05 – 2 kN studied. For both low and high carbon loadings, the V-I sweeps exhibited a straight-line relationship over the compression range, indicating an ohmic relationship (Figure 3.6). An appropriate current must also be selected to minimise noise and obtain an accurate voltage drop measurement. For

the DMM7510 multimeter, the 4W-Ω configuration has a resistance range of 100 nΩ – 1.2 GΩ, which is suitable for all the powder samples studied.

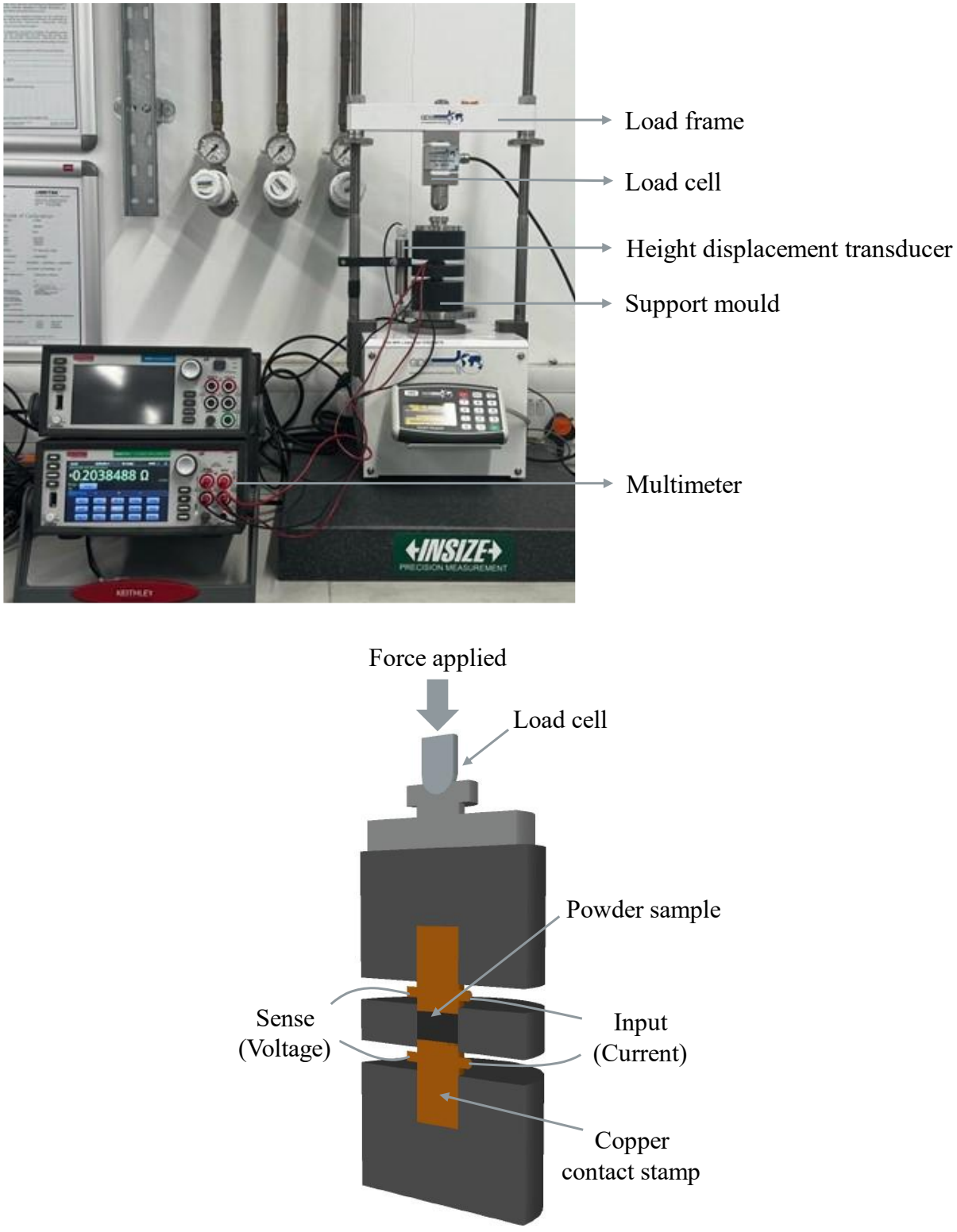

Figure 3.5: Experimental set up for the resistivity by compression technique (top) and schematic depicting the compression support mould and accompanying contact stamps (bottom).

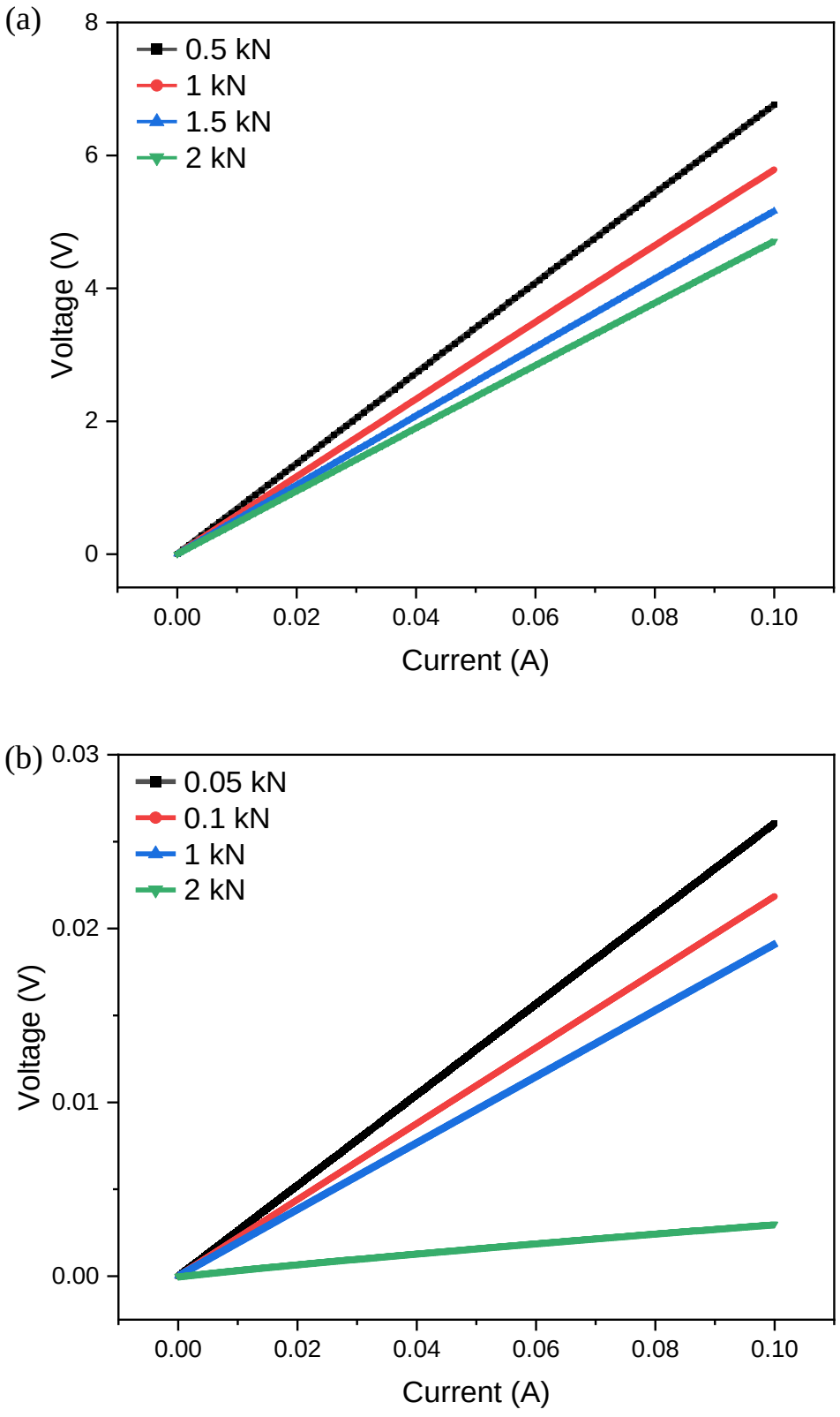

Figure 3.6: V-I sweeps for various compression forces over the range of 0.05 – 2 kN for (a) low carbon loading and (b) high carbon loading.

To carry out resistivity measurements, several grams of sample were weighed and filled into the die. As samples consist of different carbon loading, free carbon content and varying carbon black structures, powder packing can vary significantly. Since the die has a fixed volume, the remaining unfilled sample was then weighed and used to determine the total sample mass filled into the die. A separate contact stamp was used to apply pre-compaction by hand to ensure as much sample was fitted into the die as possible. Next, an initial compaction force of 50 N was applied under the load frame and the initial height of the powder sample was measured using a standard digital height gauge. All measurements were carried out at room temperature (approximately 20 °C), starting by applying a load of 100 N, with further increments of 100 N, up to 2000 N. Resistance values at corresponding compression forces were recorded after a 1 min stabilisation period after the force was applied. The corresponding height of the powder sample was measured using a 10 mm linear displacement transducer kit with an accuracy of 0.07 % FRO (GDS Instruments).

The electrical volume resistivity (φ) at the corresponding powder density (ρ) was calculated using Equations 3.4 and 3.5 based on the methodology reported by Spahr et al. [34]. The volume resistivity was denoted by the symbol σ by Spahr et al., but herein, it is denoted by the symbol φ to avoid confusion with the conventional symbol of σ for electronic conductivity.

$$\varphi = R\frac{A}{h} \tag{3.4}$$

$$\rho = \frac{m}{Ah} \tag{3.5}$$

where R is the measured electrical resistance, A is the cross-sectional area of the die, h is the sample height and m is the sample mass.

The mechanical energy (E_i) required to compress the powder sample to a specific density (ρ) was calculated using Equation 3.6. Spahr et al. [34] reported that this mechanical energy required to compact a powder mixture of active material and carbon black is dependent on the carbon black component and is mainly governed by the strength of the carbon black agglomerates and the breakdown of these structures.

$$E_i = \sum_{j=1}^{i} p_j A\left(h_{j-1} - h_j\right) = \sum_{j=1}^{i} F_j\left(h_{j-1} - h_j\right) \tag{3.6}$$

where p_j is the corresponding pressure applied, A is the cross-sectional area of the die and h is the corresponding sample height. p_j and A can be expressed as F_j, the corresponding compression force applied.

3.4.8 Electrochemical Impedance Spectroscopy (EIS)

Electrochemical impedance spectroscopy (EIS) is a useful, non-destructive tool used to characterise electrochemical reaction mechanisms. In EIS, an alternating current (AC) is applied and the response of the system to the applied potential/current is investigated as a function of time. This contrasts with a direct current (DC) where the response is independent of time. A frequency sweep allows all the processes occurring in a system to be captured. For electrochemical cells, EIS is often used to study the reactions between the two electrodes and investigate basic processes such as film formation or interface reactions [134]. The high-frequency region captures fast processes (e.g. charge transfer) while the low-frequency region captures slower phenomena (e.g. diffusion processes).

A typical Nyquist plot for electrochemical cells typically features one or more semicircles, followed by a linear region, as shown in Figure 3.7a. In the high-frequency region, a non-zero intersection with the real Z' axis indicates the ohmic resistance, which includes contributions from the electrolyte, current collectors and other cell components. This parameter is useful for assessing the overall conductivity of a cell and to identify potential losses in the system. The high-frequency region is dominated by a semi-circle corresponding to the charge transfer resistance (R_{ct}) and the double layer capacitance at the electrode-electrolyte interface. R_{ct} is represented by the diameter of the semicircle and is a critical parameter for understanding the kinetics of the electrochemical reactions within an electrochemical cell. A second semi-circle is present at lower frequencies if two distinct charge-transfer reactions are occurring at different interfaces with separate relaxation behaviours. This includes the cathode-electrolyte, anode-electrolyte interfaces or the presence of an SEI layer which introduces additional resistance and capacitance. Finally, at low frequencies, a straight line at approximately a 45^{o} angle indicates a diffusion-controlled process. This region is described by the Warburg impedance and reflects ion transport dynamics within the electrolyte and electrode materials.

EIS can also be used to characterise the conductivity of electrode slurries to understand the evolution of electronic conductivity as it progresses from active materials into a liquid slurry and finally a solid electrode. For NMC-carbon black mixtures subjected to mechanofusion, the carbon coating on NMC, free carbon content and different carbon black structures will greatly affect the electronic networks within the slurry. The slurry resistance (R_{HF}) can be determined from the real component of impedance that intersects with the zero imaginary axis at the high-frequency range (HFR). A typical Nyquist plot of a cathode slurry is shown in Figure 3.7b. Slurry conductivity (σ) can be determined by the reciprocal of resistivity (φ) using Equation 3.7:

$$\sigma = \frac{1}{\varphi} = \frac{1}{R_{HF}} \frac{L}{A} \tag{3.7}$$

where A is the contact electrode area and L is the height of the slurry sample.

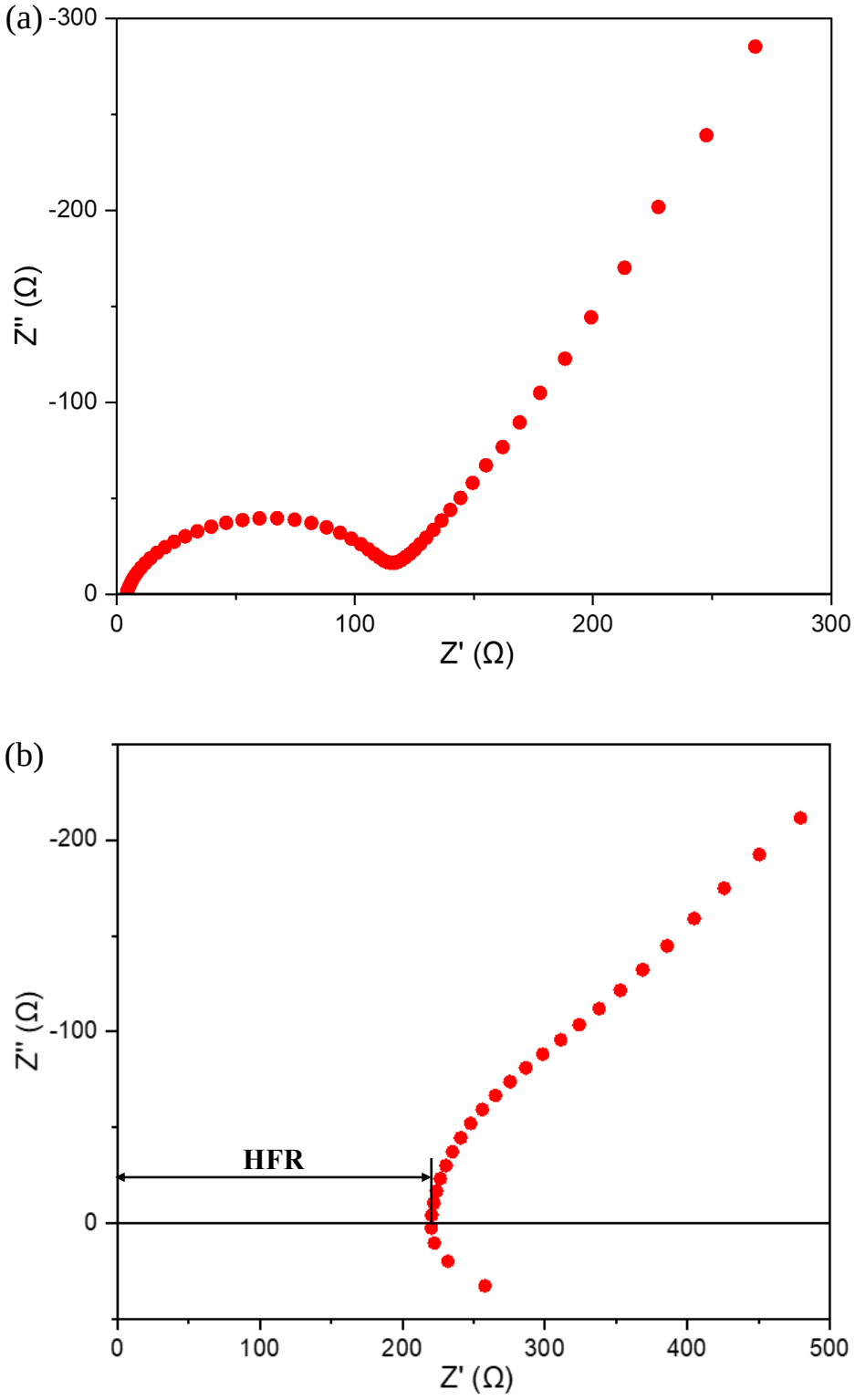

Figure 3.7: Typical EIS response of (a) an electrochemical cell and (b) a cathode slurry at the high frequency range (HFR).

Slurry impedance was measured using a ModuLab XM ECS (Solartron Analytical) modified with a Pstat cable connection (Figure 3.8). A dedicated liquid sample holder (12964A, Solartron Analytical) with Ø30 mm contact electrodes and a maximum depth of 30 mm was used to hold the liquid slurry. The height of the slurry was measured using an integrated micrometer. The top electrode was first lowered to the maximum depth and tared. Prepared slurries were filled into the sample holder and the top electrode was lowered until a small amount of slurry began to seep out of the edges between the top electrode and the sample holder wall. At this point, the height of the slurry was recorded. Frequency sweeps were carried out from 1 Hz – 1 MHz and held at a constant potential of 10 mV. The impedance data was recorded and analysed using Solartron's proprietary software, XM-studio ECS.

Figure 3.8: Electrochemical impedance spectroscopy set up showing the ModuLab XM ECS (left) and dedicated liquid sample holder (right).

3.4.9 Four-Point Conductivity

The four-point probe method is commonly used to evaluate the sheet resistance of thin films. This configuration uses four equally spaced, co-linear tungsten probes that are made in contact with the film. The main advantage of this technique is the ability to eliminate most of the contact and wire resistances. The measurement is done by applying an appropriate DC between the two outer probes and measuring the voltage drop across the two inner probes (Figure 3.9). As voltmeters are usually designed to have high electrical impedance, wire and contact resistances for probes 2 and 3 can be ignored. The voltage drop can therefore be attributed solely to the resistance between probes 2 and 3. If the thickness of the film is known, the film resistivity and conductivity can also be deduced.

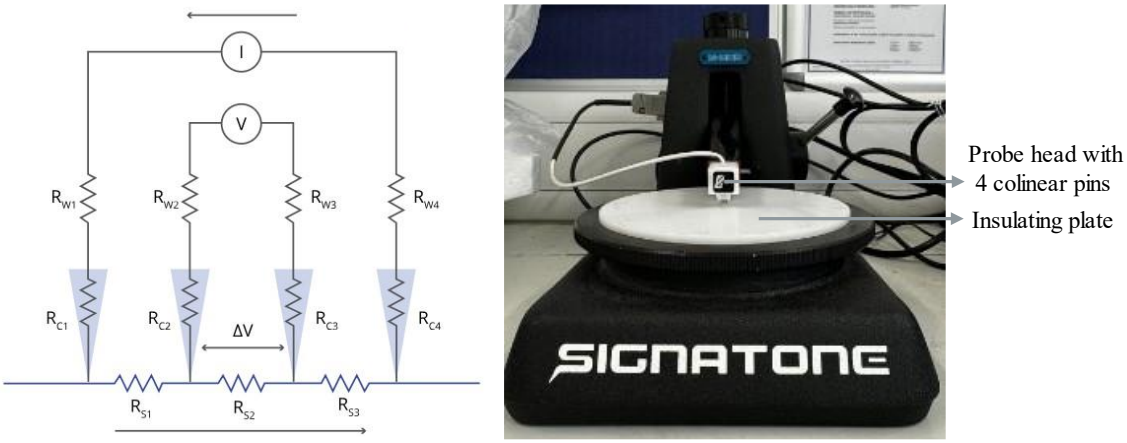

Figure 3.9: Schematic depicting the four-point probe method to determine the sheet resistance of thin films (left) [135] and Signatone for four-point measurements (right).

Coated PET films were punched into ∅14.8 mm discs using an EL-Cut high-precision electrode cutter (EL-CELL®). The thickness of the coated film was measured using a digital thickness gauge (DML3032, Digital Micrometers Ltd). The measurement was carried out using a four-point probe (Signatone S-302 SP-4 Probe) connected to a digital multimeter (DMM7510, Keithley Instruments). The PET film disc was placed onto the insulating plate and the co-linear pins were lowered to about 70 – 80 % of the pin length. The sheet resistance (R_s) was calculated based on the four-probe theory using the measured voltage drop (ΔV) and applied current (I) over a set voltage range of 1 to 7 V, as shown in Equation 3.8. Measurements were taken from various placements where the probes were in contact with different regions of the coated electrode film. The conductivity (σ) was determined by the inverse of resistivity (φ), which can be deduced using the average sheet resistance and film thickness (t), as shown in Equation 3.9.

$$R_s = \frac{\pi}{\ln(2)} \frac{\Delta V}{I} = 4.53236 \frac{\Delta V}{I} \tag{3.8}$$

$$\sigma = \frac{1}{\varphi} = R_s \cdot t \tag{3.9}$$

Chapter 4 Extending Mechanofusion Approaches to Control Particle Coating Formation on NMC as Short-Range Pathways

4.1 Introduction

Cathode active materials possess low electrical conductivity, which is further compounded by the insulating nature of the polymeric binder used in electrodes. Therefore, the addition of conductive additives is crucial for the formation of an electronically percolating network called the carbon binder domain (CBD). The CBD increases the point-to-point electrical contact of active materials for electrical conduction. The CBD is not only critical for electronic conduction but also facilitates ionic conduction through its pore networks. An ideal CBD structure is thought to consist of a combination of short and long-range electronic pathways to achieve optimal performance [38], [49], [61], [62]. However, constructing these ideal structures is often challenging in conventional wet slurry mixing, resulting in a random uncontrolled distribution of active material, conductive additive and binder. As a result, challenges arise when attempting to spatially design the distribution of these components, particularly the conductive additives within electrodes. Specifically, this poses difficulties in independently controlling the distribution of short and long-range electronic networks.

This chapter introduces mechanofusion, a novel dry mixing technique as a potential solution for overcoming the limitations of wet slurry mixing used in conventional battery manufacturing. Mechanofusion approaches are extended as a method to control carbon black deagglomeration and coating on NMC. Through the deagglomeration of carbon black, smaller structures can be obtained to facilitate these electronic pathways. Mechanofusion can also coat carbon black onto NMC, which can enhance short-range electronic conduction.

This chapter aims to investigate the carbon black deagglomeration and particle coating formation on NMC using mechanofusion. The objectives are to:

(1) assess the impact of mechanofusion on the carbon black structure and coating characteristics of film structures on NMC particles;
(2) investigate particle properties that can be correlated to carbon black deagglomeration achieved during mechanofusion;
(3) study the efficiency of the mixing process through the free carbon content after mechanofusion mixing.

4.2 Experimental Design

To study the effect of carbon black content on the resulting CBD structures formed, electrodes with formulations of 94:4:2, 95:3:2, 96:2:2 and 97:1:2 wt% of NMC622:C65:PVDF were prepared based on the slurry mixing SOP for a 96:2:2 wt% formulation as described in Section 3.2. The corresponding mass of each component for the different formulations is shown in Table 4.1. SEM and EDX analysis was carried out to evaluate and distinguish the features of CBD structures formed together with their distribution across the electrode. This work was carried out in collaboration with Dr Xuesong Lu at the University of Sheffield. The full study has been published in a peer-reviewed article (doi: 10.1002/ente.202300446) [71]. Relevant results and analysis were extracted from the article and presented in Section 4.3. For this section, Dr Lu was responsible for electrode fabrication and the author assisted with SEM imaging and EDX analysis, formal analysis of results, and created the schematics for the article.

To study the feasibility of using mechanofusion for coating formation on NMC particles, NMC622 and C65 were mechanofusion mixed in a Nobilta mixer with a carbon loading of 2 wt% and 10 wt% C65 (herein referred to as “low” and “high” carbon loading respectively). The mixing parameters varied were the mixing speed and mixing time. Various combinations of three different mixing speeds of 1000, 2300 and 5000 rpm (herein referred to as “low”, “medium”, and “high” speeds respectively) and two different mixing times of 2 and 60 min (herein referred to as “short” and “long” mixing times respectively) were studied. The experimental data sets for this work are shown in Table 4.2.

SEM of the coated particles was carried out to evaluate the surface morphology and coating characteristics. Backscattered electron imaging (BSE) was used to evaluate the coating thickness of the coated particles. The particle properties of the coated particles, i.e. particle size distribution and particle density, were also characterised to understand the mixing and carbon black deagglomeration process. The experimental procedures are detailed in Sections 3.4.3 and 3.4.4. Additionally, the amount of unbound carbon (herein referred to as “free carbon”) that is present after mixing was studied using thermogravimetric analysis (TGA) and slurry rheology based on procedures outlined in Sections 3.4.5 and 3.4.6 respectively. Slurry rheology characterisation was carried out in collaboration with Prof Emma Kendrick, Dr Carl Reynolds and PhD candidate, Sam Gray at University of Birmingham. The author was responsible for making all the slurry samples based on the slurry mixing SOP for a 98:2 wt% formulation detailed in Section 3.2. NMP solvent and the rheometer were kindly provided by University of Birmingham. The author carried out the rheology measurements with support from Dr Carl Reynolds.

Table 4.1: Slurry formulation and corresponding masses of NMC, C65, PVDF and NMP used [71].

Formulation (NMC:C65:PVDF wt%)	NMC (g)	C65 (g)	PVDF (g)	NMP (g)	Solid Concentration (%)
94:4:2	14.4	0.60	0.30	6.47	70.3
95:3:2	14.4	0.45	0.30	6.73	69.2
96:2:2	14.4	0.30	0.30	7.00	68.2
97:1:2	14.4	0.15	0.30	7.27	67.1

Table 4.2: Experiment data sets.

Formulation (NMC:C65 wt%)	NMC (g)	C65 (g)	Mixing Speed (rpm)	Mixing Time (min)
100:0	20.0	0	2300	2 60
98:2	19.6	0.4	-	-
98:2	19.6	0.4	1000	2 60
98:2	19.6	0.4	2300	2 5 10 30 60
98:2	19.6	0.4	5000	2 60
90:10	18.0	2.0	-	-
90:10	18.0	2.0	1000	2 60
90:10	18.0	2.0	2300	2 5 10 30 60
90:10	18.0	2.0	5000	2 60

4.3 CBD Structures for Long and Short-Range Electronic Pathways

4.3.1 Novel CBD Structures

Electrodes were fabricated using conventional wet slurry mixing and casting based on the formulations and methods described in Section 4.2. The results show that the carbon black content within electrodes affects the formation of CBD structures in electrodes. Through SEM imaging and EDX analysis, it was found that distinct CBD structures are present in the dried solid electrode after slurry casting and drying.

For 94:4:2 wt% electrodes, the SEM micrograph shows the presence of “fluffy, sponge-like” structures of CBD between the voids of NMC particles (Figure 4.1a). These CBD structures are crucial for electronic conduction as they facilitate a percolated electronic pathway for electron transfer. The highly porous CBD structure is also critical for ionic conduction as it enables the infiltration of electrolyte, in contact with NMC particles, throughout the electrode structure.

As the carbon black content decreases from 4 wt% to 1 wt%, the presence of these “fluffy” CBD structures also decreases, as shown in Figures 4.1a to 4.1d. The void space between NMC particles increases as these porous CBD structures are no longer present. Additionally, the framboidal texture of NMC is also less apparent which can be attributed to the high amount of carbon black that is attached to the NMC surface during slurry mixing. Such deposition of carbon black on the NMC surface is analogous to coating formation that can be achieved using various mixing techniques [64], [136].

These findings indicate that the carbon black content of a slurry containing active material, carbon black and binder dictates the features of the CBD structures formed in the final electrode. Large “fluffy, sponge-like” CBD structures were defined as bridge structures, spanning over two or more active material particles to form a “bridge-like” conduction pathway, corresponding to long-range electronic pathways. Conversely, smaller carbon black structures that cover the surface of active material particles were defined as film structures to facilitate interfacial electronic contacts, corresponding to short-range electronic pathways. Supplementary SEM micrographs of bridge and film structures present in the electrode formulations studied can be found in Appendix A.1.

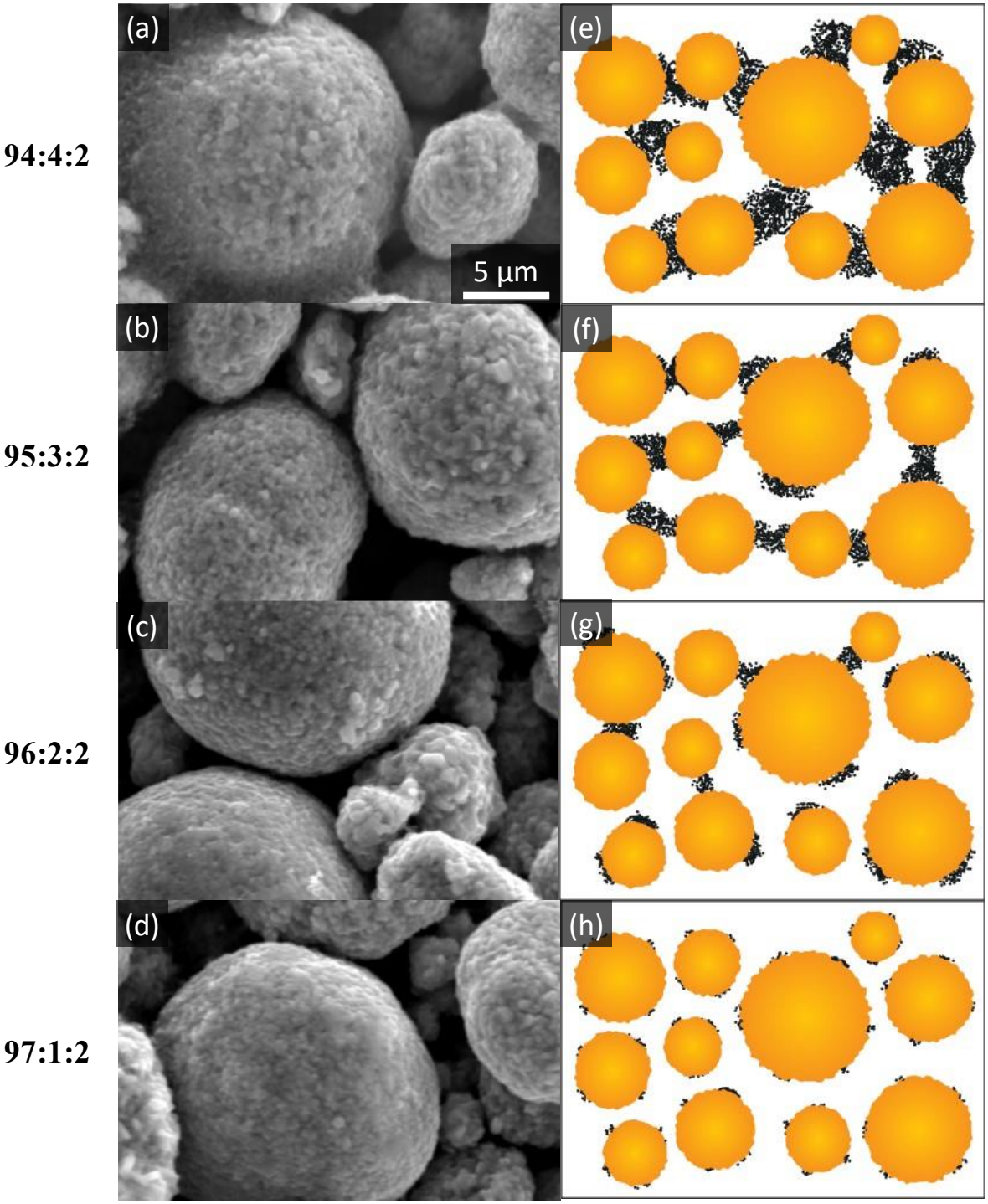

Figure 4.1: SEM micrographs of electrodes with formulations of (a) 94:4:2, (b) 95:3:2, (c) 96:2:2 and (d) 97:1:2 (NMC622:C65:PVDF wt%). Accompanying schematic diagrams depicting the CBD structures consisting of bridge and film structures are shown in (e-h).

EDX mapping of the same electrodes was also carried out to validate the presence of these different CBD structures and to investigate their distribution across the electrode. The O-mapping (Figures 4.2e to 4.2h) and C-mapping (Figures 4.2i to 4.2l) of these electrodes correlate to the NMC particles and CBD structures respectively. The O-mapping shows that NMC particles are evenly distributed across the field of view. However, the C-mapping shows that there is a variation in the CBD structures and their distribution across the electrode. For 94:4:4 wt% electrodes, the C-mapping shows that there is an overall higher concentration of carbon black distributed across the electrode (Figure 4.2i). There are also several clusters with high mapping intensity, indicating the presence of "fluffy, sponge-like" CBD structures that correspond to bridge structures connecting the NMC particles. As the carbon black content starts to decrease from 94:4:2 to 96:2:2 wt%, the number of regions with these clusters of high carbon mapping intensity starts to decrease. The size of these clusters that are present also decreases, indicating a reduction in the size of the bridge structures formed. Lastly, for 97:1:2 wt% electrodes, the absence of C-mapping was observed indicating that carbon black is not present in the field of view (Figure 4.2l). It may also be caused by a weak carbon signal due to the low carbon content. Therefore, the C-mapping shows that there are essentially no bridge structures present.

The presence of regions with a higher number of bridge structures can be associated with carbon-binder migration during drying. Carbon binder migration results in the segregation of the carbon black within the electrode, where an uneven distribution of carbon black is present with a lower concentration at the bottom of the electrode [137]. This homogeneity in electrodes can cause a huge difference in electrochemical performance. Therefore, regions where there is a higher carbon intensity correspond to regions where there is likely more carbon black on the upper region of the electrode.

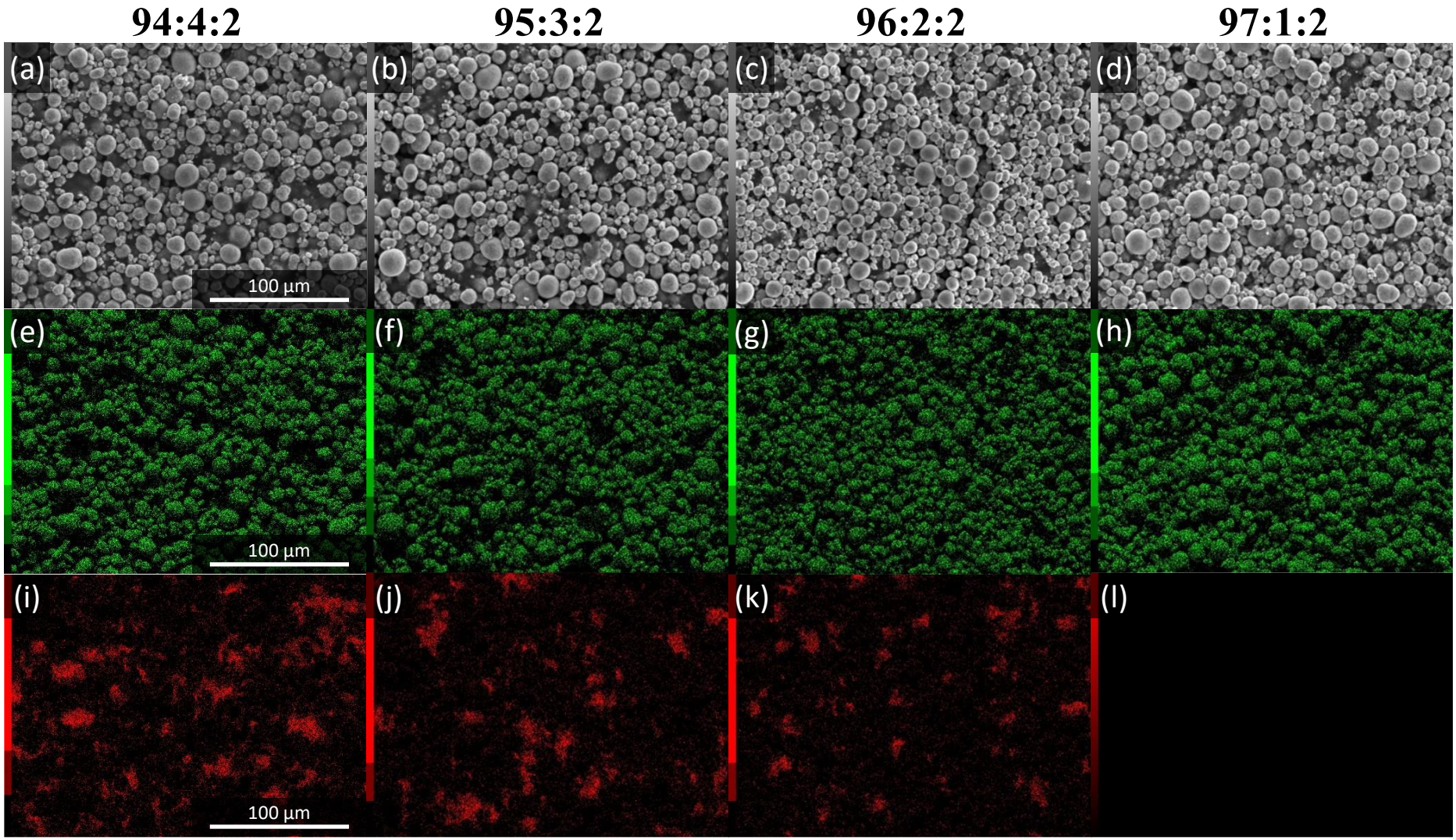

Figure 4.2: SEM micrographs of electrodes prepared using formulations of (a) 94:4:2, (b) 95:3:2, (c) 96:2:2 and (d) 97:1:2 (NMC622:C65:PVDF wt%). Corresponding EDX mappings of oxygen (e-h) and carbon (i-l) are also included.

4.3.2 Formation of Bridge and Film Structures

For the electrode formulations of 94:4:2 to 97:1:2 wt%, the carbon-to-binder ratio (C65:PVDF) decreases from 2:1 to 1:2. Reynolds et al. [133] reported that PVDF has a higher preference to be adsorbed to NMC particles, thus displacing some of the carbon black that is attached to NMC during wet slurry mixing. This displacement of the originally immobilised carbon black results in an increase in the fraction of "free carbon" within the slurry. During drying, this free carbon is mainly responsible for the formation of the "fluffy, sponge-like" CBD structure that facilitates long-range electronic conduction. This explains the reasons behind the decrease in the number of bridge structures as the carbon content decreases. In 97:1:2 wt% electrodes, the carbon content is very low which impedes the formation of bridge structures in general. Even though the C65:PVDF ratio is also very low, partial adsorption of carbon black onto the NMC surface can still occur. Since carbon content is already relatively low compared to the other formulations studied, combined with the effect of partial adsorption, competition arises for the total carbon black available to be distributed across the NMC surface and in the slurry as free carbon. It is likely that, due to the insufficient carbon black for the formation of either structure, the resulting bridge and film structures formed are very limited for 97:1:2 wt% electrodes.

The carbon black and PVDF polymeric binder form carbon black-PVDF clusters as the solvent with PVDF dissolved within is adsorbed onto the carbon black with a high surface area. During drying, the solid content within the carbon black-PVDF colloid is important for the formation of bridge structures. This is likely due to the capillary force from dense particle accumulation that can drive more PVDF, together with the carbon black, to the voids between NMC particles. A higher carbon black content in the carbon black-PVDF clusters promotes the formation of bridge structures, resulting in an increased presence of CBD structures that connect the NMC particles, as shown in Figure 4.2. The bridge structure also contributes to the electronic conductivity more than film structures [63]. The bridge structure represents a relatively large, interconnected percolation network that spans across active material particles throughout the entire electrode structure. Electrons have a preference to travel through the route with the lowest resistance. Therefore, these bridge structures formed by carbon black can facilitate electron movement, decreasing the probability of electrons in contact with NMC, which has a relatively higher resistance.

The findings show that it is relatively straightforward to control the formation of bridge structures (i.e. long-range electronic pathways) to improve electrode properties such as electronic and ionic conductivity [71]. In this study, the electrochemical performance showed the best rate capability at high C-rates with an electrode formulation of 95:3:2 wt%. Controlling the formation of film structures through wet slurry mixing remains a challenge, where the coating characteristics of the film structure can significantly affect the electrode structure and performance. Therefore, exploring methods of

controlling the coating formation as film structures for short-range electronic pathways and how they influence electronic conductivity alongside other electrode properties is an interesting avenue of research. This will be explored in the following sections.

4.4 Controlling Film Structure Formation on NMC

Controlling film structure formation in wet slurry mixing is a huge challenge, in terms of designing the spatial distribution of the carbon black on the NMC surface and achieving the desired coating characteristics. Firstly, to control film structure formation, carbon black dispersion must also be taken into account alongside coating formation. The two most commonly studied dry mixers for this purpose are the Eirich high-intensity mixer [86] and the Nobilta mechanofusion mixer from Hosokawa [64], [78], [105]. Mechanofusion is a dry, high-shear mixing technique that relies on local high-shear forces to spheronise particles or coat larger host particles with fine guest particles. Mechanofusion approaches were systematically extended as a method to control the formation of film structures on NMC622. The high shear and compression forces from mechanofusion facilitate carbon black deagglomeration and coating formation on NMC. It also avoids the breakage of NMC particles, retaining their critical properties such as secondary particle size and bulk crystal structure, all of which can affect their electrochemistry and performance. The carbon coating formed through mechanofusion dry mixing is analogous to the film structure formed during slurry mixing, where it facilitates the proposed short-range electronic pathways.

The surface morphology of polycrystalline NMC622 particles resembles a framboidal texture formed by the aggregates of the crystallites (Figure 4.3a). The grains of these crystallite aggregates form “pores” or “grooves” on the surface of the NMC secondary particle. The structure of these grooves is important as they increase the area of contact of the NMC particles with the CBD. The CBD is the cluster of conductive additive and polymeric binder formed during slurry mixing and is crucial to forming a percolated electronic pathway. From a manufacturing point of view, the carbon black-polymer clusters impart gel-like characteristics to form a rheologically stable slurry [138]. The pores on the NMC622 surface can also increase particle surface area in contact with the electrolyte to enhance ionic conduction.

Carbon black, shown in Figure 4.3b, are generally small colloidal particles with a primary particle size of 10 – 100 nm and low bulk density [139] compared to cathode active materials. These carbon black particles exist in an agglomerated structure, with a size of ~100 nm up to a few microns, due to interparticle interactions held by van der Waals forces. This is in contrast with the NMC particles where the average size is 11.1 μm. The voids between micron-sized NMC particles need to be filled with nano-sized carbon black to form electronic networks for improved electron transfer. The resultant force response curve indicates that carbon black particles experience maximum attraction at the minimum of the potential well to form agglomerates (Figure 2.11). The deagglomeration of carbon

black requires energy input to displace them from this potential well to facilitate the dispersion process.

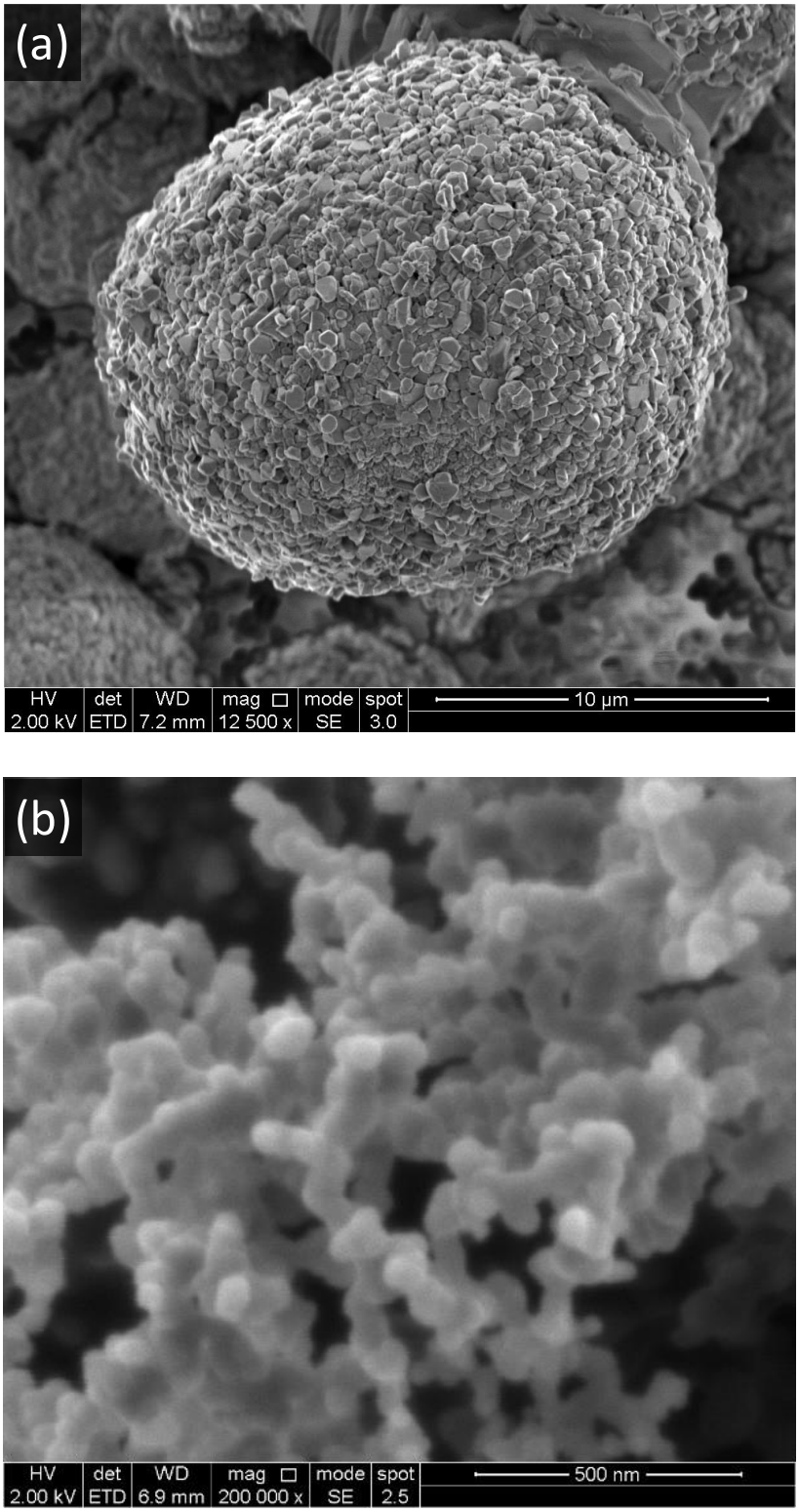

Figure 4.3: SEM micrographs of (a) a pristine NMC622 particle and (b) carbon black C65.

Dispersion of carbon black is critical to achieving a percolated electronic pathway within electrodes. An important aspect of dispersion is the deagglomeration of the carbon black structures, which can be described by the rupture and erosion process, as discussed in Section 2.3.2. This deagglomeration behaviour is observed when NMC is mixed with C65 through mechanofusion, and presumably, rupture occurs immediately when mixing starts, provided the critical shear stress has been reached. This is dependent on the mixing conditions selected, which can be a combination of the mixing time and speed, together with other parameters such as the mixing gap etc. Simultaneously, during mechanofusion, carbon black is attached to the NMC surface due to continued compression, progressively forming a coating around the NMC particle. Further mixing promotes the erosion process and results in a coating consisting of very small aggregates or primary particles. This is followed by compaction of the coating and spheronisation of the surface, resulting in a smooth carbon coating on NMC particles. As deagglomeration is a result of energy input, dictated by process parameters, it is possible to control the extent of deagglomeration and coating to tailor the desired film structures for active materials through mechanofusion.

For a short mixing time, it is expected that rupture occurs given that the critical shear stress has been achieved. Large carbon black agglomerates will break down to form aggregates and the carbon structures will start to attach to NMC to form a rough coating. Prolonged mixing leads to erosion where smaller aggregates or primary particles are obtained. The spheronisation effect of mechanofusion will also result in a smooth carbon black coating on NMC particles. The surface morphology of the coated particles was imaged to evaluate the resulting carbon black structures and coating characteristics produced.

SEM micrographs of 2 wt% C65 samples show the different carbon black structures (i.e. agglomerates, aggregates, primary particles) on the NMC surface as mixing time progresses (Figure 4.4). Initially, without mechanofusion mixing, carbon structures that are present in Figure 4.4a can be categorised as large agglomerates. After 30 min mixing, these large agglomerates are no longer present, whereas smaller structures that can be categorised as aggregates are now visible in Figure 4.4b. Some small aggregates or even primary particles are also visible on the NMC surface. With prolonged mixing (i.e. 60 min mixing), a rough carbon coating is formed on the NMC surface as shown in Figure 4.4c. Therefore, this is the first indication confirming that the carbon structures obtained through mechanofusion mixing are closely linked to the rupture and erosion process.

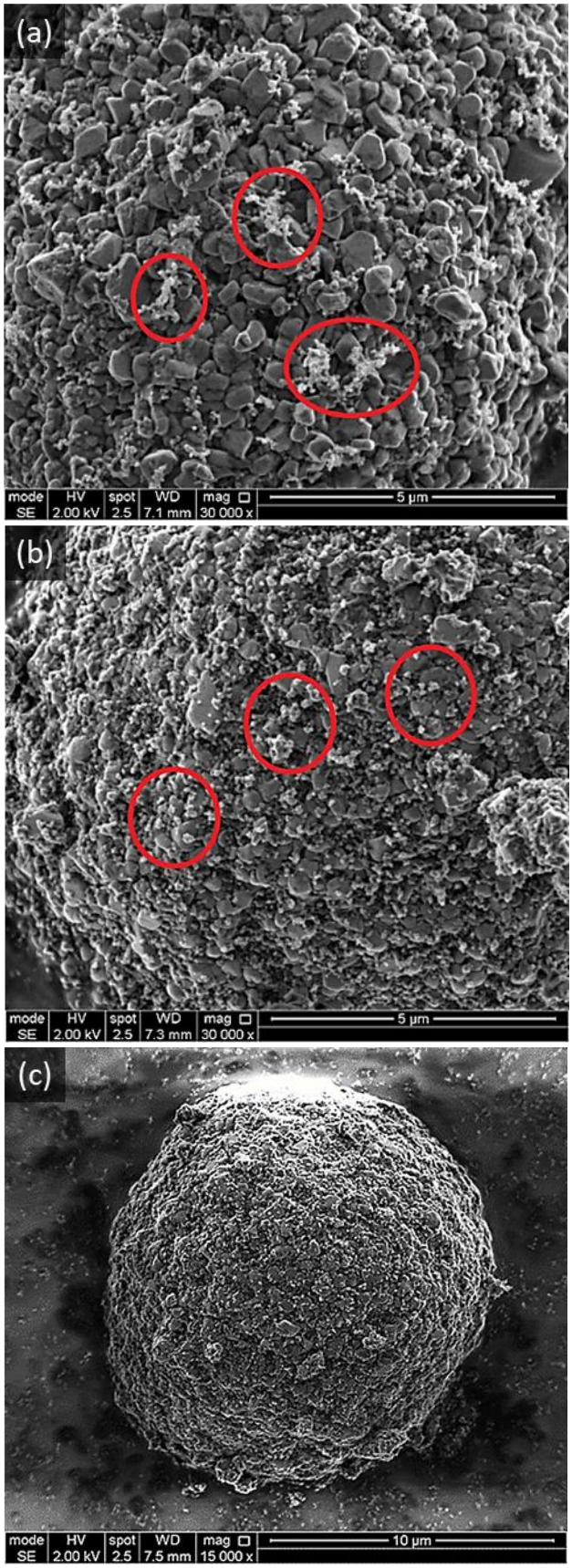

Figure 4.4: SEM micrographs depicting the different carbon black structures (indicated by red circles) of (a) agglomerates, (b) aggregates and (c) rough carbon coating on an NMC particle.

Upon closer examination of the surface morphology of the coated particles, SEM micrographs of 2 wt% and 10 wt% C65 samples show the subtle differences in carbon black structures (indicated by red arrows) on NMC particles that can be obtained through varying mixing times (Figure 4.6 and Figure 4.7). Although imaging nano-sized carbon black on micron-sized NMC using SEM poses difficulties due to limitations such as sensitivity to atomic number and resolution, it is still possible to distinguish between these two different particles through their distinct morphological features. To identify carbon black structures on NMC, the distinct contrasts of the two different particles were distinguished. Carbon black are clustered, aggregated structures made up of small, spherical particles and appear as a slightly brighter contrast. As carbon black has a high surface area compared to its volume, this can lead to an increased number of secondary electrons emitted, which translates to a brighter contrast. The background consisting of granular-shaped particles corresponds to the crystallite aggregates of NMC and appears as a slightly darker contrast. The grooves on NMC also increase the interactions with the electron beam, emitting more secondary electrons and resulting in a more textured appearance.

For a short mixing time of 2 min, carbon black attached to NMC are mainly agglomerates or large aggregates regardless of the carbon loading as shown in Figures 4.5a and 4.6a. The main difference between these two samples is the size of the carbon black structures. Samples with higher C65 loading showed relatively large carbon structures and were less distributed (Figure 4.6a), which may be a result of a less efficient deagglomeration process within the same mixing period. This can be attributed to the high carbon loading, where total energy input remained constant, but the specific shear forces experienced by carbon black decreased. It is also possible that the critical shear stress was not achieved, and therefore, rupture of the carbon black agglomerates is unlikely to occur.

After prolonged mixing of 60 min, for low carbon loading samples, a large portion of the initially large carbon black agglomerates are now reduced into small aggregates or primary particles (Figure 4.5b). However, for high carbon loading samples, Figure 4.6b shows large carbon black structures remaining due to the less efficient deagglomeration process. Similarly, for short mixing, due to the difference in carbon loading, carbon black distribution and coverage are different. For low carbon loading, the carbon black structures are distributed across the NMC surface, but the coating coverage is low, and the surface morphology of NMC is still visible. For high carbon loading, carbon black is much more distributed across the entire NMC surface and the framboidal texture of NMC is no longer visible. Supplementary SEM micrographs of the different carbon black structures at low and high carbon loadings can be found in Appendix A.2.

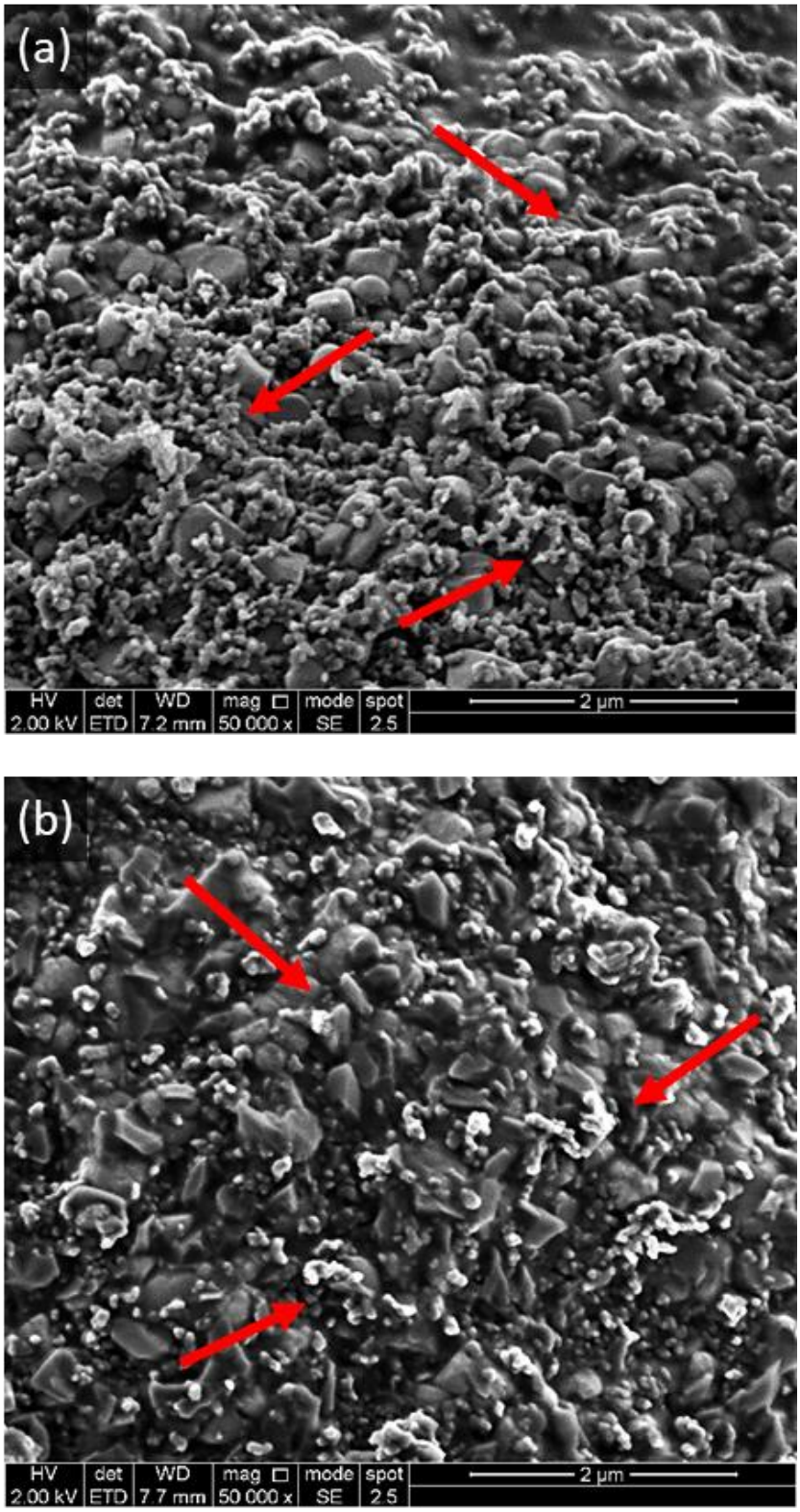

Figure 4.5: SEM micrographs of NMC622 particle surface coated with 2 wt% C65 and mixing time of (a) 2 min and (b) 60 min. Carbon black are clustered, aggregated structures made up of small, spherical particles and appear as a slightly brighter contrast. The differences in carbon black structures are indicated by red arrows.

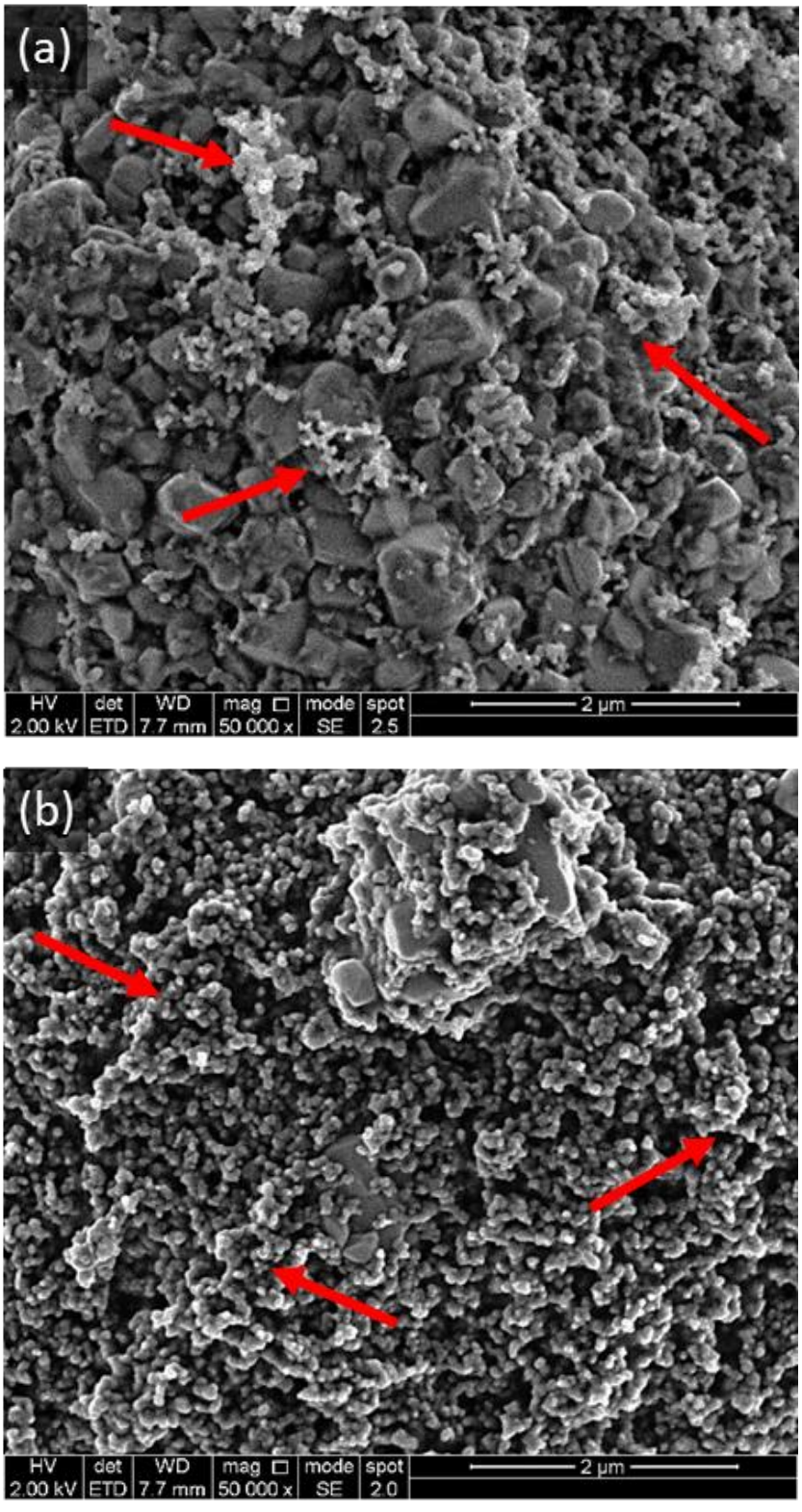

Figure 4.6: SEM micrographs of NMC622 particle surface coated with 10 wt% C65 and mixing time of (a) 2 min and (b) 60 min. Carbon black are clustered, aggregated structures made up of small, spherical particles and appear as a slightly brighter contrast. The differences in carbon black structures are indicated by red arrows.

4.5 Carbon Coating Characteristics

4.5.1 Coating Morphology

In the previous section, it has been demonstrated that mechanofusion is capable of simultaneously deagglomerating carbon black to obtain a range of carbon black structures and forming a coating on the NMC surface. To investigate the types of coating characteristics that can be obtained, samples that were mixed at “low” and “high” total energy input, based on mixing time and speed, were selected for SEM imaging. The rationale behind this is due to the understanding that a rough coating is obtained at a short mixing time, regardless of whether rupture has occurred. Obtaining a smooth coating is generally only achieved through prolonged mixing for erosion where continued shear and compression occurs during mixing.

Figures 4.6 and 4.7 show SEM micrographs of the various coating characteristics, including smooth and rough coatings obtainable by mechanofusion through varying process parameters. The formation of rough coatings is achievable at both low and high carbon loading with a short mixing time. The SEM micrographs in Figures 4.6a and 4.7a show an uneven distribution of carbon black particles on the surface of NMC. At low carbon loading (Figure 4.7a), the carbon black structures are relatively small compared to high carbon loading. For high carbon loading samples, large carbon black agglomerates with their branch structures are clearly visible on the surface of NMC, especially on the edges of the coated particle (Figure 4.8a).

The SEM micrographs show that by adjusting the mixing conditions, a rough coating can be obtained at either carbon loading. This rough coating can be an uneven distribution of the carbon black particles, where certain regions have a much higher concentration of carbon black particles or, on the contrary, a relatively even distribution of carbon black particles across the NMC surface, which does not fully cover the surface. Within these two different distributions, the size of carbon black structures is also different. The carbon black particles attached to the NMC surface can be large agglomerates, small aggregates, or even primary particles. The structures present are dependent on the combination of the mixing time and speed, where the energy and shear result in the change in the carbon black structure, and the extent of coating onto NMC.

For a smooth coating, the distribution of carbon black particles is relatively even and spreads across the whole NMC surface (Figures 4.6b and 4.7b). The distinct framboidal texture of the NMC particles is no longer visible as the surface pores and grooves are now filled with carbon black particles. With prolonged mixing, the constant shear and compression forces continuously deagglomerate the carbon black particles and smear the surface of this carbon coating to achieve a smooth coating morphology. Similarly, different coating characteristics of these smooth coatings can also be observed. At low carbon loading, a typical smooth carbon coating is obtained, although a small portion of particulates is still observed on the surface (Figure 4.7b). These could be larger structures that were not sufficiently

deagglomerated, or carbon black structures that may have re-agglomerated as samples were stored over time before imaging analysis. At high carbon loading, even though the surface features of NMC are no longer visible, there are still large regions of relatively rough features on the smooth coating surface (Figure 4.8b). This is due to the high carbon loading where lower specific energy input is experienced by the carbon black particles, and larger structures are retained.

Carbon black deagglomeration relies on high shear forces to overcome the van der Waals forces holding the particles. High shear rates are usually obtained at high mixing speeds, where the critical shear stress is achieved more easily, resulting in the size reduction of carbon black. Therefore, higher speeds are more favourable for obtaining coatings with small carbon structures. For a more even distribution coating, it is more important to control the mixing time as it increases the total energy input and the compression force experienced by the particles. With longer exposure to compression forces, carbon black particles are more likely to be smeared and spread across the NMC surface. In summary, the coating characteristics can be evaluated through the distribution and coverage of carbon black on the NMC surface, and the carbon black structures that form the coatings. The mixing time and speed can be fine-tuned to obtain a range of coating characteristics.

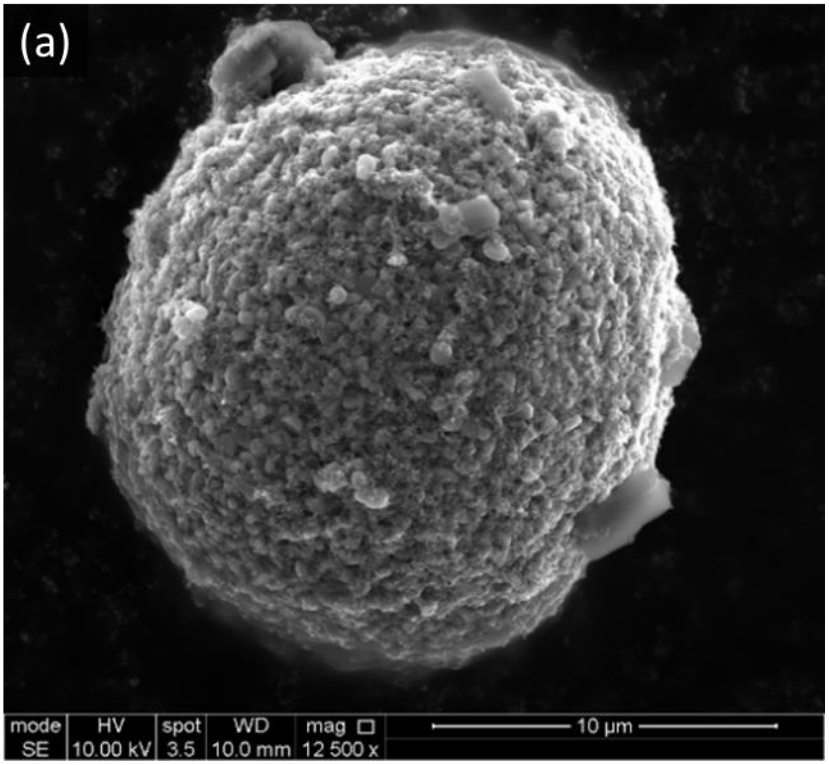

Figure 4.7: SEM micrographs of NMC622 particle surface coated with carbon black with 2 wt% C65 depicting a (a) rough coating and (b) smooth coating. Mixing conditions: (a) 2 min 2300 rpm (b) 60 min 5000 rpm

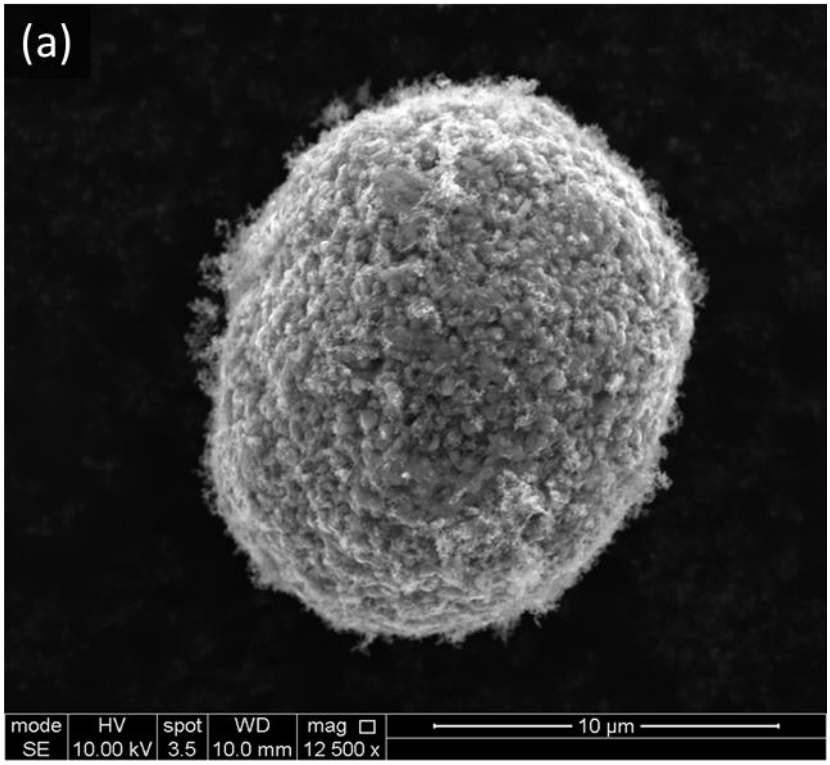

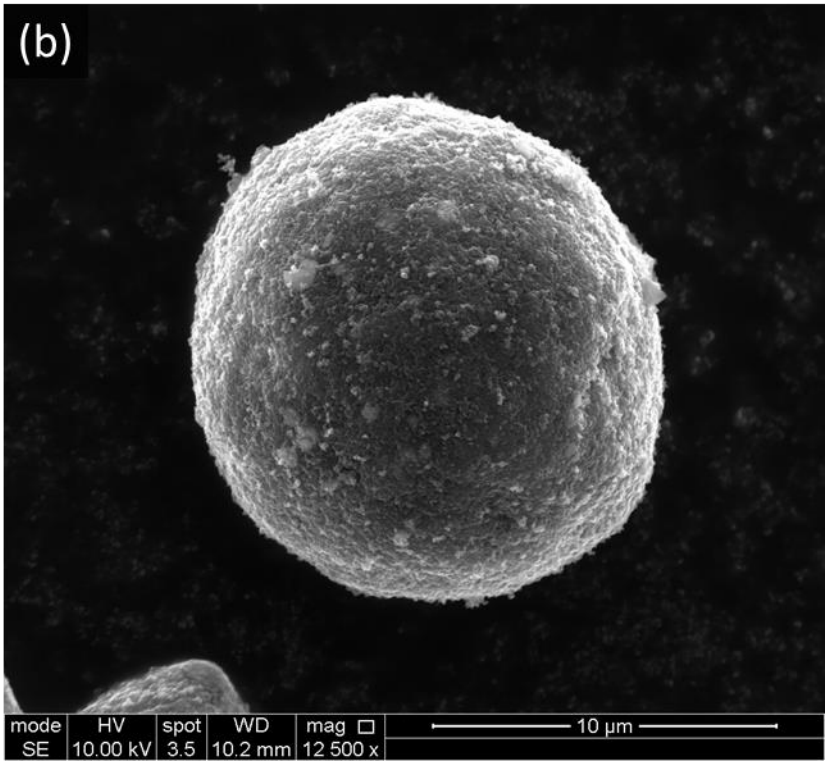

Figure 4.8: SEM micrographs of NMC622 particle surface coated with carbon black with 10 wt% C65 depicting a (a) rough coating and (b) smooth coating. Mixing conditions: (a) 60 min 1000 rpm (b) 60 min 5000 rpm

4.5.2 Qualitative Analysis of Coating Thickness and Coverage

The thickness of the carbon coating on NMC particles resulting from mechanofusion is also an important property for evaluation, and backscatter electron (BSE) imaging was used for this analysis. Heavier elements have a higher atomic number and backscatter electrons more strongly than light elements, which have a lower atomic number. This results in a contrast difference during BSE imaging where the heavier elements will appear as a brighter contrast during imaging. For the binary mixtures of NMC622 and C65, NMC622 will appear as a bright contrast, while C65 will appear as a dark contrast, which is useful for evaluating the coverage and coating thickness.

Figure 4.9 shows the BSE micrographs of 2 wt% C65 samples subjected to 2 min and 60 min mixing respectively. The bright particles correspond to NMC particles, while several dark particles correspond to the large carbon black agglomerates. Bright particles with dark regions can also be observed which can be explained by C65 particles attached to NMC. The darker these regions, the higher the amount of C65 that is present. After 60 min mixing, the dark particles are no longer present, which may indicate the reduction of large carbon black agglomerates caused by deagglomeration. However, there are no visible differences in the number of bright particles with dark regions. This may be explained by an uneven distribution of carbon black on the NMC surface and their presence as smaller carbon black structures. Even though carbon black is present, the concentration is likely not high enough to produce a distinct contrast difference to be reflected during BSE imaging.

For high carbon loading, bright NMC particles and dark C65 particles are also present as shown in Figure 4.10. The significant difference is the presence of a higher number of large dark 65 agglomerates caused by higher carbon loading. The large dark particles also have a rough outer edge that resembles the chain structures of carbon black, thus confirming that these particles are indeed C65. The NMC particles appear brighter initially compared to low carbon loading, with fewer dark regions on the particles themselves. This can be explained by the low shear and compression forces on carbon black particles due to the increased number of agglomerates initially and, therefore, less coating onto NMC. After 60 min mixing, there is a drastic increase in the dark regions on the bright NMC particles. These dark regions are now much more distinct due to the high amount of C65 that is attached to the NMC surface. The dark regions represent a relatively high coating coverage and thickness compared to low carbon loading. The distribution of C65 on the NMC surface is also now much more visible.

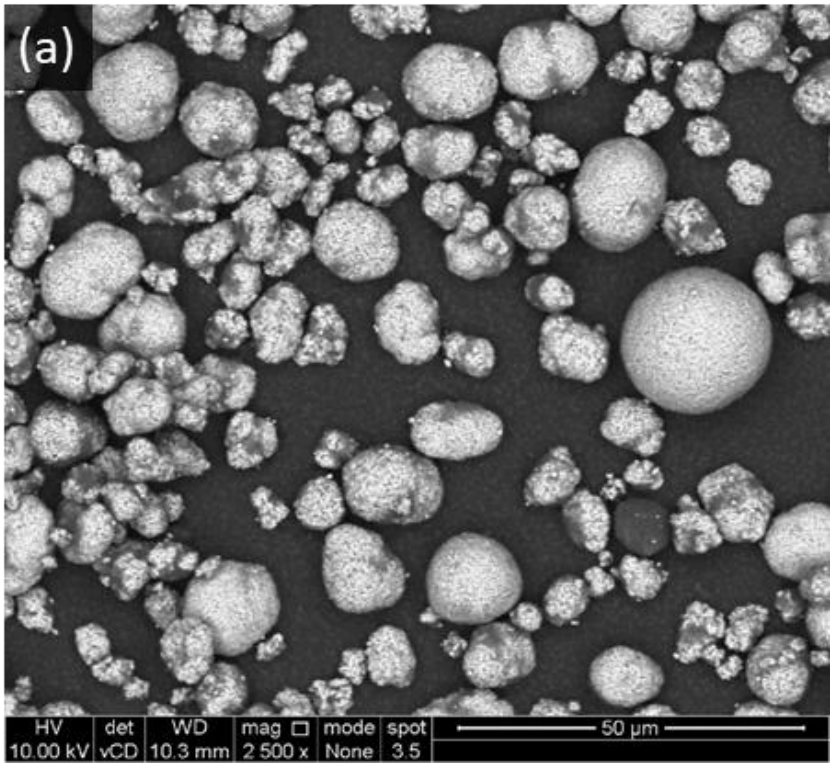

Figure 4.9: BSE micrographs of NMC622 with 2 wt% C65 mixed at 2300 rpm for (a) 2 min and (b) 60 min.

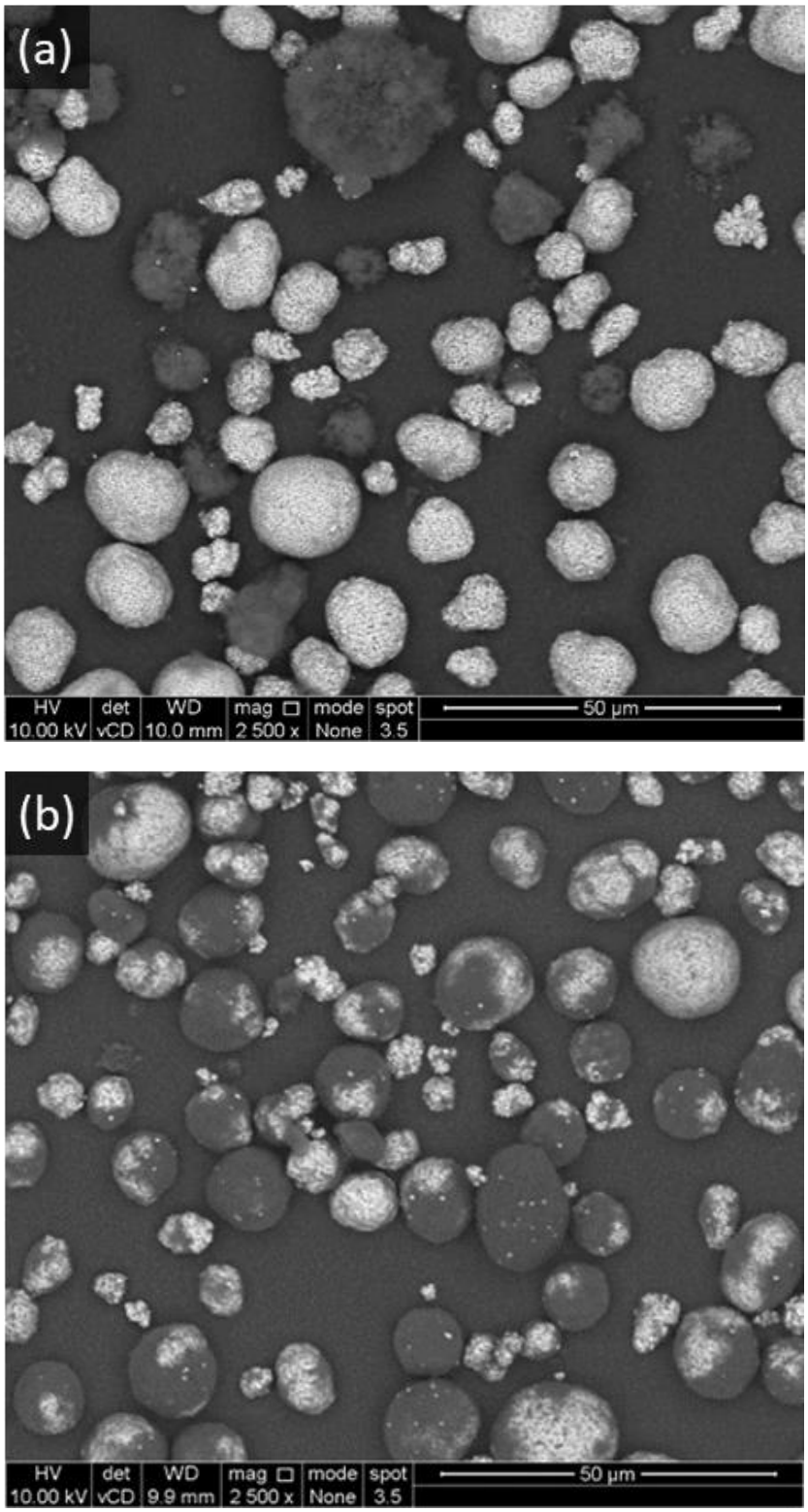

Figure 4.10: BSE micrographs of NMC622 with 10 wt% C65 mixed at 2300 rpm for (a) 2 min and (b) 60 min.

4.5.3 Coating Implications

The formation of the carbon coatings as film structures and their coating characteristics has several secondary implications on the downstream processing and final electrochemical performance. Downstream processing (i.e. wet slurry mixing, casting, and drying) can be affected by the change in surface chemistry of the carbon coating on NMC. For example, with a smooth coating, the slurry rheology might be greatly affected, as the typical gel-type behaviour of conventional cathode slurries is altered. This affects the mixing of electrode components, the drying behaviour, and the subsequent electrode microstructures. In terms of electrochemistry, for a rough coating, electronic conduction may be enhanced as additional electrical contact points have been established through the coating formation. Ionic conduction is also facilitated as the effective interface between the NMC surface and electrolyte is not greatly affected. For a smooth coating, the higher fraction of carbon black as a coating will result in higher electronic conduction, which can be achieved through a smooth coating with high coverage of the NMC surface. Since NMC has a lower conductivity, this coating can help decrease the probability of electrons experiencing resistance travelling through NMC particles. With a smooth and thick coating, it is likely that the effective interface between the NMC surface and the electrolyte is greatly reduced, which is detrimental to ionic conduction. If the porosity of the carbon coating is sufficiently low for electrolyte infiltration, ionic conduction may still be facilitated. However, this may increase the tortuosity of the Li-ion transport pathways within the coating and impede ionic conduction.

4.6 Coated Particle Properties

4.6.1 Particle Size

NMC particles are typically in the micron scale, whereas carbon black primary particles are on the nanoscale, with their aggregates and agglomerates in the submicron to micron range. Figure 4.11a shows a monomodal distribution for NMC particles with a distinct peak at around 10 μm. For carbon black, a bimodal distribution was observed with a broad distribution from 0.1 – 100 μm (Figure 4.11b). This indicates that pristine carbon black consists of a range of agglomerated structures.

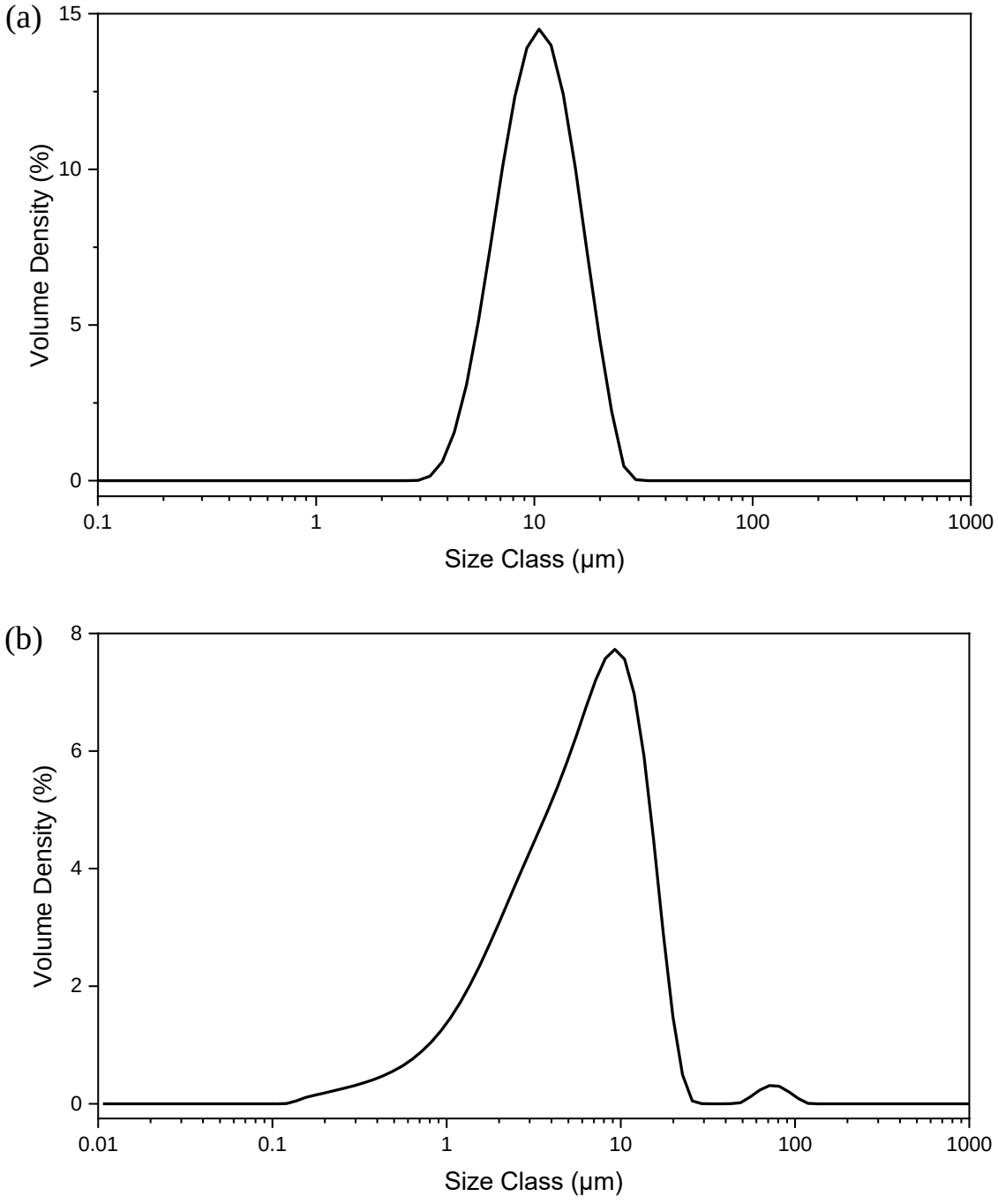

Figure 4.11: Particle size distributions of (a) pristine NMC622 and (b) carbon black C65.

To investigate the change in carbon black structures with deagglomeration, the particle size distributions of binary powder mixtures of NMC and C65 subjected to dry mixing for 0, 2, 5, 10, 30 and 60 min were evaluated. Firstly, the volume-based particle size distribution for an unmixed sample (0 min) shows a trimodal distribution with a distinct peak at 10 μm and broad peaks at 1 μm and 100 μm (Figure 4.12a), confirming the presence of three size classes of particles. The d_{50} of NMC particles is 11.1 μm and therefore confirms that the peak at approximately 10 μm corresponds to the NMC particles. The 1 μm and 100 μm peaks both correspond to small and large carbon black agglomerates. The broad size distribution from approximately 50 – 800 μm indicates that there is a range of different carbon black agglomerate sizes.

When the binary powder mixture is first subjected to mechanofusion mixing for 2 min, the broad peak around 100 μm becomes insignificant. This suggests that there is a size reduction in the large agglomerates of carbon black, which has been broken down into smaller structures. The 1 μm peak is still visible, indicating that only large agglomerates are broken down with a short mixing time. With increased mixing time from 2 to 10 min, an increase in the height of the 10 μm peak is also observed. Firstly, these carbon black particles have deagglomerated to form small aggregates which could merge into the 10 μm peak, as suggested by the increase in the percentage of particles at this size range. The carbon black aggregates at 1 μm are likely to have been further deagglomerated to submicron size. Carbon black is also coated onto NMC during mechanofusion. The size of these immobilised carbon black particles is not reflected individually in the particle size distribution. Laser diffraction measures the size of the carbon-coated NMC particles where their size is dominated by the micron-size NMC particles and contributes to the peak at approximately 10 μm. This 10 μm peak reaches a maximum at 10 min mixing and eventually starts to decrease as mixing progresses to 30 min and up to 60 min. The decrease in this peak height, as mixing progresses, can be attributed to the reduction of carbon black agglomerates within that size range and the compaction of the carbon coating.

For a volume-based particle size distribution, a small number of large particles will significantly contribute to the total volume compared to many smaller particles. Additionally, the assumption of uniform density is also less accurate for a NMC-CB mixture. Therefore, to evaluate the amount of NMC and carbon black particles present and to fully understand the size distribution of the smaller carbon black structures, the number-based particle size distribution was also evaluated (Figure 4.12b). The number-based particle size distribution shows a bimodal distribution for an unmixed sample (0 min). A large peak is observed at 1 μm followed by a small, relatively broad peak at around 7 μm. In this distribution, the absence of any peaks beyond 10 μm confirms that only a very small number of large carbon black agglomerates are present that contribute to the broad 100 μm peak observed in the volume-based distribution. On the contrary, a high fraction of particles around 1 μm are present, which can be attributed to carbon black agglomerates within the size range that correlates to the small 1 μm peak observed in the volume-based distribution. The broad peak around 7 μm may indicate a

mixture of slightly larger carbon black agglomerates together with NMC particles. With increased mixing time, the 1 µm peak height decreases while the 7 µm peak height increases. The 1 µm peak becomes insignificant at 10 min mixing, and the maximum was observed for the 7 µm peak. The observations from both the volume-based and number-based distribution suggest only a small amount of large carbon black agglomerates (> 100 µm) is present, and most exist as small agglomerates (< 10 µm). Carbon black particles are increasingly deagglomerated and coated onto NMC, as mixing progresses beyond 10 min, giving a single peak with longer mixing times that correlates to the carbon-coated NMC particles.

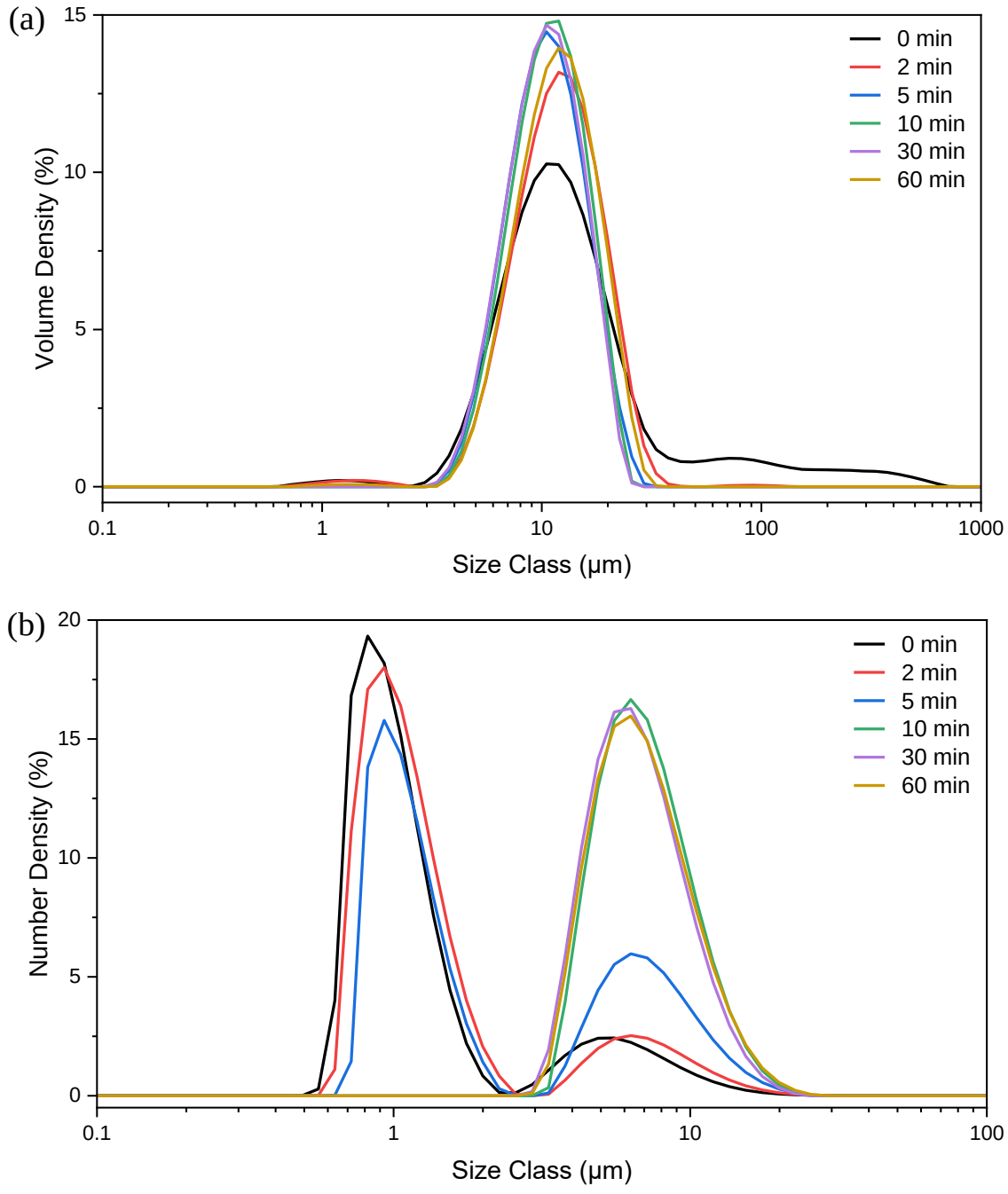

Figure 4.12: (a) Volume-based and (b) number-based particle size distribution of binary mixtures of NMC and C65 subjected to different mixing times.

4.6.2 Particle Density

The density of the powder is important as it relates to the storage and handling of materials, and more importantly, indicates the packing of particles within electrodes. It is also useful to inform about the size and shape of particles, including the irregular shapes of particles. Using these density values, carbon black deagglomeration can also be inferred. Tables 4.4 and 4.5 show that the bulk density of binary mixtures of NMC and C65 is lower than that of pristine NMC particles. This is due to the presence of carbon black particles situated between NMC particles. Where large carbon black structures are present and unable to pack into the voids between NMC, this will increase the bulk density (Figure 4.13). The tapped density is much higher than the bulk density due to better packing caused by repeated tapping. The friction between particles hinders their ability to flow freely and arrange into a tightly packed configuration. The repeated vertical tapping force helps move these particles around, allowing them to rearrange into a denser packing. Weakly held particles can also be broken down during tapping. This may occur for C65 particles, but generally, a much higher energy is required to overcome the strong van der Waals forces between the particles.

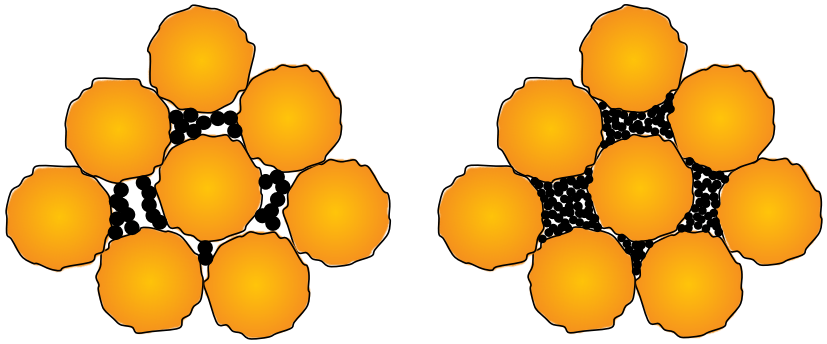

Figure 4.13: Particle packing of large (agglomerates) and small (aggregates/ primary particles) carbon black structures within voids of NMC.

Mixing time significantly changes the density of the binary powder mixtures. As mixing time is increased, both bulk and tapped densities increase, as shown in Table 4.4 and 4.5. This is attributed to large carbon black structures being broken down into smaller structures. These smaller structures can fill the voids between NMC particles more effectively, leading to better packing during density measurements. Both densities at 2 wt% C65 are higher than those at 10 wt% C65. This is because the particle packing and relevant densities are dominated by NMC at 2 wt% whereas carbon black dominates at 10 wt% C65. The effect of mixing time has a higher influence at high carbon loadings. As mixing increases from 2 to 60 min, the bulk density showed an increase of 96 % for high carbon loading, compared to only 23 % at low carbon loading. As these carbon black structures are deagglomerated with increased mixing, a large portion of these carbo black structures are now able to better pack between NMC particles. A similar trend was observed for the tapped density, where an increase of approximately 13 % and 87 % for low and high carbon loading respectively, was

observed. A similar explanation is that the smaller carbon black structures can achieve much better packing through the tapping motion.

The Hausner ratio of pristine NMC is approximately 1.37, indicating poor flowability. This is likely due to its surface features, where the aggregate crystallite can lead to interlocking between particles. The high surface area of NMC particles can also lead to increased interactions with other particles. Mechanofusion of only NMC particles has minimal impact on its flowability, as indicated by the slight decrease in the Hausner ratio from 1.37 to 1.26 (Table 4.3). As mechanofusion causes the spheronisation of the NMC surface, it may lead to better packing as the interlocking and surface interaction effects of particles are reduced. For the coated particles, the Hausner ratio is between 1.30 – 1.42 for low carbon loading and 1.36 – 1.60 for high carbon loading. The Hausner ratio decreases as mixing time increases, indicating that mixing and coating formation promotes better flowability of powders (Tables 4.4 and 4.5). Particle coating has been shown to be effective in reducing particle cohesion and improving flowability [140], [141]. However, all the mixed powders still generally indicate poor flowability. Poor flowability may lead to challenges with material handling and may cause issues during downstream processes, such as non-uniform mixing and uneven coating during slurry casting.

Table 4.3: Bulk, tapped densities and the Hausner ratio of pristine NMC and NMC subjected to 2 and 60 min mixing.

Mixing Time (min)	Bulk Density (g cm^{-3})	Tapped Density (g cm^{-3})	Hausner Ratio
0	1.843	2.519	1.37
2	1.877	2.359	1.26
60	1.825	2.299	1.26

Table 4.4: Bulk, tapped densities and the Hausner ratio of 2 wt% C65 samples subjected to 2 to 60 min mixing.

Mixing Time (min)	Bulk Density (g cm^{-3})	Tapped Density (g cm^{-3})	Hausner Ratio
0	1.252	2.086	1.67
2	1.454	2.070	1.42
5	1.590	2.205	1.39
10	1.599	2.218	1.39
30	1.717	2.309	1.34
60	1.793	2.336	1.30

Table 4.5: Bulk, tapped densities and the Hausner ratio of 10 wt% C65 samples subjected to 2 to 60 min mixing.

Mixing Time (min)	Bulk Density (g cm^{-3})	Tapped Density (g cm^{-3})	Hausner Ratio
0	0.619	0.761	1.23
2	0.689	0.985	1.43
5	0.792	1.267	1.60
10	1.003	1.487	1.48
30	1.262	1.712	1.36
60	1.352	1.844	1.36

4.7 Free Carbon Content After Mixing

A key factor to evaluate is the presence of free carbon after mechanofusion of NMC with C65. However, such analysis using scanning electron microscopy proves difficult for several reasons. Firstly, the difference in length scales between micron-sized NMC particles and submicron to nano-sized carbon black structures poses difficulties for such technique. This is especially so when carbon black particles are reduced to small aggregates or primary particles, and these structures are simply too small and below the spatial resolution limit for effective imaging using SEM. Secondly, the use of carbon tape to mount the coated particles causes challenges in differentiation during EDX analysis. Both carbon tape and carbon black will appear as a single carbon mapping and, therefore, interfere with the carbon mapping intensity, making it challenging to distinguish between them.

4.7.1 Thermal Analysis of Coated Particles

Thermogravimetric analysis (TGA) was used to attempt to quantify the amount of free carbon remaining after mixing. Prior to this, it is necessary to understand the combustion behaviour of pristine materials of NMC622 and C65 under the heating profile studied. The TGA profile for pristine NMC622 is shown in Figure 4.14a. A minimal change in mass was observed between 30 – 200 ^{o}C due to the removal of moisture adsorbed on the NMC particles. From 200 – 500 ^{o}C, initial oxidation of the components from the NMC622 structure has likely occurred to form their respective oxides: Li_2O, Ni_2O, MnO and Co_3O_4 [142]. At this stage, the formation of gaseous Li_2O and O_2 causes a loss in mass, while the formation of Ni_2O, MnO and Co_3O_4 that exist as non-gaseous products results in mass gain. Overall, it can be deduced that the formation of Li_2O and O_2 is more dominant as a decrease in mass was observed. From 500 – 800 ^{o}C, the mass stays relatively constant, likely due to slow reaction caused by limitations in reaction kinetics. Finally, beyond an elevated temperature of 800 ^{o}C, a sharp decrease in mass occurs due to increased oxidation reactions at high temperatures. The mass residual for NMC622 is approximately 98.4 %. The decomposition of C65 is much more straightforward, as shown in Figure 4.14b. The initial mass loss is minimal and is caused by the removal of moisture. As the temperature approaches approximately 600 ^{o}C, a sharp decrease in mass is observed. As the temperature approaches 700 ^{o}C, the total mass loss is 100%, confirming that all the carbon black has reacted with the oxygen to form CO_2.

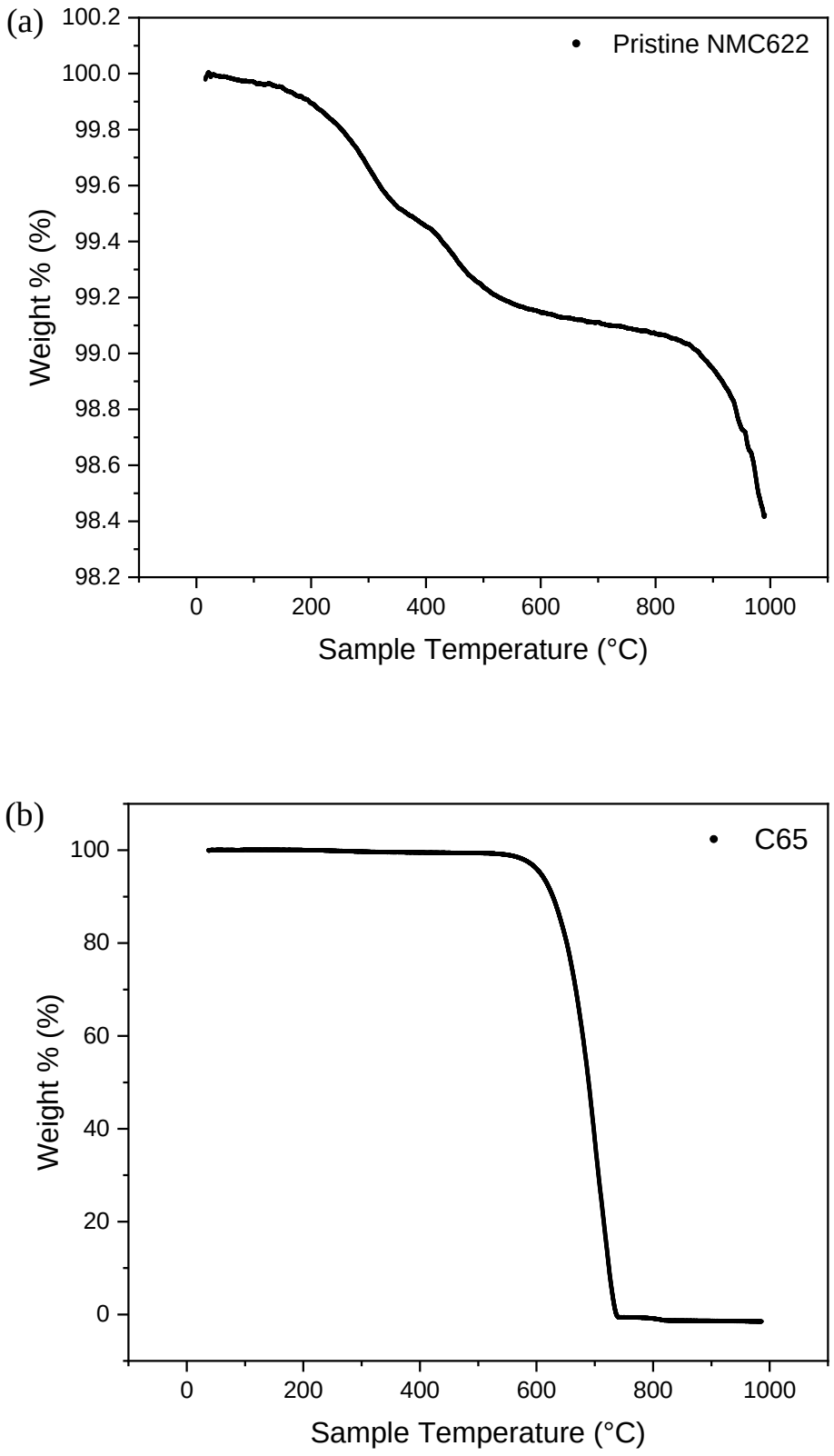

Figure 4.14: TGA profiles for (a) pristine NMC622 and (b) carbon black C65

The TGA profiles for a binary mixture containing NMC622 and C65 differ from pristine NMC622 as it is now a combination of the decomposition behaviour of both materials. For carbon blacks with deliberately manipulated structures as a result of deagglomeration, the combustion behaviour is also slightly modified. The surface area of carbon black determines their combustion behaviour, where an increase in the surface area decreases the combustion temperature [143]. For a defined temperature, the combustion reaction is much faster with increased surface area. There are two factors that determine the combustion behaviour of carbon black in a binary mixture of NMC-CB from mechanofusion. When large carbon black structures are deagglomerated into smaller structures, a higher fraction of carbon black can react with oxygen due to higher accessibility to the carbon black particle surface, as illustrated in Figure 4.15. The second factor is the carbon black structures as a coating on the NMC surface. Similar to large carbon black structures, particles that are coated onto NMC essentially decrease the surface area available for the combustion reaction. The combustion behaviour of the elements in the NMC structure must also be considered along with the factors discussed.

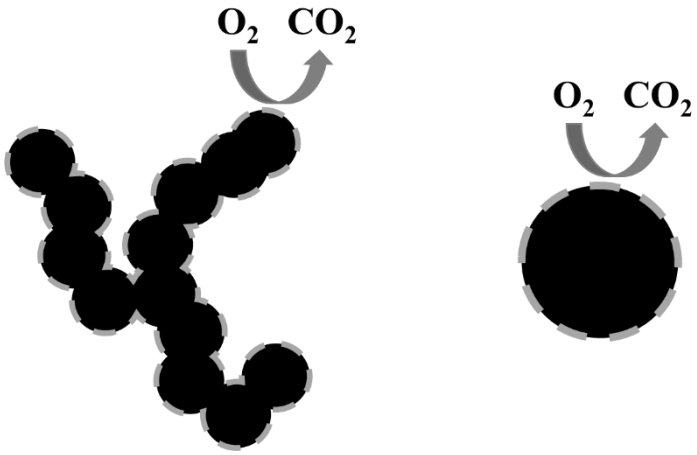

Figure 4.15: Schematic showing the differences in reaction for varying surface area caused by carbon black structures. Grey dotted lines on particle surfaces are used to illustrate the differences in surface area accessible for combustion reactions.

Therefore, for both 2 wt% and 10 wt% C65 samples, it is expected that the mass loss for C65 will occur at a slightly lower temperature for samples mixed for 60 min. Specifically, for samples containing 2 wt% C65 and mixed for 60 min, the carbon combustion will occur at the lowest temperature due to, presumably, the highest degree of deagglomeration because of low carbon loading and long mixing time. Samples with 10 wt% C65 mixed for 2 min are likely to have the highest reaction temperature due to high carbon content and short mixing time resulting in minimal deagglomeration of large structures. These different carbon structures from mechanofusion exhibit different degrees of surface area available for combustion reactions.

The mass loss of respective samples at the knee point between 400 – 600 ^{o}C is shown in Table 4.6. It was observed that for both 2 wt% C65 samples mixed at 2 and 60 min, a sharp decrease of ~2 % is

obtained between 400-500 ºC as shown in Figure 4.16a. This decrease in mass is likely a combination of the loss of oxides from the NMC structure and carbon combustion. However, the mass loss is relatively low for 60 min samples compared to 2 min samples (Figure 4.16a). This indicates that there is less carbon reacted for 60 min samples. Although carbon black structures for samples subjected to 60 min mixing are smaller, there may be a lower free carbon content as carbon black attaches to the NMC surface, thus reducing its surface area for the combustion reaction. At this specific temperature, the free carbon that has a smaller structure participates in the combustion reaction, contributing to the observed mass loss. This is the first indication of the amount of free carbon within the different mixtures where 2 min samples have a higher fraction of free carbon. A similar observation was obtained for 10 wt% C65 samples. Samples subjected to a shorter mixing time of 2 min showed a higher mass loss (Figure 4.16b).

Table 4.6: Mass residual and mass loss at the knee point of TGA profiles from approximately 400 – 600 ºC.

C65 Loading (wt%)	Mixing Time (min)	Residual Percentage (%)	Mass Loss (%)
2	2	97.8	2.2
2	60	98.0	2.0
10	2	88.3	12.7
10	60	88.7	12.3

Another distinct observation is the mass gained at approximately 600 – 700 ºC for 60 min samples at both carbon loadings. This may be due to traces of impurities (Fe, Ni) within C65 from the manufacturing synthesis process. Based on the same understanding of increased surface area due to smaller structures at 60 min, the impurities within the carbon black can easily react with oxygen to form their respective oxides. These oxides (Fe_2O_3, Ni_2O_3) exist as a solid and results in mass gain. For samples containing 2 wt% C65, as carbon black structures are more easily deagglomerated compared to that containing 10 wt% C65, the mass gain is more apparent. Additionally, it was found that this mass gain occurred at an elevated temperature of around 750 – 800 ºC for 2 min samples for both carbon loadings. This may be attributed to the large carbon structures and, therefore, less accessibility to react with oxygen.

To summarise, based on the combustion behaviours of coated particle samples with different carbon loadings and varying mixing times, there is an indication that more free carbon is present at short mixing. However, the observed behaviours likely represent a complex interplay of the free carbon content, changes in carbon black structures from mechanofusion, and the fraction of carbon black that is attached to NMC as a coating. Further investigation is needed to precisely quantify the free carbon content in each individual sample.

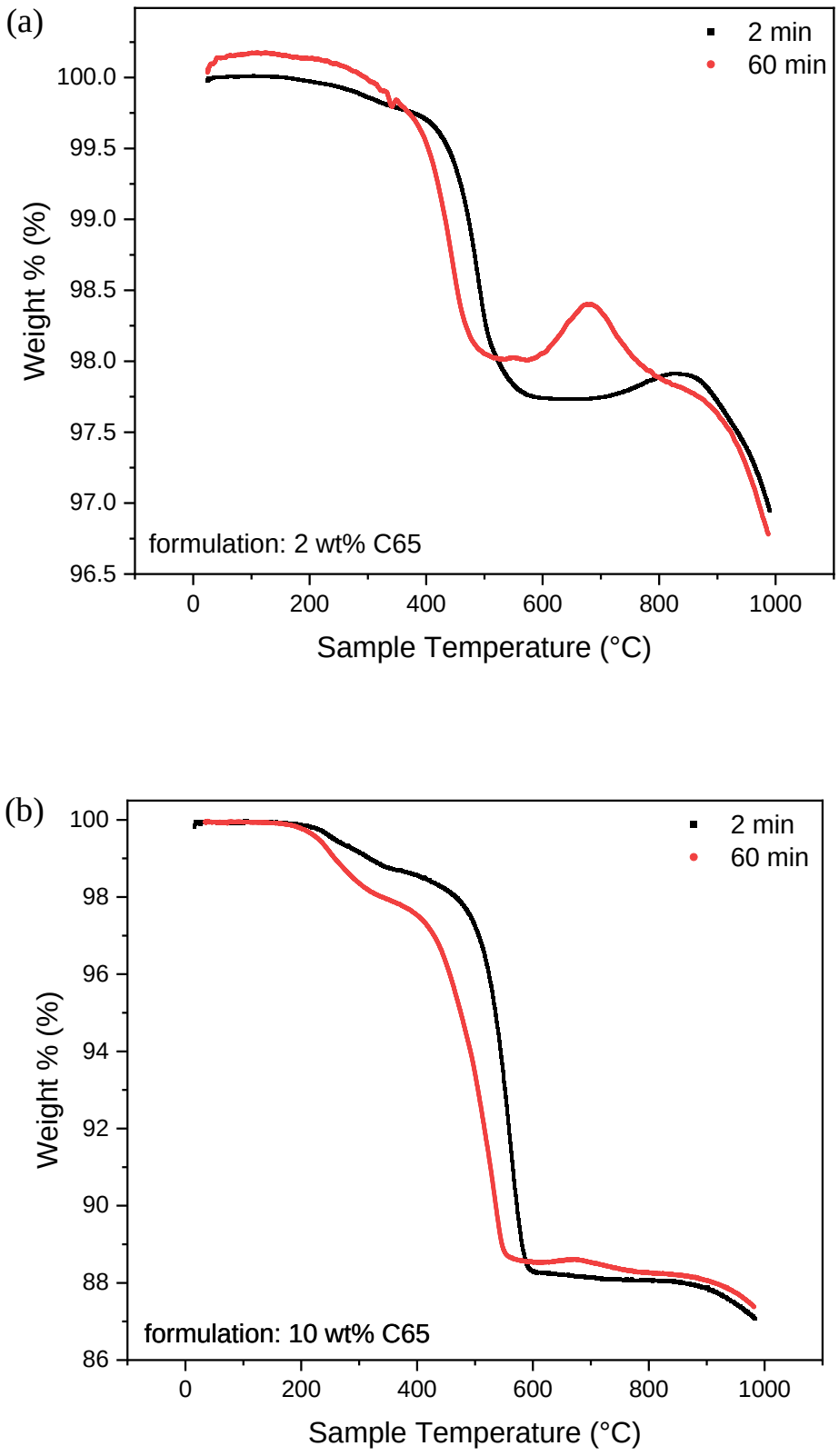

Figure 4.16: TGA profiles of binary powder mixtures of NMC with (a) 2 wt% and (b) 10 wt% C65, dry mixed for 2 and 60 min.

4.7.2 Slurry Rheology

Slurry rheology was studied to further investigate the amount of free carbon in the powder mixture. For a given C65 loading, the rheological behaviour of the slurry containing the binary powder mixture is dictated by the carbon network. This network formed during slurry mixing is dependent on the carbon black structures. Conventionally, pristine carbon black, in its large, agglomerated form, is added during wet slurry mixing and subsequently dispersed and deagglomerated. Here, the carbon network is formed from the aggregates of carbon black, which can hold the solvent, giving rise to the typical gel-like behaviour of slurries and preventing aggregation. The combination of carbon black and polymer binder also provides sufficient gel strength to stabilise the relatively large micron-sized NMC particles against sedimentation [79].

Samples that were subjected to different mechanofusion mixing times and thus differences in carbon structures were added into a PVDF-NMP mixture to form the slurry. The rheological behaviour tends to reflect the difference in these carbon black structures. The typical gel-type behaviour of slurries is expected to transition to a fluid-type behaviour due to the reduction in carbon black structure and immobilisation of carbon black. The flow curves show that the binary mixture of an unmixed sample (0 min) has a high initial viscosity and viscosity decreases as the shear rate increases (Figure 4.17). This is a typical behaviour of NMC slurries which indicate gel-type behaviour and shear thins. Upon mechanofusion mixing, all samples show a transition to fluid-type behaviour, where viscosity remains almost constant across the shear rates studied. The viscosity for samples mixed for 2 min is much lower than the unmixed sample. For samples mixed for 10, 30 and 60 min, they have a similar low viscosity and behaviour. These findings indicate that there is insufficient carbon black in the slurry to form a gel network, thus suggesting there is a low fraction of free carbon within the mixed samples.

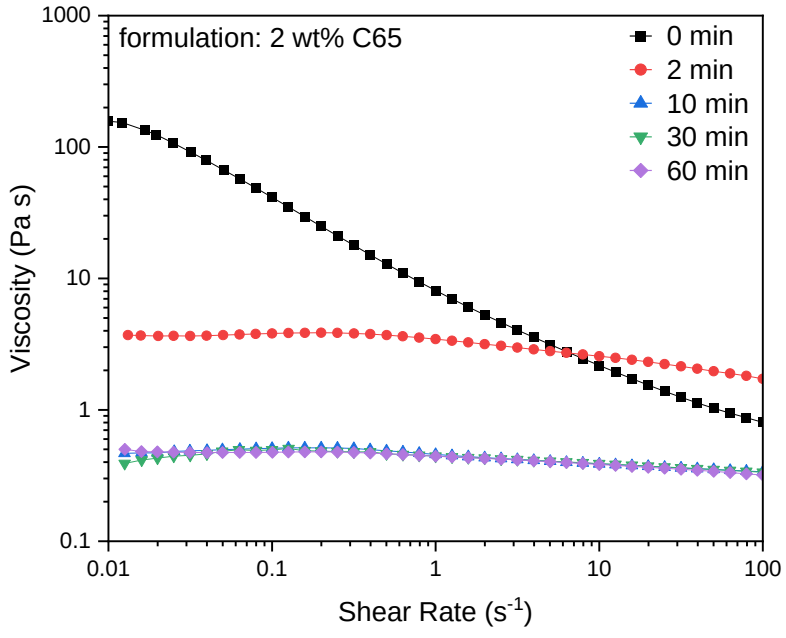

Figure 4.17: Flow curves of NMP slurries containing mechanofusion mixed NMC622 with 2 wt% C65.

The amplitude sweeps of the slurries, shown in Figure 4.18, also indicate a similar finding. Only unmixed samples exhibit a high storage modulus (G') at low-strain regions, and loss modulus dominates at high strain. This again reflects the behaviour of conventional cathode slurries with an elastic, gel-type behaviour. All other samples showed a higher loss modulus (G"), indicating inelastic, fluid-type behaviour.

Carbon black that is attached to NMC during mechanofusion becomes immobilised and has minimal influence on the rheology of the slurry. Essentially, the rheological behaviour of carbon-coated NMC becomes similar to pristine NMC. In contrast, unmixed samples exhibit different behaviour, which indicates the presence of free carbon that is available to form a gel network within the slurry. This gel-like behaviour is likely attributed to the carbon black agglomerates, or aggregates resulting from wet slurry mixing. The solvent adsorbs onto the high surface area of carbon black particles. This causes a change in the molecular dynamics of carbon black and changes the slurry rheology [144]. As mechanofusion mixing time increases, the resulting carbon black structures become smaller. Further dispersion during slurry mixing can potentially cause a greater reduction in the size of these structures. Therefore, this can result in a decreased ability of gel network formation. This translates to a lower viscosity for the slurries with 10, 30 and 60 min mixed samples. The observed changes in rheology can also be partially attributed to the reduction in the free carbon content. However, the exact contribution of free carbon content is still difficult to determine. The final rheology of the slurries is likely a combined effect of both the differences in carbon black structures and the free carbon content. Further investigation is still needed to understand these two individual factors.

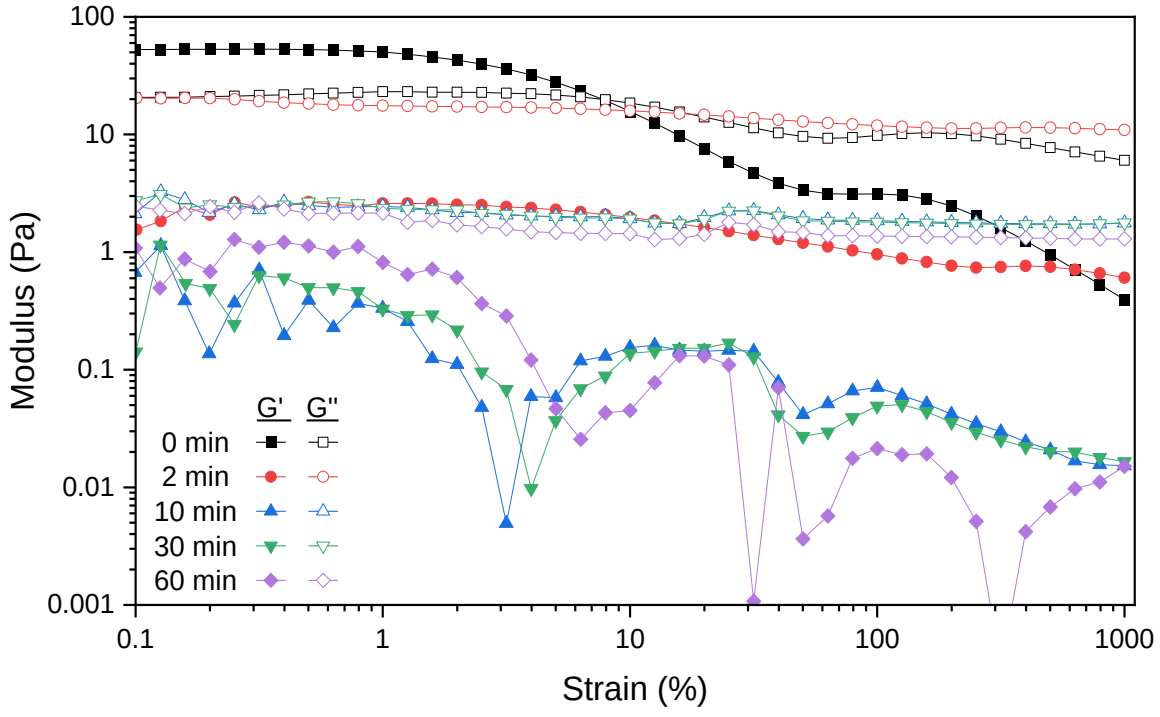

Figure 4.18: Amplitude sweeps of NMP slurries containing mechanofusion mixed NMC622 with 2 wt% C65 mixed at different times. The storage and loss modulus are denoted by G' and G" respectively

4.8 Conclusions

In this chapter, two novel CBD structures that correspond to the two different electronic pathway lengths were proposed: (1) a bridge structure linking two or more active material particles to form long-range electronic pathways and (2) film structures covering the surface of active materials, providing short-range electronic contacts. While the formation of bridge structures can be controlled through carbon black loading in wet slurry mixing, achieving ideal film structures remains challenging. This chapter also demonstrated mechanofusion as a promising deagglomeration-coating technique for tailoring film structures on NMC particles. The coating characteristics, particle properties and free carbon content were investigated, with the following conclusions drawn:

1. Qualitative analysis of coated particle morphology showed that short mixing times yielded a coating formed mainly of large carbon black structures. Conversely, prolonged mixing yielded smaller carbon black structures with better distribution. The degree of carbon black deagglomeration and distribution differs for low and high carbon loading.

2. A range of coating characteristics (e.g. smooth or rough coating) can be achieved by fine-tuning mixing conditions. The distribution and coverage of carbon black on the NMC surface can also be controlled similarly. BSE micrographs suggest that a thin and uneven distribution of carbon black is achieved at low carbon loadings. For high carbon loadings, it is easier to achieve better coverage and thicker film structure on NMC.

3. Particle size distribution analysis confirmed the reduction of initially large carbon black agglomerates into smaller structures with increased mixing. The deagglomeration process was also supported by changes in bulk and tapped density values. A significant change in tapped density is observed with increased mixing, suggesting better particle packing of smaller carbon structures in the voids between NMC particles.

4. Quantifying the amount of free carbon remains a challenge. Thermogravimetric analysis and slurry rheology findings suggest a decrease in free carbon content. However, these observations are also likely the combined effect of both free carbon content and changes in carbon black structure due to deagglomeration on the observed changes. Further work is required to isolate and study the contributions of these factors to quantify the exact free carbon content.

Although these findings indicate that mechanofusion mixing leads to carbon black deagglomeration, investigating the degree of deagglomeration through quantitative analysis is still a challenge. The current characterisation methods also lack relevance to electrochemistry and limit the ability to understand the relationship between carbon structure and electrode performance. Therefore, the selection of a proxy metric to evaluate and indirectly quantify carbon black deagglomeration could have great utility. The next chapter builds on this concept by investigating carbon black deagglomeration through bulk powder resistivity of coated particles, which will provide useful insights into the electrochemical impact of varying carbon structures and coating as film structures on NMC.

Chapter 5 Probing Carbon Black Deagglomeration Through Powder Resistivity Metrics

5.1 Introduction

Recent publications on quantifying carbon black deagglomeration were carried out through slurry rheological properties [37], or electrode and CBD structures [87], [88] correlated with cell electrochemical performance. The process is time-consuming and requires significant experimental effort for slurry preparation or electrochemical testing before any indications of dispersion can be determined. Additionally, some techniques, such as those involving slurry properties, are not suited for dry electrode processing, where the distribution of the conductive additives and binder remains an important aspect.

This chapter demonstrates the use of bulk powder resistivity as a proxy metric to investigate carbon black deagglomeration behaviour during mechanofusion mixing and the subsequent degree of dispersion for NMC and carbon black. For a binary powder mixture of cathode active material and conductive additives, the resistivity is dependent on the conductive additive content. When carbon black agglomerates are broken down into smaller aggregates or primary particles, this signifies a breakdown in the interconnected chain-like structures of carbon black. The change in carbon black structures can affect their ability to form a continuous electron travelling pathway, resulting in a change in the bulk resistivity. The change in resistivity of a binary powder mixture containing NMC and carbon black will depend on the electronic pathways, mainly facilitated by carbon black. The electronic pathways are dictated by the arrangement of carbon black particles and are directly related to their structure and size. Since the change in structure and size is directly influenced by the energy input of the mechanofusion mixing process, it is crucial to develop a mechanistic understanding of how the process parameters, along with the binary mixture loading and formulation, affect deagglomeration.

The aim of this chapter is to understand and quantify carbon black deagglomeration behaviour during mechanofusion mixing using bulk powder resistivity metrics. The objectives are to:

(1) investigate the effect of carbon black loading and total sample loading on bulk resistivity;
(2) study carbon black deagglomeration behaviour at low and high carbon loadings;
(3) study the impact of carbon black properties on final bulk resistivity;
(4) assess the applicability of this technique to non-conventional conductive additives (e.g. carbon nanotubes).

5.2 Experimental Design

Powder mixtures of NMC622 and C65 were dry mixed in a Nobilta mixer, as detailed in Section 3.2. For studies on carbon loading, the carbon loading used was 2 wt% and 10 wt% C65, with a mixing speed of 2300 rpm and mixing times of 2 and 60 min. For studies on sample loading, a carbon loading of 2 wt% C65 with a mixing speed of 2300 rpm and mixing times of 2 and 60 min was used. The total sample loading was varied from 20 to 50 and 100 g. For studies on mixing process parameters, the mixing speeds used were 1000, 2300 and 5000 rpm with mixing times of 2, 5, 10, 30 and 60 min. The carbon loading used was 2 wt% and 10 wt% C65 to study the carbon black deagglomeration behaviour at different carbon loadings. After mechanofusion mixing, the volume resistivity of powder mixtures was measured using the methodology detailed in Section 3.4.7. For comparison between different formulations and mixing conditions, the resistivity values of corresponding samples were extracted at a sample density of 4.0 g cm^{-3}.

For studies on carbon black properties, five different carbon blacks (C45, C65, LHP, L200 and L300), each with different BET surface area and structure levels, indicated by the oil absorption number (OAN), were dry mixed with NMC622 at 2300 rpm for 2 and 60 min. Raman spectroscopy was used to determine the Raman intensity ratio (I_D/I_G) of these carbon blacks (characterisation conducted by Dr Xuesong Lu, University of Sheffield). The properties of the carbon blacks are shown in Table 5.1.

Table 5.1: Properties of carbon blacks used in this study.

Carbon Black	BET Surface Area ($m^2 g^{-1}$)	Oil Absorption Number (OAN)	Raman Intensity Ratio [c] (I_D/I_G)
C45	45 [a]	720 [a]	0.93633
C65	62 [a]	640 [a]	0.92593
LHP	100 [b]	240 [b]	1.00503
L200	150 [b]	162 [b]	0.94877
L300	165 [b]	160 [b]	0.89767

[a] Obtained from data sheet provided by manufacturer, Imerys

[b] Obtained from data sheet provided by manufacturer, Cabot Corp.

[c] Measurement carried out by Dr Xuesong Lu, University of Sheffield

The use of carbon nanotubes (CNT) as the material for film formation was also explored (experimental work carried out by MEng student, Tian-Jay Mason, University of Sheffield). To study the feasibility of CNT as conductive additives for dry coating of NMC, multi-walled CNT (MWCNT) CNT1015 and CNT3080 were mechanofusion mixed with NMC at 2300 rpm for 30 min. The key properties of the two CNTs are shown in Table 5.2. The experimental data sets are shown in Table 5.3.

Table 5.2: Properties of carbon nanotubes used in this study.

Carbon Nanotubes	Diameter (nm)	Length (μm)	Specific Surface Area ($m^2 g^{-1}$)
CNT1015	10 – 15	< 100	150 – 250
CNT3080	30 – 80	< 20	80 –120

* All properties obtained from data sheet provided by manufacturer, Imerys

Table 5.3: Experiment data sets.

Formulation (NMC:CA wt%)	Conductive Additive Type	NMC622 (g)	Conductive Additive (g)	Mixing Speed (rpm)	Mixing Time (min)
98:2	C65	19.6	0.4	1000	2 60
98:2	C65	19.6	0.4	2300	2 5 10 30 60
98:2	C65	19.6	0.4	5000	2 60
98:2	C65	49	1	2300	2 60
98:2	C65	98	2	2300	2 60
98:2	C45	19.6	0.4	2300	2 60
98:2	LHP	19.6	0.4	2300	2 60
98:2	L200	19.6	0.4	2300	2 60
98:2	L300	19.6	0.4	2300	2 60
98:2	CNT1015	19.6	0.4	2300	2 60
98:2	CNT3080	19.6	0.4	2300	2 60
90:10	C65	18.0	2.0	1000	2 60
90:10	C65	18.0	2.0	2300	2 5 10 30 60
90:10	C65	18.0	2.0	5000	2 60

5.3 NMC622 Bulk Resistivity

The intrinsic resistivity of NMC is temperature-dependent and gradually increases with increasing temperature [145]. The bulk resistivity also differs from the intrinsic resistivity (i.e. individual particle resistivity) as the contact interfaces between particles can contribute additional resistances to charge transport. For NMC622, the bulk electronic conductivity was reported to be 10^{-3} – 10^{-2} S cm^{-1}, corresponding to a resistivity of 100 – 1000 Ω cm, based on dense sintered pellets [145]. In this study, it was found that the resistivity of NMC622 powder compressed to a density of 4.0 g cm^{-3} was approximately 528 Ω cm. Although this value is in rough agreement with the values reported in the literature, it does not represent the actual intrinsic electronic conductivity, as complete contact between particles can never be achieved, even with high compression force.

Furthermore, the resistivity of NMC is also state of lithiation dependent [146]. In general, resistivity decreases with decreasing state of lithiation of NMC. This is attributed to the increase in Ni^{4+} ions, leading to holes in the (Ni^{4+}/Ni^{3+}) band, and the decreased distance of Ni^{4+}–O^{2-} from higher covalency, making Ni^{3+}–O^{2-}–Ni^{4+} hopping easier [147]. For NMC532 (relative sample density 96 – 98 %) with a reported electronic conductivity (σ) of 1.3 x 10^{-3} S cm^{-1}, this corresponds to a state of lithiation of approximately 30 – 50 % (log σ = -2.89) [146]. Ni is considered an active conduction site that may aid electron hopping so NMC622 should possess a slightly higher conductivity than NMC532 at the same state of lithiation. Note that for NMC532, 622 and 811, their variation in electronic conductivity is minimal.

In this study, NMC622 has a log σ value of -2.72 based on the calculated resistivity at a sample density of 4.0 g cm^{-3}. The relative density is approximately 85 % based on the true density of NMC622, and this resistivity showed minimal deviation with increasing compression. Therefore, it is assumed that the resistivity recorded is representative of the bulk of the sample. This indicates that, here, the state of lithiation of NMC622 is estimated to also be between 30 – 50 %, potentially slightly lower than that of NMC532 in the referenced study [146]. However, the distribution of electronic conductivity is inhomogeneous within a single particle and, therefore, represents a variation in the state of lithiation on different parts of a single particle [148]. Despite this limitation, the estimated value still provides a useful indication of the average state of lithiation for the NMC622 particles used in this study.

5.4 Effect of Carbon Loading

As a conductive additive, carbon black has a lower resistivity compared to NMC particles and, therefore, forms a more efficient pathway for electron movement. Electrons experience less resistance and can travel more efficiently through the percolated pathways, which results in lower bulk resistivity. Figure 5.1 shows the resistivity of pristine NMC along with binary mixtures of NMC622 with low and high C65 loading, both of which were subjected to 2 and 60 mins of mixing at a speed of 2300 rpm. The two mixing times were selected as they represent the extremes within the broad mixing time studied and were shown to have significant differences in resistivity, which will be discussed in Section 5.5.

In general, the addition of carbon black resulted in a significant decrease in the powder resistivity. Pristine NMC showed the highest resistivity, which decreased significantly by 1 to 3 orders of magnitude as the carbon loading increased to 2 wt% and 10 wt% C65. The density of the bulk powder increases with compression force due to improved packing of NMC and C65, which is attributed to particle rearrangement and partial fragmentation of agglomerates. At the same time, this increases the electrical interparticle contact when particles rearrange to fill the voids in between, maximising the contact area between particles and potentially reducing the length of the pathways required for electron transfer or even establishing new electronic pathways.

For both low and high carbon loading samples, the resistivity for samples mixed for 2 min is lower than that of 60 min. The volume resistivity axis is presented in a logarithmic scale in Figure 5.1, reflecting that this difference for 2 wt% C65 is much more significant than that for 10 wt% C65. This difference indicates that a short mixing time, corresponding to a low degree of deagglomeration, is favourable to achieving low resistivity.

Resistivity continues to decrease with increased compression but eventually starts to level off. Figure 5.1 shows that there is a minimum resistivity, typically beyond a density of 4.0 g cm^{-3}, where the resistivity remains almost constant with increasing powder density. It is likely that at this density, a very high particle packing has been achieved, and therefore, the resistivity is representative of the entire sample volume. Beyond this point, compression is still possible, resulting in slightly better packing and, thus, a higher density, but the resistivity is not likely to exhibit a significant change. For low particle packing at low sample densities, there is a possibility of selective representation of resistivity. The minimum resistivity value is attributed to the resistivity of the NMC, and therefore, the resistivity of the binary powder mixture will not approach the conductivity of pure C65. When approaching very high carbon black loadings, the bulk resistivity is likely to be dominated by the resistivity of carbon black. However, electrons are still likely to come into contact and travel through NMC particles, which will increase the resistance experienced by electrons. This value represents the lowest resistivity that can be achieved for a specific carbon loading, mixing technique and mixing

conditions. With increasing carbon black loading, the electronic pathways for electron transfer will increasingly be made up of long “chain-like” structures of carbon black and are less likely to travel through NMC particles. Nevertheless, there will be a minimum resistivity that is almost constant, and this can also be observed in a typical percolation curve, as shown in Figure 2.6. Upon reaching the percolation threshold, the change in resistivity becomes less apparent and eventually remains constant when approaching very high conductive additive content.

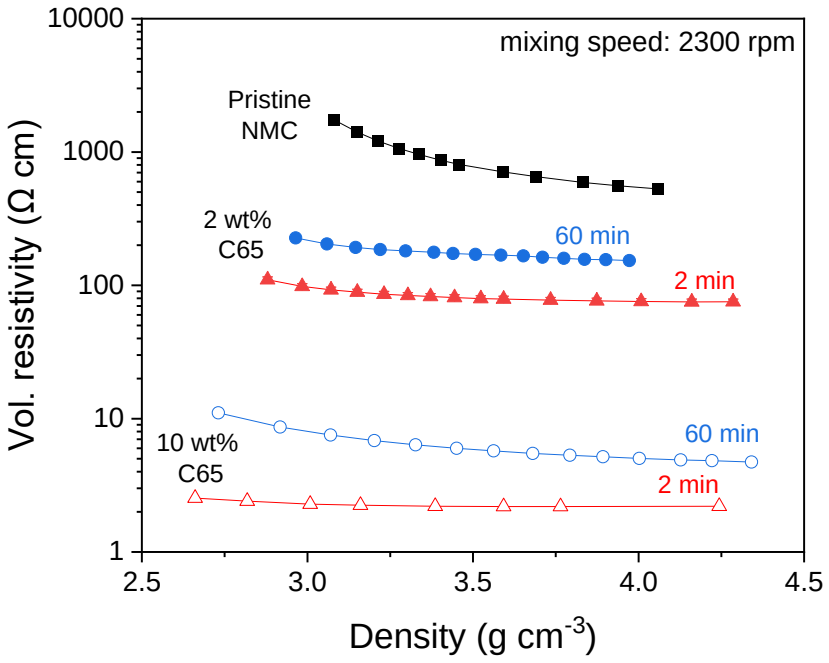

Figure 5.1: Resistivity of pristine NMC and powder mixtures of NMC with 2 wt% and 10 wt% C65, both subjected to 2 and 60 min of mixing.

5.5 Effect of Sample Loading

Carbon black deagglomeration ultimately depends on the overall energy input of the mixing process and the total sample loading can affect the mixing efficiency. Figure 5.2 shows a similar trend as described in Section 5.4, where 2 min mixing yielded a lower resistivity, whereas 60 min yielded a higher resistivity. The results also suggest that an increase in powder sample loading led to an increase in resistivity, again indicating that there are subtle differences in the degree of deagglomeration of carbon black. For example, for 60 min mixing, a sample loading of 20 g showed the lowest resistivity, followed by an increase for 50 g and 100 g. This difference is less distinct for samples mixed for 2 min, as the degree of deagglomeration of carbon black between the different sample loadings is not as significant within a short mixing time. This is reflected in the similar resistivity values recorded for 20 g, 50 g and 100 g sample loadings. For 60 min mechanofusion mixing, the difference in resistivity across different sample loadings becomes more apparent. The total energy input is much higher for 60 min compared to 2 min mixing, and this is reflected in the resistivity values.

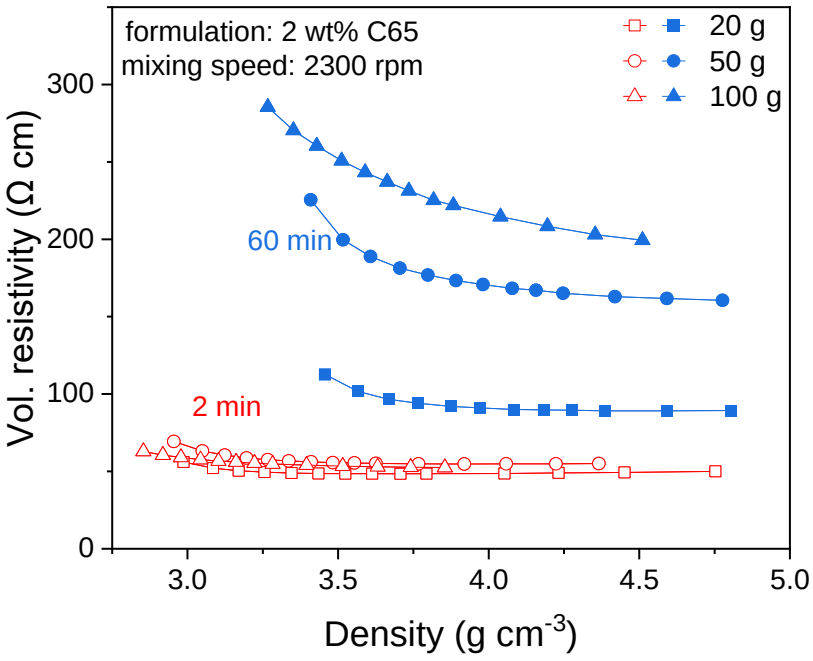

Figure 5.2: Resistivity of powder mixtures with varying sample loading of 20, 50 and 100 g, subjected to 2 and 60 min of mixing.

The mixing nature of mechanofusion can be categorised as intensive high-shear mixing, where high, intense mechanical shear forces are generated during mixing. In the Nobilta mixer, particles are forced through a tiny gap at the tip of the rotating rotor blade where the NMC and carbon black particles grind and shear between each other and the mixing chamber wall. The particles interact with the chamber wall to generate these shear forces. The energy input overcomes the van der Waals forces between carbon black particles and causes agglomerates to break up into smaller constituents. Increasing the total sample loading while keeping the binary mixture formulation constant

corresponds to an increase in the overall number of carbon black agglomerates in the mixture. The total energy input into the system is constant with identical process conditions, resulting in a lower specific energy supplied to the agglomerates as the amount of carbon black increases. Increasing the total loading can also lead to a lack of free space available for particles to move and interact. As a result, the change in the mixing profile can lead to less shear forces experienced by particles and less uniform mixing. Some particles may remain in the inner region during mixing and do not distribute to the outer region of the mixer and pass through the converging space. The combination of these two leads to a less efficient deagglomeration process, which affects the dispersion and coating formation on NMC. The implication is that carbon black remains in its large agglomerate structures and is not efficiently dispersed between NMC. During resistivity by compression measurements, large carbon black structures are less likely to be distributed between the voids of NMC particles, and thus, the electron pathway is less efficient due to contact with NMC.

A noticeable observation during measurements was that the higher the sample loading, the higher the energy required to compress the samples to a specific density (Figure 5.3). At 2 min mixing, a similar energy is needed to compress the samples to a particular density with 20 g and 50 g loading. A significantly higher energy is required for samples with the highest loading of 100 g. For 60 min mixing, the sample with a total loading of 20 g required the least energy to be compressed to a specific density, followed by 100 g and 50 g. For 60 min mixing, Figure 5.3 also suggests that mixing may be less efficient at 50 g loading compared to 100 g loading based on the higher energy required to achieve a particular sample density. However, the resistivity for 50 g loading is indeed lower than that of 100 g. Therefore, it is also crucial to determine the critical metrics for assessing mixing efficiency. For assessing carbon black deagglomeration behaviour, the bulk resistivity is more useful as it provides an indication of the small and large carbon black structures that form the electronic pathways within the sample. In terms of assessing the particle packing, the energy required for compression might be more useful.

The findings indicate that it is more difficult for particles to achieve higher packing caused by the large carbon black structures at increased loading. The larger agglomerates are unable to fill the voids between NMC, leading to an increase in the void volume and, therefore, overall a higher bulk density, as illustrated in Figure 4.13. Higher compression forces are required to increase the energy to overcome the interparticle forces that hold and form the carbon black agglomerates, in order to break these agglomerates, allowing them to fill the voids between NMC particles better. This is also reflected in the higher initial densities achieved by samples with 60 min mixing in Figure 5.2, compared to 2 min mixing, where a similar compression range of 100 – 2000 N was applied. Smaller carbon structures are obtained after long mixing and, therefore, have better packing, resulting in higher density during compression.

Conversely, underloading can also impact the shear rate, especially in a system where large NMC particles and smaller C65 particles are present. The particles may experience a higher specific energy input, resulting in more intense interactions that may cause NMC particle breakage. It is also possible that the energy input is wasted due to insufficient interactions between particles.

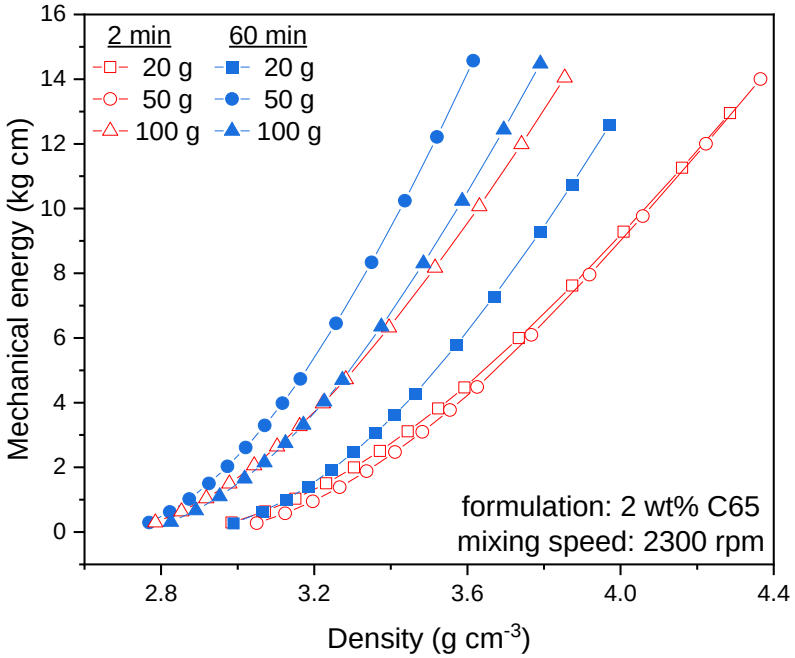

Figure 5.3: Mechanical energy required to compress powder mixtures of NMC and 2 wt% C65 of varying sample loading and mixing times to corresponding densities.

Therefore, for short mixing times, the effect of sample loading is less dominant, and the degree of deagglomeration of carbon black is similar. For longer mixing times, the uneven distribution of shear on the particles will result in a significant variation in the degree of deagglomeration, which is reflected in the bulk resistivity values. It is a balance between maximising process throughput and achieving consistent, optimal shear rates to achieve optimal mixing performance. As a result, it is crucial to develop a mechanistic understanding of how mechanofusion process parameters, combined with sample formation and loading, affect mixing efficiency.

5.6 Effect of Mechanofusion Process Parameters

Mixing process parameters play a significant role in determining the number and probability of interactions that occur between particles. The total energy input into the binary powder mixture is also controlled by the mixing time and mixing speed. A prolonged mixing time maximises the amount of energy input while increasing the mixing speed leads to higher shear rates for more intense mixing.

Figure 5.4a shows resistivity results for a binary mixture of NMC with 2 wt% C65 without the aid of mechanofusion mixing (0 min) with the highest resistivity. The remaining samples were mixed at 2300 rpm for 2, 5, 10, 30 and 60 min. An increase in resistivity with mixing time is observed. Among these mixtures, samples mixed for the shortest time of 2 min showed the lowest resistivity, while samples subjected to long mixing times of 30 and 60 min showed the highest and similar resistivities. A similar trend was also obtained for samples mixed at high carbon loading, where 2 min mixing showed the lowest resistivity (Figure 5.4b) across all the mixing times studied. These findings conclude that a short mixing time is favourable for achieving low resistivity for micron-sized NMC with nano-sized carbon black. A long mixing time does decrease the bulk resistivity for low carbon loading but can increase the resistivity beyond pristine NMC particles at 30 and 60 min.

An interesting observation is the slight increase in resistivity when approaching higher sample densities, as shown by the unmixed (0 min) sample in Figure 5.4b. High compression force is applied to achieve high sample density, which may also cause the breakage of carbon black agglomerates. Since resistivity is dominated by carbon black for high carbon loading samples, the breakage of these agglomerates results in a less interconnected conductive pathway. As a result, the sample resistivity increases.

An implication of these findings is that uniform dispersion is not necessary, as supported by Huang et al. [45] for the case of conductive applications. Dannenberg [149] proposed that there is an optimum dispersion time before agglomerates are broken down and the distance between particles is increased. Cembrola [150] stated that the dispersion process must be carefully controlled to avoid under or over-dispersion of carbon black, which may affect conductivity. Uniform dispersion is usually achieved by a prolonged time of mixing, which may include higher energy input to achieve a high degree of deagglomeration, resulting in a homogenous mixture and narrow particle size distribution. Short mixing yielding low resistivity implies that only minimal agglomeration is required, and most of the carbon black within the mixture should remain in their larger structures. This also implies that there is an optimum combination of small and large carbon black structures that constitutes the optimal combination of short- and long-range electronic pathways to achieve low resistivity.

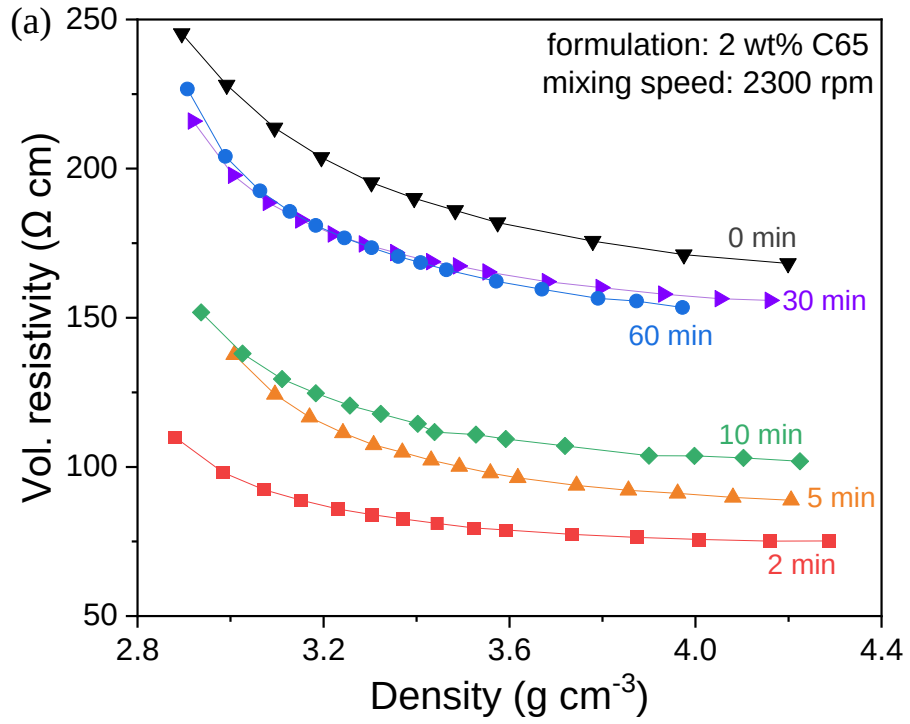

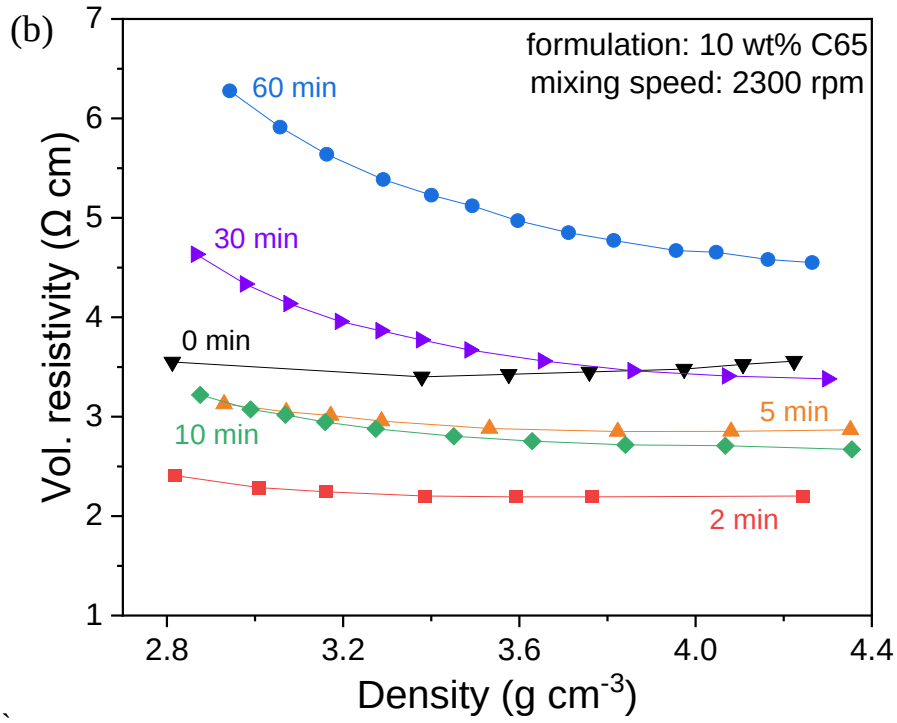

Figure 5.4: Resistivity of powder mixtures of NMC with (a) 2 wt% C65 and (b) 10 wt% C65, subjected to 0 (unmixed), 2, 5, 10, 30 and 60 min mixing.

The resistivities for both carbon loading samples, at various mixing times, at a sample density of 4.0 g cm^{-3} were extracted and are presented in Figure 5.5. For low carbon loading, the resistivity is more sensitive to mixing time compared to high carbon loading. This is evident in Figure 5.5a with a large increase in resistivity of 75.7 Ω cm to 153.4 Ω cm when mixing time is increased from 2 min to 60 min respectively. The increase in resistivity with mixing time can be firstly explained by a higher degree of deagglomeration of carbon black. Carbon black exists as long, "chain-like" structures within the interparticle voids of NMC particles. These structures act as an interconnected electronic network that facilitates electron movement. When deagglomeration of these structures occurs, this interconnected network is said to be disrupted, thus resulting in a disconnected electronic pathway. Prolonged mixing can also increase the spheronisation effect of mechanofusion, resulting in a smoother particle surface. Initially, large carbon black agglomerates are broken down into smaller constituents. They also start to attach to the surface of NMC due to high compression forces as the particles are forced through the converging space. Prolonged mixing then results in erosion, gradually reducing these aggregates into smaller particles and continued compression leads to compaction of the carbon black coating. The carbon-coated NMC surface is consistently sheared and polished during the mixing process, which results in a reduction in surface area. In comparison with loosely bound carbon black "chain-like" structures on the particle surface, the smooth carbon-coated surface limits contact area with other surrounding particles. In addition to the smaller carbon structures resulting from mechanofusion mixing, the effect of increased resistivity becomes more apparent.

For high carbon loading, the resistivity increases from 2.2 Ω cm to 4.6 Ω cm at 2 min and 60 min respectively, as shown in Figure 5.5b. In this case, the bulk resistivity is now dominated by carbon black at high carbon loading. The electronic pathways are mainly formed by a complex and more interconnected chains of carbon black, where electrons have a relatively low probability of coming into contact with NMC particles. Since carbon black has a relatively higher electronic conductivity compared to NMC particles, electrons will favour travelling through carbon black due to lower resistance. The higher the probability of electrons travelling through NMC particles, the higher the resistance experienced compared to a pathway constituted mainly of conductive additive. Additionally, an increase in carbon black agglomerates with the same energy input results in slower and less deagglomeration of these agglomerates. Thus, a higher proportion of large carbon black structures are retained, even after a long mixing time of 60 min compared to low carbon loading. Ultimately, the interconnected electron pathway is still retained, which results in a low bulk resistivity.

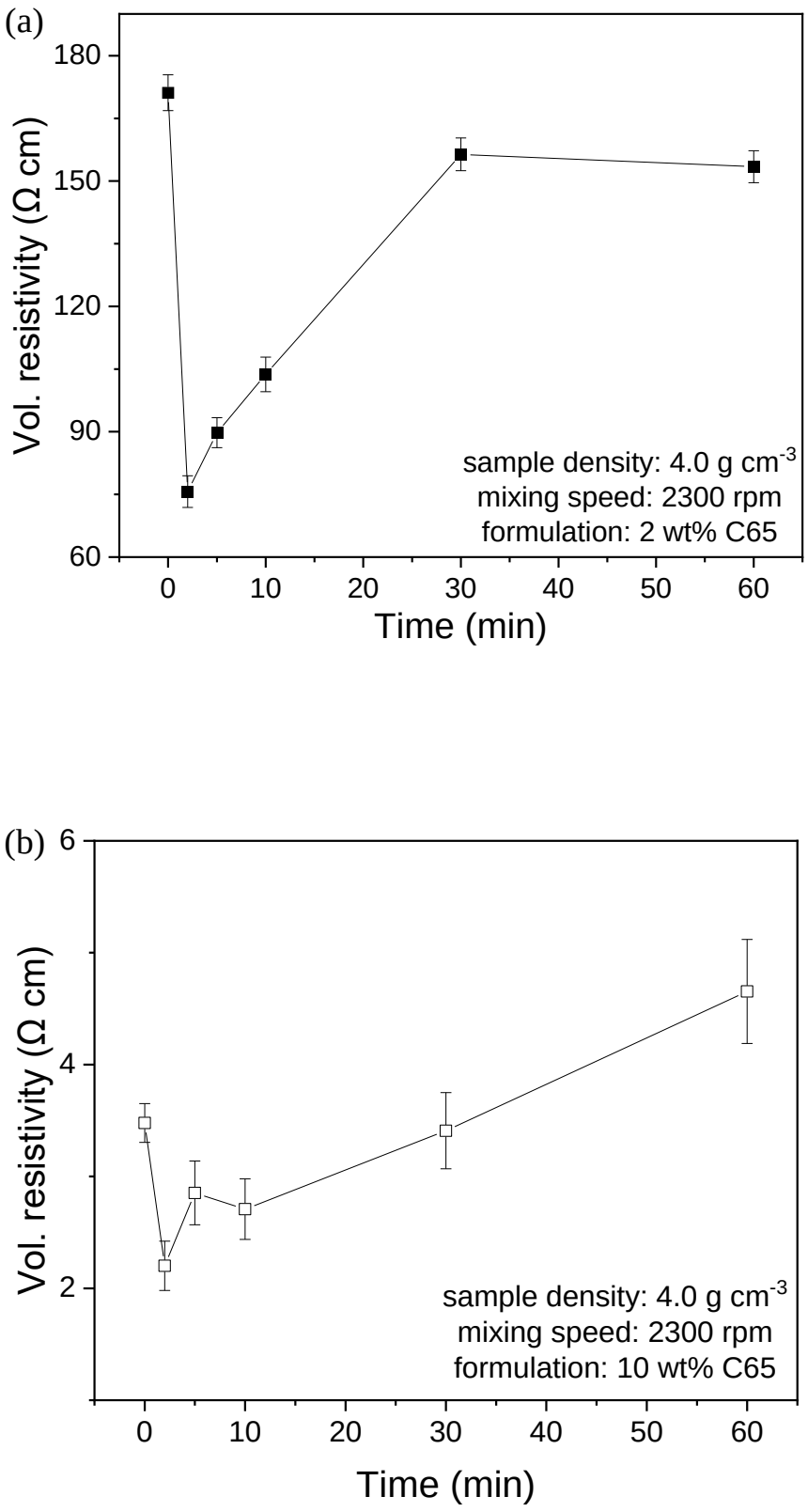

Figure 5.5: Change in resistivity with mixing time for powder mixtures of NMC with (a) 2 wt% C65 and (b) 10 wt% C65.

The relationship between mixing speed and resistivity is dependent on the carbon black loading. Grießl et al. [37] demonstrated the interdependency between carbon black loading and the circumferential speed of the mixing blade, which will affect the selection of other parameters during mixing. To study the influence of mixing speed, 3 different speeds of 1000, 2300 and 5000 rpm were selected. Herein, these speeds are referred to as “low”, “medium” and “high” speeds, respectively, for comparison purposes.

For 2 wt% C65, mixing time is a key consideration when selecting the optimal mixing speed, as shown in Figure 5.6a. At a short mixing time of 2 min, the use of medium to high speed is desired, while lower speeds are desired for a long mixing time of 60 min. The selection of the combination of mixing speed and time can be related to the total energy input required to achieve the ideal combination of short- and long-range contacts for low resistivity. In general, an appropriate speed must be selected for a specific mixing time to achieve the required energy input for adequate mixing. If low mixing speeds are required for long mixing times, this implies that similar energy input is needed for high mixing speeds to achieve a similar degree of deagglomeration and its corresponding resistivity. Therefore, it can be deduced that high mixing speeds, where the shear rates are much higher, should require a comparatively short mixing time to achieve a similar mixing intensity.

A different observation applies to samples with a carbon loading of 10 wt% C65. The lowest resistivity was obtained at low mixing speeds, regardless of the mixing time, as shown in Figure 5.6b. At a short mixing time of 2 min, the resistivity remains constant with increasing speeds. However, for a long mixing time of 60 min, a sharp increase in resistivity is observed as the mixing speed increases. At high carbon loading, the conductive networks are formed mainly by carbon black, and low mixing speeds result in very little deagglomeration compared to low carbon loading. As a result, there is a higher probability of large structure carbon black remaining after mixing and retaining the interconnected electronic pathways. Figure 5.7a shows that a large portion of carbon black agglomerates is clearly visible under SEM imaging after 2 min mixing, confirming minimal deagglomeration during mixing at low speeds. After 60 min mixing, aggregates were observed, indicating that prolonged mixing led to an increase in energy input that is sufficient for deagglomeration to occur (Figure 5.7b). One reason to explain this is due to insufficient shear stress produced during short mixing for carbon black rupture to occur. However, as powders are subjected to compression during resistivity measurements, these long-chain structures can still be re-established to form the interconnected network, leading to a decrease in resistivity. This is evident from Figure 5.6b, where similar resistivities were obtained for both 2 and 60 min samples mixed at 1000 rpm.

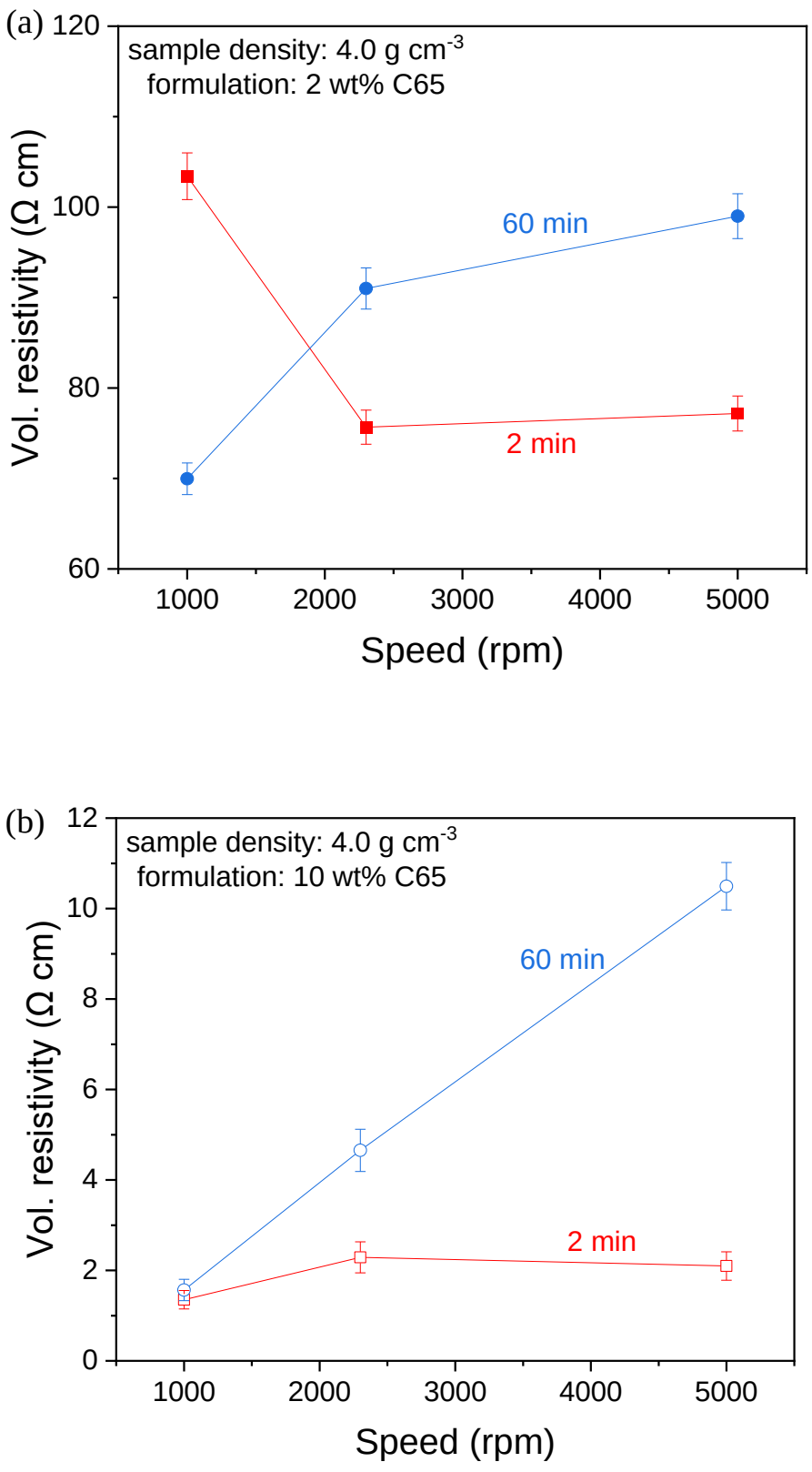

Figure 5.6: Change in resistivity with mixing speed for powder mixtures of NMC with (a) 2 wt% C65 and (b) 10 wt% C65.

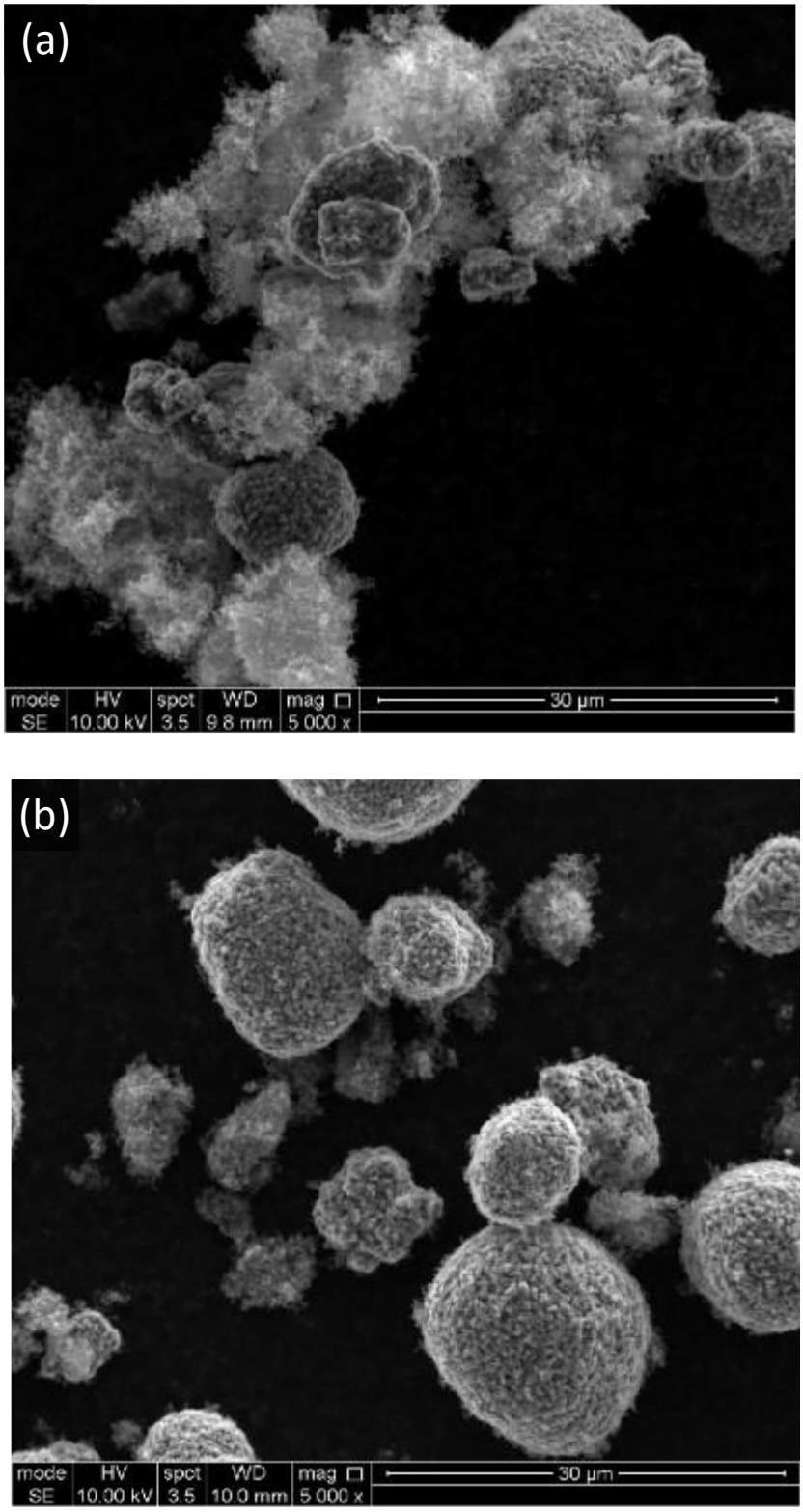

Figure 5.7: SEM micrographs of NMC with 10 wt% C65 mixed at 1000 rpm for (a) 2 min and (b) 60 min. (a) shows large carbon black agglomerates that act as an interconnected electronic network for long-range conduction. (b) shows disruption of the interconnected network due to smaller aggregates from long mixing.

Increasing the mixing speed corresponds to an increase in shear rates [151]. A schematic depicting the differences in deagglomeration between low and high carbon loading samples and the resulting carbon structures and electronic pathways is shown in Figure 5.8. Prolonged mixing increases the energy input into the system and results in a relatively higher degree of deagglomeration of agglomerates, giving large aggregates. In this instance, it represents a disruption to these interconnected pathways, where the long chain-like structures are no longer present. Note that in Figure 5.7b although large carbon black structures are no longer visible in the SEM micrograph, there are still small, fine aggregates present that are less visible in the background due to powder samples being attached to carbon tape. In this case, even though the percolated pathways still exist, electrons may have an increased probability of travelling through NMC particles, leading to increased resistivity as depicted in Figure 5.8b.

For long mixing, increasing the mixing speed has a more apparent effect on resistivity. With mixing at 5000 rpm for 60 min, a large amount of carbon black was deagglomerated and coated onto NMC, which is evident from large NMC particles with smooth surfaces due to C65 filling the surface pores of NMC, as shown in Figure 5.9. These particles also experience the spheronisation effect of mechanofusion when subjected to long mixing at high speeds. Although the resistivity of these particles is very low, it likely has a detrimental effect on ionic conductivity due to the inaccessibility of NMC surface, limiting the surface area in contact with electrolyte when fabricated into electrodes.

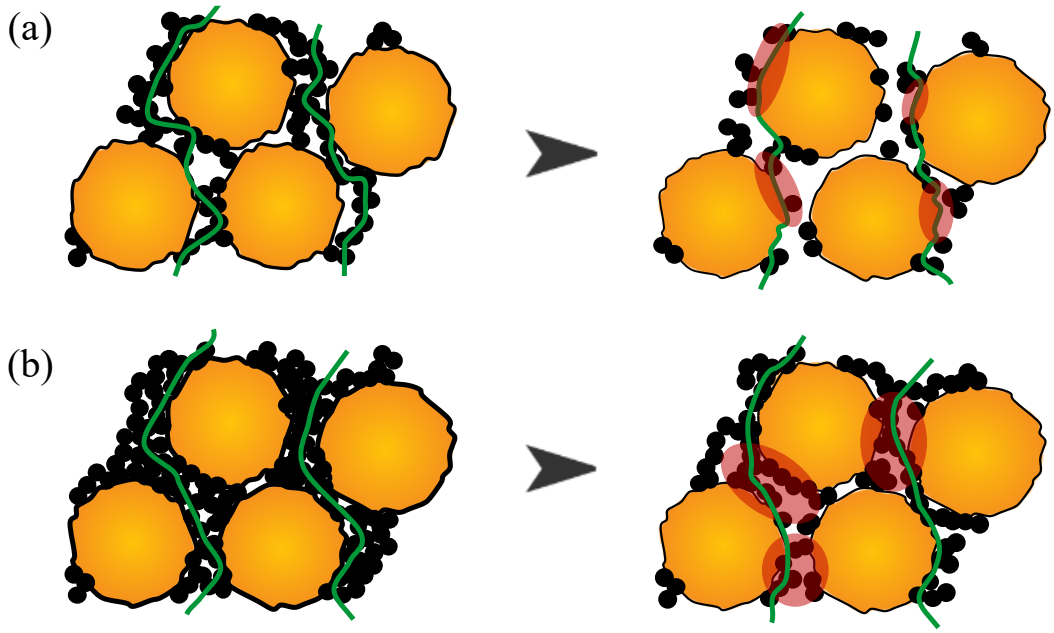

Figure 5.8: Schematics depicting the change in interconnected pathways formed by carbon black after mixing for a mixture of NMC and C65 with (a) low and (b) high carbon loading.

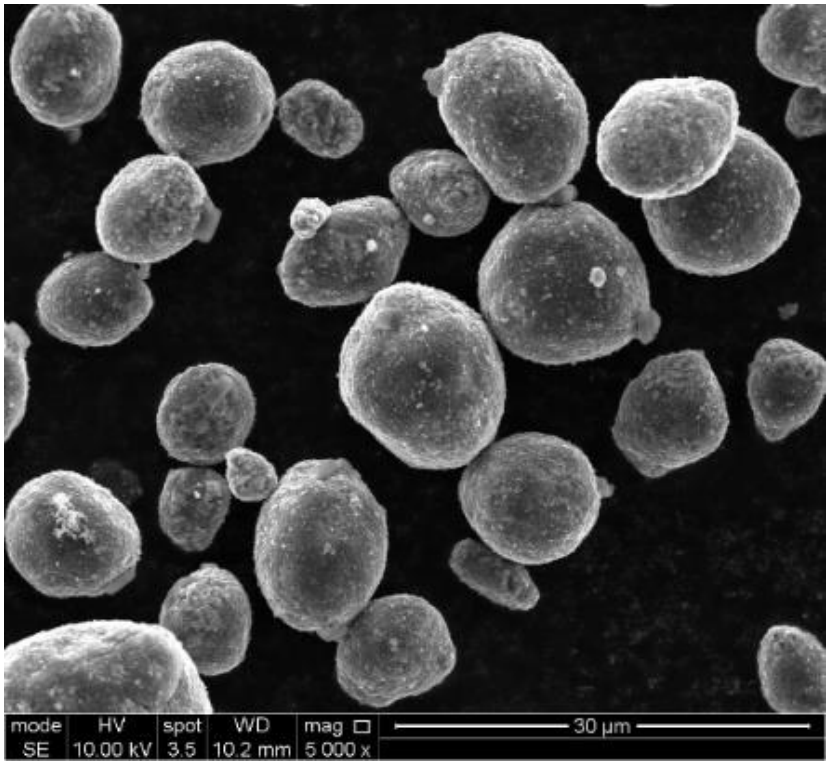

Figure 5.9: SEM micrograph of NMC with 10 wt% C65 mixed at 5000 rpm for 60 min, showing relatively smooth NMC surfaces due to carbon coating formation and spheronisation effect from mechanofusion.

The shear rate and energy input are dictated by the mixing speed. High shear mixing speeds are often linked to the power input and tip speed of the rotor [112]. The dimensionless Froude-tool number (Fr_t) has been used as a method of quantifying mixing intensity between different techniques. It is defined as the ratio of inertial forces to gravitational forces, and for mechanofusion can be defined as [152], [153]:

$$\mathrm{Fr_t} = \frac{\omega_t^2 r_t}{g} \tag{5.1}$$

where ω_t is the rotor speed, r_t is the rotor radius and g is the gravitational constant.

In this study, the rotor radius (r_t) was kept constant and, therefore, the higher the Fr_t indicates the higher the mixing intensity is. Westphal et al. investigated the dry mixing of graphite with carbon black and found that $\mathrm{Fr_t}$ up to 75 has minimal effect on electrode resistivity as only homogenisation of powders is achieved [78]. When $\mathrm{Fr_t}$ exceeds 75, the resistivity is increased. Haselrieder et al. [152] found that structural changes of carbon black agglomerates and coating onto NMC surfaces can be observed in cathodes consisting of particles processed with a low $\mathrm{Fr_t}$ of 50 for 2 and 8 min mechanofusion mixing. The findings also complement the observations reported by Bockholt et al. with a $\mathrm{Fr_t}$ of 400 [105]. Powder packing density was increased, but the conductance of powders remained low.

While the use of Fr_t has been studied on electrode resistivity and the interactions between graphite-carbon black and NMC-carbon black are vastly different, a similar approach can be taken to establish the relationship between Fr_t and powder resistivity of a binary powder mixture of active material and conductive additive. In this study, a Fr_t of around 50 (speed: 1000 rpm) represents the region where the lowest resistivity can be achieved for all cases, except at low carbon loading with short mixing times. For this specific case, a higher Fr_t of 260 (speed: 2300 rpm) up to around 1230 (speed: 5000 rpm) is more favourable for achieving low resistivity. The Fr_t is also less important as mixing does not greatly affect the resistivity and, thus, the carbon black structures at this condition.

For $Fr_t > 6 – 7$, corresponding to a mixing speed of approximately 350 rpm, powders are already centrifugated and form an annular on the mixer wall. The Fr_t ranges of 260 to 1230 show that the centrifugal force is several magnitudes higher than the gravity force during mechanofusion mixing. At these ranges, the high shear mixing is very intense, which results in deagglomeration. In general, a high Fr_t is preferred for short mixing and a low Fr_t is preferred for long mixing, regardless of carbon loading. The results complement the literature discussed; beyond a certain Fr_t, the resulting resistivity is similar. Therefore, it can be inferred that the structure of carbon black is also similar and thus indicates a similar degree of carbon black deagglomeration.

5.7 Carbon Black Properties

Carbon black is a conductive additive that is commonly used in industrial electrode manufacturing due to its excellent conductivity and low production costs. Specifically, C65 is favourable for its low surface area, which can minimise binder deposition [60]. Its properties have also been well studied, and it was demonstrated that resistivity by compression can be used to quantify its deagglomeration behaviour in dry mechanofusion mixing. The same approach was extended to validate the applicability of resistivity by compression approaches to study the influence of carbon black properties on the final bulk resistivity.

The structure level of carbon blacks is used to describe the branch structure of the aggregates and agglomerates and is indicated by the oil absorption number (OAN). A higher OAN indicates a more branched and open structure. In general, the ease of dispersion of carbon black increases with their OAN as a more open and branched structure results in weaker attractive forces and more surface area available for interaction during dispersion. The particle size of the primary particles of carbon black can be inferred from their BET surface area, where a higher BET surface area corresponds to a smaller particle size. Contrary to the OAN, the ease of dispersion decreases with increasing BET surface area as a smaller particle size often possesses higher attractive forces between particles. In terms of resistivity, both high OAN and high BET surface area result in lower resistivity due to their ability to form a more interconnected pathway for electron movement. A schematic depicting the features of carbon black with varying structure levels and surface areas (particle sizes) is shown in Figure 5.10a.

Using Raman spectroscopy, these carbon blacks were found to exhibit different intensity ratio values (I_D/I_G). The I_D/I_G provides the ratio of disordered carbon to ordered carbon and can be used as an indication of the fraction of ordered graphitic carbon within the carbon black structure. Carbon black particles consist of an amorphous core surrounded by graphene layers. These graphene layers are zero bandgap semiconductors due to sp^2-hybridised carbon (Figures 5.10b and 5.10c) where electrons can travel freely in the delocalised π-orbitals of the layers, giving rise to high electronic conductivity [60]. The amorphous core contains a relatively disordered network from a mix of sp^2 and sp^3 hybridisations are present resulting in limited electron mobility. Hence, an increase in graphene layers, corresponding to a higher fraction of graphitic carbon, can be correlated to a higher electronic conductivity for carbon blacks. Pantea et al. [154] reported that the conductivity of carbon blacks increases (i.e. resistivity decreases) with their graphitic character.

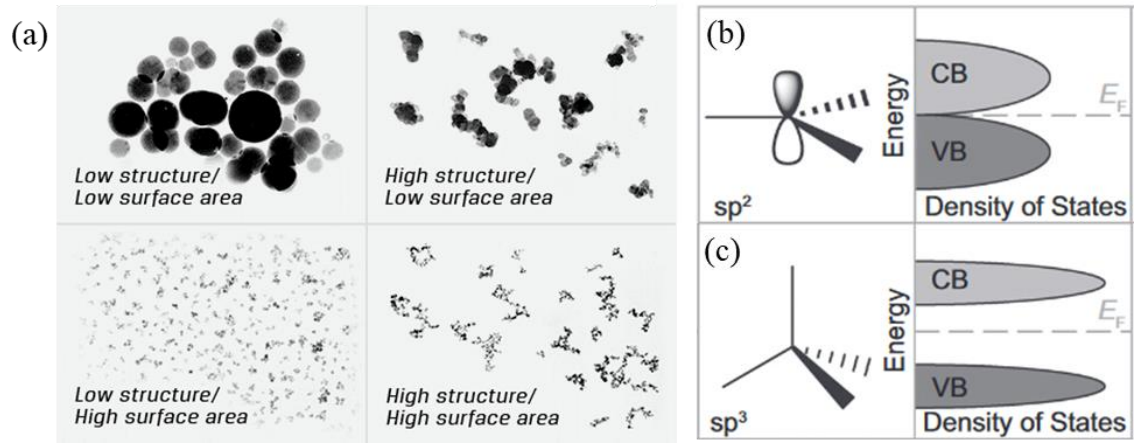

Figure 5.10: (a) Carbon black characteristics with varying structure level and surface area. Geometry and schematic of band structures of (b) sp^2-hybridised carbon (graphene) and (c) sp^3-hybridised carbon (diamond). Adapted from [60], [155].

The resistivity of the dry mixed samples is shown in Figure 5.11. For 2 min mixing, LHP and L300 both showed the lowest and similar resistivities, while C45 and C65 both showed the highest and similar resistivities. After 60 min mixing, all samples showed an increase in resistivity, consistent with the observations discussed in preceding sections where prolonged mixing causes higher resistivity due to the breakdown of long-range electronic networks. The lowest resistivity was obtained for L300, whereas the highest resistivity was observed for C45.

The deagglomeration mechanisms for carbon blacks remain the same. In terms of the short and long-range contacts resulting from dry mixing, there is also an optimal mixing time to achieve the ideal ratio of short and long-range pathways that is facilitated by the small and larger carbon black structures. The resistivity of the binary powder decreases with mixing until the optimal mixing time. It then starts to increase due to the breakdown of the long-range pathways, as indicated by the increase in resistivity when mixing is increased from 2 min to 60 min. However, the change in resistivity of different NMC-CB mixtures was observed. The findings show that carbon black properties such as BET surface area, OAN and intensity ratio affect the final resistivity. These properties are related to their primary particle size, structure level and the fraction of graphitic carbon. The findings also indicate that certain carbon blacks may be more compatible with dry mixing to yield low bulk resistivity.

Based on Figure 5.12, C45 showed the most significant increase in resistivity after mixing, from 81.3 Ω cm at 2 min to 502.5 Ω cm at 60 min. L300 showed the least increase in resistivity and yielded the lowest resistivity of 67 Ω cm after 60 min mixing. To discuss the differences in resistivity observed, these carbon blacks were separated into two categories based on their OAN – low structure level carbon blacks (LHP, L200, L300) and high structure level carbon blacks (C45, C65).

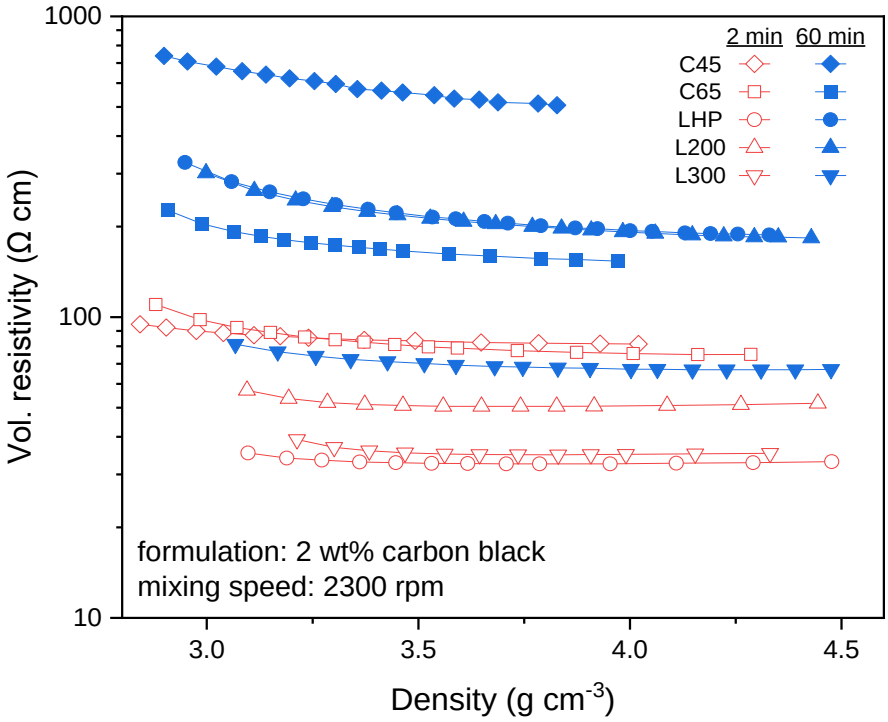

Figure 5.11: Resistivity of powder mixtures of NMC with 2 wt% of various carbon blacks with different OAN and BET, subjected to 2 and 60 min mixing.

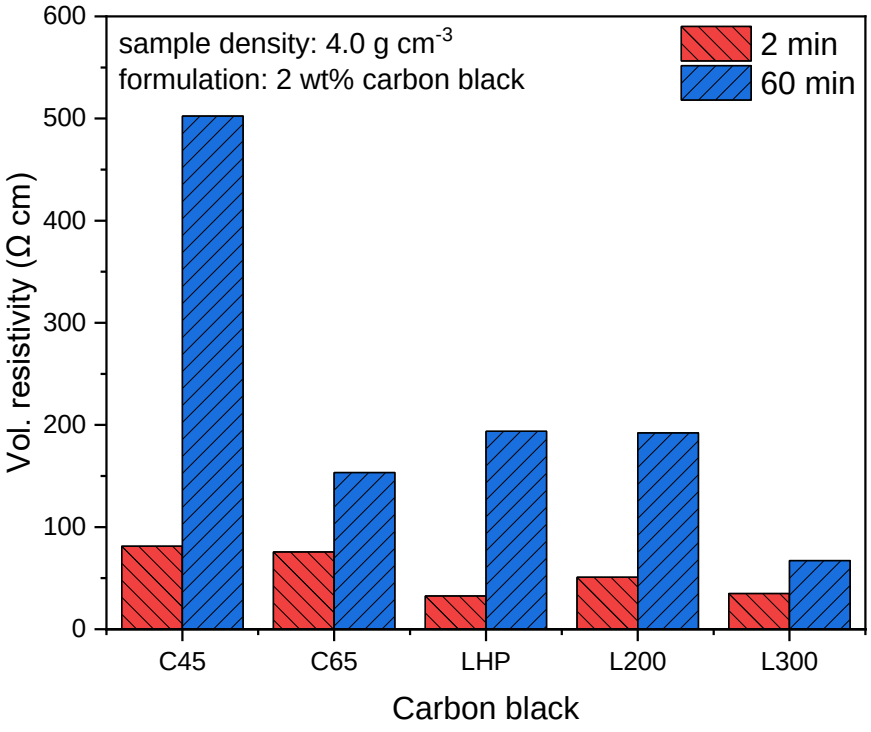

Figure 5.12: Comparison of resistivities of binary mixtures of NMC and 2 wt% of different carbon blacks subjected to 2 and 60 min mixing.

All three low structure level carbon black mixtures initially showed a relatively low resistivity at 2 min mixing, which may be related to their material properties. The OAN decreases from LHP to L300, indicating that the ease of dispersion decreases during mechanofusion mixing. Therefore, it is possible to deduce that the degree of deagglomeration may be higher for LHP (i.e. resulting in smaller carbon structures), followed by L200 and L300. The electrical resistivity of the carbon blacks decreases with increasing OAN (increasing structure level) and increasing BET surface area (decreasing particle size). After 60 min mixing, where carbon blacks are deagglomerated, its BET surface area and I_D/I_G become more influential in determining the change in bulk resistivity. Initially, by comparing L200 and L300, both carbon blacks have a very similar OAN, indicating similar dispersibility. However, L300 has the smallest particle size and the highest fraction of graphitic carbon, which may explain the low resistivity obtained after mixing. L200 showed a smaller particle size and lower I_D/I_G compared to LHP. In theory, this should yield a lower resistivity. Interestingly, the resistivity of L200 obtained is similar to that of LHP, which has a larger particle size and higher I_D/I_G.

The discrepancies suggest that the dispersion of the carbon black within the powder mixture, influenced by the OAN, plays a role in the final resistivity. After considering the dispersion based on the OAN, the BET surface area and I_D/I_G may be useful material properties to indicate the resistivity of the powder mixture. As such, there is a complex interplay between the OAN, BET surface area and I_D/I_G in determining the final resistivity. The precise correlation between these properties and final resistivity is currently unclear, and further investigation is needed.

For high structure level carbon blacks, both C45 and C65 showed a similar initial resistivity with 2 min mixing. Similarly, these resistivities may be related to the three material properties. After 60 min mixing, C45 showed a sharp increase in resistivity, while the increase for C65 was less significant. Due to the high OAN of both carbon blacks, their ease of dispersion is very high and they are both likely to be deagglomerated into much smaller structures. The BET surface area now becomes an important property for predicting resistivity as C45 has a larger particle size than C65, indicating higher resistivity. Similarly, the higher I_D/I_G of C45 also indicates higher resistivity compared to C65. One reason could be the impact of the high particle resistivity of C45 is magnified when the degree of deagglomeration is high and leads to more disruption to the interconnected electronic network initially formed by the chain structures of carbon black.

To summarise, the resistivity resulting from short mixing could be said to be largely dependent on the intrinsic resistivity resulting from the carbon black properties i.e. BET surface area, OAN and I_D/I_G. For long mixing, carbon black with high OAN is more easily dispersed, resulting in a higher degree of deagglomeration. Combined with a large particle size with high intrinsic resistivity, the bulk resistivity resulting from mixing is also high. For carbon blacks with low OAN, the effect of dispersion becomes more significant and must be considered. After dispersion, the resistivity is then

likely to be largely dictated by the particle size indicated by the BET and the I_D/I_G. There are no direct correlations between these individual properties and the final resistivity (Appendix B). Furthermore, it may be a coincidence that both the low and high structure carbon blacks exhibit the same trend with a decrease in BET surface area and an increase in I_D/I_G, both leading to lower resistivity. As such, further validation is required to understand the complex interplay of these properties. Additionally, the effect of high shear mixing on the I_D/I_G should be studied.

5.8 Carbon Nanotubes Feasibility Study

Carbon nanotubes (CNT) are one-dimensional graphene layers rolled into their well-known tubular shape, giving them a one-dimensional structure. This is in contrast with zero-dimensional carbon black, where a secondary structure (agglomerate or aggregate) is formed from primary particles consisting of turbostratic graphitic surfaces and amorphous cores, as shown in Figures 5.13a and 5.13b. CNT have a relatively high aspect ratio (i.e. length/diameter ratio) of 100 – 10000 compared to that of carbon black of 1 – 10. As a result, CNT, as a conductive additive, generally have lower resistivity. This allows the formation of a more interconnected conductive network at lower conductive additive content and, thus, a lower percolation threshold compared to conductive carbon black (Figure 5.13c).

CNT can be categorised as single-walled or multi-walled based on the number of graphene layers stacked within the tubular structure. They naturally exist in an "entangled" state in clusters formed of individual cylindrical strands. As such, the "deagglomeration" of CNT under shear forces can be described as the "disentanglement" of the tubular strands. This disentanglement and dispersion process is equally crucial for CNT to allow uniform distribution across the electrode. The fibrous carbon strands have high flexibility and tensile strength, and their natural dimensions make them a good selection for establishing long-range pathways in theory.

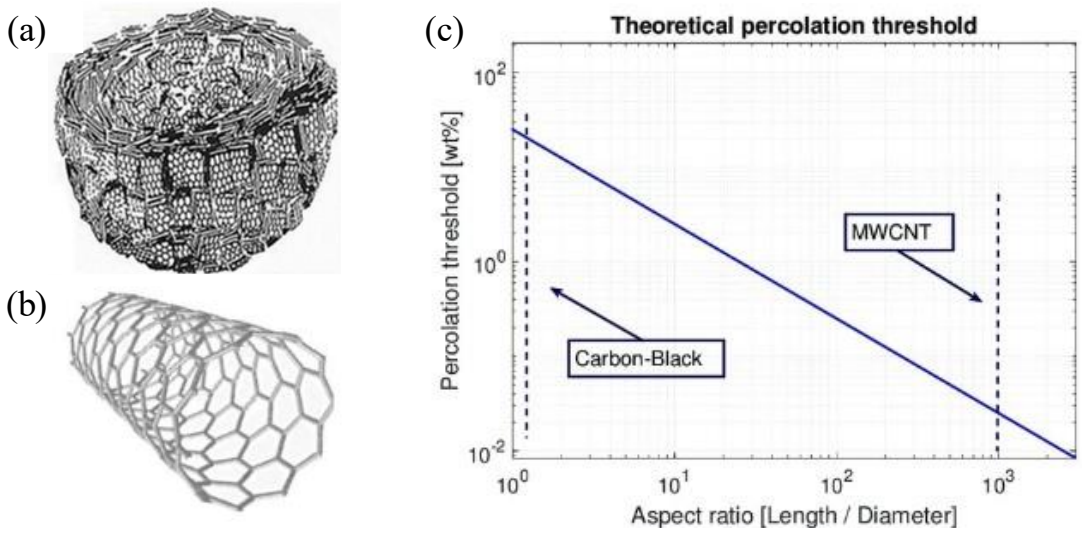

Figure 5.13: Schematic of a (a) carbon black particle, (b) carbon nanotubes and (c) comparison of the theoretical percolation threshold of carbon black and carbon nanotubes. Adapted from [156].

The surface morphologies of the resulting MWCNT-coated NMC particles are shown in Figures 5.14 and 5.15. Both samples show a distinct surface coating with CNT strands, which is different from carbon black coatings that are made up of carbon particulates, as shown in Figure 4.5 and 4.6. For samples containing CNT1015, untangled individual CNT strands can be observed across the NMC surface (Figure 5.14). Samples containing CNT3080 showed similar morphology, but it is worth highlighting the presence of clumps across the surface that are believed to be smaller structures of entangled CNT (Figure 5.15). Supplementary SEM micrographs of CNT1015 and CNT3080-coated NMC particles can be found in Appendix A.3 and A.4 respectively.

The deagglomeration and dispersion of CNT during mixing are related to their aspect ratio, which is influenced by their diameter and length. Small-diameter CNT exhibits stronger van der Waals forces between layers due to the large surface area to volume ratio. Therefore, this indicates that small-diameter CNT are less easily dispersed and require more energy to be dispersed compared to large-diameter CNT. Although small diameters have stronger attraction forces, they are, however, more prone to damage at very high shear forces, which can significantly alter their dimensions. Physical dispersion (e.g. shear mixing) can fragment CNT, making them shorter and thinner due to the peeling of the graphene layers [157].

In terms of their length, short CNT are generally easier to disperse due to reduced entanglement and their low aspect ratio. Huang and Terentjev [158] reported that MWCNT clusters exist in a crossed mesh configuration. They are subjected to van der Waals binding at contact junctions, and the binding energy largely depends on the number of contacts formed between neighbouring CNT pairs. The longer the CNT, the higher the number of contact junctions, which indicates more energy is required during dispersion to disentangle and disperse the CNT. To separate long CNT strands, it is also unavoidable that the tubular structure will also be destroyed during high-shear mixing [158].

Although CNT1015 has a smaller diameter and higher length, both of which result in less effective dispersion, the resulting CNT structures are more disentangled and dispersed. Due to very high shear forces generated during mechanofusion, CNT1015 may be more prone to breakage, resulting in the short and thin strands seen in Figure 5.14b. For CNT3080, although the ease of dispersion is higher due to its shorter length, its relatively higher diameter may provide some degree of structural benefits that retain the tubular structure of CNT, giving rise to the agglomerated structures observed in Figure 5.15b.

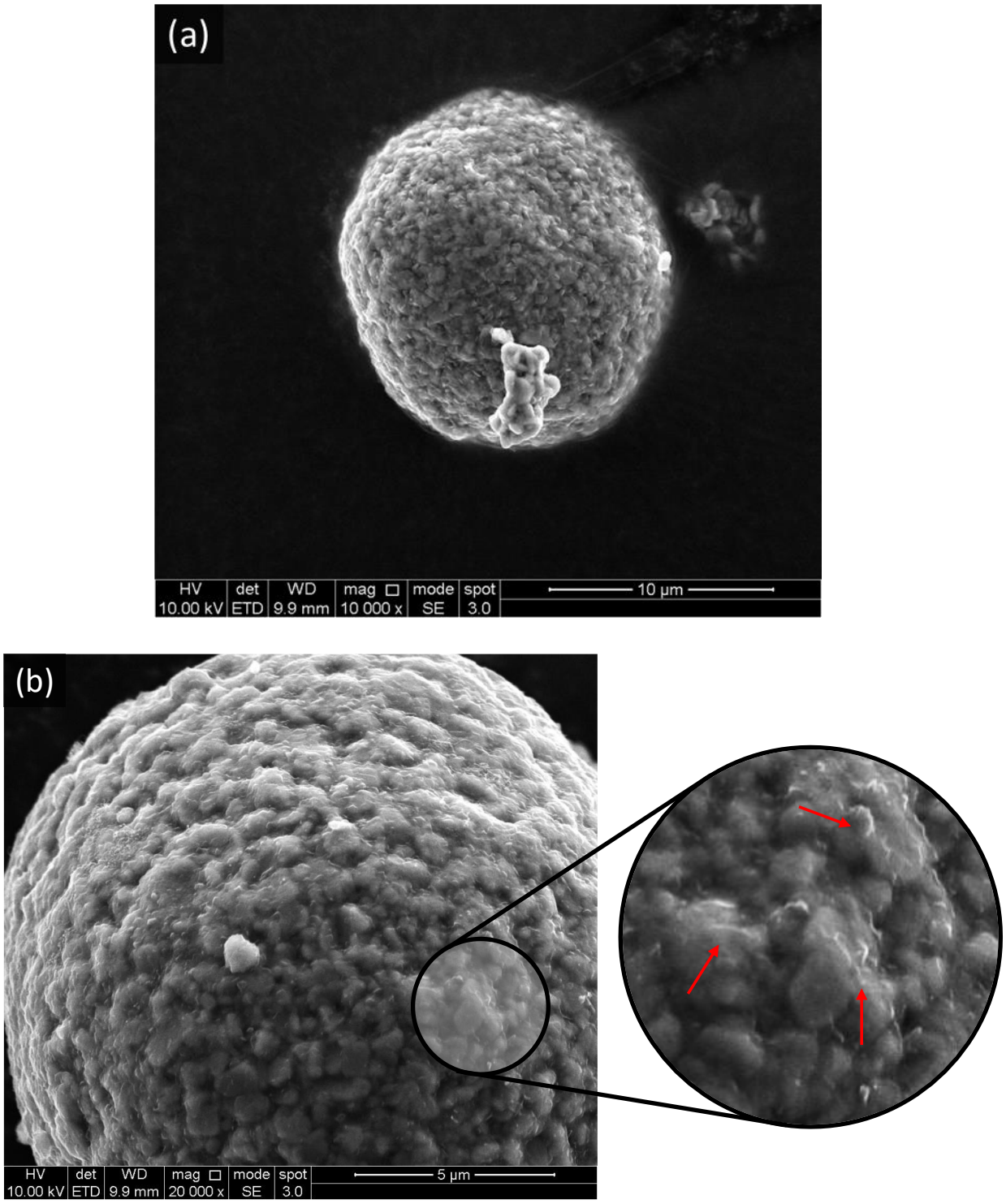

Figure 5.14: SEM micrographs of CNT1015-coated NMC (a) particle and (b) surface with visible CNT strands.

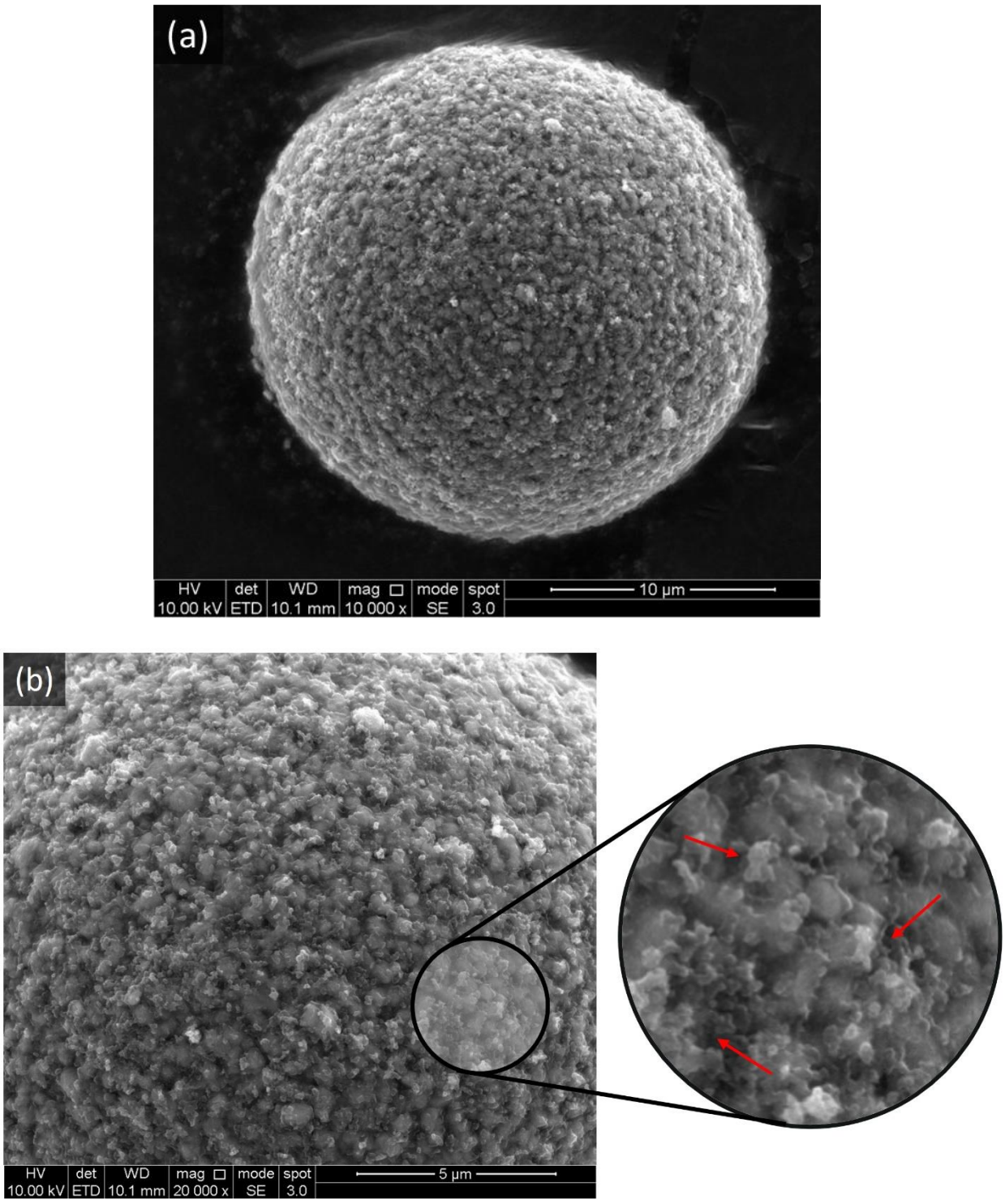

Figure 5.15: SEM micrographs of CNT3080-coated NMC (a) particle and (b) surface with visible CNT strands and aggregates.

The resistivity of powder mixtures containing NMC with C65, CNT1015 and CNT3080 is shown in Figure 5.16. Samples containing CNT showed a resistivity that is approximately one magnitude lower than that of C65. These observations are expected as CNTs are known to possess a lower resistivity compared to carbon black. For pristine MWCNT, resistivities of as low as 5 x 10^{-6} Ω cm have been reported in the literature [159], which is significantly lower than the resistivity of carbon black of 0.2 – 0.5 Ω cm [154]. Furthermore, samples containing CNT3080 showed a lower resistivity than CNT1015, which can be explained by their dimensions.

Generally, a high aspect ratio is favourable to establishing an interconnected electronic network. Initially, before mixing, CNT1015 had a higher aspect ratio than CNT3080. Based on the assumption that CNT1015 is more prone to breakage and reduction in dimensions during high shear mixing, it is expected that its aspect ratio will also decrease significantly after mixing. Whereas for CNT3080, its final aspect ratio may be relatively higher than CNT1015 after mixing. As a result, the lower resistivity of samples containing CNT3080 may be attributed to this reason. The higher aspect ratio of CNT3080 can form a more efficient network for electron movement after mixing.

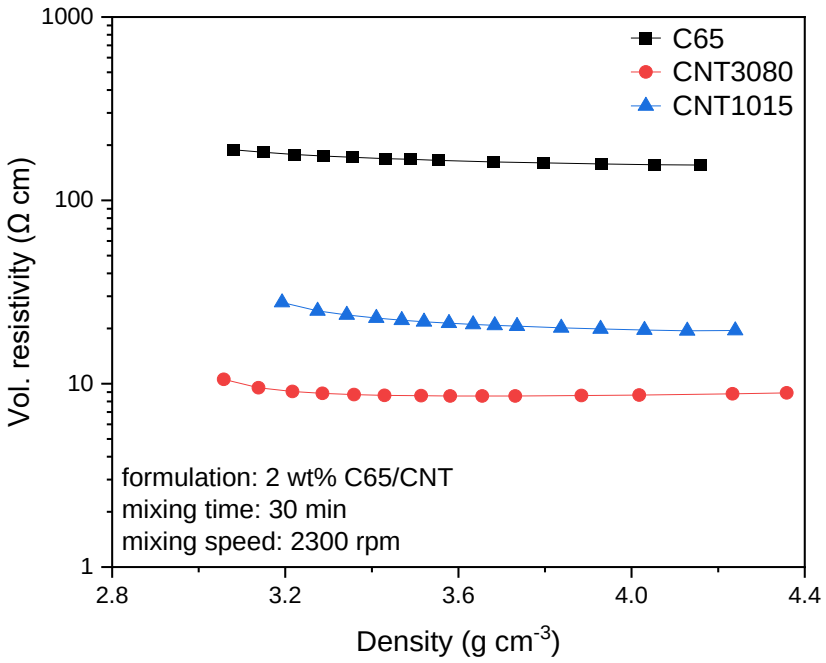

Figure 5.16: Resistivity of powder mixtures of NMC with 2 wt% of carbon black C65, carbon nanotubes CNT1015 and CNT3080 subjected to 30 min mixing.

5.9 Conclusions

Deagglomeration of carbon black involves a complex interplay of various process parameters and material properties such as carbon black loading, mixing time and speed, with the selection of appropriate characterisation methods. This chapter demonstrated the use of mechanofusion to control carbon black deagglomeration as a method of tailoring film structures for short-range electrical contacts. From the findings of this chapter, the following conclusions are drawn:

1. The deagglomeration behaviour for nano-sized carbon black C65 with micron-sized NMC622 particles is highly dependent on the energy input, which is largely dictated by the mixing time and speed. The general guidance is to provide sufficient energy to facilitate deagglomeration, but only to a certain extent, so large agglomerate structures are retained.

2. Short mixing times result in a rough coating formed of aggregates of carbon black on NMC and are generally favourable to achieving low resistivity for coated particles. The presence of the carbon black attached to the NMC surface serves as short-range contacts, while the remaining free carbon acts as "long-range" pathways. The selection of mixing speed depends on the mixing time and carbon loading. This is related to the mixing efficiency.

3. Resistivity is influenced by carbon black properties such as BET surface area, OAN and I_D/I_G. For short mixing, the final resistivity is mainly influenced by the intrinsic resistivity dictated by these properties. For long mixing, resistivity is influenced by the BET surface area and I_D/I_G for both low and high structure level carbon blacks. Additionally, for low structure level carbon black, the OAN must also be considered as dispersibility may contribute to the final resistivity. Further work is required to study the interdependency of the different properties on deagglomeration and final resistivity.

4. For non-conventional additives such as carbon nanotubes, the use of resistivity metrics to evaluate deagglomeration may be useful. A more comprehensive study of the deagglomeration mechanism of these conductive additives under intensive high-shear mixing is needed to validate this approach.

5. The resistivity measurement is only applicable if the mixing process does not negatively affect the active material. The findings also only apply to micron-sized active material and nano-sized conductive additives.

This chapter presents a different approach to characterising carbon black deagglomeration, departing from conventional metrics, such as slurry properties and cell performance, for such analysis. A more comprehensive understanding of the technical aspects associated with conductive additive dispersion can serve as guidance to improve the efficiency of the battery manufacturing process. In practical terms, for high power and energy density electrodes, only a minuscule amount (< 2 wt%) of carbon black should be used to maximise active material content. Therefore, medium to high mixing speeds with a short mixing time are preferred. However, coating formation on NMC particles can have secondary implications on slurry and electrode properties, which dictate the final cell performance. These are discussed in the next chapter, which explores the influence of these coated particles on slurry and electrode microstructures and their electronic conductivities.

Chapter 6 Designed Conductive Pathways Within Cathode Slurries and Electrodes

6.1 Introduction

Mechanofusion has been demonstrated to effectively control carbon black deagglomeration and facilitate the formation of carbon coatings on NMC. These carbon coatings function as film structures that could potentially enhance the interfacial electronic conduction on the NMC surface. This can also improve the overall conductivity of electrodes in combination with bridge structures. Powder resistivity metrics indicate that only short dry mixing is necessary for low resistivity with low carbon loadings in powder mixtures. This observation can be attributed to the optimal mix of small and large carbon structures responsible for the short and long-range electronic conduction in powder mixtures. However, the implications of these coatings extend beyond deagglomeration and could impact downstream processing and the resulting slurry and electrode properties.

Building on the understanding of carbon black deagglomeration and film structures on NMC, this chapter seeks to unravel the designed conductive pathways containing the two different electronic pathway lengths through slurry and electrode properties. By altering the carbon black content in mechanofusion dry mixing and wet slurry mixing, it is possible to control the combination of short and long-range pathways within cathodes. This approach offers an opportunity to tailor the distribution of conductive additives to promote the formation of film and bridge structures for electronic conduction. In conventional industrial practice, cathode manufacturing relies on legacy knowledge and know-how, usually developed through a trial-and-error approach due to the high sensitivity of slurry mixing to variations in process parameters and material properties. Even minor changes in formulations, such as varying carbon black loadings or altering particle properties through coating formation, can significantly affect the slurry and final electrode properties.

This chapter aims to investigate the impact of designed conductive pathways containing short and long-range electronic pathways on the formation of slurry and electrode structures. The objectives of this chapter are to:

(1) investigate the slurry conductivity resulting from the designed electronic pathways;
(2) determine the film conductivity of electrodes with designed conductive pathways;
(3) evaluate the variation in electrode structures produced using coated particles.

6.2 Experimental Design

Cathode slurries were prepared using a formulation of 96:2:2 wt% NMC622:C65:PVDF based on the standard slurry mixing SOP as described in Section 3.3. Within this formulation, 2 wt% C65 refers to carbon black that is added into the slurry mixture during wet slurry mixing. The term “free carbon” is used to refer to the carbon black available in the slurry in the context of wet mixing in this chapter. The total carbon loading chosen was 2 wt% as this loading has been well studied in the previous chapters and provides a baseline comparable with conventional slurry mixed electrodes. To prepare electrodes with varying distributions of the two electronic pathway lengths, the total carbon loading of 2 wt% was distributed accordingly across dry and wet mixing. The dry mixing conditions used for mechanofusion for all samples were 2 min / 2300 rpm, as this was the lowest powder resistivity obtained with short mixing for low carbon loadings, as demonstrated in Chapter 5. Three different theoretical ratios of short and long-range pathways within electrodes were studied. The amount of carbon black mixed in dry and wet mixing was determined based on this theoretical ratio of short and long-range pathways, respectively.

Firstly, for short-range pathway dominated formulations, all 2 wt% C65 were dry mixed with NMC using mechanofusion to form coatings that act as film structures for short-range contacts. The coated particles were used to form a slurry with no additional C65 added during wet mixing. The slurry was prepared based on the slurry mixing SOP for a 98:2 wt% formulation, as detailed in Section 3.3. For equal distribution of short and long-range pathways electrodes, the total carbon loading of 2 wt% was split equally between dry and wet mixing. 1 wt% C65 was dry mixed with NMC using mechanofusion and then subjected to a standard wet mixing process, with the remaining 1 wt% C65 added into the slurry. The slurry was prepared based on the slurry mixing SOP for a 96:2:2 wt% formulation. Lastly, for a long-range pathway dominated electrode, 0.5 wt% C65 was dry mixed with NMC using mechanofusion, with the remaining 1.5 wt% C65 added during wet mixing. Similarly, the slurry was prepared based on the slurry mixing SOP for a 96:2:2 wt% formulation. The formulations studied are shown in Table 6.1.

The experiment data sets with the amount of NMP solvent used for slurry preparation for each sample are shown in Table 6.2. The amount of NMP required was estimated through trial and error, guided by the gel behaviour of the slurry after mixing. The objective was to achieve a viscosity comparable to that of a conventional slurry of the same formulation, by visual assessment. In general, the amount of NMP used increases (i.e. lower solid concentration) with the presence of larger carbon black structures and higher free carbon content. These properties are usually achieved when a lower fraction of carbon black is dry mixed and/or when a shorter dry mixing time (i.e. 2 min) is used. For example, for equal distribution of short and long-range pathways and long-range pathways dominated electrodes, 60 % solid concentration was used for samples dry mixed for 2 min while 65 % solid

concentration was used for samples dry mixed for 60 min. For short-range pathways dominated electrodes, a solid concentration of 70 % was required to achieve a similar viscosity as the other samples, likely due to a higher degree of deagglomeration in dry mixing relative to wet mixing and the lack of free carbon within the slurry.

The electrochemical reaction mechanisms within the slurries were evaluated using electrochemical impedance spectroscopy based on the methodology described in Section 3.4.8. Additionally, the slurry electronic conductivity was also determined. For the electronic conductivity of electrodes, the four-point method was used, as detailed in Section 3.4.9.

Table 6.1: Formulations with varying distributions of short and long-range pathways for wet slurry mixing.

Formulation	Mechanofusion		Wet Slurry Mixing	Solid Concentration (%)
	Mixing Time (min)	C65 (wt%)	C65 (wt%)	
Short-range dominated (100 % mechanofusion)	2	2	0	70
	60	2	0	70
Equal distribution of short and long-range (50 % mechanofusion, 50 % slurry)	2	1	1	60
	60	1	1	65
Long-range dominated (25 % mechanofusion, 75 % slurry)	2	0.5	1.5	60
	60	0.5	1.5	65
Conventional wet mixing (100 % slurry)	-	0	2	60

Table 6.2: Experiment data sets.

Formulation	Mechanofusion			Wet Slurry Mixing			
	Mixing Time (min)	NMC622 (g)	C65 (g)	NMC622 (g)	C65 (g)	PVDF (g)	NMP (g)
Short-range dominated (100 % mechanofusion)	2	19.6	0.20	0	0	0.2	2.14
	60	19.6	0.20	0	0	0.2	2.14
Equal distribution of short and long-range (50 % mechanofusion, 50 % slurry)	2	19.6	0.10	0	0.1	0.2	3.33
	60	19.6	0.10	0	0.1	0.2	2.7
Long-range dominated (25 % mechanofusion, 75 % slurry)	2	19.6	0.05	0	0.15	0.2	3.33
	60	19.6	0.05	0	0.15	0.2	2.7
Conventional wet mixing (100 % slurry)	-	0	0	19.6	0.2	0.2	3.33

6.3 Electronic Conduction Within Slurries

6.3.1 Solvent Requirement for Slurries

During wet mixing, NMP plays a critical role, acting as a solvent to dissolve the PVDF binder and facilitate higher active material loading. Carbon black is also electrostatically stable in NMP as they are charged by a counterion from a dissociated surface group [160]. Additionally, NMP promotes the formation of a uniform and stable slurry, ensuring even distribution of all materials throughout the slurry mixture, which is critical for consistent electrode performance [79]. For a typical cathode slurry, the recommended solid concentration is approximately 64 – 66% [160]. This concentration range is ideal for the formation of flocculation bridges between the solid particles. In this scenario, the conductive additive and binder are distributed evenly within the voids between NMC particles and on the particle surfaces [160]. This distribution promotes the formation of both bridge and film structures, along with a weak flocculation network structure that enhances the dispersion uniformity and stability of the slurry.

A crucial parameter for achieving a uniform coating is the viscosity of the resulting slurry which is directly affected by the solid concentration. Due to the high surface area of carbon black particles, NMP solvent molecules adsorb onto these particles and become partially immobilised. This phenomenon creates a resistance to flow, resulting in an increase in slurry viscosity. Additionally, large carbon black structures possess a network of voids within their agglomerate structures that contribute to trapping the solvent. These partially immobilised NMP molecules also result in an overall increase in slurry viscosity.

Mechanofusion of carbon black leads to deagglomeration, which results in a decrease in the carbon black structure level and free carbon content within the powder mixture. Consequently, using a constant solid concentration of 60 % across slurries containing varying degrees of carbon black structure levels and free carbon content from mechanofusion mixing results in a significant variation in slurry viscosity. For instance, samples containing smaller carbon black structures and/or low free carbon content will yield a lower viscosity due to the decreased ability of these carbon black to trap the solvent within their voids. On the contrary, the presence of large carbon black structures and/or high free carbon content can result in a highly viscous slurry as more solvent is immobilised.

The sequence of addition of materials is also important due to the different interactions that occur during wet mixing [65], [161]. In conventional cathode slurry preparation, carbon black is first added to a pre-dissolved PVDF-NMP mixture for dispersion, forming CB-PVDF clusters within the solvent. This crucial step determines how the remaining components interact as mixing progresses. Subsequently, when NMC is added to this mixture, the CB-PVDF clusters can adsorb to the NMC surface to promote the formation of the CBD. Additionally, carbon black can also adsorb onto the NMC surface. Reynolds et al. [133] investigated the viscoelastic behaviour of slurries and found that

slurry mixtures of NMC+CB and NMC+CB+PVDF are vastly different. NMC+CB+PVDF slurries exhibit higher viscoelasticity compared to slurries containing only NMC+CB, indicating that there is a higher fraction of carbon black in the slurry that dictates its overall behaviour. PVDF was also reported to have higher preferential adsorption onto the NMC surface and may partially displace CB that is adsorbed to the NMC surface. The displaced carbon black becomes unbound, contributing to the total free carbon in the slurry and resulting in its gel-type behaviour.

For coated particles, the carbon coating alters the interactions of the NMC particles with the other slurry components. PVDF molecules can adsorb onto the carbon coating on the NMC surface but are less likely to displace the carbon black that forms the coating. Due to the high compression forces during mechanofusion, the carbon black particles have an intimate contact with the NMC surface. This close proximity of the two particles results in the carbon black particles being held by strong van der Waals forces. Consequently, the carbon coating is also sufficiently robust to withstand the high shear forces experienced during dispersion in wet mixing.

6.3.2 Impedance Response of Slurries

Electronic conduction within a cathode slurry is directly related to the spatial arrangement and distribution of the active material and conductive additives within the slurry structure. In particular, efficient particle contact between these two different particles is critical to achieving high electronic conductivity for the slurry. Through electrochemical impedance analysis, the slurry microstructure and the electrochemical interactions occurring within can be studied. A typical Nyquist plot for slurries, acquired through electrochemical impedance spectroscopy, is shown in Figure 6.1. In a conventional cathode slurry, the Nyquist plot assumes a non-uniform (uncontrolled) distribution of the active material and conductive additives within the slurry mixture.

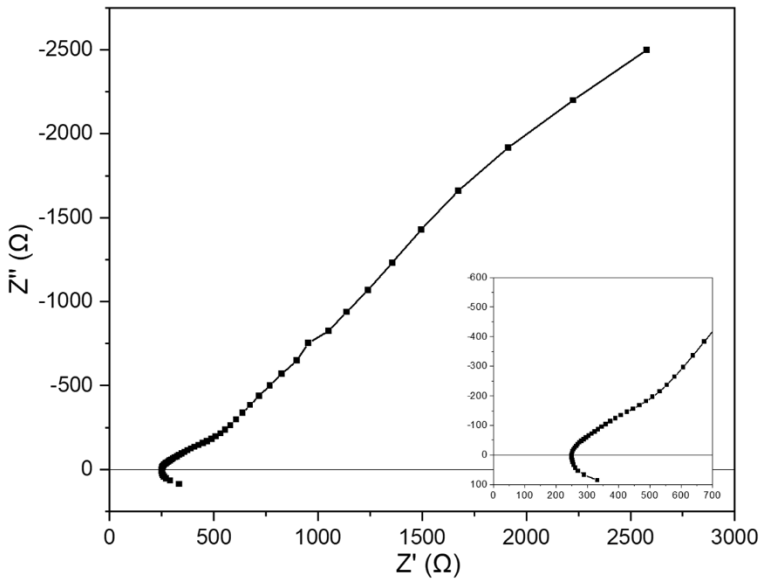

Figure 6.1: Nyquist plot of a typical NMP slurry containing an active material, conductive additive and polymeric binder. Inset figure shows the shape of the Nyquist plot at the high frequency region.

The Nyquist plot begins with a downward curve below the real Z' axis at high frequencies with a positive imaginary impedance value (Z''). This characteristic behaviour suggests the presence of inductive effects arising from the metallic elements within the experimental setup, such as the connection wires and the electrode probe itself. Following this high-frequency region, a non-zero ohmic resistance that intersects the real Z' axis is observed. This ohmic resistance reflects the overall electrochemical characteristics of the entire slurry sample, encompassing the combined resistances of the solvent solution, the particles within the slurry system and the interfacial resistances present. It provides an overall measure of the slurry's resistance.

Following the ohmic resistance, the plot typically displays two unresolved semi-circles, each corresponding to distinct resistance contributions within the slurry system. The first semi-circle is often associated with the resistance of NMC particles within the slurry, representing the inherent resistance within the particles. The second semi-circle is generally linked to the charge transfer resistance at the electrode-electrolyte interface, which can be interpreted as the particle-solvent interface in the context of a slurry. This resistance originates from the kinetic limitations involving electron transfer between the NMC particles and the ions within the solvent. Lastly, an inclined spike at low frequencies is observed, which is indicative of the solid-state diffusion of ions within the NMC particles in the slurry.

By omitting the inductance response below the real Z' axis, the Nyquist plot for a typical cathode slurry can be described using a simplified electrical equivalent circuit as shown in Figure 6.2. In this circuit, R_{Ω} represents the ohmic resistance that is associated with the bulk resistance arising from the components within the slurry system (active material, conductive additive, binder and solvent). R_p represents the resistance of electronic conductive pathways formed by the particles within the system. A constant phase element (CPE), CPE_p, is fitted in parallel to account for the behaviour of a non-ideal capacitor due to factors such as particle surface roughness and varying coating characteristics. Similarly, R_{ct} and CPE_{ct} are used to describe the charge transfer resistance and electrical double-layer capacitance respectively. CPE_{ct} accounts for the formation of the electrical double layer where ions accumulate at a region close to the interface that can influence the capacitance. Lastly, CPE_{diff} represents the solid-state diffusion that is associated with the particles within the system.

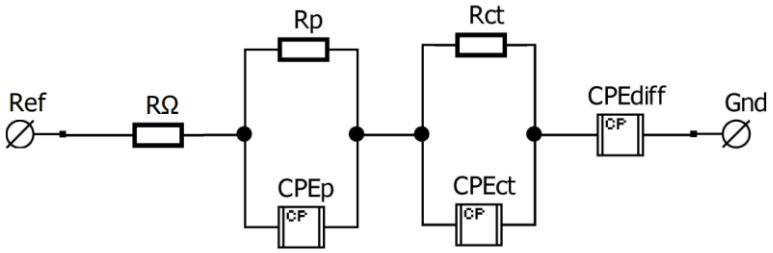

Figure 6.2: Simplified electrical equivalent circuit for a conventional slurry.

The Nyquist plot of a conventional wet mixing formulation is shown in Figure 6.3, whereas Figures 6.4 to 6.6 show the Nyquist plots of slurries containing carbon-coated NMC particles. The introduction of coated particles into the slurry results in a change in the impedance response. Firstly, for the long-range pathway dominated formulations, the Nyquist plots these formulations resemble that of a conventional slurry, exhibiting two unresolved semi-circles with a diffusion line (Figure 6.4). A rough coating with low coverage is likely present due to the relatively low amount of carbon black (0.5 wt%) used during dry mixing.

As the proportion of long-range pathways decreases to 50% for equal distribution of short and long-range formulations, the corresponding Nyquist plots in Figure 6.5 begin to show a subtle inflection point (marked by red arrows) compared to the previous two long-range pathway dominated formulations. These inflection points are associated with the charge transfer resistance. Assuming the carbon coating formed during mechanofusion is sufficiently robust to withstand wet mixing and stays intact after mixing, the formation of this additional carbon coating likely introduces a new interfacial resistance, which contributes to the overall charge transfer resistance. This new interfacial resistance is related to the pore resistance of the coating layer and also has an effect on the double-layer capacitance.

The presence of the inflection point becomes more pronounced for short-range pathway dominated formulations, as all the carbon black is dry mixed with NMC (Figure 6.6). As a result, the degree of coating increases due to the greater amount of carbon black available for dry mixing, leading to a decrease in the ratio of long-range pathways. Consequently, the second semi-circle, corresponding to the charge transfer resistance, becomes increasingly resolved.

Although it is challenging to fully resolve the semi-circle to accurately determine the values of the charge transfer resistance, the diameter of the semi-circle can serve as a rough indication of the charge transfer resistance of the slurry system. The Nyquist plots shown in Figures 6.4 to 6.6 show that as the fraction of carbon black that is added into dry mixing is increased, the diameter of the semi-circle also increases. This increase in diameter likely reflects an increase in the charge transfer resistance within the slurry systems. The charge transfer resistance originates from the interface between the particles and the solvent, where the electrochemical reaction occurs. At this interface, electrons from the NMC particles interact with the ions from the solvent. For effective electrochemical reactions to occur, electrons from the particles must be readily available at the interface to react with the incoming ions. An efficient transfer of these electrons and ions is crucial to maintain a low charge transfer resistance.

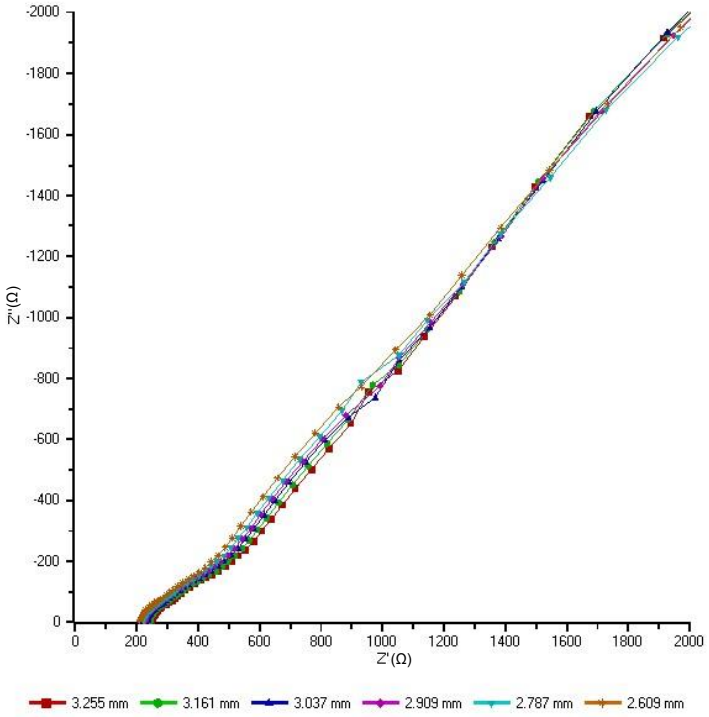

Figure 6.3: Nyquist plot of a conventional slurry prepared using wet mixing where 2 wt% C65 was added during wet mixing. Legends indicate the distance between the two contact electrodes (i.e. slurry height).

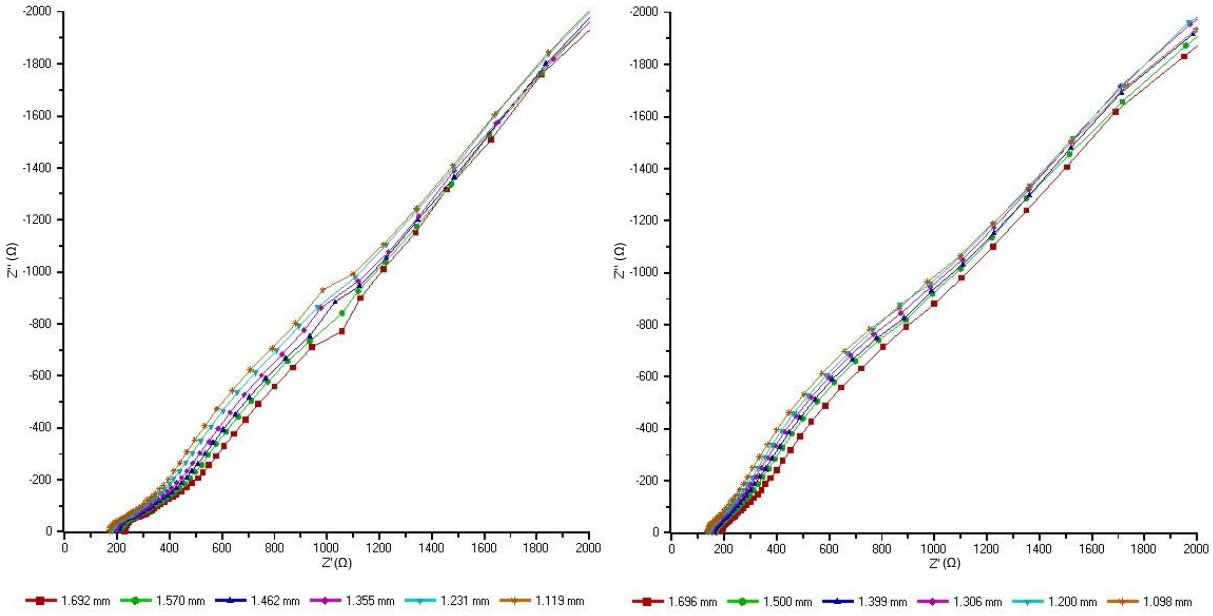

Figure 6.4: Nyquist plot of a long-range pathway dominated slurry containing 1.5 wt% C65 as free carbon added during wet mixing and 0.5 wt% C65 dry mixed with NMC for 2 min (left) and 60 min (right). Legends indicate the distance between the two contact electrodes (i.e. slurry height).

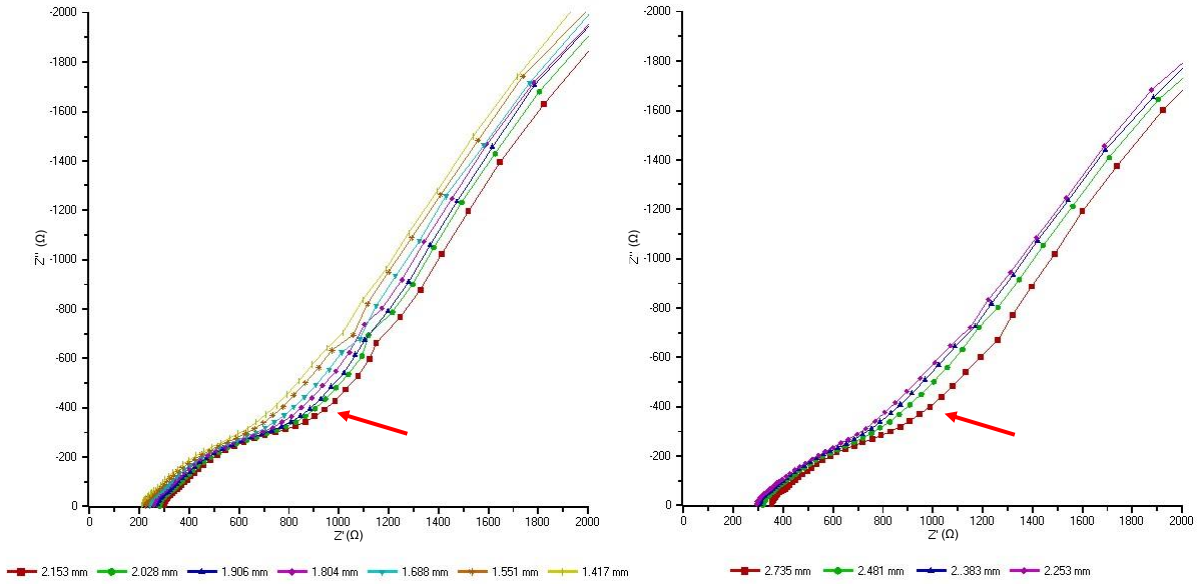

Figure 6.5: Nyquist plot of an equal distribution of short and long-range pathway slurry containing 1 wt% C65 as free carbon added during wet mixing and 1 wt% C65 dry mixed with NMC for 2 min (left) and 60 min (right). The inflection points are indicated by red arrows. Legends indicate the distance between the two contact electrodes (i.e. slurry height).

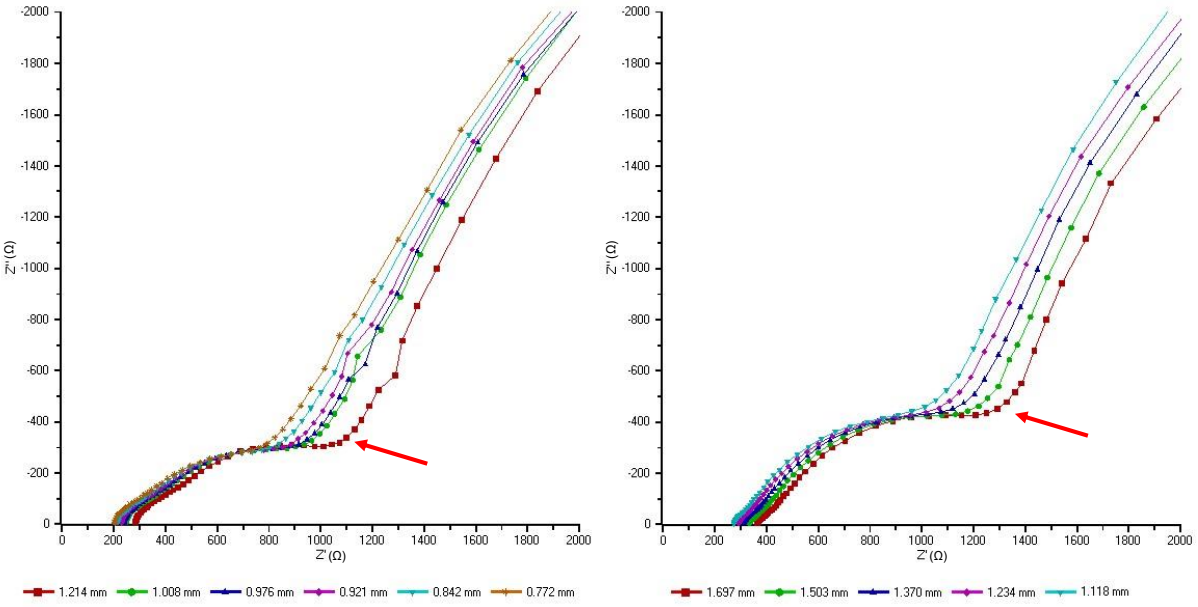

Figure 6.6: Nyquist plot of a short-range pathway dominated slurry containing 0.5 wt% C65 as free carbon added during wet mixing and 1.5 wt% C65 dry mixed with NMC for 2 min (left) and 60 min (right). The inflection points are indicated by red arrows. Legends indicate the distance between the two contact electrodes (i.e. slurry height).

The presence of a coating layer creates a physical barrier for both ions and electrons (Figure 6.7). Due to the variability in coating characteristics, including the differences in coating porosity, the coating presents a more complex pathway for electron and ion movement. Ions are required to travel a longer and more tortuous path before reaching the active sites on the particle surface. Similarly, electrons are also forced to travel an extended pathway as they move through the particle, followed by the coating layer. However, the impact of the coating layer on ions and electrons may differ.

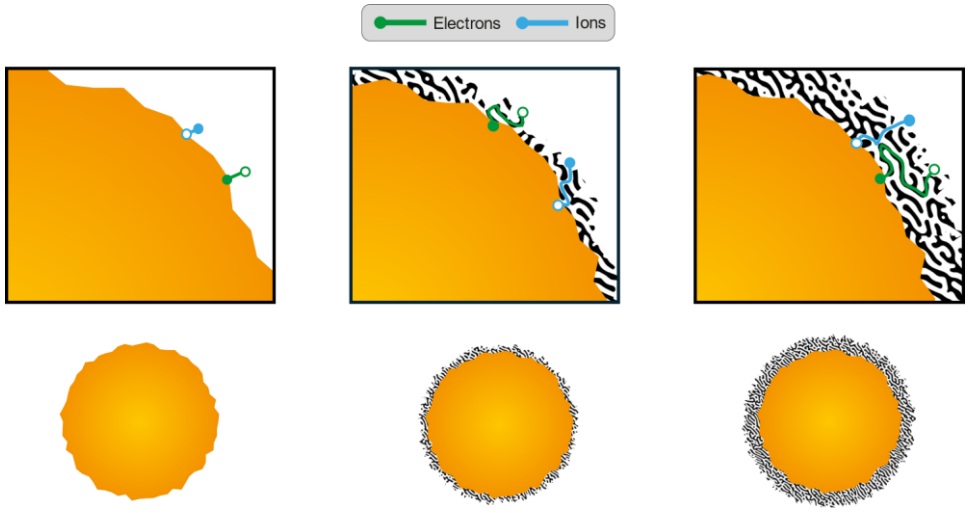

Figure 6.7: Schematic depicting the change in pathway length for electron and ion movement with increasing coating thickness.

Carbon black is a highly conductive material that can help mitigate the hindrance of electron transfer due to its inherent conductivity. Thus, the effect on electronic conduction is less pronounced due to the ease of electron movement through the conductive coating layer. Additionally, the surface area of the NMC that is in contact with the solvent varies due to the different degrees of carbon black deagglomeration and coating. With coating formation, it is likely that the contact surface area of NMC with the solvent is low, which can further complicate charge transfer.

The main challenge lies with ionic conduction, as the coating layer exhibits significantly lower ionic conductivity compared to the solvent. This disparity in ionic conductivity leads to the accumulation of ions which results in a concentration gradient that affects the driving force for electron flow towards the particle-solvent interface. The driving force for electron movement is the potential difference, which drives electrons from high to low potential towards the interface to react with ions, facilitating the charge transfer reaction. A high concentration of ions near the interface can partially neutralise the potential difference due to the formation of an electrical double layer caused by the presence of a high excess positive charge. The double layer reduces the overall potential gradient, decreasing the likelihood of electrons flowing towards the interface and participating in the charge transfer reaction. Ultimately, this results in increased charge transfer resistance.

6.3.3 Slurry Conductivity

The ohmic resistance, representing the overall resistance of the slurry, can be determined from the intersection of the Nyquist plot with the real Z' axis. The slurry conductivity is then calculated using Equation 3.7. Figures 6.3 to 6.6 show that as the slurry height decreases, the intersection point on the real Z' axis also decreases, causing the overall impedance response to shift to the left. This shift indicates that as the slurry height decreases, the distance over which the current must travel through the slurry is reduced. According to Ohm's law and as demonstrated in Equation 3.7, a decrease in distance (L) results in a corresponding decrease in resistance (R), as expressed in Equation 6.1:

$$R_{HF} = \frac{1}{\sigma}\frac{L}{A} \tag{6.1}$$

The conductivity of slurries is presented in Table 6.3. Overall, the slurry conductivity increases with the addition of carbon black in wet mixing, as the free carbon content within the slurry increases. This results in an increase in the theoretical long-range electronic pathways, where higher free carbon content promotes the formation of CB-PVDF clusters that establish an interconnected conductive network within slurries. For slurry samples containing NMC particles dry mixed with C65, those dry mixed for 60 min exhibited higher conductivity compared to those mixed for only 2 min. This finding contrasts with the trend observed in binary powder mixtures of NMC and CB, where powder conductivity for samples dry mixed for 60 min is lower than those mixed for 2 min. This difference is largely due to the absence of large carbon black structures essential for long-range conduction. The discrepancy suggests for a slurry system, large carbon black structures are less critical to forming conduction pathways, and the presence of carbon coatings on NMC particles enhances electron transfer.

Table 6.3: Electronic conductivity of slurries containing 2 wt% C65 with varying distributions of short and long-range pathways.

Slurry Formulation	Mechanofusion Mixing Time (min)	Slurry Conductivity (mS m^{-1})
Short-range dominated (100% mechanofusion)	2	5.36 ± 0.35
	60	6.16 ± 0.25
Equal distribution of short and long-range (50% mechanofusion, 50% slurry)	2	9.35 ± 0.35
	60	10.94 ± 0.06
Long-range dominated (25% mechanofusion, 75% slurry)	2	10.23 ± 0.61
	60	10.38 ± 1.09
Conventional wet mixing (100% slurry)	-	17.26 ± 0.75

For powders, the formation of conductive pathways is influenced by the spatial arrangement of particles and the interparticle contact within the binary powder mixture. The higher conductivity observed in slurries containing samples dry mixed for 60 min indicates that conductivity is not solely dependent on the interparticle contact between NMC and CB. PVDF adsorbs to NMC and also carbon black to form CB-PVDF clusters. However, these clusters may not significantly enhance electronic conduction unless they are in close proximity to NMC particles or make contact with other clusters within the slurry. Thus, in a slurry system, conductive pathways rely not only on NMC particle-particle contact but also on the interaction between CB-PVDF clusters and NMC particles. Furthermore, the deposition of PVDF on NMC particles, or on the carbon coating on NMC, creates an insulating polymer shell, which can impede electronic conduction.

The slurry conductivity for a conventional wet mixing formulation is 17.26 mS m^{-1}. This value assumes a non-uniform distribution of carbon black in the slurry, with a smaller fraction of carbon black deposited on the NMC surface, similar to that demonstrated in Section 4.3. A higher fraction of carbon black is suspended in the slurry as CB-PVDF clusters, which enhances long-range electronic conduction. Since PVDF has high preferential adsorption to NMC, it promotes closer proximity between these clusters and the NMC surface. Consequently, the overall slurry conductivity is primarily dictated by these clusters, analogous to bridge structures dictating the conductivity of electrodes. These clusters form a more interconnected conduction network within the slurry system compared to the carbon black directly deposited on the NMC surface, which requires a high degree of particle-particle contact for electronic conduction.

As the fraction of carbon black dry mixed with NMC prior to slurry mixing increases, the free carbon content within the slurry decreases. For long-range pathway dominated formulations, both slurries with samples dry mixed for 2 and 60 min showed a similar conductivity of 10.23 and 10.38 mS m^{-1} respectively. The comparable values suggest that the free carbon within the slurry remains the dominant factor controlling overall conductivity, as the free carbon content is significantly higher than that for dry mixing. Therefore, the variations in the carbon coating resulting from different dry mixing times are not apparent, and the overall conductivity is largely unaffected. For a long-range pathway dominated formulation, the relatively high free carbon content results allow for more PVDF adsorption to form CB-PVDF clusters. The low coating coverage of carbon black on the NMC surface facilitates increased PVDF adsorption onto the NMC surface. Adsorption onto the uncoated NMC surface can partially displace carbon black that was deposited during wet mixing, redistributing it back into the slurry.

For formulations with equal distribution of short and long-range pathways, the total carbon loading of 2 wt% was divided equally between dry and wet mixing. The slurry conductivity with samples dry mixed for 2 min is 9.35 mS m^{-1}, whereas that of samples dry mixed for 60 min is 10.94 mS m^{-1}. The

discrepancy in conductivity values suggests that an increase in the fraction of carbon black in dry mixing enhances the impact of short-range electrical contacts. It is known that for a binary powder mixture of NMC and C65, mixing for a longer period of time results in a higher degree of deagglomeration, which reduces the free carbon after mixing and produces smaller free carbon black structures. However, this also leads to an increase in the amount of carbon black adhering to the NMC surface as a conductive carbon coating. The higher slurry conductivity for the 60 min samples suggests that the carbon coating around NMC particles is beneficial to establishing electronic pathways within a slurry system. This is due to the decrease in free carbon content in wet mixing, which reduces the formation of long-range pathways, making the carbon coating more efficient in facilitating electronic conduction. This increased ease in establishing conductive pathways contrasts with the 2 min samples, where larger carbon black structures and more free carbon are retained after dry mixing but with a lower degree of coating of carbon black on the NMC surface. While the free carbon after dry mixing can contribute to cluster formation, their small structures limit the cluster sizes and their ability to form extensive conduction pathways.

For formulations designed to have an equal distribution of short and long-range pathways, PVDF can adsorb to both the free carbon black within the slurry and the carbon coating on the NMC surface. Since a higher degree of coating is achieved for samples mixed for 60 min compared to 2 min, more carbon black is coated onto NMC. This may increase the probability of PVDF adsorption onto the surface of these carbon-coated NMC particles. However, the higher conductivity for 60 min samples shows that a higher coating coverage enhances electron transfer even though there is an increased probability of forming the insulating layer on the carbon coating surface. The competition for PVDF between the carbon coating and the free carbon black can help limit the formation of the insulating barrier. Therefore, the combination of a conductive carbon coating on NMC particles and the competition for PVDF resulting in less adsorption on carbon coating overall enhances conduction. The presence of the CB-PVDF clusters formed from the free carbon can also contribute to the overall conductivity.

For short-range pathway-dominated formulations, the difference in slurry conductivity between samples dry mixed for 2 min and 60 min becomes more pronounced. The slurry conductivity with samples dry mixed for 2 and 60 min is 5.36 mS m^{-1} and 6.16 mS m^{-1} respectively. This lower conductivity compared to other formulations is due to the substantial reduction in free carbon within the slurry. A large fraction of the carbon black is coated onto the NMC surface as all carbon black is added in dry mixing. Without any additional free carbon added during wet mixing, PVDF predominantly adsorbs onto the carbon coating on NMC particles. This results in an insulating polymer shell that impedes electron transfer and thus reduces the slurry conductivity. The effective formation of conductive pathways in this system depends on both NMC particle-particle contact and the presence of the small CB-PVDF clusters near the NMC surface. The low free carbon content after

dry mixing and smaller carbon black structures result in fewer clusters and smaller cluster sizes, further limiting conductivity. Conversely, for samples mixed for 60 min, the high carbon coating coverage enhances electronic conduction. Although the number of clusters available is low, the increased probability of NMC particle-particle contact through the conductive coating is higher, which facilitates better conduction and results in higher conductivity.

6.4 Electronic Conduction Within Electrodes

6.4.1 Implications of Coated Particles on Electrode Formation

From the previous section, it is evident that the formation of a carbon coating on NMC particles significantly influences both the mixing interactions and resulting slurry microstructure, thereby affecting the slurry conductivity. Consequently, this alteration impacts the final electrode microstructure and associated CBD structures. The high surface area of carbon black relative to NMC particles leads to increased adsorption of PVDF onto carbon black particles. When PVDF adsorbs onto carbon black particles that are immobilized as coatings on the NMC, there is a reduction in the PVDF available for adsorption onto the free carbon in the slurry. This change in PVDF availability affects the slurry viscosity, as evidenced by the requirement for different solid concentrations to achieve stable viscosity in samples with varying carbon black structures and free carbon content, as discussed in Section 6.2.

The drying process of slurries also plays a crucial role in shaping the final electrode microstructure, particularly in the formation of the CBD, which can significantly impact electronic conductivity. A primary concern during drying is the occurrence of carbon binder migration. NMP is removed from the slurries through solvent evaporation to form a solid electrode film. PVDF binder molecules that are dissolved within the solvent migrate upwards, along the direction of solvent flow, and accumulate in the upper region of the electrode. Since PVDF binder molecules are adsorbed to the free carbon to form CB-PVDF clusters within the slurry, solvent drag can also result in the migration of carbon black particles. In an initially homogenous slurry, this can introduce homogeneity into the final electrode microstructure, potentially leading to a carbon-poor region at the bottom of the electrode as the carbon black migrates upwards. This uneven distribution of the slurry components can further destabilise the slurry suspension and lead to sedimentation of the heavier NMC particles, further contributing to electrode homogeneity.

During drying, the slurry undergoes aggregation, where the particles, binder and solvent coalesce to form a semi-solid state [39]. As solvent evaporation progresses, a solid layer forms at the top of the coated slurry film. This consolidation layer continues to grow as solvent evaporation continues, during which carbon binder migration takes place. Eventually, the film shrinks further, and any remaining solvent in the pores is removed. The final solid electrode is formed as all the components, originally within the wet film, come into contact. During solvent evaporation, capillary effects can

occur where surface tension draws the remaining solvent, along with the CB-PVDF clusters, into the small voids between the NMC particles. Upon the completion of the drying process, the presence of these clusters is essential to the formation of bridge structures between the voids of NMC particles. Variations in PVDF adsorption behaviour and the final location where PVDF is adsorbed can influence the drying process, affecting the overall conductivity of the electrode film. This phenomenon is explored in subsequent sections, where the influence of coated particles on PVDF adsorption and the final electrode conductivity is investigated.

6.4.1 Four-Point Method for Electrode Film Conductivity

The four-point method measures the in-plane conductivity of the electrode film. The in-plane conductivity refers to the current that travels parallel to the surface of the electrode film, providing insights into the distribution of the conductive pathways across the plane [49]. However, this method was originally developed to investigate the conductivities of thin films with thicknesses of less than 1 μm [162]. For electrode films with a thickness significantly greater than 1 μm, the measured conductivity represents the conductivity of the upper region of the electrode.

The four-point method is more sensitive to the compositional changes in conductive additives along the parallel direction of the electrode. The measured conductivity can vary based on the electrode area in contact with the contact probes. Although this technique does not fully capture the through-plane conductivity of the electrodes, it still provides a useful comparative analysis between electrodes of different formulations to study the CBD structures and conductive pathways formed within the electrodes. Such comparative analysis can provide insights into the formation and distribution of the CBD structures within the electrode and their influence on the overall conductivity.

Since the CBD distribution can vary across the plane parallel to the film, measurements were taken at five different positions on a single electrode film. The probes are typically in contact with the centre of the electrode film. The electrode film was then rotated to ensure that the probes were in contact with different areas of the electrode. The respective film conductivities determined using the four-point method are shown in Table 6.4.

For comparison purposes, the film conductivity of a conventional long-range dominated electrode with 1 wt% C65 was also provided as 1.0 S m^{-1} (measured by Dr Xuesong Lu, University of Sheffield). Additionally, to discuss the electrode and CBD structures formed, an SEM micrograph of a conventional 2 wt% C65 electrode is also provided in Figure 6.8 (supplementary SEM micrographs provided in Appendix A.5). This approach allows for a more detailed understanding of how the conductive additives and the corresponding CBD structures are distributed within the electrode and is crucial for optimising the electrode design and performance with these coated active materials.

Table 6.4: Electronic conductivity of electrodes containing 2 wt% C65 with varying distributions of short and long-range pathways.

Electrode Formulation	Mechanofusion Mixing Time (min)	Film Conductivity ($S\ m^{-1}$)
Short-range dominated (100 % mechanofusion)	2	0.050 ± 0.008
	60	0.010 ± 0.001
Equal distribution of short and long-range (50 % mechanofusion, 50 % slurry)	2	0.289 ± 0.054
	60	0.356 ± 0.056
Long-range dominated (25 % mechanofusion, 75 % slurry)	2	1.168 ± 0.150
	60	1.653 ± 0.309
Conventional wet mixing (100 % slurry)	-	2.206 ± 0.350

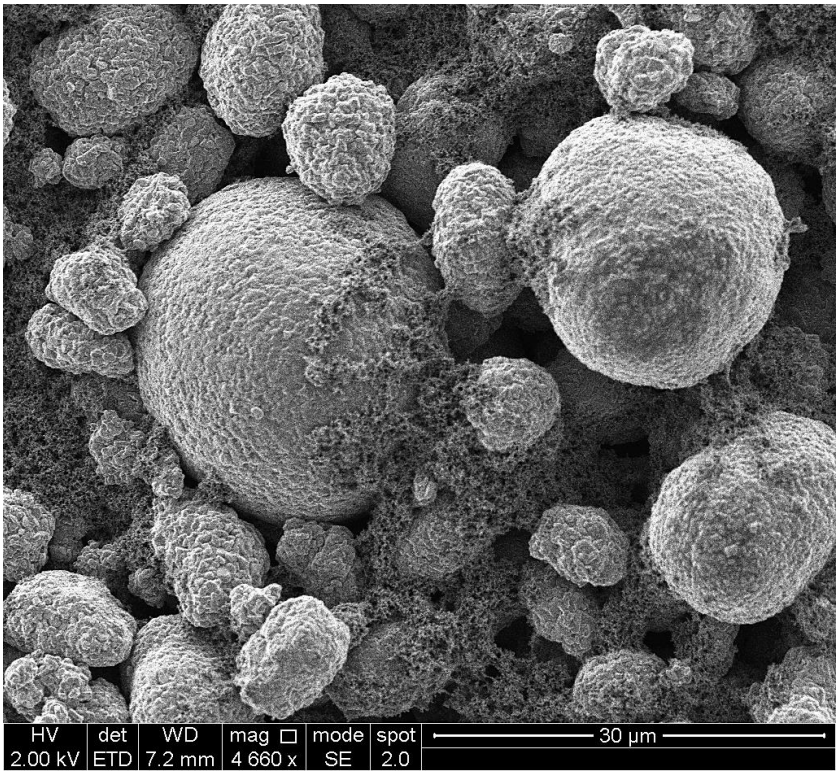

Figure 6.8: SEM micrograph (top view) of a conventional wet slurry mixed electrode with 2 wt% C65.

6.4.3 Short-Range Pathway Dominated Electrodes

The film conductivities for electrodes with short-range pathway dominated structures reveal a poor electronic conduction network within electrodes. Electrodes containing samples dry mixed for 2 min and 60 min showed film conductivities of 0.05 and 0.01 S m^{-1} respectively. These values are significantly lower compared to a conventional wet slurry mixed electrode with an identical carbon loading of 2 wt% C65, which exhibits a conductivity of 2.206 S m^{-1}. For both these samples, all 2 wt% of C65 was dry mixed, leading to deagglomeration and a fraction of carbon black participates in coating formation onto NMC to form the film structure. The remaining free carbon black after wet mixing exists as smaller structures and is further dispersed during wet mixing.

The immobilised carbon black on the NMC surface does not contribute to gel formation, as demonstrated in Section 4.7.2 and supported by several studies where carbon-coated NMC particles exhibit behaviour similar to pristine NMC particles [42], [133]. SEM micrographs (Figure 6.9) reveal that most of the NMC particles exhibit a similar surface morphology, characterised by a rough coating with small carbon black structures. In contrast to conventional electrodes, the typical framboidal texture of the NMC particle surface is no longer visible. This may indicate that the film structures on NMC particles established by mechanofusion have better coverage and distribution. However, this carbon coating may not be entirely beneficial as PVDF adsorption can result in an insulating polymer shell around the carbon coating [42]. This insulating layer blocks electron transfer between the surrounding electronic networks and other coated NMC particles.

The low conductivity of short-range pathway dominated electrodes indicates that conduction is still possible, but there is a lack of an interconnected electronic network within the electrode structure. The unbound carbon from mechanofusion acts as the free carbon during wet mixing, which may facilitate the formation of bridge structures to a certain degree. There are two mechanisms for electronic conduction within the short-range pathway dominated electrode structures. Firstly, the bridge structures formed from the low free carbon content can contribute to electron movement. These bridge structures are less effective as they only appear in certain regions of the electrodes to connect NMC particles. In addition, electron movement can also be facilitated by the carbon black on the NMC surface (i.e. film structures), where the carbon coating is not fully covered by the insulating binder layer. For film structures, NMC particles must be in contact with each other for electron conduction or in close proximity for electron hopping to occur. SEM micrographs of these electrodes further confirm that there are very few bridge structures present compared to a conventional electrode. The bridge structures are also relatively small and span across one or two NMC particles (Figure 6.9a). This is in contrast with conventional electrodes, where the bridge structures are much more complex and span across several NMC particles with a high coverage on the particle surfaces (Figure 6.7).

When NMC and C65 are subjected to prolonged mechanofusion mixing at 60 min, a higher degree of deagglomeration is achieved, resulting in free carbon with small structures. The lower number and smaller size of CB-PVDF clusters formed in the slurry results in a lower probability of forming bridge structures for long-range conduction. Even though some bridge structures might be present, they do not significantly improve electronic conductivity due to their inability to connect NMC particles to form an efficient conduction network. This explains the variation of conductivity where samples mixed for 60 min exhibit lower conductivity than those mixed for 2 min. This is also supported by the lack of visible bridge structures in these electrodes in the SEM micrograph shown in Figure 6.9b. Supplementary SEM micrographs can be found in Appendix A.6.

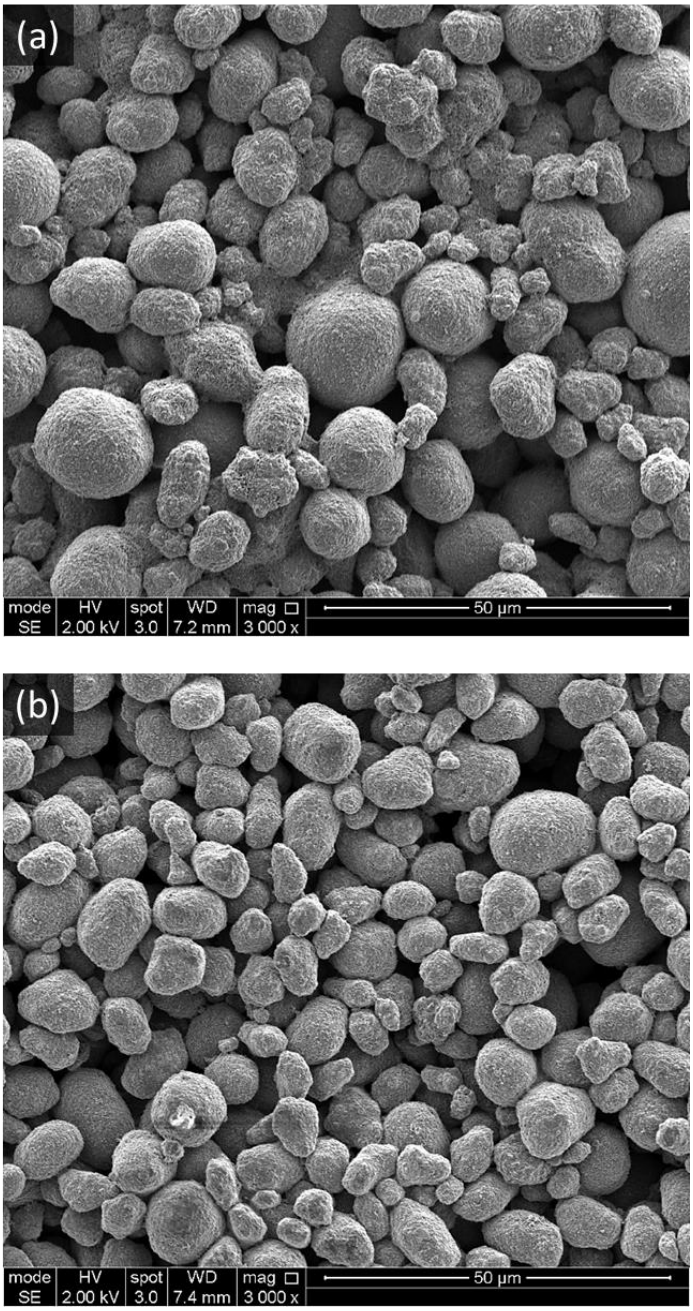

Figure 6.9: SEM micrograph (top view) of short-range pathway dominated electrodes containing NMC particles dry mixed with 2 wt% C65 for (a) 2 min and (b) 60 min.

6.4.4 Equal Distribution of Short and Long-Range Pathway Electrodes

As the fraction of carbon black added to wet mixing increases to 50%, a slight increase in the electronic conductivity of electrode films is observed. Electrode films with samples dry mixed for 2 and 60 min showed conductivities of 0.29 and 0.36 S m^{-1} respectively. Within this formulation, a decrease in carbon content for mechanofusion (1 wt% C65) likely leads to relatively lower coverage and smaller free carbon structures compared to that in short-range dominated formulations. This is due to the increased specific energy input experienced by the lower number of carbon black particles during mechanofusion. Additionally, the increase in free carbon content in wet mixing increases the ability to form bridge structures. Therefore, it is expected that the conductivity of the NMC particles will be enhanced with carbon coatings, and the increase in bridge structures will improve the overall electrode conductivity.

For samples dry mixed for 2 min, the coating is expected to be less distributed, while free carbon structures are relatively large due to less deagglomeration. Free carbon can, therefore, attach to the uncoated NMC surface during wet mixing. Since PVDF has higher preferential adsorption for NMC, it can adsorb to the NMC surface to displace these carbon black back into the slurry to increase the total free carbon available for CB-PVDF cluster formation. The PVDF can also interact with the carbon black coating on the NMC surface but does not affect the total free carbon content in the slurry. The carbon black displacement by PVDF on the NMC surface should theoretically result in a higher probability of forming bridge structures and, eventually, an interconnected electronic network. However, this is not entirely the case, as indicated by the low electrode film conductivities.

SEM micrographs of samples dry mixed for 2 and 60 min show that when 1 wt% C65 is added during wet mixing, the resulting electrodes begin to exhibit an increase in bridge structures (Figure 6.10). However, these bridge structures are only found in certain regions, indicating an uneven distribution or insufficient bridge structures established for an interconnected network. These SEM micrographs also highlight the substantial difference in the size and distribution of the bridge structures. For samples dry mixed for 2 min, bridge structures are relatively large and concentrated in specific regions, rather than spread across the entire field of view (Figure 6.10a). Conversely, Figure 6.10b shows that smaller bridge structures are obtained with samples dry mixed for 60 min, with a better distribution of bridge structures across the whole field of view. This is likely the reason why a slightly higher conductivity was obtained for these samples. The improved distribution of bridge structures can better facilitate electronic conduction across the entire electrode structure. The difference in size and distribution of these bridge structures is also related to the degree of deagglomeration of carbon black particles caused by mechanofusion, as discussed in Section 6.4.3. Smaller carbon black structures from prolonged dry mixing, followed by further dispersion in wet mixing can result in the formation of small CB-PVDF clusters but in higher numbers. This then results in small bridge

structures with better distribution across the electrode structure upon drying. Supplementary SEM micrographs can be found in Appendix A.7.

Although these electrode films show an increase in conductivity compared to the short-range pathway dominated electrode films, their conductivities are still very low. The total carbon content of these electrode films is 2 wt%, with an equal loading of 1 wt% C65 added during both dry and wet mixing. For a similar conventional wet slurry mixed electrode, where the total carbon content of 1 wt% is added during wet mixing as free carbon, the conductivity is 1.0 S m^{-1}. This shows that these electrode films still have a significantly lower conductivity compared to a conventional electrode. This difference in conductivity further confirms that the carbon-coated NMC particles influence the interactions between the components in wet mixing and the subsequent CBD formation. It also shows that the bridge structures formed are not as efficient as those in conventional electrodes.

The competition for PVDF between the carbon coating and free carbon within the slurry may result in a more localised distribution of the PVDF, which is mainly concentrated either on the carbon coating on the surface of NMC particles or with the free carbon within the slurry to form carbon black-PVDF clusters. With increased coating coverage, the inability of PVDF to adsorb onto the NMC surface also results in the decreased proximity of the CB-PVDF clusters with NMC particles. Since there is less PVDF available to adsorb to the free carbon, the extent of carbon migration is also affected. Although this may be beneficial to the homogeneity of the electrodes, the bridge structures present within the electrode, formed from these clusters, are likely not localised next to the NMC surface.

Solvent evaporation does not affect these immobilised carbon black particles on the NMC surface. Only the free carbon migrates together with the adsorbed PVDF dissolved within the solvent. As such, the decreased availability of PVDF to form CB-PVDF clusters may result in a decreased amount of these clusters available to be drawn towards the voids between NMC particles by capillary action. Consequently, this results in fewer bridge structures within the voids to connect NMC particles upon drying. Ultimately, the lack of sufficient bridge structures between NMC particles and the insulating layer on the coated NMC particles limits the ability for electron movement and overall results in low electrode conductivity.

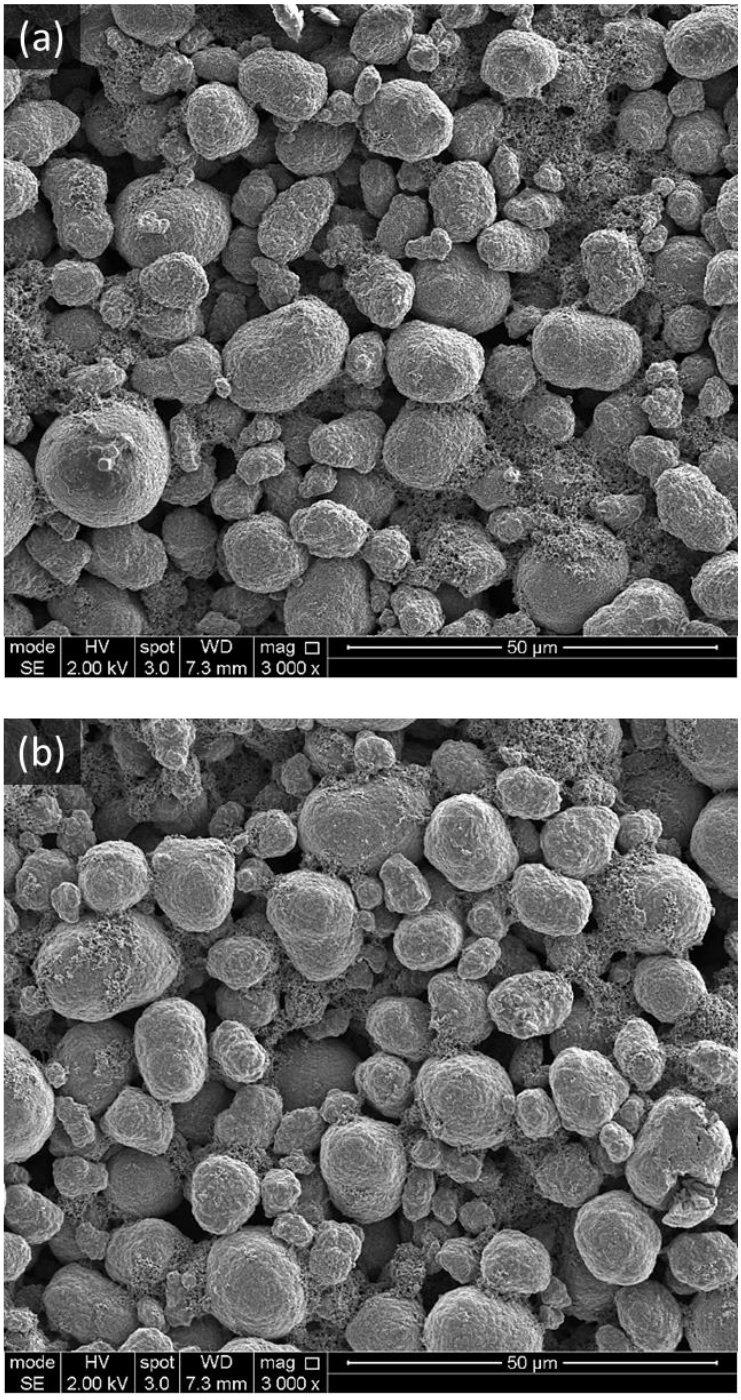

Figure 6.10: SEM micrographs (top view) of equal distribution of short and long-range pathway electrodes where 1 wt% C65 was dry mixed with NMC622 for (a) 2 min and (b) 60 min. The remaining 1 wt% of C65 was added during wet mixing.

6.4.5 Long-Range Pathway Dominated Electrodes

The electrode conductivity and structural characteristics observed from the previous two formulations with designed conductive pathways suggest that while a conductive carbon coating may be beneficial to electron conduction, the presence of free carbon during wet mixing is crucial for establishing long-range electronic conduction. For electrodes with a long-range pathway dominated formulation, a large increase in the film conductivity was observed when the free carbon content was increased to 1.5 wt%. Specifically, electrodes with samples dry mixed for 2 min exhibited a conductivity of 1.168 S $m^{-1,}$ whereas electrodes with samples dry mixed for 60 min showed a substantial increase in conductivity to 1.653 S m^{-1}.

SEM micrographs of these electrodes reveal a significant increase in the characteristic "fluffy, sponge-like" CBD structure observed in a conventional wet slurry mixed electrode (Figure 6.11). The typical framboidal texture of the NMC surface is also more apparent in these electrodes, indicating a reduced carbon coating coverage on the NMC surface due to the lower carbon loading for dry mixing. Based on the SEM micrographs, there are no substantial differences in the distribution and size of the bridge structures that can be identified by visual inspection compared to a conventional electrode. However, the higher electrode conductivity with samples mixed for 60 min can be attributed to a similar rationale where a higher coating coverage can enhance the electronic network. Supplementary SEM micrographs can be found in Appendix A.8.

As the coating coverage increases, the likelihood of contact with the conductive coating is also higher, leading to an increase in conductivity. This improvement is due to an increased probability of bridge structures establishing contact with the conductive coating instead of the uncoated NMC surface, which exhibits lower conductivity. Similarly, with a rough coating, PVDF has a higher probability of interaction with the NMC surface during wet mixing due to less coating coverage. This allows a higher fraction of free carbon attached to the NMC to be displaced back into the slurry.

Despite observed improvements in the electronic conductivity with increased free carbon content, the conductivities of these electrodes remain lower than that of a conventional electrode, which exhibits a conductivity of 2.206 S m^{-1}. This discrepancy can be attributed to the availability of free carbon influencing the adsorption behaviour of PVDF during slurry mixing and subsequent drying behaviour, as discussed previously. Thus, even a small fraction of carbon coating on NMC particles can result in this effect.

While the increase in bridge structures does enhance the electronic conductivity, the benefits of short-range contacts are not fully realised due to the non-uniform distribution of carbon black on the rough coating. This non-uniform distribution might impede the establishment of an interconnected network, as the bridge structures need to be in contact with regions where the rough carbon coating is present to benefit from enhanced short-range conduction. Given the lower free carbon content compared to

conventional electrodes, the bridge structures must therefore be in direct contact with the film structures to maintain the electronic network. However, the probability of achieving optimal contact between the bridge and film structures is currently uncontrolled, leading to suboptimal conductivity.

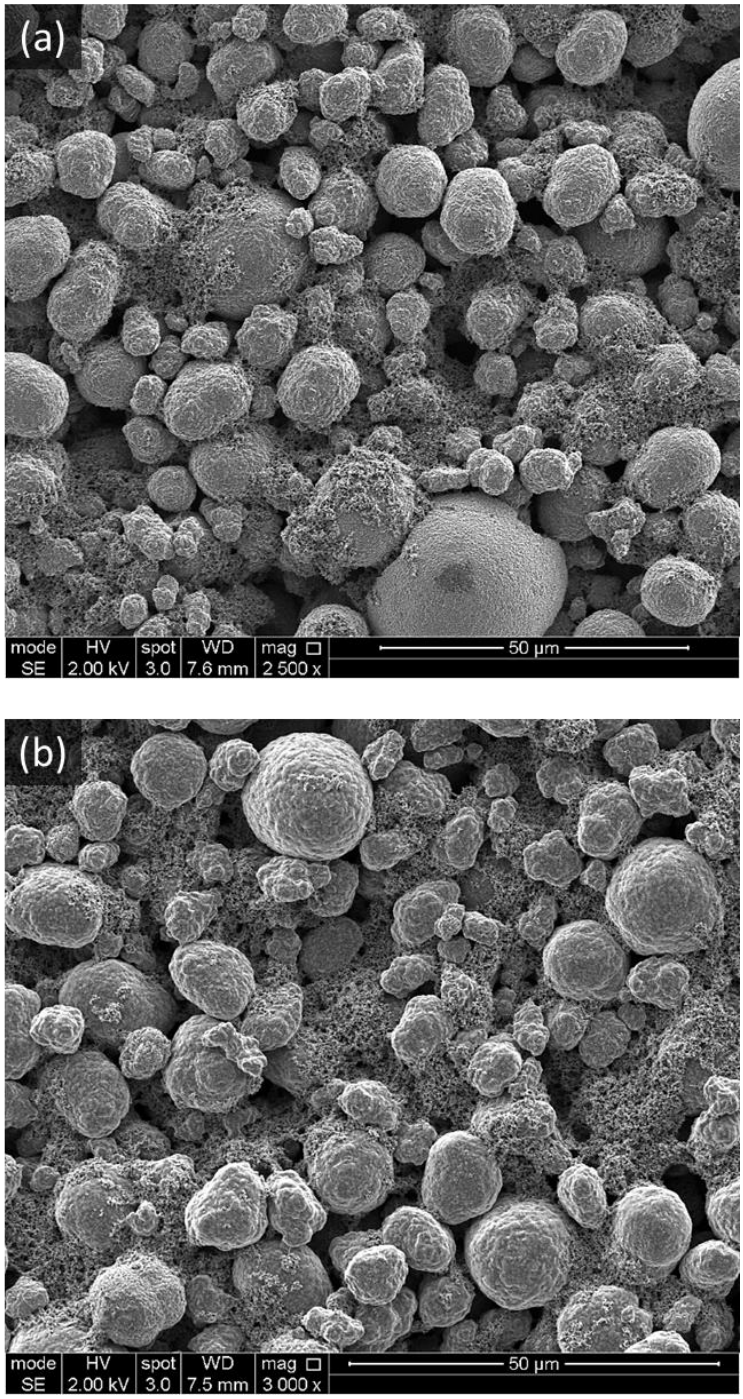

Figure 6.11: SEM micrographs (top view) of long-range dominated pathway electrodes where 0.5 wt% C65 was dry mixed with NMC622 for (a) 2 min and (b) 60 min. The remaining 1.5 wt% of C65 was added during wet mixing.

6.4.6 Summary

This study demonstrates that both the presence and spatial distribution of carbon black, along with the interactions with PVDF in wet mixing, critically affect the electrode properties. In conventional slurries, PVDF preferentially adsorbs to NMC particles while also adsorbing significantly to carbon black due to their high surface area (Figure 6.12a). The displacement of carbon black by PVDF on NMC surface enhances the free carbon content to promote the formation of CB-PVDF clusters, forming bridge structures in the voids between NMC particles for long-range conduction.

Figure 6.12b illustrates the slurry film microstructure during drying with coated particles in the slurry. When NMC particles are coated with carbon black, PVDF adsorption behaviour changes. The coating competes with free carbon for PVDF and reduces the amount of PVDF available for CB-PVDF cluster formation. Increased coating coverage, typically achieved by higher carbon loading for dry mixing, further contributes to this issue by lowering the free carbon content within the slurry. Additionally, prolonged dry mixing produces small free carbon structures, combined with PVDF competition, leading to fewer and smaller CB-PVDF clusters formed. This reduction results in fewer clusters available to be drawn into the voids between NMC via capillary action during drying. The increased coating coverage can also promote the formation of a complete insulating layer and further impede electronic conduction (Figure 6.12c). As a result, the final electrode lacks sufficient bridge structures and the presence of the insulating layer disrupts the conductive network between NMC particles.

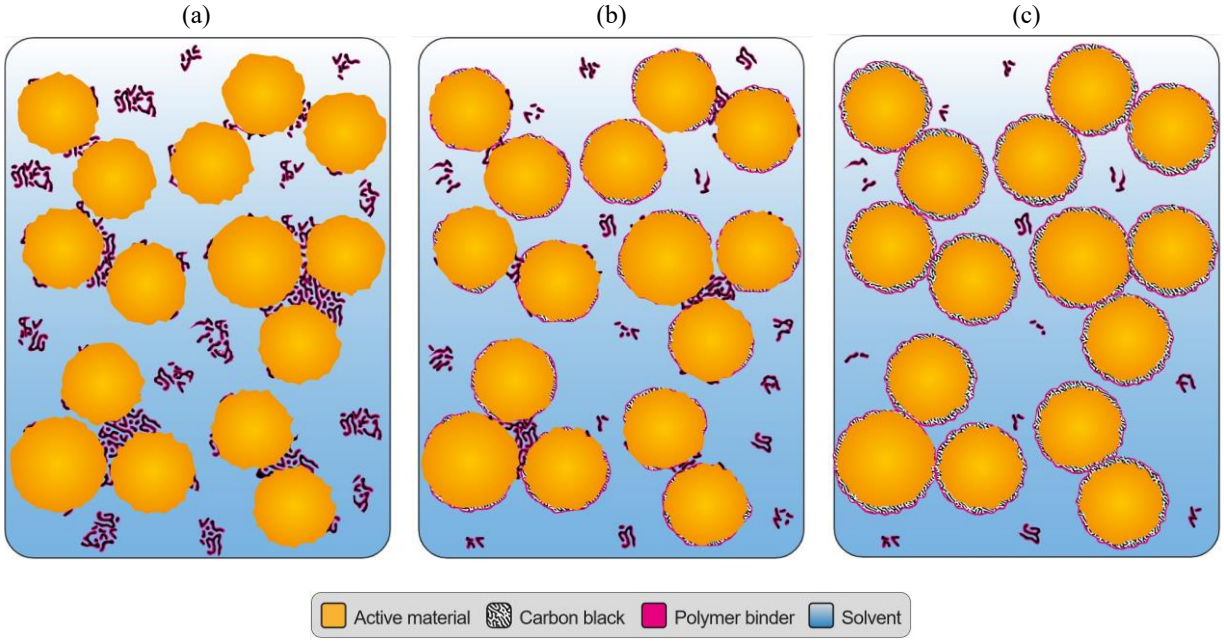

Figure 6.12: Schematic depicting the microstructure of the semi-solid slurry film during drying and the variation in the distribution of PVDF, and CB-PVDF clusters within the slurry and in the voids between NMC due to capillary action. (a) Conventional wet mixed slurry, (b) slurry with low coating coverage particles, (c) slurry with high coating coverage particles.

6.5 Conclusions

By systematically adjusting the carbon loading during both dry and wet mixing, it is possible to control the theoretical ratio of short and long-range pathways within electrodes. This chapter demonstrated the practicality of producing electrodes with various ratios of the two electronic conductive pathway lengths and their impact on slurry and electrode conductivity. From the findings of this chapter, the following conclusions are drawn:

1. The variation in the degree of carbon coating on NMC particles greatly influences both slurry and electrode microstructures, leading to substantial differences in electronic conductivities. All formulations with designed conductive pathways exhibit lower conductivities compared to conventional wet mixing.

2. Increased carbon content in dry mixing increases the coverage of the coating on NMC particles, which introduces additional resistance to ionic conduction due to the increased tortuosity of the pathways. However, electronic conduction remains largely unaffected due to the conductive nature of the carbon coating.

3. Slurry and electrode conductivity decreases as the ratio of short-range pathways increases due to lower free carbon content within the slurry formulation. Electronic conductivity in both systems is dominated by long-range conduction, facilitated by CB-PVDF clusters in slurries and bridge structures in electrodes. Higher coating coverage improves conductivity in the absence of CB-PVDF clusters by promoting better particle-particle contact in regions with enhanced conductivity.

4. The presence of the carbon coating on NMC alters the PVDF adsorption and drying behaviour. The competition for PVDF between the carbon coating and free carbon affects CB-PVDF cluster formation. As the ratio of short-range pathways increases, the number and size of these clusters formed within the slurry decreases due to the reduced availability of PVDF.

5. A decrease in CB-PVDF cluster formation limits the number of clusters available to migrate into voids between NMC particles via capillary action during drying. This leads to fewer bridge structures formed upon drying, resulting in an inefficient conduction network and the disruption in electronic conductivity within the small voids between NMC particles.

Chapter 7 Conclusions and Outlook

7.1 Conclusions

This thesis introduces a novel manufacturing and design-led approach to address the critical gap of controlling conductive additive distribution for electrode microstructure design in battery research. For the first time, particle engineering approaches through coating formation on NMC particles were used to facilitate the engineering of conductive pathways within electrodes. By adapting a high-shear dry mixing technique, mechanofusion, from the pharmaceutical industry, this work demonstrates a method to control the formation of CBD structures within electrodes. Through this approach, the objectives achieved include controlling the formation of CBD film structures, developing powder metrics to evaluate conductive additive dispersion and evaluating the resulting slurry and electrode microstructures and conductivity. These findings expand on the current understanding of electronic conduction pathways and enable the design of advanced 3D electrode architectures.

Mechanofusion was demonstrated as an effective technique for controlling film structure formation on NMC particles, a task that is challenging to achieve in conventional wet slurry mixing. Various coating characteristics such as rough or smooth morphologies, coating coverage and thickness and the carbon black structures on the coating were explored. Rough coatings are likely to be preferable for electrolyte infiltration, although a smooth coating with appropriate porosity may also facilitate this process. Particle analysis suggests that carbon black deagglomeration and coating formation on NMC are impacted by mixing parameters and carbon black loading in mechanofusion. However, precise quantification of the free carbon content still remains a challenge due to the interplay of free carbon content and changes in carbon black structures in characterisation methods.

A common two-point resistivity method was adapted to assess carbon black deagglomeration behaviour in mechanofusion, departing from traditional analysis methods such as slurry and electrode properties that require significant experimental effort. The study revealed that for a system with micron-sized NMC622 and nano-sized carbon black C65, carbon black deagglomeration is highly dependent on the energy input. This is primarily controlled by the mixing time and speed and influenced by the carbon loading. Only a short mixing time is required to yield powder mixtures with low bulk resistivity, indicating that a low degree of deagglomeration is favourable. This further implies that only a small portion of deagglomerated carbon black structures is needed, with the remaining carbon black predominantly retaining its large structure for long-range electronic conduction. Resistivity is also affected by carbon black properties (i.e. surface area, structure level and graphitic character) and is dependent on the mixing. The complex interplay of these properties requires further investigation. For non-conventional additives such as carbon nanotubes, their

deagglomeration mechanism under high shear mixing must first be understood before this technique can be applied to study their deagglomeration behaviour.

Lastly, the use of carbon-coated NMC particles to produce designed conductive pathways within electrodes was investigated. By systematically varying the carbon content for mechanofusion dry mixing and wet slurry mixing, formulations with different theoretical ratios of short and long-range pathways were designed. This approach effectively manipulated the slurry and electrode microstructure. Increased coverage of carbon coating introduces additional charge transfer resistance due to increased tortuosity of ionic pathways within the coating layer, while electronic conduction is maintained due to the conductive nature of the coating. The characteristics of the CBD structures within electrodes also differed, including the distribution and size of bridge structures and the distribution and coverage of film structures on NMC particles. The findings reinforce the dominance of long-range conduction in both slurries and electrodes, facilitated by CB-PVDF clusters and bridge structures respectively. Additionally, the coated particles significantly impact slurry mixing interactions and drying behaviour. Specifically, carbon migration resulting from PVDF competition between free carbon and the carbon coating results in differences in the size and distribution of bridge structures due to decreased CB-PVDF clusters available for capillary action. Although these designed pathways currently exhibit lower electronic conductivity compared to conventional methods, they hold the potential to enhance short-range contacts at the nanoscale on the NMC surface. Further optimisation of the downstream processes, through a comprehensive understanding of changes in mixing interactions and drying behaviours, is needed to fully realise to unlock the potential benefits.

This thesis underscores the potential for controlling the spatial distribution of conductive additives within lithium-ion battery electrodes. Although the initial electronic conductivity of the designed electrode architectures has yet to surpass conventional methods, this research highlights the significant impact of active material pre-processing on downstream processes. By manipulating the distribution of conductive additives, coated particles can alter slurry properties such as rheology and homogeneity, ultimately affecting electrode structures and conduction networks. The findings present a practical investigation into theoretical electronic pathway design, emphasising the increased control of carbon black distribution via coating formation. This work lays the groundwork for developing more efficient and effective use of conductive additives at various length scales within electrodes.

7.2 Future Work

This work presents a wide scope for future research to investigate the interconnection of the process parameters and product properties at individual manufacturing stages. One key recommendation is to increase the use of in-line metrology to provide valuable insights into these relationships. Establishing a comprehensive process-structure-performance relationship is crucial to unlock the potential of next-generation electrode manufacturing. To fully realise the potential of designed conductive pathways and 3D architecture within electrodes, future research should also prioritise several key areas.

With the growing traction of dry processing, another recommendation is to address the unique challenges of carbon black dispersion, which differs substantially from wet mixing. Optimising mechanofusion process parameters through a mechanistic understanding is crucial for achieving fine control over carbon coating characteristics. Additional parameters, such as the blade geometry and blade gap, where particle interactions occur, should be studied. Different blade configurations may have an influence on coating uniformity and the blade gap may produce different shear gradients and mixing profiles. Here, the development of dimensionless relationships, such as the Froude tool number described in Chapter 5, using the Buckingham-Pi Theorem, would be useful to describe dry mixing flow behaviours. This understanding could enable the prediction of optimal mixing conditions through energy input based on desired particle properties. Such relationships can also be used to develop regime maps to guide the selection of parameters that yield desired properties for coated particles. The prerequisite is that two relevant dimensionless numbers that capture the material, product and mixing characteristics must be identified. Currently, to the best of our knowledge, this is still absent in literature for such systems, i.e. micron-sized NMC and nano-sized carbon black, with simultaneous deagglomeration and coating formation. As deagglomeration and coating are the main aims of the mechanofusion process, dimensionless relationships revolving around these two processes may be useful. For deagglomeration, one could design a dimensionless number relating carbon black particles' cohesive strength to the shear forces generated during mechanofusion to predict if deagglomeration may occur and to what extent. As for coating formation, it might be useful to relate the compression forces induced by mechanofusion and interparticle forces that may act against it to inhibit coating formation.

A further recommendation is the development of methods for precise quantitative analysis of free carbon content can serve as an indicator of mixing efficiency. Separation of unbound, free carbon, potentially using size-based separation techniques, followed by characterisation through rheometry or thermogravimetric analysis (TGA) may be useful (as shown in Chapter 4). However, the range in sizes of free carbon particles may pose difficulties in the selection of appropriate separation techniques. The difference in density between free carbon particles and carbon-coated NMC particles could potentially enable density-based separation techniques such as cyclones. Care must be taken to

ensure free carbon structures are not significantly modified during the separation process if free carbon structures are also a focus of the study.

Another important recommendation is to refine downstream processes to ensure compatibility with dry or low-solvent processing. Advanced characterisation techniques are essential for understanding the complex relationship between coated particles, slurry properties, drying behaviour and final electrode structures. Rheology provides information on the flow properties of slurries and provides insights into how viscosity and shear response may impact coating uniformity. Spectroscopy techniques such as Fourier-Transform Infrared Spectroscopy (FTIR) or X-ray photoelectron spectroscopy (XPS) can provide insights into slurry homogeneity. By analysing the surface chemistry and bonding interactions between materials, these techniques may be useful to investigate particle dispersion and stability within the slurry. Such techniques may be useful to study the competition for PVDF between free and immobilised carbon black, leading to variations in CB-PVDF clusters available for carbon migration during drying, as discussed in Chapter 6. 3D tomography allows non-destructive visualisation of the internal particle or electrode structures and can reveal the subtle differences in the distribution of conductive additives within coatings on particles or CBD structures in electrodes. Cross-sectional analysis may be useful to offer high-resolution images of coating layers and particle interfaces. This is usually carried out through cross-sectioning techniques such as focused ion beam (FIB) milling or microtoming coupled with SEM or TEM analysis. Mercury intrusion porosimetry (MIP) can also quantify pore size distributions within the electrode, highlighting the differences caused by the designed conductive pathways to study ionic conductivity.

The exploration of innovative electrode architectures and conductive additives is also strongly recommended. Research should focus on the use of different carbon blacks that are more suited to dry mixing, or even unconventional conductive carbon allotropes (e.g. carbon nanotubes, graphene, carbon nanofibers etc.) that may have synergistic effects and enhance conductive pathways. Ultimately, electrochemical performance is the key metric for real-world applications. High-rate cycling tests will reveal the extent to which these electrodes with designed architecture offer any performance enhancements compared to conventional electrodes. EIS can also be used to study the underlying mechanisms (i.e. electronic, ionic and charge transfer behaviours) to complement the electrochemical results.

Scalability is another critical area of focus for advancing dry processing from lab-scale research to industrial production. Mechanofusion as a dry process offers significant advantages, including improved control over coating uniformity due to smaller interaction spaces and reduced dependence on bulk flow dynamics. These features simplify scale-up, making the transition more predictable and reducing variability. Commercially available large-scale mixers, such as those by Hosokawa Micron and Eirich, further support scalability with well-established scale-up studies. Additionally, dry

processing can improve energy efficiency by eliminating the need for solvent evaporation and recovery, though challenges like heat management, cooling demands, consistent energy input and effective material handling must be addressed. Maintaining electrode mechanical stability, particularly to prevent cracking during calendering, is also critical to achieving consistent quality and efficiency at industrial scales. Cost constraints associated with retrofitting existing systems or implementing new technologies, as well as maintaining process stability, also pose significant barriers.

To conclude, achieving a comprehensive process-structure-performance relationship through rigorous experimental characterisation is essential for addressing key challenges in dry processing. Additionally, scalability and efficiency are fundamental to advancing dry processing for next-generation lithium-ion battery electrode manufacturing. Computational approaches such as discrete element method (DEM) modelling can further support optimisation by enabling precise control over mixing parameters to achieve desired electrode microstructures (e.g. porosity, tortuosity etc.). These models can also predict critical electrochemical metrics, including rate capability and capacity fade, facilitating the design of robust and high-performing electrodes. These investigations will not only validate the practicality of the proposed electrode designs while providing a benchmark for further optimisation to provide advancements for next-generation lithium-ion battery electrodes.

Chapter 8 References

[1] ‘Faraday Institution to lead UK Government’s Ayrton Challenge on Energy Storage’, The Faraday Institution. Accessed: Apr. 07, 2024. [Online]. Available: https://www.faraday.ac.uk/aces-press-release/

[2] F. M. N. U. Khan, M. G. Rasul, A. S. M. Sayem, and N. Mandal, ‘Maximizing energy density of lithium-ion batteries for electric vehicles: A critical review’, *Energy Rep.*, vol. 9, pp. 11–21, Oct. 2023, doi: 10.1016/j.egyr.2023.08.069.

[3] T. Li, D. Li, Q. Zhang, J. Gao, L. Zhang, and X. Liu, ‘Improving Fast Charging-Discharging Performances of Ni-Rich LiNi0.8Co0.1Mn0.1O2 Cathode Material by Electronic Conductor LaNiO3 Crystallites’, *Materials*, vol. 15, no. 1, p. 396, Jan. 2022, doi: 10.3390/ma15010396.

[4] P. S. Grant *et al.*, ‘Roadmap on Li-ion battery manufacturing research’, *J. Phys. Energy*, vol. 4, no. 4, p. 042006, Nov. 2022, doi: 10.1088/2515-7655/ac8e30.

[5] S. Babinec, H. Tang, A. Talik, S. Hughes, and G. Meyers, ‘Composite cathode structure/property relationships’, *J. Power Sources*, vol. 174, no. 2, pp. 508–514, 2007, doi: 10.1016/j.jpowsour.2007.06.071.

[6] P. Verma, P. Maire, and P. Novák, ‘A review of the features and analyses of the solid electrolyte interphase in Li-ion batteries’, *Electrochimica Acta*, vol. 55, no. 22, pp. 6332–6341, Sep. 2010, doi: 10.1016/j.electacta.2010.05.072.

[7] C. Deng *et al.*, ‘Recent advances in rocking chair batteries and beyond’, *Energy Storage Mater.*, vol. 60, p. 102820, Jun. 2023, doi: 10.1016/j.ensm.2023.102820.

[8] S. P. V. Nadimpalli *et al.*, ‘Quantifying capacity loss due to solid-electrolyte-interphase layer formation on silicon negative electrodes in lithium-ion batteries’, *J. Power Sources*, vol. 215, pp. 145–151, Oct. 2012, doi: 10.1016/j.jpowsour.2012.05.004.

[9] N. Akhmetov, A. Manakhov, and A. S. Al-Qasim, ‘Li-Ion Battery Cathode Recycling: An Emerging Response to Growing Metal Demand and Accumulating Battery Waste’, *Electronics*, vol. 12, no. 5, p. 1152, Feb. 2023, doi: 10.3390/electronics12051152.

[10] J. Xu *et al.*, ‘High-Energy Lithium-Ion Batteries: Recent Progress and a Promising Future in Applications’, *ENERGY Environ. Mater.*, vol. 6, no. 5, p. e12450, 2023, doi: 10.1002/eem2.12450.

[11] P. Zhu, P. R. Slater, and E. Kendrick, ‘Insights into architecture, design and manufacture of electrodes for lithium-ion batteries’, *Mater. Des.*, vol. 223, p. 111208, Nov. 2022, doi: 10.1016/j.matdes.2022.111208.

[12] G. Hatton, ‘How to design a Motorsport Battery in 7 steps’, Racecar Engineering. Accessed: Apr. 07, 2024. [Online]. Available: https://www.racecar-engineering.com/tech-explained/how-to-design-a-motorsport-battery-in-7-steps/

[13] A. Wise, M. Dowson, L. Cooper, C. Shepherd, J. Regnart, and B. Shah, ‘From Research and Manufacturing to Application and End of Life – Enabling Electrification Across Sectors. Battery Targets and priorities across sectors, 2020 to 2035.’, The University of Warwick, Discussion Document, Oct. 2020. Accessed: Apr. 06, 2024. [Online]. Available: https://i.emlfiles4.com/cmpdoc/8/5/0/4/3/1/files/93002_20201015-wmg-battery-manufacturing-targets-report.pdf?utm_campaign=1850317_Bulletin%20NOV%202020&utm_medium=email&utm_source=dotdigital&dm_i=2VFU,13NPP,6I81KD,48L3Q,1

[14] P. Zhu, D. Gastol, J. Marshall, R. Sommerville, V. Goodship, and E. Kendrick, ‘A review of current collectors for lithium-ion batteries’, *J. Power Sources*, vol. 485, no. November 2020, p. 229321, 2021, doi: 10.1016/j.jpowsour.2020.229321.

[15] A. K. Mishra, Monika, and B. S. Patial, ‘A review on recent advances in anode materials in lithium ion batteries’, *Mater. Today Electron.*, vol. 7, p. 100089, May 2024, doi: 10.1016/j.mtelec.2024.100089.

[16] D. Andre, H. Hain, P. Lamp, F. Maglia, and B. Stiaszny, ‘Future high-energy density anode materials from an automotive application perspective’, *J. Mater. Chem. A*, vol. 5, no. 33, pp. 17174–17198, 2017, doi: 10.1039/c7ta03108d.

[17] J. Asenbauer, T. Eisenmann, M. Kuenzel, A. Kazzazi, Z. Chen, and D. Bresser, ‘The success story of graphite as a lithium-ion anode material-fundamentals, remaining challenges, and recent developments including silicon (oxide) composites’, *Sustain. Energy Fuels*, vol. 4, no. 11, pp. 5387–5416, 2020, doi: 10.1039/d0se00175a.

[18] S. H. Yu, X. Feng, N. Zhang, J. Seok, and H. D. Abruña, ‘Understanding Conversion-Type Electrodes for Lithium Rechargeable Batteries’, *Acc. Chem. Res.*, vol. 51, no. 2, pp. 273–281, 2018, doi: 10.1021/acs.accounts.7b00487.

[19] P. Meister, H. Jia, J. Li, R. Kloepsch, M. Winter, and T. Placke, ‘Best Practice: Performance and Cost Evaluation of Lithium Ion Battery Active Materials with Special Emphasis on Energy Efficiency’, *Chem. Mater.*, vol. 28, no. 20, pp. 7203–7217, 2016, doi: 10.1021/acs.chemmater.6b02895.

[20] C. M. Julien, A. Mauger, K. Zaghib, and H. Groult, ‘Comparative Issues of Cathode Materials for Li-Ion Batteries’, *Inorganics*, vol. 2, no. 1, Art. no. 1, Mar. 2014, doi: 10.3390/inorganics2010132.

[21] J.-J. Marie and S. Gifford, ‘Developments in lithium-ion battery cathodes’, no. 18, 2023.

[22] M.-J. Uddin, P. K. Alaboina, and S.-J. Cho, ‘Nanostructured cathode materials synthesis for lithium-ion batteries’, *Mater. Today Energy*, vol. 5, pp. 138–157, Sep. 2017, doi: 10.1016/j.mtener.2017.06.008.

[23] Y. Wang, E. Wang, X. Zhang, and H. Yu, ‘High-Voltage “Single-Crystal” Cathode Materials for Lithium-Ion Batteries’, *Energy Fuels*, vol. 35, no. 3, pp. 1918–1932, Feb. 2021, doi: 10.1021/acs.energyfuels.0c03608.

[24] X. Xu *et al.*, ‘Radially Oriented Single-Crystal Primary Nanosheets Enable Ultrahigh Rate and Cycling Properties of $LiNi_{0.8}Co_{0.1}Mn_{0.1}O_2$ Cathode Material for Lithium-Ion Batteries’, *Adv. Energy Mater.*, vol. 9, no. 15, p. 1803963, Apr. 2019, doi: 10.1002/aenm.201803963.

[25] M. N. Obrovac, L. Zheng, and M. D. L. Garayt, ‘Engineered Particle Synthesis by Dry Particle Microgranulation’, *Cell Rep. Phys. Sci.*, vol. 1, no. 6, p. 100063, 2020, doi: 10.1016/j.xcrp.2020.100063.

[26] T. Thien Nguyen, U. H. Kim, C. S. Yoon, and Y. K. Sun, ‘Enhanced cycling stability of Sn-doped Li[Ni0.90Co0.05Mn0.05]O2 via optimization of particle shape and orientation’, *Chem. Eng. J.*, vol. 405, no. July 2020, p. 126887, 2021, doi: 10.1016/j.cej.2020.126887.

[27] Q. Zhang, Z. Yu, P. Du, and C. Su, ‘Carbon Nanomaterials Used as Conductive Additives in Lithium Ion Batteries’, *Recent Pat. Nanotechnol.*, vol. 4, no. 2, pp. 100–110, May 2010, doi: 10.2174/187221010791208803.

[28] Z. Chen *et al.*, ‘Manganese phosphate coated Li[Ni0.6Co0.2Mn0.2]O2 cathode material: Towards superior cycling stability at elevated temperature and high voltage’, *J. Power Sources*, vol. 402, no. September, pp. 263–271, 2018, doi: 10.1016/j.jpowsour.2018.09.049.

[29] S. T. Myung, K. Izumi, S. Komaba, Y. K. Sun, H. Yashiro, and N. Kumagai, ‘Role of alumina coating on Li-Ni-Co-Mn-O particles as positive electrode material for lithium-ion batteries’, *Chem. Mater.*, vol. 17, no. 14, pp. 3695–3704, 2005, doi: 10.1021/cm050566s.

[30] M. Singh, J. Kaiser, and H. Hahn, ‘Thick Electrodes for High Energy Lithium Ion Batteries’, *J. Electrochem. Soc.*, vol. 162, no. 7, p. A1196, Apr. 2015, doi: 10.1149/2.0401507jes.

[31] A. M. Boyce *et al.*, ‘Design of Scalable, Next-Generation Thick Electrodes: Opportunities and Challenges’, *ACS Nano*, vol. 15, no. 12, pp. 18624–18632, Dec. 2021, doi: 10.1021/acsnano.1c09687.

[32] Y. Kuang, C. Chen, D. Kirsch, and L. Hu, ‘Thick Electrode Batteries: Principles, Opportunities, and Challenges’, *Adv. Energy Mater.*, vol. 9, no. 33, p. 1901457, 2019, doi: 10.1002/aenm.201901457.

[33] Y. K. Lee, ‘The Effect of Active Material, Conductive Additives, and Binder in a Cathode Composite Electrode on Battery Performance’, *Energies*, vol. 12, no. 4, Art. no. 4, Jan. 2019, doi: 10.3390/en12040658.

[34] M. E. Spahr, D. Goers, A. Leone, S. Stallone, and E. Grivei, ‘Development of carbon conductive additives for advanced lithium ion batteries’, *J. Power Sources*, vol. 196, no. 7, pp. 3404–3413, Apr. 2011, doi: 10.1016/j.jpowsour.2010.07.002.

[35] J. Chen, J. Liu, Y. Qi, T. Sun, and X. Li, ‘Unveiling the Roles of Binder in the Mechanical Integrity of Electrodes for Lithium-Ion Batteries’, *J. Electrochem. Soc.*, vol. 160, no. 9, p. A1502, Jul. 2013, doi: 10.1149/2.088309jes.

[36] F. Cadiou *et al.*, ‘Numerical Prediction of Multiscale Electronic Conductivity of Lithium-Ion Battery Positive Electrodes’, *J. Electrochem. Soc.*, vol. 166, no. 8, pp. A1692–A1703, 2019, doi: 10.1149/2.1221908jes.

[37] D. Grießl, K. Huber, R. Scherbauer, and A. Kwade, ‘Dispersion kinetics of carbon black for the application in lithium-ion batteries’, *Adv. Powder Technol.*, vol. 32, no. 7, pp. 2280–2288, Jul. 2021, doi: 10.1016/j.apt.2021.05.003.

[38] R. M. Saraka, S. L. Morelly, M. H. Tang, and N. J. Alvarez, ‘Correlating Processing Conditions to Short- and Long-Range Order in Coating and Drying Lithium-Ion Batteries’, *ACS Appl. Energy Mater.*, vol. 3, no. 12, pp. 11681–11689, Dec. 2020, doi: 10.1021/acsaem.0c01305.

[39] Y. S. Zhang *et al.*, ‘A Review of Lithium-Ion Battery Electrode Drying: Mechanisms and Metrology’, *Adv. Energy Mater.*, vol. 12, no. 2, p. 2102233, 2022, doi: 10.1002/aenm.202102233.

[40] D. Schreiner, A. Klinger, and G. Reinhart, ‘Modeling of the calendering process for lithium-ion batteries with DEM simulation’, *Procedia CIRP*, vol. 93, pp. 149–155, 2020, doi: 10.1016/j.procir.2020.05.158.

[41] X. Zhong *et al.*, ‘Binding mechanisms of PVDF in lithium ion batteries’, *Appl. Surf. Sci.*, vol. 553, p. 149564, Jul. 2021, doi: 10.1016/j.apsusc.2021.149564.

[42] W. Bauer, D. Nötzel, V. Wenzel, and H. Nirschl, ‘Influence of dry mixing and distribution of conductive additives in cathodes for lithium ion batteries’, *J. Power Sources*, vol. 288, pp. 359–367, Aug. 2015, doi: 10.1016/j.jpowsour.2015.04.081.

[43] S. Datta, *Quantum Transport*. Cambridge, 2005.

[44] D. Toker, D. Azulay, N. Shimoni, I. Balberg, and O. Millo, ‘Tunneling and percolation in metal-insulator composite materials’, *Phys. Rev. B*, vol. 68, no. 4, p. 041403, Jul. 2003, doi: 10.1103/PhysRevB.68.041403.

[45] M. Lowell, ‘Carbon Black Filled Conducting Polymers and Polymer Blends’, vol. 21, no. 4, pp. 299–313, 2002, doi: 10.1002/adv.10025.

[46] M. Ali, L. Lin, and D. Cartridge, ‘High electrical conductivity waterborne dispersions of carbon black pigment’, *Prog. Org. Coat.*, vol. 129, pp. 199–208, Apr. 2019, doi: 10.1016/j.porgcoat.2018.12.010.

[47] A. Alekseev, T. H. Wu, L. G. J. van der Ven, R. A. T. M. van Benthem, and G. de With, ‘Global and local conductivity in percolating crosslinked carbon black/epoxy–amine composites’, *J. Mater. Sci.*, vol. 55, no. 21, pp. 8930–8939, Jul. 2020, doi: 10.1007/s10853-020-04650-2.

[48] H.-J. Choi, M. S. Kim, D. Ahn, S. Y. Yeo, and S. Lee, ‘Electrical percolation threshold of carbon black in a polymer matrix and its application to antistatic fibre’, *Sci. Rep.*, vol. 9, no. 1, p. 6338, Apr. 2019, doi: 10.1038/s41598-019-42495-1.

[49] J. Entwistle, R. Ge, K. Pardikar, R. Smith, and D. Cumming, ‘Carbon binder domain networks and electrical conductivity in lithium-ion battery electrodes: A critical review’, *Renew. Sustain. Energy Rev.*, vol. 166, Sep. 2022, doi: 10.1016/j.rser.2022.112624.

[50] P. J. Flory, *Principles of Polymer Chemistry*. New York: Cornell University Press, 1953.

[51] F. Bueche, ‘Electrical resistivity of conducting particles in an insulating matrix’, vol. 43, p. 4837, 1972.

[52] M. J. Cruz-Estrada, R.H., Folkes, ‘Structure formation and modelling of the electrical conductivity in SBS-polyaniline blends Part I Percolation theory approach’, no. 130, pp. 1427–1429, 2002, doi: 10.1023/A:1019918817183.

[53] S. Kirkpatrick, ‘Percolation ancl Conduction’, vol. 45, 1973.

[54] S. Mandal, J. M. Amarilla, J. Ibáñez, and J. M. Rojo, ‘The Role of Carbon Black in LiMn 2 O 4 -Based Composites as Cathodes for Rechargeable Lithium Batteries The Role of Carbon Black in LiMn 2 O 4 -Based Composites as Cathodes for Rechargeable Lithium Batteries’, *J. Electrochem. Soc.*, pp. 2–8, 2001.

[55] M. Haghgoo, R. Ansari, and M. K. Hassanzadeh-Aghdam, ‘Predicting effective electrical resistivity and conductivity of carbon nanotube/carbon black-filled polymer matrix hybrid nanocomposites’, *J. Phys. Chem. Solids*, vol. 161, p. 110444, Feb. 2022, doi: 10.1016/j.jpcs.2021.110444.

[56] A. Awarke, S. Lauer, S. Pischinger, and M. Wittler, ‘Percolation–tunneling modeling for the study of the electric conductivity in LiFePO4 based Li-ion battery cathodes’, *J. Power Sources*, vol. 196, no. 1, pp. 405–411, Jan. 2011, doi: 10.1016/j.jpowsour.2010.07.048.

[57] S. Akhtar, W. Lee, M. Kim, M. S. Park, and W. S. Yoon, ‘Conduction mechanism of charge carriers in electrodes and design factors for the improvement of charge conduction in li-ion batteries’, *J. Electrochem. Sci. Technol.*, vol. 12, no. 1, pp. 1–20, 2021, doi: 10.33961/jecst.2020.01564.

[58] A. Kasgoz, D. Akın, and A. Durmus, ‘Rheological and electrical properties of carbon black and carbon fiber filled cyclic olefin copolymer composites’, *Compos. Part B Eng.*, vol. 62, pp. 113–120, Jun. 2014, doi: 10.1016/j.compositesb.2014.02.017.

[59] S. L. Morelly, N. J. Alvarez, and M. H. Tang, ‘Short-range contacts govern the performance of industry-relevant battery cathodes’, *J. Power Sources*, vol. 387, no. January, pp. 49–56, 2018, doi: 10.1016/j.jpowsour.2018.03.039.

[60] J. F. Baumgärtner, K. V. Kravchyk, and M. V. Kovalenko, ‘Navigating the Carbon Maze: A Roadmap to Effective Carbon Conductive Networks for Lithium-Ion Batteries’, *Adv. Energy Mater.*, vol. n/a, no. n/a, p. 2400499, doi: 10.1002/aenm.202400499.

[61] K. Konda, M. S. Jacob, J. R. Seth, V. A. Juvekar, R. Gopalan, and S. B. Moodakare, ‘Capacity degradation of lithium-ion cell: The role of free carbon black content in the slurry and drying induced cracks in LiFePO4 electrode’, *J. Energy Storage*, vol. 74, p. 109477, Dec. 2023, doi: 10.1016/j.est.2023.109477.

[62] M. J. Lain, G. Apachitei, L. Román-Ramírez, M. Copley, and J. Marco, ‘Cross-sectional analysis of lithium ion electrodes using spatial autocorrelation techniques’, *Phys. Chem. Chem. Phys.*, vol. 24, no. 48, pp. 29999–30009, Dec. 2022, doi: 10.1039/D2CP03094B.

[63] B. L. Trembacki, A. N. Mistry, D. R. Noble, M. E. Ferraro, P. P. Mukherjee, and S. A. Roberts, ‘Mesoscale Analysis of Conductive Binder Domain Morphology in Lithium-Ion Battery Electrodes’, *J. Electrochem. Soc.*, vol. 165, no. 13, pp. E725–E736, 2018, doi: 10.1149/2.0981813jes.

[64] H. Bockholt, W. Haselrieder, and A. Kwade, ‘Intensive powder mixing for dry dispersing of carbon black and its relevance for lithium-ion battery cathodes’, *Powder Technol.*, vol. 297, pp. 266–274, 2016, doi: 10.1016/j.powtec.2016.04.011.

[65] M. Wang, D. Dang, A. Meyer, R. Arsenault, and Y.-T. Cheng, ‘Effects of the Mixing Sequence on Making Lithium Ion Battery Electrodes’, *J. Electrochem. Soc.*, vol. 167, no. 10, p. 100518, Jun. 2020, doi: 10.1149/1945-7111/ab95c6.

[66] H. Bockholt, M. Indrikova, A. Netz, F. Golks, and A. Kwade, ‘The interaction of consecutive process steps in the manufacturing of lithium-ion battery electrodes with regard to structural and electrochemical properties’, *J. Power Sources*, vol. 325, pp. 140–151, Sep. 2016, doi: 10.1016/j.jpowsour.2016.05.127.

[67] R. Dominko, M. Gaberscek, J. Drofenik, M. Bele, S. Pejovnik, and J. Jamnik, ‘The role of carbon black distribution in cathodes for Li ion batteries’, in *Journal of Power Sources*, Jun. 2003, pp. 770–773. doi: 10.1016/S0378-7753(03)00250-7.

[68] H. Hamed *et al.*, ‘A limitation map of performance for porous electrodes in lithium-ion batteries’, *iScience*, vol. 24, no. 12, Dec. 2021, doi: 10.1016/j.isci.2021.103496.

[69] S. Yari *et al.*, ‘Constructive versus Destructive Heterogeneity in Porous Electrodes of Lithium-Ion Batteries’, *ACS Appl. Energy Mater.*, vol. 3, no. 12, pp. 11820–11829, 2020, doi: 10.1021/acsaem.0c01966.

[70] D. Guy, B. Lestriez, R. Bouchet, and D. Guyomard, ‘Critical Role of Polymeric Binders on the Electronic Transport Properties of Composites Electrode’, *J. Electrochem. Soc.*, vol. 153, no. 4, p. A679, 2006, doi: 10.1149/1.2168049.

[71] X. Lu *et al.*, ‘Microstructure of Conductive Binder Domain for Electrical Conduction in Next-Generation Lithium-Ion Batteries’, *Energy Technol.*, p. 2300446, Aug. 2023, doi: 10.1002/ente.202300446.

[72] X. Lu *et al.*, ‘Effect of carbon blacks on electrical conduction and conductive binder domain of next-generation lithium-ion batteries’, *J. Power Sources*, vol. 592, p. 233916, Feb. 2024, doi: 10.1016/j.jpowsour.2023.233916.

[73] R. Ge *et al.*, ‘Numerical Design of Microporous Carbon Binder Domains Phase in Composite Cathodes for Lithium-Ion Batteries’, *ACS Appl. Mater. Interfaces*, vol. 15, no. 23, pp. 27809–27820, Jun. 2023, doi: 10.1021/acsami.3c00998.

[74] R. Ge, A. M. Boyce, Y. Shui Zhang, P. R. Shearing, D. J. Cumming, and R. M. Smith, ‘Discrete element method and electrochemical modelling of lithium ion cathode structures characterised by X-ray computed tomography’, *Chem. Eng. J.*, vol. 465, p. 142749, Jun. 2023, doi: 10.1016/j.cej.2023.142749.

[75] H.-S. Kim, K. Kim, S.-I. Moon, I.-J. Kim, and H.-B. Gu, ‘A study on carbon-coated LiNi1/3Mn1/3Co1/3O2 cathode material for lithium secondary batteries’, *J. Solid State Electrochem.*, vol. 12, no. 7, pp. 867–872, Aug. 2008, doi: 10.1007/s10008-008-0552-0.

[76] S. A. Hong, D. H. Kim, K. Y. Chung, W. Chang, J. Yoo, and J. Kim, ‘Toward uniform and ultrathin carbon layer coating on lithium iron phosphate using liquid carbon dioxide for enhanced electrochemical performance’, *J. Power Sources*, vol. 262, pp. 219–223, 2014, doi: 10.1016/j.jpowsour.2014.03.132.

[77] S.-M. Oh, S.-W. Oh, C.-S. Yoon, B. Scrosati, K. Amine, and Y.-K. Sun, ‘High-Performance Carbon-LiMnPO4 Nanocomposite Cathode for Lithium Batteries’, *Adv. Funct. Mater.*, vol. 20, no. 19, pp. 3260–3265, 2010, doi: 10.1002/adfm.201000469.

[78] B. G. Westphal *et al.*, ‘Influence of high intensive dry mixing and calendering on relative electrode resistivity determined via an advanced two point approach’, *J. Energy Storage*, vol. 11, pp. 76–85, Jun. 2017, doi: 10.1016/j.est.2017.02.001.

[79] W. Bauer and D. Nötzel, ‘Rheological properties and stability of NMP based cathode slurries for lithium ion batteries’, *Ceram. Int.*, vol. 40, no. 3, pp. 4591–4598, 2014, doi: 10.1016/j.ceramint.2013.08.137.

[80] G. Georgousis *et al.*, ‘Study of the reinforcing mechanism and strain sensing in a carbon black filled elastomer’, *Compos. Part B Eng.*, vol. 80, pp. 20–26, Oct. 2015, doi: 10.1016/j.compositesb.2015.05.021.

[81] C. G. Robertson and N. J. Hardman, ‘Nature of carbon black reinforcement of rubber: Perspective on the original polymer nanocomposite’, *Polymers*, vol. 13, no. 4, pp. 1–28, 2021, doi: 10.3390/polym13040538.

[82] ‘Dispersion’, Cabot Corporation. Accessed: Apr. 10, 2024. [Online]. Available: https://www.cabotcorp.com/solutions/applications/industrial-rubber-products/dispersion

[83] ‘Tip Surface Interaction’. Accessed: Apr. 14, 2024. [Online]. Available: https://www.doitpoms.ac.uk/tlplib/afm/tip_surface_interaction.php

[84] M. Weber, J. K. Mayer, and A. Kwade, ‘The Carbon Black Dispersion Index DICB: A Novel Approach Describing the Dispersion Progress of Carbon Black Containing Battery Slurries’, *Energy Technol.*, 2023, doi: 10.1002/ente.202201299.

[85] S. P. Rwei, I. Manas-Zloczower, and D. L. Feke, ‘Observation of carbon black agglomerate dispersion in simple shear flows’, *Polym. Eng. Sci.*, vol. 30, no. 12, pp. 701–706, Jun. 1990, doi: 10.1002/pen.760301202.

[86] C. Lischka, S. Gerl, J. Kappes, A. Chauhan, and H. Nirschl, ‘Experimental & simulative assessment of mixing quality for dry Li-Ion cathode production in an Eirich intensive mixer’, *Powder Technol.*, vol. 431, p. 119072, Jan. 2024, doi: 10.1016/j.powtec.2023.119072.

[87] J. K. Mayer *et al.*, ‘Influence of the Carbon Black Dispersing Process on the Microstructure and Performance of Li-Ion Battery Cathodes’, *Energy Technol.*, vol. 8, no. 2, pp. 1–11, 2020, doi: 10.1002/ente.201900161.

[88] J. K. Mayer, H. Bockholt, and A. Kwade, ‘Inner carbon black porosity as characteristic parameter for the microstructure of lithium-ion electrodes and its effect on physical and electrochemical properties’, *J. Power Sources*, vol. 529, p. 231259, May 2022, doi: 10.1016/j.jpowsour.2022.231259.

[89] Granutools, ‘How GranuPack assess carbon black deagglomeration in battery manufacturing’, Granutools. Accessed: Apr. 04, 2024. [Online]. Available: https://www.granutools.com/en/news/222_how-granupack-assess-carbon-black-deagglomeration-in-battery-manufacturing

[90] B. Marinho, M. Ghislandi, E. Tkalya, C. E. Koning, and G. de With, ‘Electrical conductivity of compacts of graphene, multi-wall carbon nanotubes, carbon black, and graphite powder’, *Powder Technol.*, vol. 221, pp. 351–358, May 2012, doi: 10.1016/j.powtec.2012.01.024.

[91] J. J. Kuo, S. D. Kang, and W. C. Chueh, ‘Contact Resistance of Carbon–Lix(Ni,Mn,Co)O2 Interfaces’, *Adv. Energy Mater.*, vol. 12, no. 31, Aug. 2022, doi: 10.1002/aenm.202201114.

[92] S. Kane, S. Warnat, and C. Ryan, ‘Improvements in methods for measuring the volume conductivity of electrically conductive carbon powders’, *Adv. Powder Technol.*, vol. 32, no. 3, pp. 702–709, Mar. 2021, doi: 10.1016/j.apt.2021.01.016.

[93] N. Mainusch *et al.*, ‘New Contact Probe and Method to Measure Electrical Resistances in Battery Electrodes’, *Energy Technol.*, vol. 4, no. 12, pp. 1550–1557, 2016, doi: 10.1002/ente.201600127.

[94] N. Rey-Raap *et al.*, ‘An electrical conductivity translator for carbons’, *Measurement*, vol. 56, pp. 215–218, Oct. 2014, doi: 10.1016/j.measurement.2014.07.003.

[95] C. Wang and J. Hong, ‘Ionic/Electronic Conducting Characteristics of LiFePO4 Cathode Materials: The Determining Factors for High Rate Performance’, *Electrochem. Solid-State Lett.*, vol. 10, no. 3, p. A65, Jan. 2007, doi: 10.1149/1.2409768.

[96] ‘Status and prospects of lithium iron phosphate manufacturing in the lithium battery industry | MRS Communications’. Accessed: Nov. 28, 2024. [Online]. Available: https://link.springer.com/article/10.1557/s43579-024-00644-2

[97] B. Ramasubramanian, S. Sundarrajan, V. Chellappan, M. V. Reddy, S. Ramakrishna, and K. Zaghib, ‘Recent Development in Carbon-LiFePO4 Cathodes for Lithium-Ion Batteries: A Mini Review’, *Batteries*, vol. 8, no. 10, Art. no. 10, Oct. 2022, doi: 10.3390/batteries8100133.

[98] Y.-D. Cho, G. T.-K. Fey, and H.-M. Kao, ‘The effect of carbon coating thickness on the capacity of LiFePO4/C composite cathodes’, *J. Power Sources*, vol. 189, no. 1, pp. 256–262, Apr. 2009, doi: 10.1016/j.jpowsour.2008.09.053.

[99] J. Wang *et al.*, ‘Doping Strategy in Nickel-Rich Layered Oxide Cathode for Lithium-Ion Battery’, *Renewables*, vol. 1, no. 3, pp. 316–340, May 2023, doi: 10.31635/renewables.023.202200022.

[100] Y. Wu *et al.*, ‘Performance and Stability Improvement of Layered NCM Lithium-Ion Batteries at High Voltage by a Microporous Al2O3 Sol-Gel Coating’, *ACS Omega*, vol. 4, no. 9, pp. 13972–13980, 2019, doi: 10.1021/acsomega.9b01706.

[101] M. J. Herzog, D. Esken, and J. Janek, ‘Improved Cycling Performance of High-Nickel NMC by Dry Powder Coating with Nanostructured Fumed Al 2 O 3 , TiO 2 , and ZrO 2 : A Comparison’, *Batter. Supercaps*, vol. 4, no. 6, pp. 1003–1017, 2021, doi: 10.1002/batt.202100016.

[102] Z. Chen, Y. Qin, K. Amine, and Y. K. Sun, ‘Role of surface coating on cathode materials for lithium-ion batteries’, *J. Mater. Chem.*, vol. 20, no. 36, pp. 7606–7612, 2010, doi: 10.1039/c0jm00154f.

[103] M. Qi *et al.*, ‘Improved electrochemical performances of carbon-coated LiFePO4 microspheres for Li-ion battery cathode’, *Mater. Res. Express*, vol. 6, no. 11, p. 115520, Oct. 2019, doi: 10.1088/2053-1591/ab4915.

[104] Y. Chen, J. Cheng, S. Sun, Y. Wang, and L. Guo, ‘Coating a Na3V2(PO4)3 cathode material with carbon to improve its sodium storage’, *New Carbon Mater.*, vol. 36, no. 6, pp. 1118–1126, Dec. 2021, doi: 10.1016/S1872-5805(21)60098-7.

[105] H. Bockholt, W. Haselrieder, and A. Kwade, ‘Intensive Dry and Wet Mixing Influencing the Structural and Electrochemical Properties of Secondary Lithium-Ion Battery Cathodes’, *ECS Trans.*, vol. 50, no. 26, pp. 25–35, Apr. 2013, doi: 10.1149/05026.0025ecst.

[106] ‘PMH / PML Planetary Mixer’, Grinding & Dispersing. Accessed: Aug. 02, 2024. [Online]. Available: https://grinding.netzsch.com/en/products-and-solutions/mixing-de-aerating/pmh-pml-planetary-mixer

[107] ‘Mixing system - Mischtechnik - Mischer - Intensivmischer’. Accessed: Aug. 02, 2024. [Online]. Available: https://www.eirich.com/en/processes/mixing-technology/mixing-system

[108] Y. Cao, T. D. Hatchard, R. A. Dunlap, and M. N. Obrovac, ‘Mechanofusion-derived Si-alloy/graphite composite electrode materials for Li-ion batteries’, *J. Mater. Chem. A*, vol. 7, no. 14, pp. 8335–8343, 2019, doi: 10.1039/c9ta00132h.

[109] ‘DEM Analysis of Mechanofusion | Ghadiri Research Group’. Accessed: Apr. 13, 2024. [Online]. Available: https://ghadiri-group.leeds.ac.uk/our-research/numerical-simulations/dem-analysis-of-mechanofusion/

[110] ‘HOSOKAWAMICRON CORPORATION’. Accessed: Apr. 14, 2024. [Online]. Available: https://www.hosokawamicron.co.jp/en/product/machines/detail/215.html

[111] M. Alonso, M. Satoh, and K. Miyanami, ‘Mechanism of the combined coating-mechanofusion processing of powders’, *Powder Technol.*, vol. 59, no. 1, pp. 45–52, 1989, doi: 10.1016/0032-5910(89)80094-4.

[112] Q. T. Zhou, L. Qu, I. Larson, P. J. Stewart, and D. A. V. Morton, ‘Effect of mechanical dry particle coating on the improvement of powder flowability for lactose monohydrate: A model cohesive pharmaceutical powder’, *Powder Technol.*, vol. 207, no. 1–3, pp. 414–421, 2011, doi: 10.1016/j.powtec.2010.11.028.

[113] W. Chen, R. N. Dave, R. Pfeffer, and O. Walton, ‘Numerical simulation of Mechanofusion system’, *Powder Technol.*, vol. 146, no. 1–2, pp. 121–136, 2004, doi: 10.1016/j.powtec.2004.07.014.

[114] Q. Zhou, B. Armstrong, I. Larson, P. J. Stewart, and D. A. V. Morton, ‘Improving powder flow properties of a cohesive lactose monohydrate powder by intensive mechanical dry coating’, *J. Pharm. Sci.*, vol. 99, no. 2, pp. 969–981, 2010, doi: 10.1002/jps.21885.

[115] T. Yokoyama, K. Urayama, M. Naito, M. Kato, and T. Yokoyama, ‘The Angmill Mechanofusion System and its Applications’, *KONA Powder Part. J.*, vol. 5, no. 9, pp. 59–68, 1987, doi: 10.14356/kona.1987011.

[116] F. Jay, V. Gauthier, and S. Dubois, ‘Iron particles coated with alumina: Synthesis by a mechanofusion process and study of the high-temperature oxidation resistance’, *J. Am. Ceram. Soc.*, vol. 89, no. 11, pp. 3522–3528, 2006, doi: 10.1111/j.1551-2916.2006.01266.x.

[117] L. Zheng, C. Wei, M. D. L. Garayt, J. MacInnis, and M. N. Obrovac, ‘Spherically Smooth Cathode Particles by Mechanofusion Processing’, *J. Electrochem. Soc.*, vol. 166, no. 13, pp. A2924–A2927, Aug. 2019, doi: 10.1149/2.0681913jes.

[118] L. Zheng, T. D. Hatchard, and M. N. Obrovac, ‘A high-quality mechanofusion coating for enhancing lithium-ion battery cathode material performance’, *MRS Commun.*, vol. 9, no. 1, pp. 245–250, Mar. 2019, doi: 10.1557/mrc.2018.209.

[119] N. Phattharasupakun *et al.*, ‘Core-shell Ni-rich NMC-Nanocarbon cathode from scalable solvent-free mechanofusion for high-performance 18650 Li-ion batteries’, *Energy Storage Mater.*, vol. 36, no. January, pp. 485–495, 2021, doi: 10.1016/j.ensm.2021.01.032.

[120] S. Liu *et al.*, ‘Enhancing Electrochemical Performance of LiNi0.6Co0.2Mn0.2O2 by Lithium-ion Conductor Surface Modification’, *Electrochimica Acta*, vol. 224, pp. 171–177, 2017, doi: 10.1016/j.electacta.2016.12.024.

[121] J. Wutthiprom, N. Phattharasupakun, C. Tomon, and M. Sawangphruk, ‘Scalable solvent-free mechanofusion and magnesiothermic reduction processes for obtaining carbon nanospheres-encapsulated crystalline silicon anode for Li-ion batteries’, *Electrochimica Acta*, vol. 352, p. 136457, 2020, doi: 10.1016/j.electacta.2020.136457.

[122] V. Wenzel, R. S. Moeller, and H. Nirschl, ‘Influence of Mixing Technology and the Potential to Modify the Morphological Properties of Materials used in the Manufacture of Lithium-Ion Batteries’, *Energy Technol.*, vol. 2, no. 2, pp. 176–182, Feb. 2014, doi: 10.1002/ente.201300091.

[123] J. Mun *et al.*, ‘New dry carbon nanotube coating of over-lithiated layered oxide cathode for lithium ion batteries’, *J. Mater. Chem. A*, vol. 2, no. 46, pp. 19670–19677, 2014, doi: 10.1039/c4ta04818k.

[124] C. D. Reynolds, P. R. Slater, S. D. Hare, M. J. H. Simmons, and E. Kendrick, ‘A review of metrology in lithium-ion electrode coating processes’, *Mater. Des.*, vol. 209, p. 109971, Nov. 2021, doi: 10.1016/j.matdes.2021.109971.

[125] ‘Exploring Uncharted Realms with Electron Microscopy’. ThermoFisher Scientific. Accessed: Feb. 19, 2024. [Online]. Available: https://assets.thermofisher.com/TFS-Assets/MSD/Handbooks/Exploring-uncharted-realms-with-electron-microscopy.pdf

[126] ‘Scanning Electron Microscopy | Nanoscience Instruments’. Accessed: Jun. 14, 2024. [Online]. Available: https://www.nanoscience.com/techniques/scanning-electron-microscopy/

[127] ‘Scanning electron microscopy (SEM), what is it for? - ATRIA Innovation’. Accessed: Jun. 30, 2024. [Online]. Available: https://atriainnovation.com/en/blog/scanning-electron-microscopy-uses/

[128] ‘What is EDS/EDX? - Nanoanalysis’, Oxford Instruments. Accessed: Jul. 01, 2024. [Online]. Available: https://nano.oxinst.com/campaigns/what-is-eds/edx

[129] ‘A Guide to Particle Characterization Techniques | Malvern Panalytical’. Accessed: Jun. 14, 2024. [Online]. Available: https://www.malvernpanalytical.com/en/learn/knowledge-center/whitepapers/wp120620basicguidepartchar

[130] I. Akseli *et al.*, ‘Reproducibility of the Measurement of Bulk/Tapped Density of Pharmaceutical Powders Between Pharmaceutical Laboratories’, *J. Pharm. Sci.*, vol. 108, no. 3, pp. 1081–1084, Mar. 2019, doi: 10.1016/j.xphs.2018.10.009.

[131] Granutools, ‘Bulk powder characterization to optimise battery manufacturing and performance’, Granutools. Accessed: Jul. 01, 2024. [Online]. Available: https://www.granutools.com/en/news/229_bulk-powder-characterization-to-optimise-battery-manufacturing-and-performance

[132] J. Fitzpatrick, ‘12 - Powder properties in food production systems’, in *Handbook of Food Powders*, B. Bhandari, N. Bansal, M. Zhang, and P. Schuck, Eds., in Woodhead Publishing Series in Food Science, Technology and Nutrition. , Woodhead Publishing, 2013, pp. 285–308. doi: 10.1533/9780857098672.2.285.

[133] C. D. Reynolds, S. D. Hare, P. R. Slater, M. J. H. Simmons, and E. Kendrick, ‘Rheology and Structure of Lithium-Ion Battery Electrode Slurries’, *Energy Technol.*, vol. 10, no. 10, p. 2200545, 2022, doi: 10.1002/ente.202200545.

[134] L. A. Middlemiss, A. J. R. Rennie, R. Sayers, and A. R. West, ‘Characterisation of batteries by electrochemical impedance spectroscopy’, *Energy Rep.*, vol. 6, pp. 232–241, May 2020, doi: 10.1016/j.egyr.2020.03.029.

[135] ‘Four-Probe Method | Sheet Resistance Formula’, Ossila. Accessed: Jul. 01, 2024. [Online]. Available: https://www.ossila.com/pages/sheet-resistance-theory

[136] S.-J. Sim, S.-H. Lee, B.-S. Jin, and H.-S. Kim, ‘Use of carbon coating on LiNi0.8Co0.1Mn0.1O2 cathode material for enhanced performances of lithium-ion batteries’, *Sci. Rep.*, vol. 10, p. 11114, Jul. 2020, doi: 10.1038/s41598-020-67818-5.

[137] C. Zihrul, M. Lippke, and A. Kwade, ‘Model Development for Binder Migration within Lithium-Ion Battery Electrodes during the Drying Process’, *Batteries*, vol. 9, no. 9, Art. no. 9, Sep. 2023, doi: 10.3390/batteries9090455.

[138] ‘Rheology and Structure of Lithium-Ion Battery Electrode Slurries - Reynolds - 2022 - Energy Technology - Wiley Online Library’. Accessed: Jan. 10, 2024. [Online]. Available: https://onlinelibrary.wiley.com/doi/full/10.1002/ente.202200545

[139] S. Lu and D. D. L. Chung, ‘Viscoelastic behavior of carbon black and its relationship with the aggregate size’, *Carbon*, vol. 60, pp. 346–355, Aug. 2013, doi: 10.1016/j.carbon.2013.04.047.

[140] R. Sharma and G. Setia, ‘Mechanical dry particle coating on cohesive pharmaceutical powders for improving flowability - A review’, *Powder Technol.*, vol. 356, pp. 458–479, 2019, doi: 10.1016/j.powtec.2019.08.009.

[141] Z. Gao, J. Fu, C. Podder, X. Gong, Y. Wang, and H. Pan, ‘Particle interactions during dry powder mixing and their effect on solvent-free manufactured electrode properties’, *J. Energy Storage*, vol. 83, p. 110605, Apr. 2024, doi: 10.1016/j.est.2024.110605.

[142] S. S. Nisa *et al.*, ‘A Fast Approach to Obtain Layered Transition-Metal Cathode Material for Rechargeable Batteries’, *Batteries*, vol. 8, no. 1, Art. no. 1, Jan. 2022, doi: 10.3390/batteries8010004.

[143] ‘Carbon Black’, NETZSCH - Analyzing and Testing. Leading in Thermal Analysis, Rheology and Fire Testing. Accessed: Mar. 27, 2024. [Online]. Available: https://analyzing-testing.netzsch.com/en/training-know-how/glossary/carbon-black

[144] G. Wu, S. Asai, and M. Sumita, ‘Carbon Black as a Self-Diagnosing Probe To Trace Polymer Dynamics in Highly Filled Compositions’, *Macromolecules*, vol. 35, no. 5, pp. 1708–1713, Feb. 2002, doi: 10.1021/ma011658f.

[145] S. Wang, M. Yan, Y. Li, C. Vinado, and J. Yang, ‘Separating electronic and ionic conductivity in mix-conducting layered lithium transition-metal oxides’, *J. Power Sources*, vol. 393, pp. 75–82, Jul. 2018, doi: 10.1016/j.jpowsour.2018.05.005.

[146] R. Amin and Y.-M. Chiang, ‘Characterization of Electronic and Ionic Transport in Li1-xNi0.33Mn0.33Co0.33O2 (NMC333) and Li1-xNi0.50Mn0.20Co0.30O2 (NMC523) as a Function of Li Content’, *J. Electrochem. Soc.*, vol. 163, no. 8, p. A1512, May 2016, doi: 10.1149/2.0131608jes.

[147] I. Saadoune and C. Delmas, ‘On the LixNi0.8Co0.2O2System’, *J. Solid State Chem.*, vol. 136, no. 1, pp. 8–15, Feb. 1998, doi: 10.1006/jssc.1997.7599.

[148] A. Jetybayeva *et al.*, ‘Unraveling the State of Charge-Dependent Electronic and Ionic Structure–Property Relationships in NCM622 Cells by Multiscale Characterization’, *ACS Appl. Energy Mater.*, vol. 5, no. 2, pp. 1731–1742, Feb. 2022, doi: 10.1021/acsaem.1c03173.

[149] E. M. Dannenberg, ‘Carbon Black Dispersion and Reinforcement’, *Rubber Chem. Technol.*, vol. 25, no. 4, pp. 843–857, Dec. 1952, doi: 10.5254/1.3543445.

[150] R. J. Cembrola, ‘The relationship of carbon black dispersion to electrical resistivity and vulcanizate physical properties’, *Polym. Eng. Sci.*, vol. 22, no. 10, pp. 601–609, 1982, doi: 10.1002/pen.760221004.

[151] E. Hayakawa, H. Nakamura, S. Ohsaki, and S. Watano, ‘Dry mixing of cathode composite powder for all-solid-state batteries using a high-shear mixer’, *Adv. Powder Technol.*, vol. 33, no. 8, p. 103705, Aug. 2022, doi: 10.1016/j.apt.2022.103705.

[152] W. Haselrieder *et al.*, ‘Influence of formulation method and related processes on structural, electrical and electrochemical properties of LMS/NCA-blend electrodes’, *Prog. Solid State Chem.*, vol. 42, no. 4, pp. 157–174, Dec. 2014, doi: 10.1016/j.progsolidstchem.2014.04.009.

[153] R. Habermann, ‘NOBILTA™ - Solids mixing with high energy intensity’, *Keram. Z.*, vol. 59, no. 4, pp. 254–259, 2007.

[154] H. Darmstadt, S. Kaliaguine, and C. Roy, ‘Electrical conductivity of conductive carbon blacks: influence of surface chemistry and topology’, *Appl. Surf. Sci.*, vol. 217, no. 1–4, pp. 181–193, Jul. 2003, doi: 10.1016/S0169-4332(03)00550-6.

[155] J. Hou *et al.*, ‘Platinum-group-metal catalysts for proton exchange membrane fuel cells: From catalyst design to electrode structure optimization’, *EnergyChem*, vol. 2, no. 1, p. 100023, Jan. 2020, doi: 10.1016/j.enchem.2019.100023.

[156] K. Jurkiewicz, M. Pawlyta, and A. Burian, ‘Structure of Carbon Materials Explored by Local Transmission Electron Microscopy and Global Powder Diffraction Probes’, *C*, vol. 4, no. 4, Art. no. 4, Dec. 2018, doi: 10.3390/c4040068.

[157] K. L. Lu, R. M. Lago, Y. K. Chen, M. L. H. Green, P. J. F. Harris, and S. C. Tsang, ‘Mechanical damage of carbon nanotubes by ultrasound’, *Carbon*, vol. 34, no. 6, pp. 814–816, Jan. 1996, doi: 10.1016/0008-6223(96)89470-X.

[158] Y. Y. Huang and E. M. Terentjev, ‘Dispersion of Carbon Nanotubes: Mixing, Sonication, Stabilization, and Composite Properties’, *Polymers*, vol. 4, no. 1, Art. no. 1, Mar. 2012, doi: 10.3390/polym4010275.

[159] A. Lekawa-Raus, J. Patmore, L. Kurzepa, J. Bulmer, and K. Koziol, ‘Electrical Properties of Carbon Nanotube Based Fibers and Their Future Use in Electrical Wiring’, *Adv. Funct. Mater.*, vol. 24, no. 24, pp. 3661–3682, 2014, doi: 10.1002/adfm.201303716.

[160] L. Ouyang *et al.*, ‘The effect of solid content on the rheological properties and microstructures of a Li-ion battery cathode slurry’, *RSC Adv.*, vol. 10, no. 33, pp. 19360–19370, May 2020, doi: 10.1039/D0RA02651D.

[161] K. M. Kim, W. S. Jeon, I. J. Chung, and S. H. Chang, ‘Effect of mixing sequences on the electrode characteristics of lithium-ion rechargeable batteries’, *J. Power Sources*, vol. 83, no. 1, pp. 108–113, Oct. 1999, doi: 10.1016/S0378-7753(99)00281-5.

[162] J. C. Li, Y. Wang, and D. C. Ba, ‘Characterization of Semiconductor Surface Conductivity by Using Microscopic Four-Point Probe Technique’, *Phys. Procedia*, vol. 32, pp. 347–355, Jan. 2012, doi: 10.1016/j.phpro.2012.03.568.

Appendix A SEM Micrographs

A.1 CBD Bridge and Film Structures

94:4:2

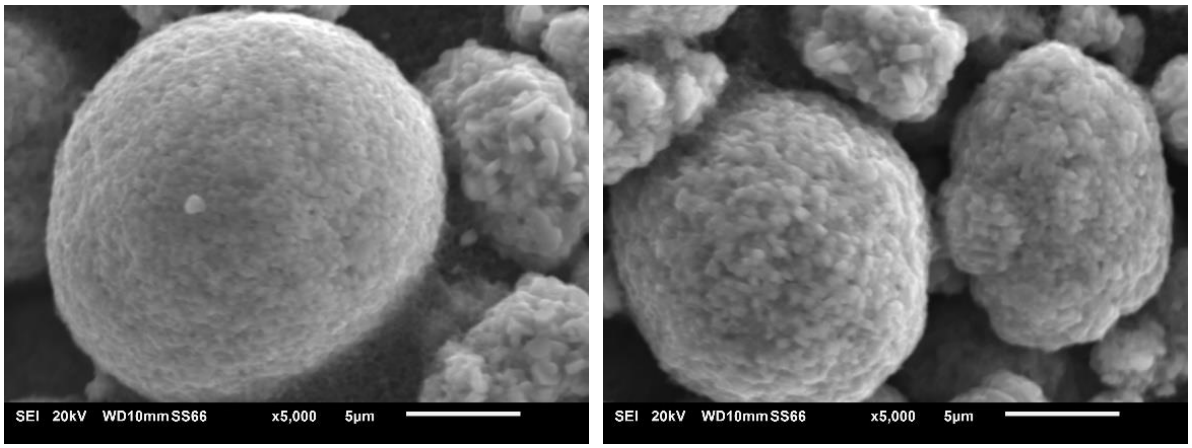

95:3:2

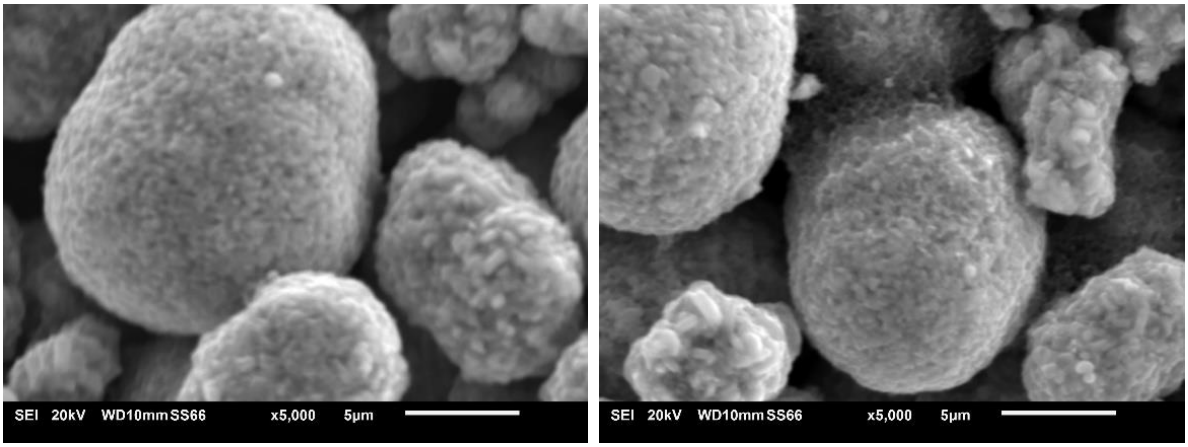

96:2:2

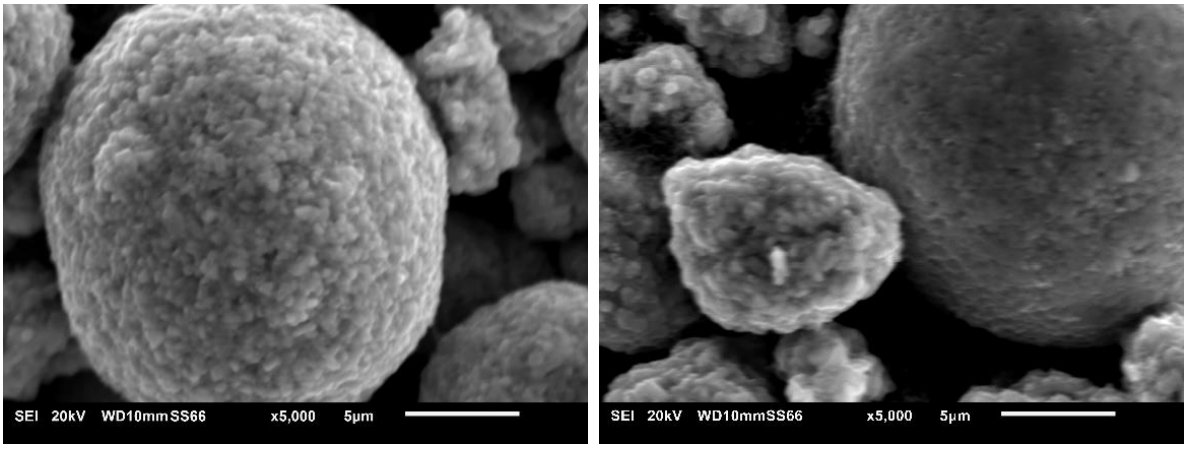

97:1:2

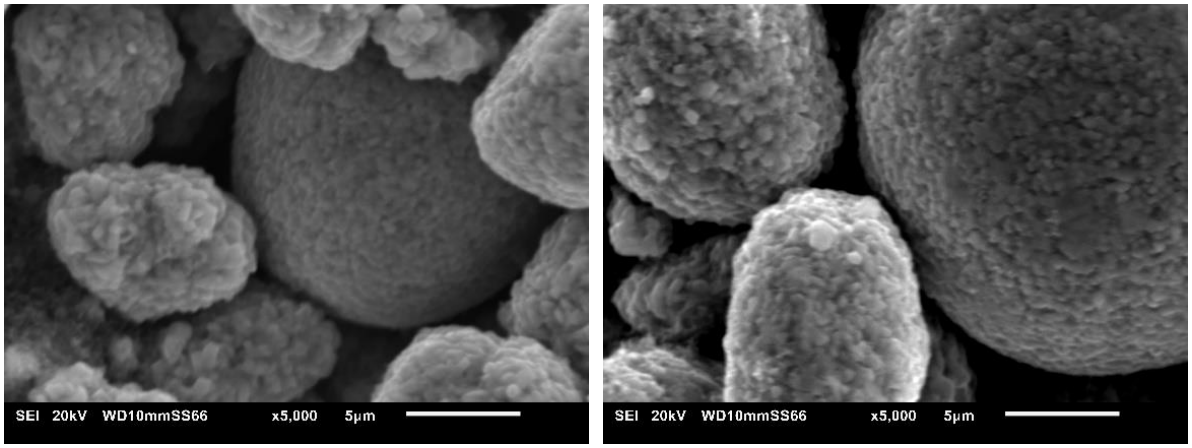

Figure A.1: SEM micrographs of electrodes with formulations of 94:4:2, 95:3:2, 96:2:2 and 97:1:2 (NMC622:C65:PVDF wt%).

A.2 Differences in Carbon Black Structures

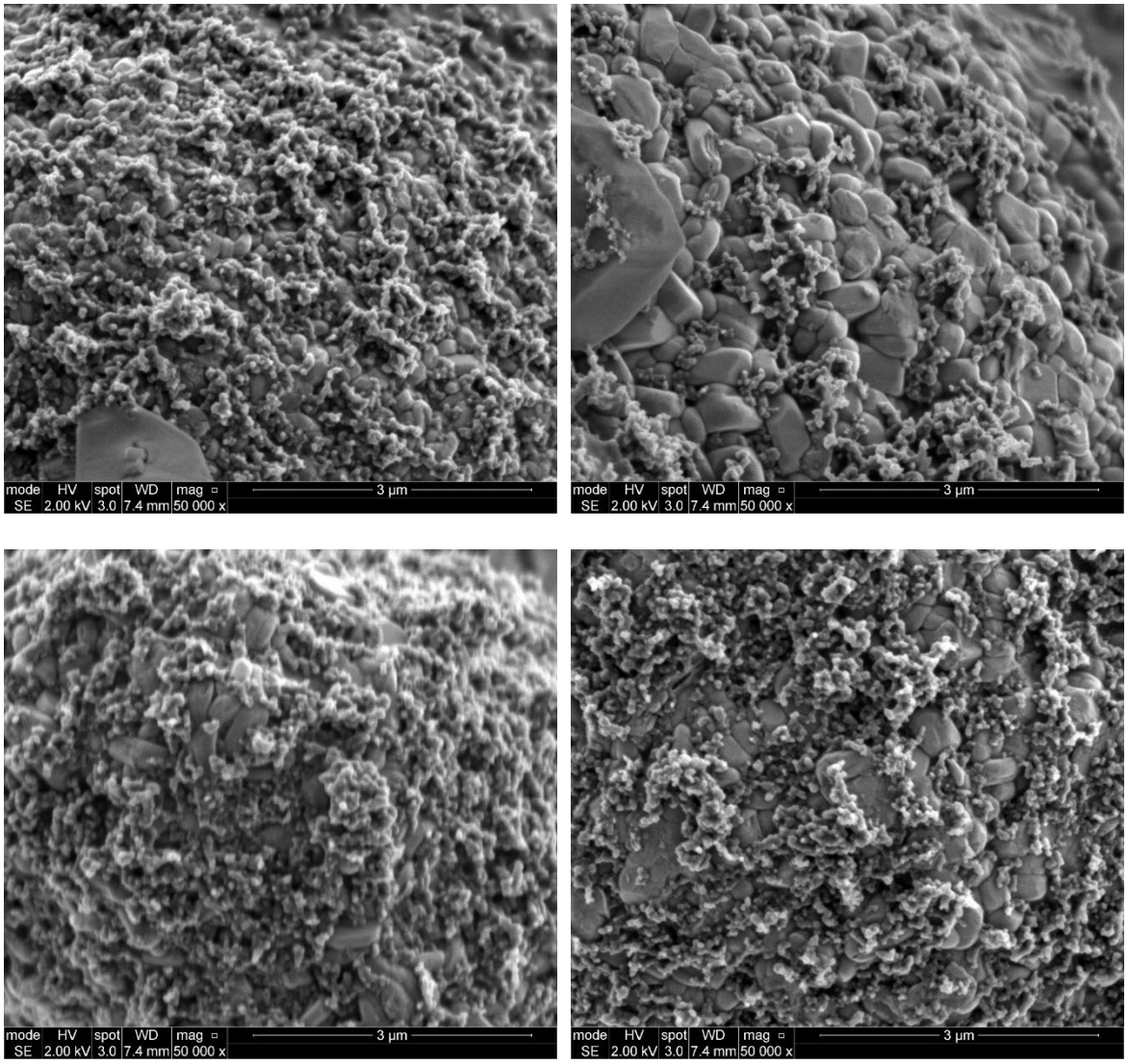

Figure A.2: SEM micrographs of NMC622 particle surface coated with carbon black with 2 wt% C65 and mixing time of 2 min.

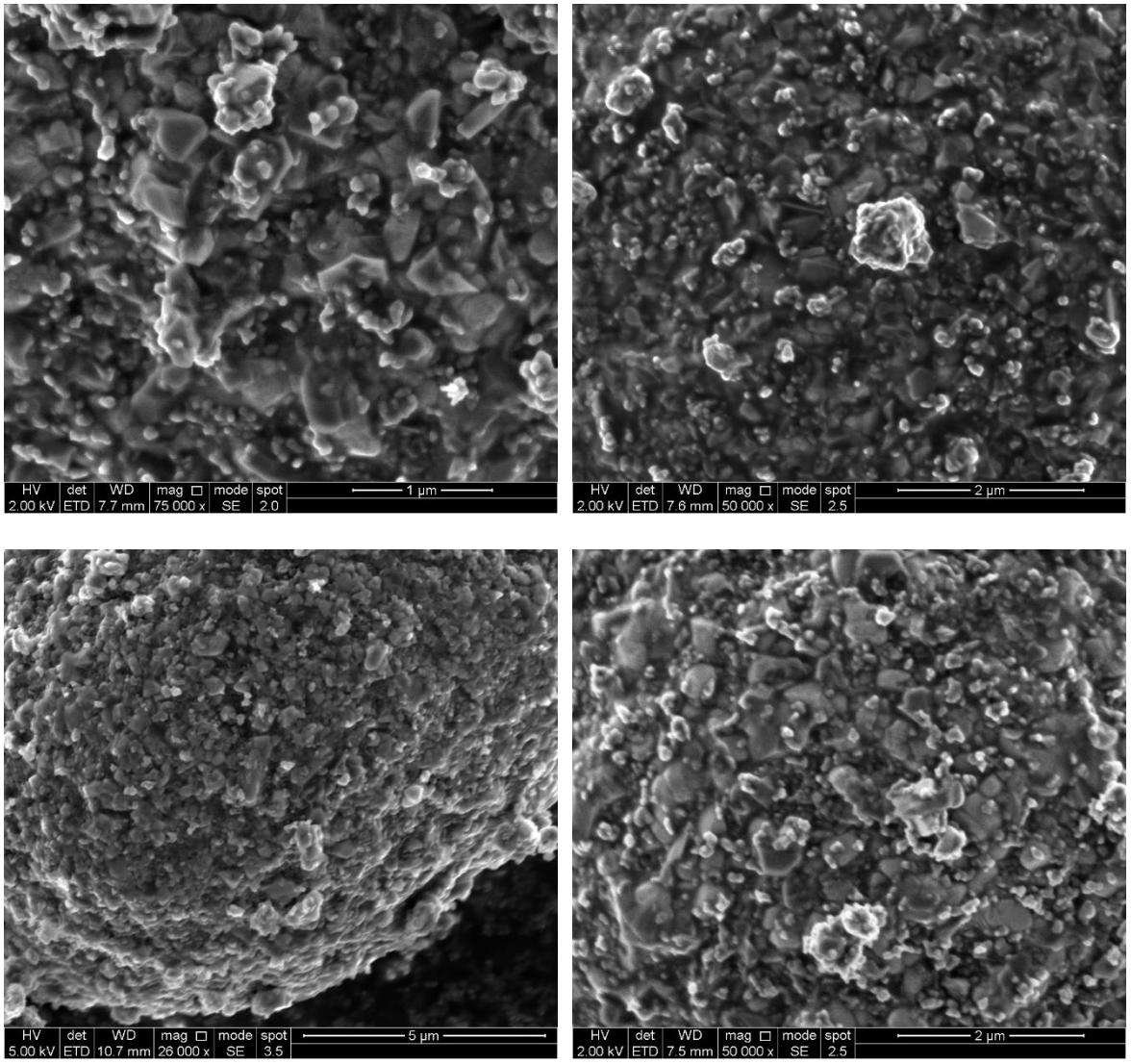

Figure A.3: SEM micrographs of NMC622 particle surface coated with carbon black with 2 wt% C65 and mixing time of 60 min.

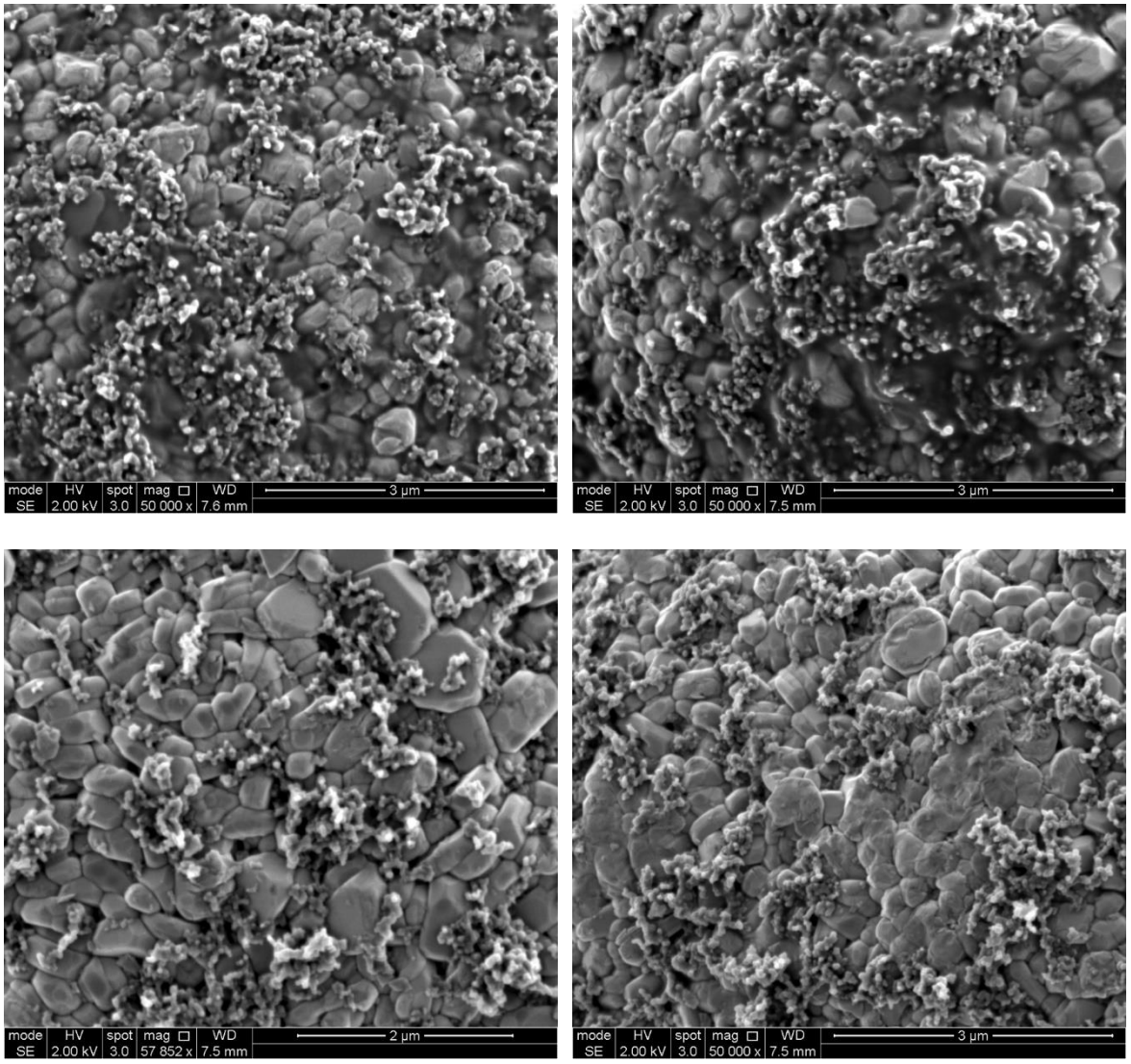

Figure A.4: SEM micrographs of NMC622 particle surface coated with carbon black with 10 wt% C65 and mixing time of 2 min.

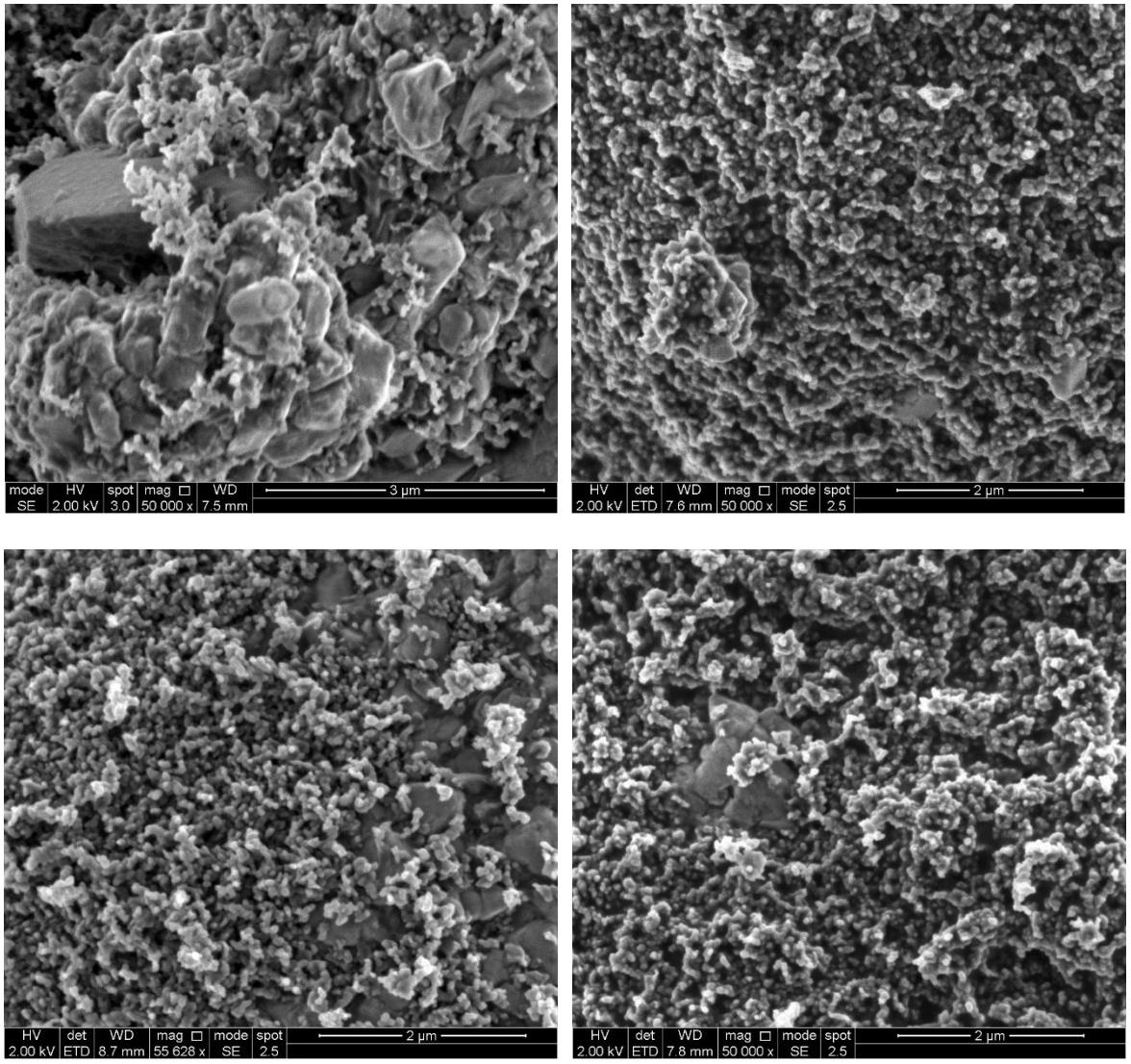

Figure A.5: SEM micrographs of NMC622 particle surface coated with carbon black with 10 wt% C65 and mixing time of 60 min.

A.3 CNT1015-Coated NMC Particles

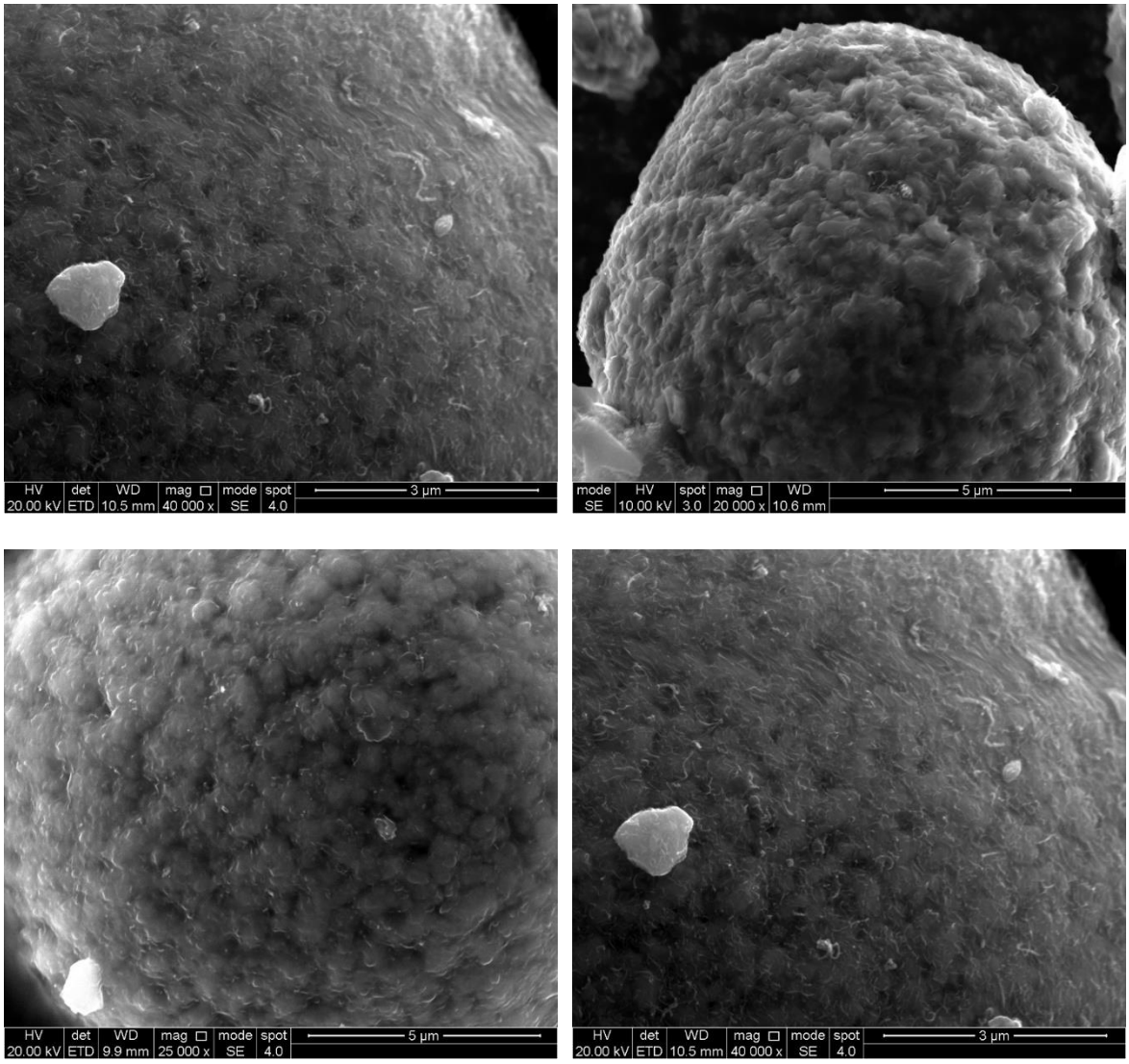

Figure A.6: SEM micrographs of CNT1015-coated NMC surface with visible CNT strands.

A.4 CNT3080-Coated NMC Particles

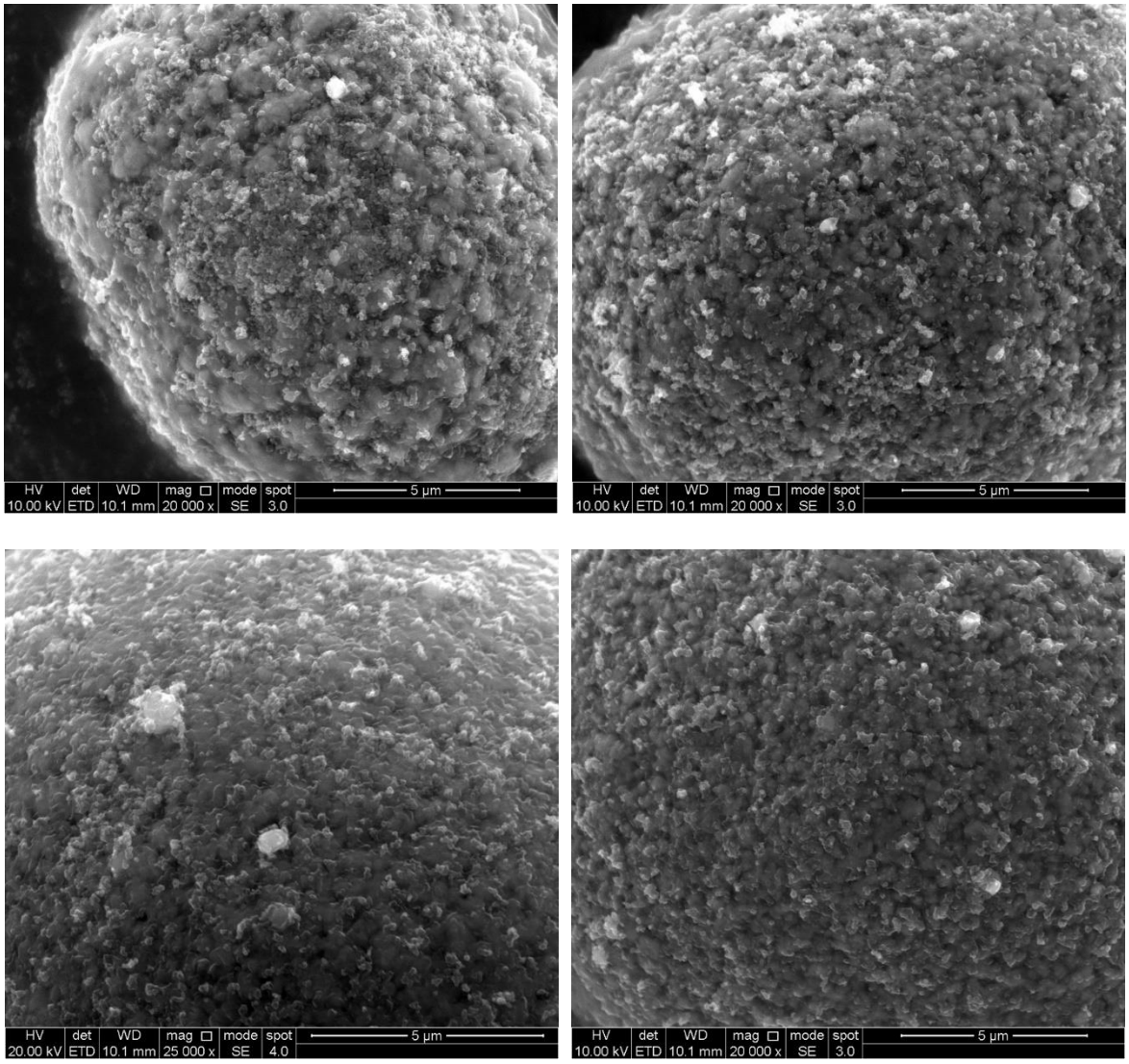

Figure A.7: SEM micrographs of CNT3080-coated NMC surface with visible CNT strands and aggregates.

A.5 Conventional Wet Slurry Mixed Electrodes

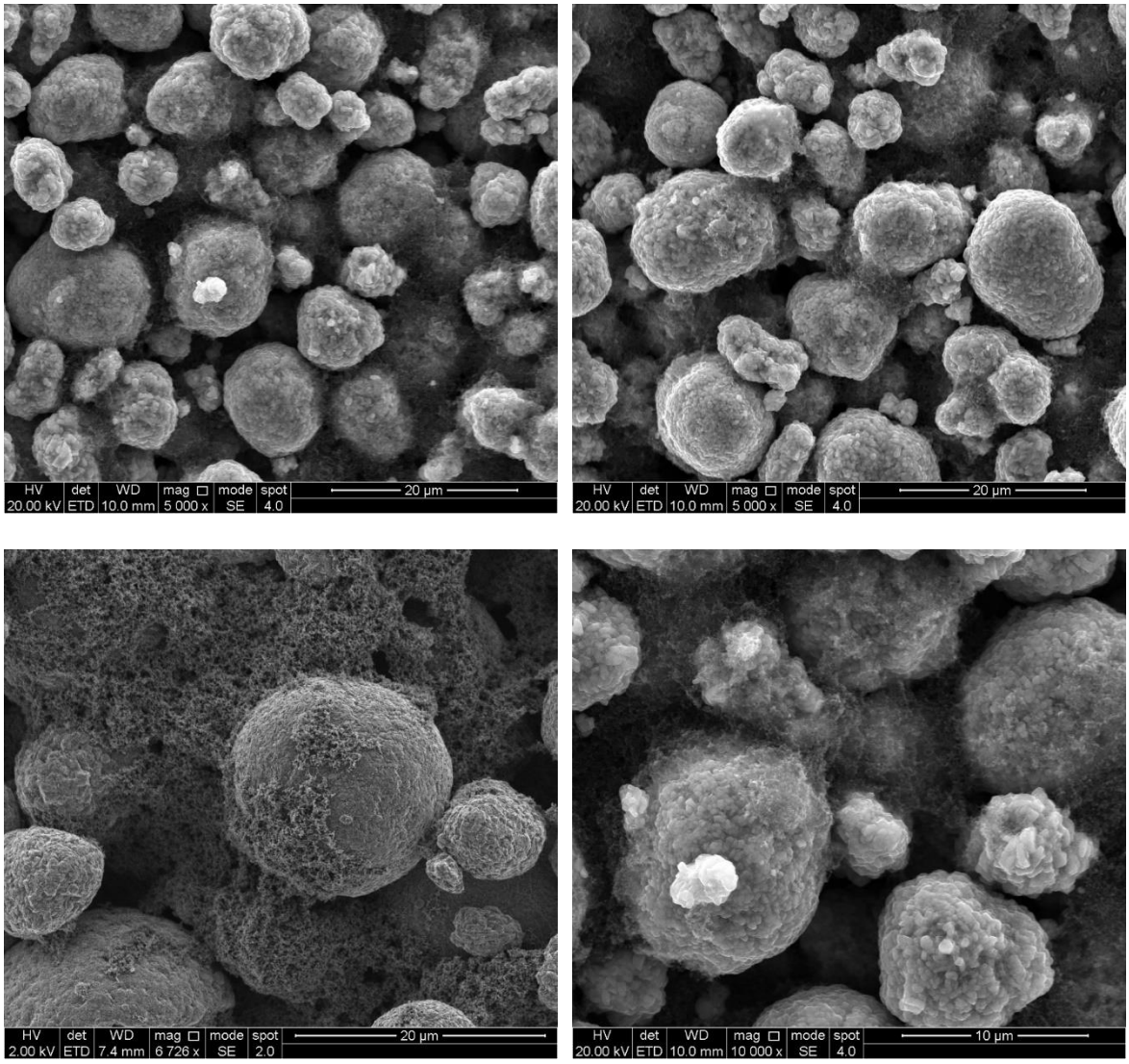

Figure A.8: SEM micrograph (top view) of a conventional wet slurry mixed electrode with 2 wt% C65.

A.6 Short-Range Pathway Dominated Electrodes

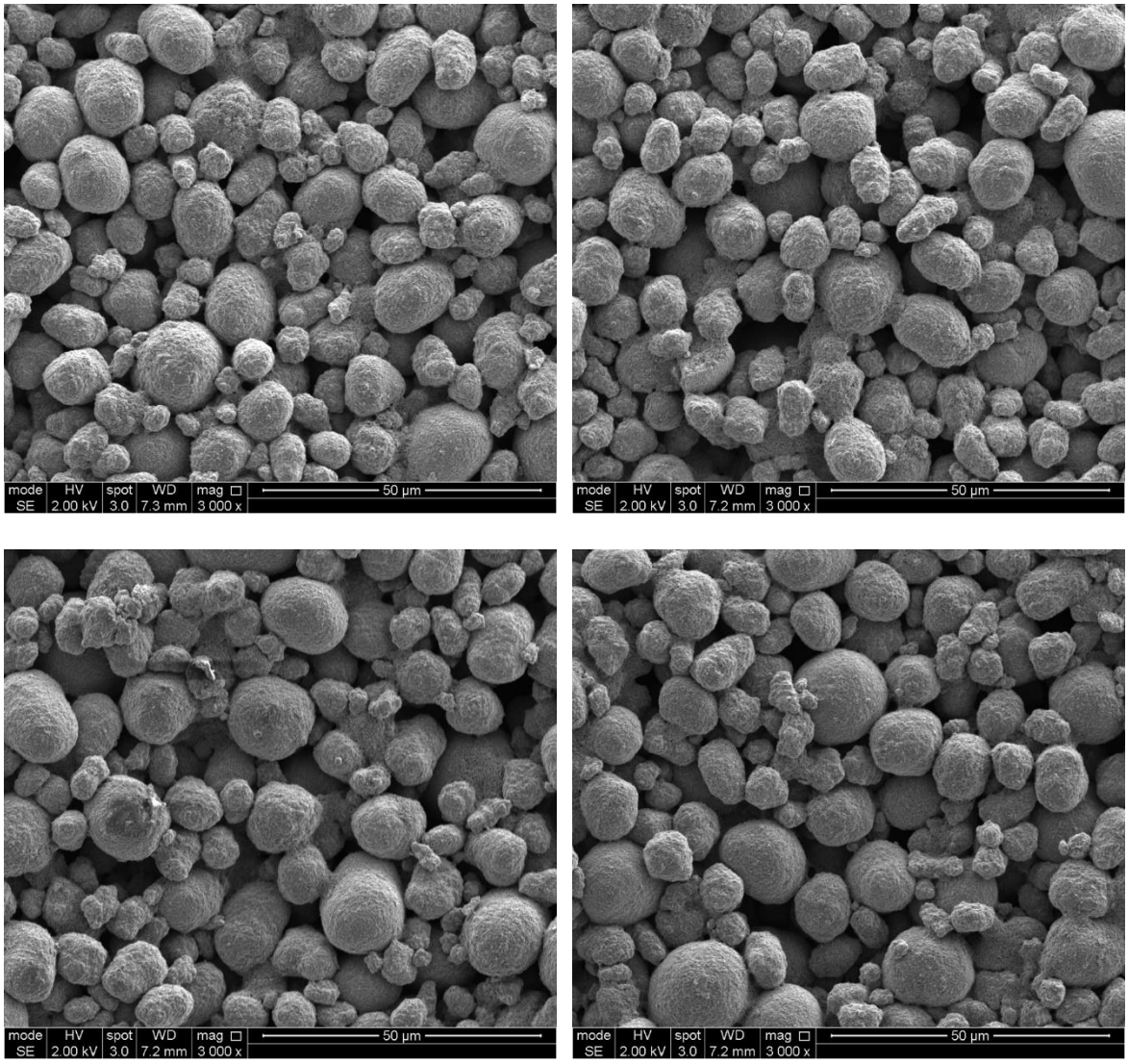

Figure A.9: SEM micrograph (top view) of short-range pathway dominated electrodes containing NMC particles dry mixed with 2 wt% C65 for 2 min.

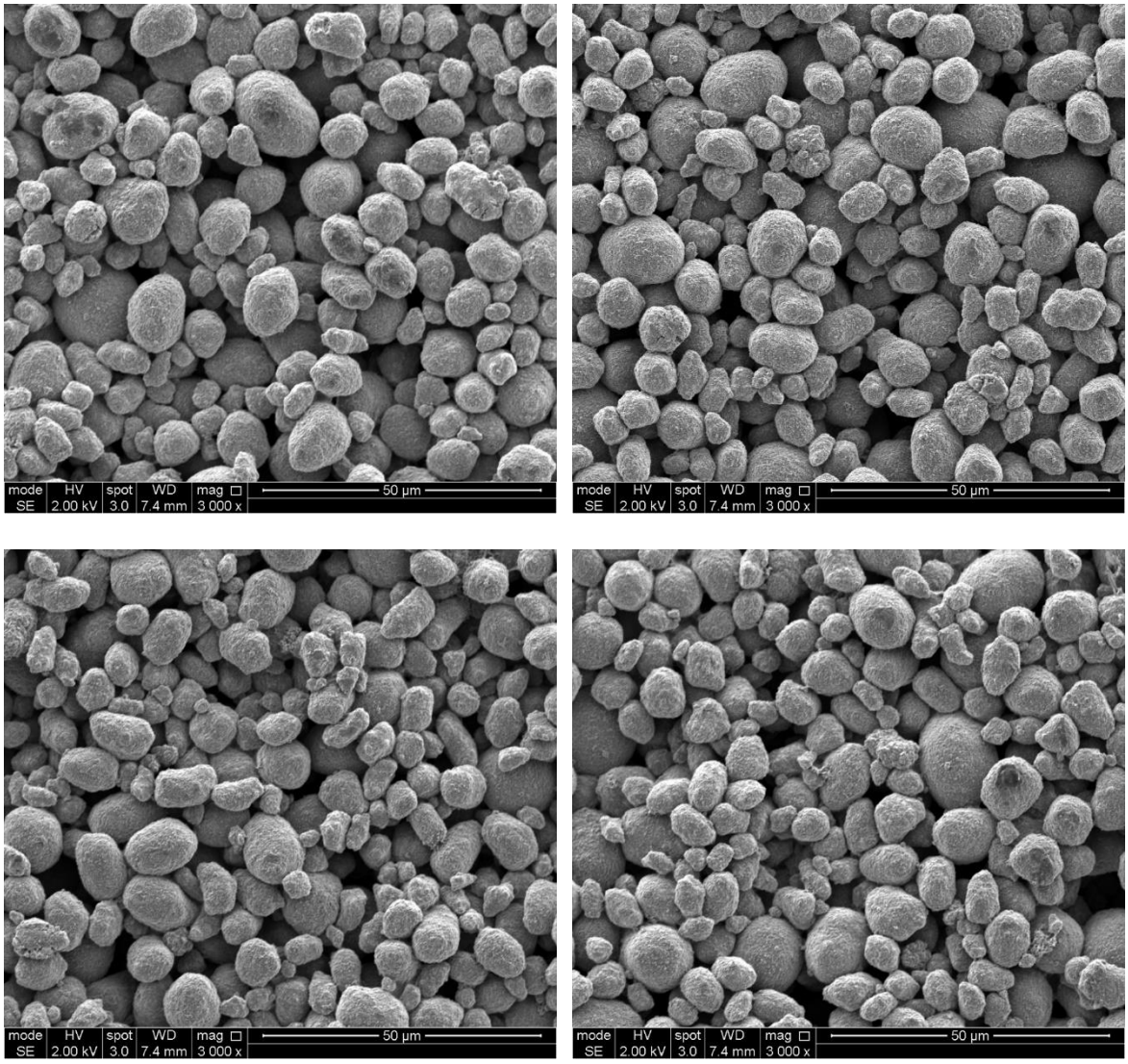

Figure A.10: SEM micrograph (top view) of short-range pathway dominated electrodes containing NMC particles dry mixed with 2 wt% C65 for 60 min.

A.7 Equal Distribution of Short and Long-Range Pathway Electrodes

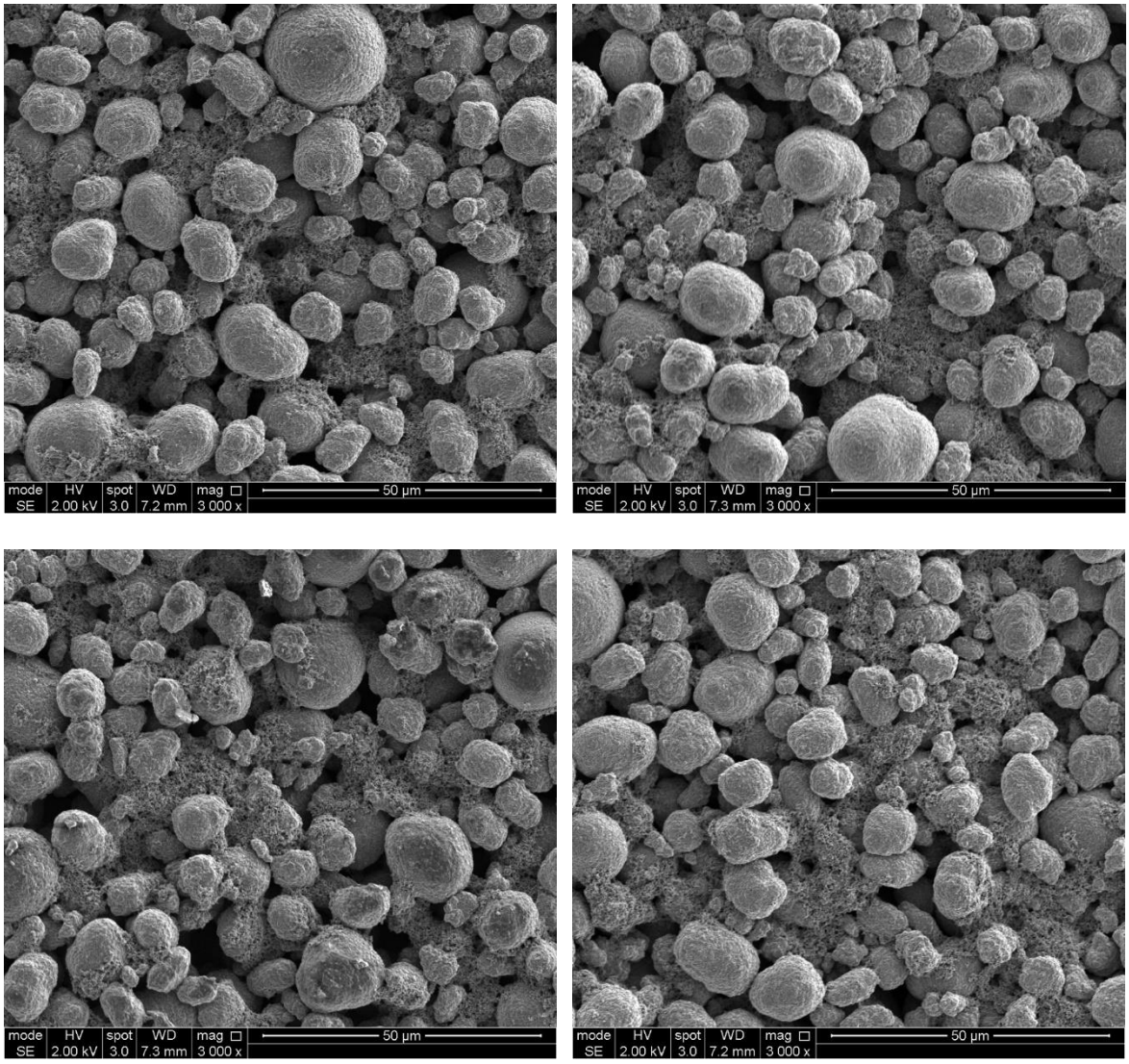

Figure A.11: SEM micrographs (top view) of equal distribution of short and long-range pathway electrodes where 1 wt% C65 was dry mixed with NMC622 for 2 min. The remaining 1 wt% of C65 was added during wet mixing.

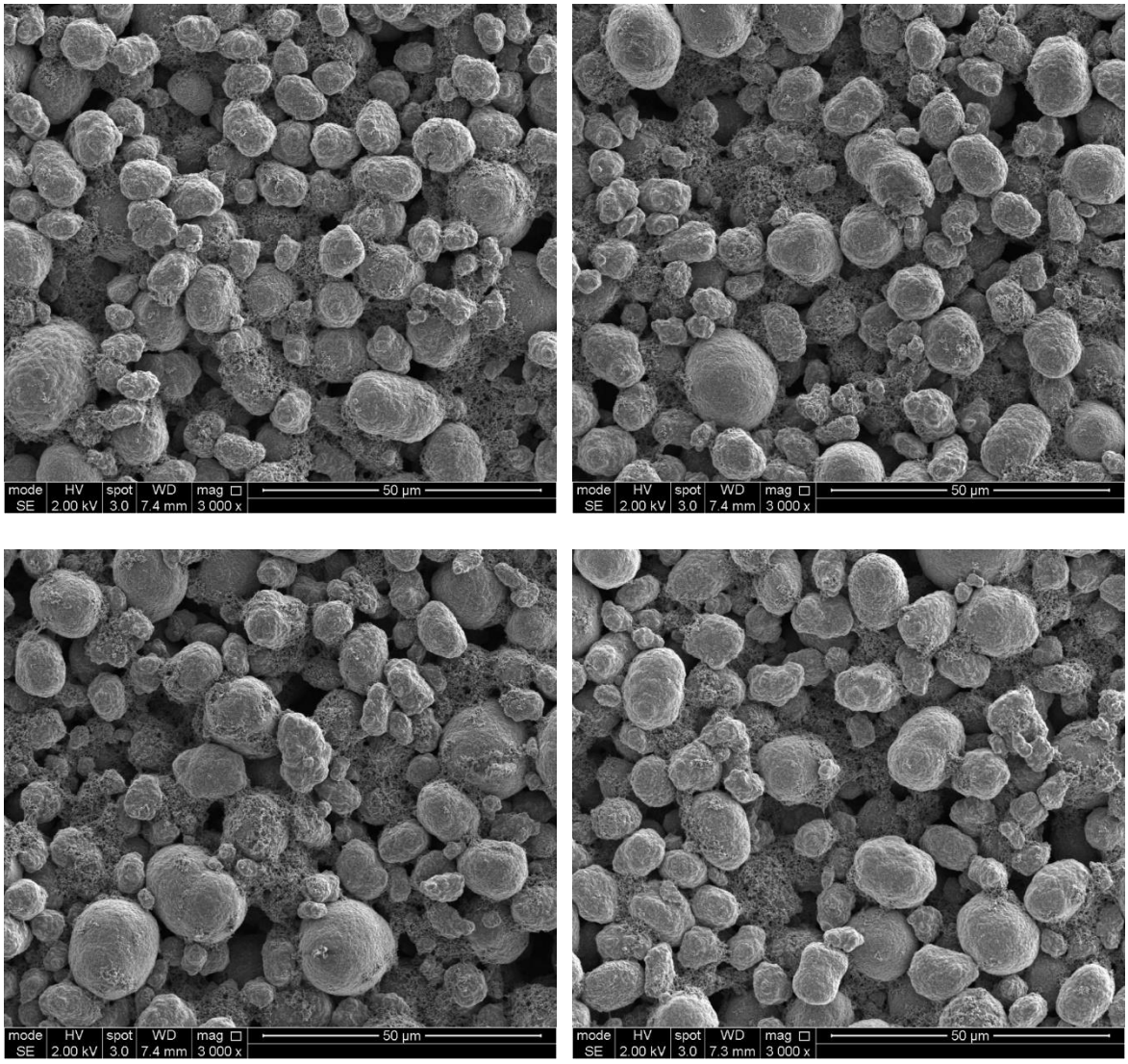

Figure A.12: SEM micrographs (top view) of equal distribution of short and long-range pathway electrodes where 1 wt% C65 was dry mixed with NMC622 for 60 min. The remaining 1 wt% of C65 was added during wet mixing.

A.8 Long-Range Pathway Dominated Electrodes

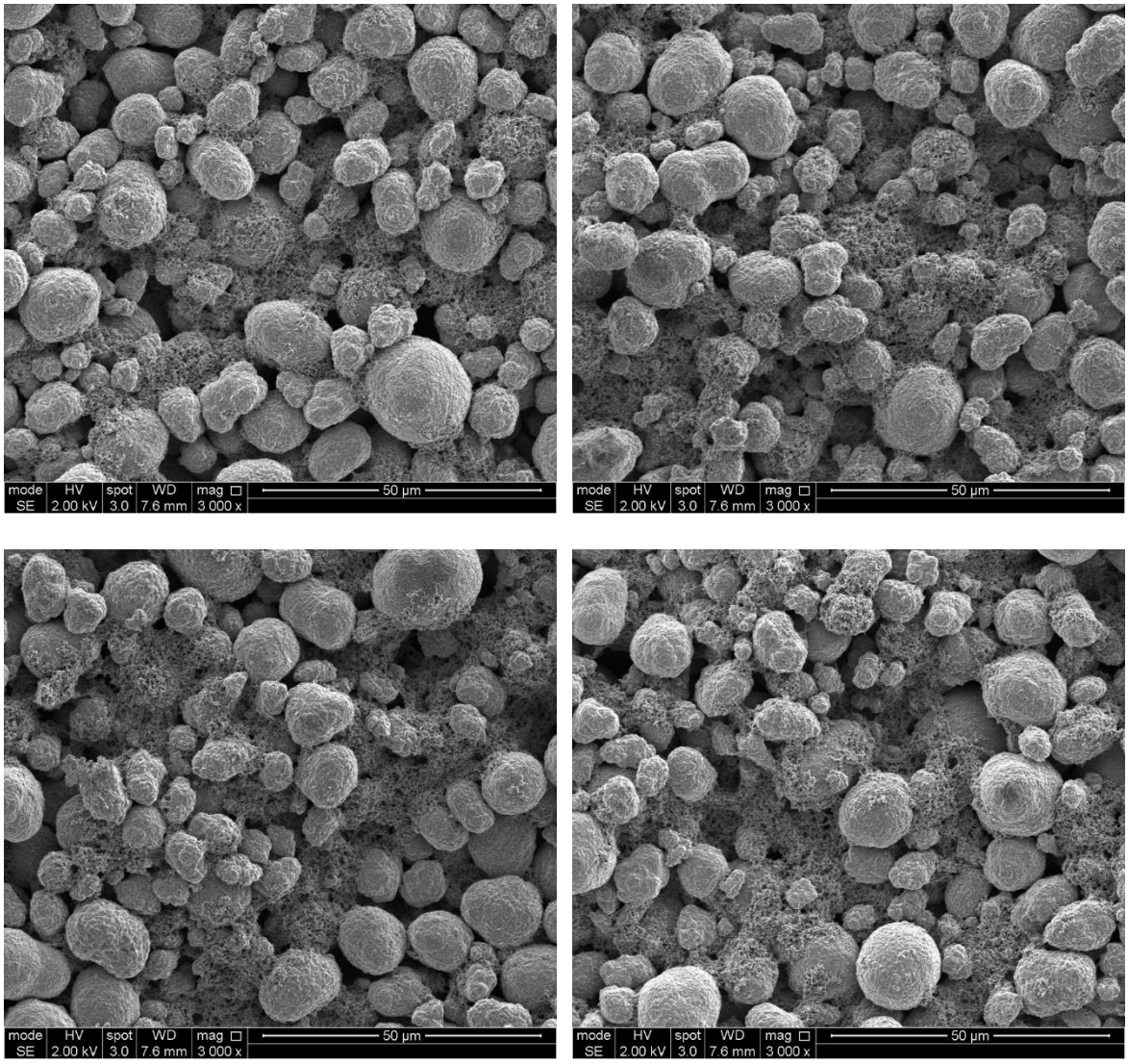

Figure A.13: SEM micrographs (top view) of long-range dominated pathway electrodes where 0.5 wt% C65 was dry mixed with NMC622 for 2 min. The remaining 1.5 wt% of C65 was added during wet mixing.

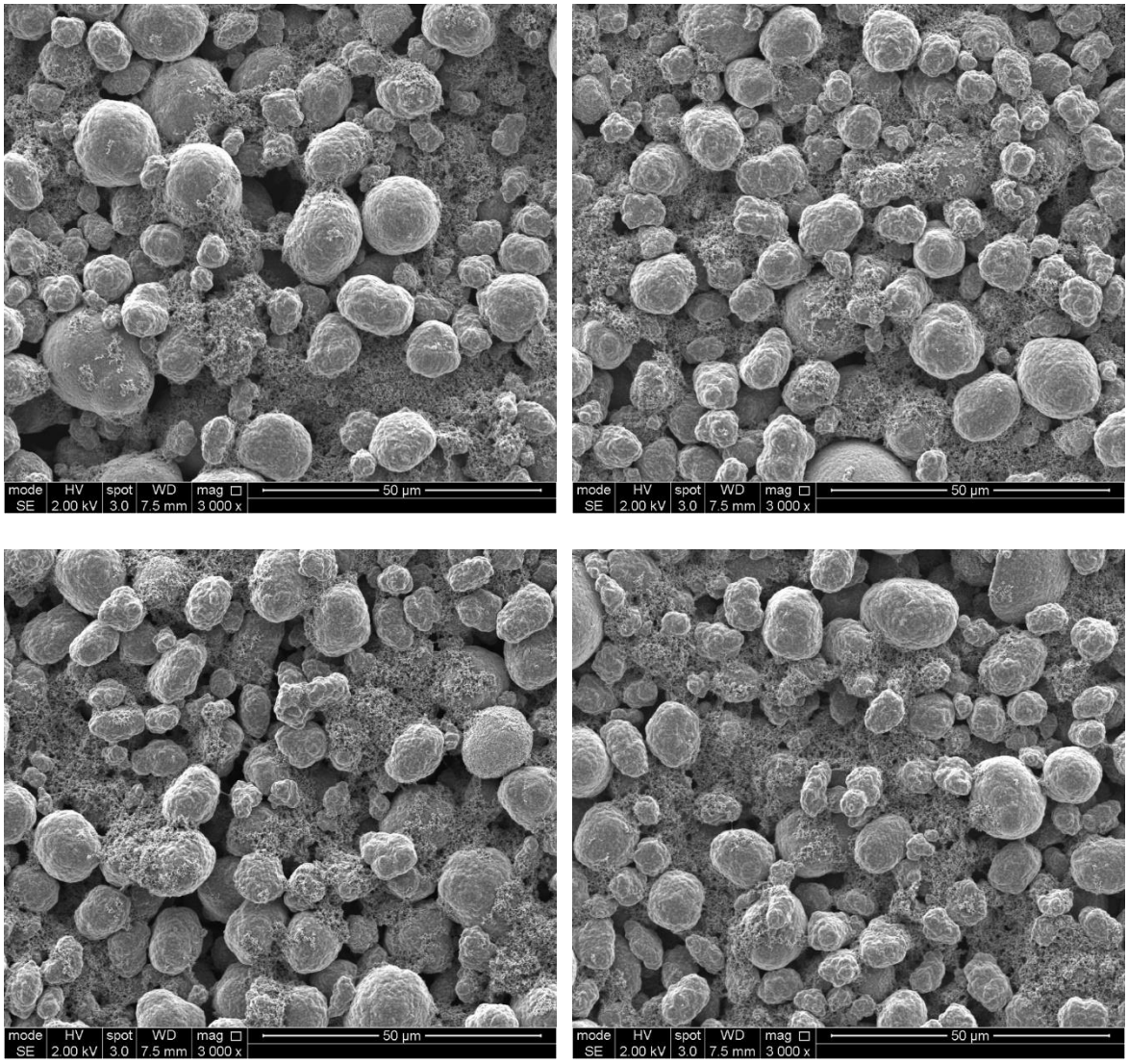

Figure A.14: SEM micrographs (top view) of long-range dominated pathway electrodes where 0.5 wt% C65 was dry mixed with NMC622 for 60 min. The remaining 1.5 wt% of C65 was added during wet mixing.

Appendix B Carbon Black Properties

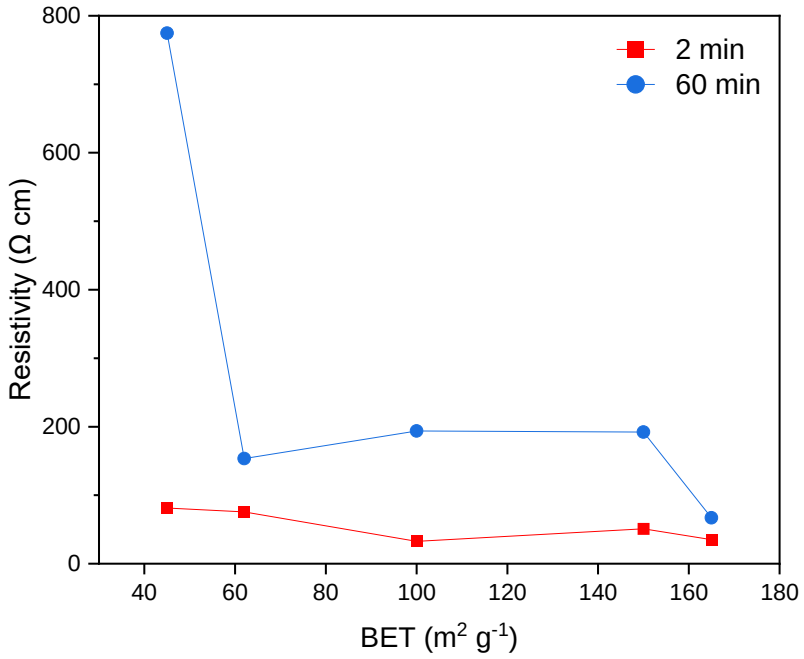

Figure B.1: Change in resistivity of powder mixtures of NMC with 2 wt% of carbon black against the BET surface area of different carbon blacks.

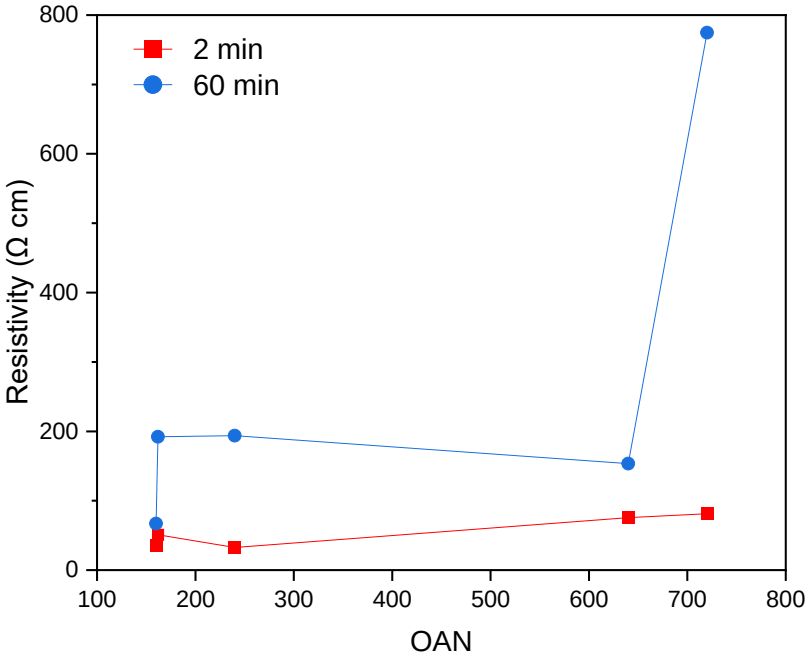

Figure B.2: Change in resistivity of powder mixtures of NMC with 2 wt% of carbon black against the OAN of different carbon blacks.

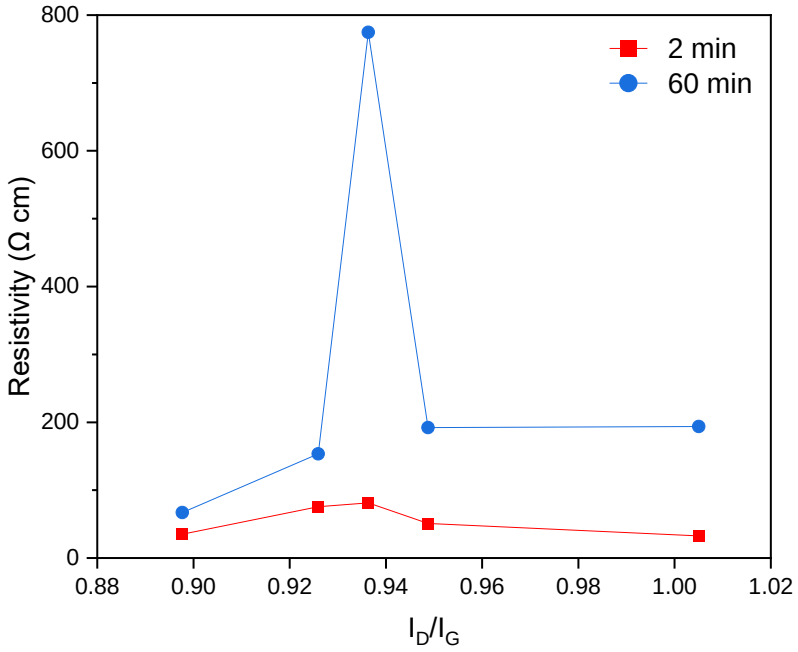

Figure B.3: Change in resistivity of powder mixtures of NMC with 2 wt% of carbon black against the I_D/I_G of different carbon blacks.